Philipps Universität Marburg

Control of morphogenesis in the budding Alphaproteobacterium *Hyphomonas neptunium*

Dissertation
zur Erlangung des Doktorgrades
der Naturwissenschaften
(Dr. rer. nat.)

dem
Fachbereich Biologie
der Philipps-Universität Marburg

von

Emőke Cserti

aus Budapest, Ungarn

Marburg (Lahn), Juli 2016

Vom Fachbereich Biologie der Philipps-Universität Marburg (HKZ: 1180)

als Dissertation angenommen am __.__.2016

Erstgutachter: Prof. Dr. Martin Thanbichler

Zweitgutachter: Prof. Dr. Peter Graumann

Tag der mündlichen Prüfung: 26.09.2016

Die Untersuchungen zur vorliegenden Arbeit wurden von Oktober 2011 bis September 2014 am Max-Planck-Institut für terrestrische Mikrobiologie und von Oktober 2014 bis Mai 2016 am Fachbereich Biologie unter der Leitung von Prof. Dr. Martin Thanbichler durchgeführt.

Die während der Promotion erzielten Ergebnisse sind zum Teil in folgenden Originalpublikationen veröffentlicht:

Cserti E, Klingl A, Kanngießer S, and Thanbichler M. (2016) Bactofilins coordinate cell growth and stalk biogenesis in *Hyphomonas neptunium* (in Vorbereitung)

Cserti E, Rosskopf S, Chang YW, Eisheuer S, Regh C, Jensen G, Thanbichler M. (2016) Dynamics of the peptidoglycan biogenesis machinery during budding in *Hyphomonas neptunium* (eingereicht)

Ergebnisse aus in dieser Dissertation nicht erwähnten Projekten sind in folgenden Orginalpublikationen veröffentlicht:

Jung A, Eisheuer S*, **Cserti E***, Leicht O, Strobel W, Möll A, Schlimpert S, Kühn J, and Thanbichler M. (2015) Molecular Toolbox for Genetic Manipulation of the Stalked Budding Bacterium *Hyphomonas neptunium*. Appl Environ Microbiol 81:736-744.

*contributed equally to this work

Családomnak

Abstract

The size and shape of bacteria are manifold just as their modes of propagation. The cell wall, composed of peptidoglycan (PG), is the major cell shape determinant in most bacteria. So far research on spatiotemporal coordination of morphology and cell division has mainly focused on rod-shaped bacteria like *Escherichia coli* and *Bacillus subtilis*. In this study, we investigate the dimorphic Alphaproteobacteria *Hyphomonas neptunium* as a new model organism for the study of asymmetric morphology and reproduction by budding at the distal end of a stalk.

Our goal was to comprehensively analyse the growth mode and budding mechanism of *H. neptunium*. Detailed electron cryo-tomography images revealed that, unlike previously suggested, the stalk and the bud form a continuum with the mother cell up until cell division. We show that during budding the daughter cell incorporates part of the stalk belonging to the mother cell to complete its own growth. Furthermore, we demonstrate that *H. neptunium* can accomplish more replicative cycles than previously proposed. By monitoring the incorporation of nascent PG with HADA, we identified four different growth phases in *H. neptunium* that can be divided into dispersed (swarmer cell growth and bud formation) and zonal growth (stalk biogenesis and cell division). PG composition analysis revealed a very high PG turnover rate as well as an unusually high incorporation of glycine instead of alanine at the 5^{th} position of the stem peptide. A comprehensive analysis of the PG biosynthesis machinery in *H. neptunium* shows that the conserved actin homologue MreB, the PG synthases PBP2 and PBP3, and the PG hydrolase LmdC play a vital role in cell growth in *H. neptunium*. Polar PG biogenesis seems to be modulated by an array of mostly redundant synthases and hydrolases, in which LD-transpeptidases do not partake. We postulate that the morphological asymmetry of *H. neptunium* underlies a much more complex intracellular asymmetry determined by distinct, multiple sites of dispersed and zonal growth.

To maintain its correct cell shape, *H. neptunium* requires MreB as well as a coiled-coil rich protein termed CCRP and the non-canonical bactofilins, which are a new class of nucleotide-independent polymer-forming cytoskeletal elements. Upon inhibition of MreB with A22 or MP265, cells become increasingly spherical and eventually cease growing. The deletion of *ccrp* causes elongated stalks accompanied by slight cell chaining and irregular cell shape. In the absence of both bactofilin paralogues BacA and BacB, *H. neptunium* cells adopt a severely distorted cell morphology with multiple and branched stalks. In addition to bud formation at the distal end of the stalk, these mutants can generate buds directly from the cell body of the mother cell. Both bactofilins localize dynamically at the future stalked pole throughout the cell cycle and within the stalk just adjacent to the tip and later at the future division site. Time-lapse microscopy of the double deletion mutant revealed that the first step which leads to loss of cell morphology is the relinquishment of the stalk as a reproductive organelle, which is unimpededly incorporated by the emerging bud. Thus the stalk is lost, which leads to deregulation of cell wall biogenesis within the complete cell, generating amorphous cell bodies. However, further experiments indicate that bactofilins are not essential for stalk biogenesis, they merely seem to pay a role in confining cell growth to the terminal region of the stalk. In short,

bactofilins play a vital role in the maintenance of PG incorporation at the stalked pole and consequently ensure proper cell morphology.

Zusammenfassung

Die Größe und Form von Bakterien ist vielfältig, genau wie ihre Vermehrungsstrategien. Die Zellmorphologie von Bakterien wird durch ihre Zellwand bestimmt, welche hauptsächlich aus Peptidoglykan (PG) besteht. Bisher wurde die räumlich-zeitliche Regulierung von Zellwachstum und Zellteilung hauptsächlich in stäbchenförmigen Bakterien wie *Escherichia coli* and *Bacillus subtilis* untersucht. In dieser Studie untersuchen wir das dimorphe Alphaproteobakterium *Hyphomonas neptunium* als ein neuer Modellorganismus für das Studium von asymmetrischer Zellmorpholigie und Vermehrung durch Knospung am Ende eines Stiels.

Unser Ziel war eine umfassende Analyse des Zellwachstums und des Knospungmechanismus in *H. neptunium*. Detaillierte Elektronen-Kryotomographie-Bilder zeigten, dass der Stiel sowie die Knospe ein Kontinuum mit der Mutterzelle bilden, was früheren Annahmen widerspricht. Wir konnten zudem zeigen, dass die Tochterzelle einen gewissen Teil des Stiels der Mutterzelle einbaut, um sein eigenes Wachstum zu vervollständigen. Darüberhinaus konnten wir zeigen, dass *H. neptunium* weitaus mehr replikative Zyklen durchlaufen kann, als bisher angenommen wurde. Eine Analyse des Einbaus von neuem PG mittles HADA führte zur identifizierung von vier verschieden Wachstumsphasen in *H. neptunium*, welche sich durch diffusen (Wachstum der Schwärmer-zelle und Enstehung der Knospe) oder zonalen (Stielbiogenese und Zellteilung) PG-Einbau auszeichnen. Zellwand-Analysen deuten auf eine sehr hohe PG-Umsatzrate hin sowie auf einen ungewöhnlich hohen Anteil an Glycin anstelle von Alanin an der fünften Position des Stammpeptids. Eine umfassende Analyse der PG-Biosynthese-Maschinerie in *H. neptunium* zeigt, dass das konservierte Aktin-Homolog MreB, die PG-Synthasen PBP2 und PBP3 sowie die PG-Hydrolase LmdC eine wichtige Rolle während des Zellwachstum in *H. neptunium* spielen. Die polare PG-Biogenese scheint durch eine Reihe von meist redundanten Synthasen und Hydrolasen moduliert zu werden, wobei LD-Transpeptidasen keine Rolle spielen. Wir postulieren, dass die asymmetrische Zellgeometrie von *H. neptunium* auf einer komplexen intrazellulären Asymmetrie beruht, die durch verschiedene Wachstumszonen mit dispersem und zonalem Wachstum gekennzeichnet ist.

Zur Aufrechterhaltung der korrekten Zellform benötigt *H. neptunium* MreB, ein coiled-coil-reiches Protein (genannt CCRP) sowie die nicht-kanonischen Bactofiline, die eine neue Klasse von Nukleotid-unabhängigen polymerbildenden Zytoskelettelementen darstellen. Wird MreB durch A22 oder MP265 gehemmt, nehmen die Zellen eine runde Form an, bis das Zellwachstums komplet zum Stillstand kommt. Wird das *ccrp* Gen deletiert, entstehen kurze Zellketten sowie leicht deformierte Zellkörper. In Abwesenheit der beiden Bactofilin-Paraloge, BacA und BacB, entstehen pleomorphe Zellkörper mit mehreren, zum Teil verzweigten Stielen. Bei einigen dieser Mutanten können zusäztlich zu der Knospe am Ende des Stiels, auch Knospen aus dem Zellkörper der Mutterzelle entstehen. Beide Bactofiline lokalisieren dynamisch am gestieltem Pol während des gesamten Zellzyklus und sind später zusätzlich im Stiel direkt neben der Spitze und an der zukünftigen Zellteilungsebene lokalisiert. Zeitraffer-Mikroskopie-Aufnahmen von der Doppeldeletionsmutante zeigten, dass der erste Schritt, der zum Verlust der Zellmorphologie führt, die Vernachlässigung des Stiels als Fortpflanzungsorganell

ist, welche durch die wachsende Knospen ungehindert einverleibt wird. Der Verlust des Stiels hat zur Folge, dass die Zellwandbiogenese in der gesamten Zelle dereguliert ist, was am Ende zu amorphen Zellkörpern führt. Allerdings deuten mehrere Experimente darauf hin, dass die Bactofiline für die Stielbiogenese nicht erforderlich sind, aber sie scheinen eine tragende Rolle bei der Aufrecherhaltung des Stiels zu haben. Kurzum spielen Bactofiline eine essentielle Role bei der Aufrechterhaltung des PG-Einbaus am gestieltem Pol, was letzendlich entscheidend zur Erhaltung der korrekten Zellmorphologie beiträgt.

Contents

Abstract vii

Zusammenfassung ix

Contents xi

List of abbreviations xv

1. Introduction 1

1.1. The architecture and biosynthesis of peptidoglycan 1

1.1.1. The chemical composition and architecture of PG 1

1.1.2. The synthesis of the PG precursors in the cytoplasm 3

1.1.3. The polymerization of PG in the periplasm 4

1.1.4. The cleavage of PG in the periplasm 6

1.1.4.1. N-Acetylmuramyl-L-alanine amidases 7

1.1.4.2. Endo- and carboxypeptidases 7

1.1.4.3. Glycosidases 9

1.2. The bacterial cytoskeleton 9

1.2.1. FtsZ and other tubulin homologues 10

1.2.2. MreB and other actin homologues 11

1.2.3. Crescentin and other intermediate filament-like proteins 14

1.2.4. Coiled-coil rich proteins 15

1.2.5. Bacteria-specific cytoskeletal proteins 16

1.2.6. Bactofilins, limited to bacteria but divers in function 17

1.3. PG incorporation during cell growth and cell division 20

1.3.1. Growing along with the elongasome 20

1.3.2. Splitting with the divisome 21

1.3.3. Establishing rod-shape and alternative growth modes 22

1.4. *Hyphomonas neptunium* as a model organism for stalked budding bacteria 24

1.5. Scope 25

2. Results 27

2.1. Dynamics of the peptidoglycan biogenesis machinery during budding in *H. neptunium* 27

2.1.1. The mother cell forms one unit with the stalk and the bud 27

2.1.2. *H. neptunium* growth dynamics is cell cycle-dependent 28

2.1.3. The stalk grows at the stalked pole *H. neptunium* 29
2.1.4. Unique glycine-enriched PG composition of *H. neptunium* 31
2.1.5. Redundant PG hydrolases determine cell shape 33
2.1.6. PBPs contribute to cell growth 38
2.1.7. MreB and its associated proteins localize to the sites of PG synthesis 40
2.1.8. MreB plays a prominent role in growth and the coordination PG insertion 43
2.2. Morphology of *H. neptunium* relies on a coiled-coil-rich protein 47
2.3. Bactofilins control cell morphology in *H. neptunium* 49
2.3.1. Bactofilins are essential to uphold cell shape 49
2.3.2. Bactofilins are required for proper stalk maintenance 52
2.3.3. Finding potential interaction partners for bactofilins 57
3. Discussion 61
3.1. The advantages of budding at the distal end of a stalk 61
3.1.1. PG biogenesis in *H. neptunium* 63
3.1.2. MreB and its role in growth and morphology 64
3.2. Coiled-Coil-Rich Proteins 65
3.3. Staying in shape with bactofilins 65
3.3.1. BacA as the stalk-defining bactofilin in *H. neptunium* 66
3.3.2. The role of BacB 68
3.4. Concluding remarks about cell shape and budding 69
4. Materials and Methods 71
4.1. Materials 71
4.1.1. Source of used reagents and enzymes 71
4.1.2. Buffers and solutions 71
4.1.3. Media 71
4.1.4. Oligonucleotides and plasmids 72
4.2. Microbiological and cell biological methods 73
4.2.1. Cultivation of *E. coli* 73
4.2.2. Cultivation of *H. neptunium* 73
4.2.3. Cultivation of *C. crescentus* 73
4.2.4. Storage of bacteria 73
4.2.5. Determination of cell densities 73

4.2.6. Growth curves 73
4.2.7. Biofilm assay 73
4.2.8. Synchronization 74
4.3. Microscopic methods 75
4.3.1. Nucleoid staining 75
4.3.2. Labelling peptidoglycan of live bacteria through fluorescent D-amino acids (FDAAs) 75
4.3.3. Time-lapse microscopy on pads 75
4.3.4. Time-lapse microscopy in the microfluidic system 76
4.3.5. Transmission electron microscopy 76
4.4. Molecular biology methods 76
4.4.1. Isolation of microbial DNA 76
4.4.2. DNA sequencing 76
4.4.3. Polymerase Chain Reaction (PCR) 76
4.4.4. Restriction digestion (also blunt ending and PNK) and ligation of DNA fragments 78
4.4.5. Agarose gel electrophoresis 79
4.4.6. Plasmid construction 79
4.4.6.4. Plasmid for the expression of N- and C- terminal fusion in *H. neptunium* 79
4.4.6.5. Plasmids for the construction of markerless deletions or insertions in *H. neptunium* 80
4.4.6.6. Plasmids for complementation of in-frame deletion mutants of *H. neptunium* 84
4.4.6.7. Plasmids for co-localization and bacterial two-hybrid analysis in *E. coli* 84
4.4.6.8. Plasmids for expression in *E. coli* 86
4.4.7. Preparation and transformation of chemically competent *E. coli* 86
4.4.8. Bacterial Adenylate Cyclase Two Hybrid (BACTH) Assay 87
4.4.9. Conjugation of *H. neptunium* 87
4.4.10. Lyophilization of cells for PG analysis 88
4.4.11. Peptidoglycan muropeptide analysis 88
4.5. Biochemical methods 88
4.5.1. SDS-Polyacryl gel electrophoresis (SDS-PAGE) 88
4.5.2. Immunoblot analysis 89
4.5.3. Protein purification 90
4.5.4. Antibody synthesis 91
4.5.5. Co-immunoprecipitation and mass-spectroscopy 91

4.6. Bioinformatic methods 91
5. Appendix 93
5.1. Supplemental figures 93
5.2. Supplemental tables 101
5.3. Supplemental Movies 111
References 113
Einverständniserklärung xvii

List of abbreviations

A22	S-(3,4-Dichlorobenzyl) isothiourea hydrochloride
AFM	atomic force microscopy
APS	ammonium persulfate
ATP	adenosine triphosphate
bp	base pair
BATCH	bacterial adenylate cyclase two-hybrid
CFP	cyane fluorescent protein
Co-IP	co-immunoprecipitation
DAPI	4',6-diamidino-2-phenylindole
DIC	differential interference contrast
DMSO	dimethyl sulfoxide
DNA	deoxyribonucleic acid
dNTPs	deoxyribonucleotides
ECT	electron cryo-tomography
EDTA	ethylenediaminetetraacetic acid
EM	electron microscopy
EP	endopeptidase
h	hour
HA	human influenza hemagglutinin
HADA	hydroxy coumarin-carbonyl-amino-D-alanine
IM	inner (cytoplasmic) membrane
kDa	kilo Dalton
m-DAP	*meso*-diaminopimelic acid
Min	minute
MP265	S-(4-Chlorobenzyl) isothiouronium chloride
NADH	nicotinamide adenine dinucleotide
NADPH	nicotinamide adenine dinucleotide phosphate
Ni-NTA	nickel-nitrilotriacetic acid
Nm	nanometer
NMR	nuclear magnetic resonance
OM	outer membrane
P	phosphate
PEP	phosphoenolpyruvate
PG	peptidoglycan
RFP	red fluorescent protein
rpm	revelation per minute
s	seconds
SAP	schrimp alakaline phosphatase
SDS	sodium dodecyl sulfate
SH3	SRC Homology 3 domain
STEM	scanning transmission electron microscopy
TEM	transmission electron microscopy
TG	transglycosylase
TIRF	total internal reflection fluorescence
TP	transpepetidase

SIM	structured illumination microscopy
UDP	uridine diphosphate
WT	wild type
X-gal	5-Bromo-4-chloro-3-indolyl- β-D-galactopyranoside
YFP	yellow fluorescent protein

1. Introduction

Bacteria occur in a plethora of shapes and sizes (1). Notably, morphological characteristics are passed on and preserved unchanged in the following generations (2). The question of how bacteria grow and maintain their morphology has been a major focus of research for decades. In the last couple of years *H. neptunium* is fast approaching as a new model organism for budding in stalked Alphaproteobacteria (3).

1.1. The architecture and biosynthesis of peptidoglycan

In most bacteria, cell shape is determined by a cell wall (sacculus) composed of peptidoglycan (PG), also referred to as murein, which is a mesh-like polymer that encompasses the entire cell and is essential to withstand the internal osmotic pressure as well as to uphold cell shape (4). Thus, successful PG synthesis, maintenance, and remodelling are vital for survival in most bacterial species (2). Sculpting of the PG sacculus is a dynamic process that requires high precision and often activation of synthases for the generation and attachment of new PG as well as hydrolytic enzymes, which facilitate the insertion of nascent PG into the existing cell wall (5). The orchestration of such an elaborate machinery requires precise organization and timing. The current data is mainly derived from studies performed in the Gram-negative bacterium *Escherichia coli* unless stated otherwise.

1.1.1. The chemical composition and architecture of PG

In general, bacteria can be divided into two distinct groups, Gram-negative and Gram-positive, based on the chemical and physical properties of their cell wall, which can partially be deduced by Gram staining. The major difference between these two groups is the presence or absence of an outer membrane and the thickness of the murein sacculus surrounding the cells (6). In Gram-negative bacteria like *E. coli* the PG mesh is located between the inner (cytoplasmic) membrane and the outer membrane in an aqueous compartment termed the periplasm (7). The PG mesh usually consists of one layer with a thickness of 3-6 nm (8). The PG layer is anchored to the outer membrane by murein (Braun's) lipoprotein (Lpp) (9), which in consequence is the most abundant protein with more than 500,000 proteins per *E. coli* cell (10). The outer membrane is a Gram-negative-specific, asymmetric lipid bilayer, which is largely composed of glycolipids, mainly of lipopolysaccharide (LPS), and contains select proteins as well as lipoproteins (11). Since Gram-positive bacteria lack an outer membrane, their PG is anchored to the cytoplasmic membrane via lipoteichoic acids (12). In contrast to Gram-negative species, the PG of Gram-positive bacteria has a thickness of 30 - 100 nm composed of multiple layers and accommodates covalently attached wall teichoic acids and capsular polysaccharides (8).

The chemical structure of the glycan backbone of PG is shared by most bacteria. PG is composed of a glycan backbone consisting of alternating repeats ß-1,4-linked *N*-acetylglucosamine (GlcNAc) and *N*-acetylmuramic acid (MurNAc) (Figure 1A). The subunits in different glycan strands are connected by peptide bridges that are attached to the MurNAc to form a mesh-like polymer around the cell (6).

The glycan strands terminate with GlcNAc attached to a 1,6-anhydro-MurNAc, which is MurNAc with an intra-molecular ether-linkage from C1 to C6 (13). Some bacteria contain various degrees of O-acetylation at the C6 of MurNAc, which provides resistance against the PG hydrolase lysozyme (14). Approximately 3-6 % of the murein subunits have a 1,6-anhydro-MurNAc (anhMurNAc), which varies between strains and growth conditions. Consequently, the average length of glycan strands ranges from 25 to 40 disaccharide units (15, 16). In contrast, atomic force microscopy (AFM) of *B. subtilis* sacculi revealed that glycan strands can be up to 500 disaccharide units long (17), whilst in *Staphylococcus aureus* the average glycan length is 6 disaccharide subunits (18).

The pentapeptide side chain is attached via an amide bond to the lactyl group of the MurNAc. In *E. coli* the sequence of the unaltered side chain is L-alanine (Ala)–D-Glutamate (Glu)–meso-diamino-pimelic acid (DAP)–D-Ala–D-Ala. The striking feature of this side chain is its composition from rare amino acids, which can only be found in the bacterial cell wall and some antibiotics (19). Instead of D-Ala at the 4th or 5th position, under special growth conditions some species can substitute a small fraction with a glycine (Gly) (Figure 1C) (20). Upon isolation of the murein sacculus, the length of the peptide side chain varies from pentapeptides to mainly tetrapeptides (L-Ala–D-Glu–*meso*-DAP–D-Ala) as well as tripeptides (L-Ala–D-Glu–*meso*-DAP) and dipeptides (L-Ala–D-Glu), depending on the proteolytic degradation in the given species (19). In murein isolated from *E. coli*, pentapeptides are rare due the rapid turnover of its PG (5), whilst the pentapeptide content of murein isolated from the Gram-negative *Caulobacter crescentus* is very high, which is attributed to a low activity of murein degradation (20).

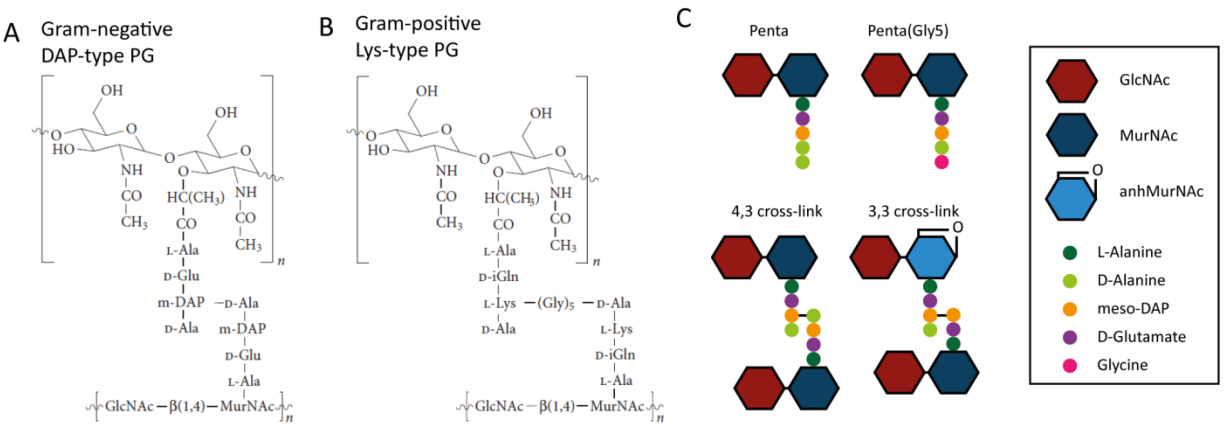

Figure 1. Peptidoglycan subunit structure. A) PG structure of Gram-negative bacteria, which is characterized by *meso*-DAP as the third amino acid within the stem peptide. In DAP-type PG, peptide side chains are directly linked. **B)** PG structure of Gram-positive bacteria, which is defined by L-Lys as the third amino acid within the peptide side chain. In Lys-type PG, the interpeptide bridge linking two peptide side chains can vary in length and sequence depending on the species. Adapted from Royet and Dziarski, 2007 (21). **C)** Schematic representation of (Gram-negative) PG subunits depicting the difference in stem peptide composition and cross-linking.

PG is a large macromolecule consisting of more than 50 different species of subunits (15). Although the glycan backbone of PG is conserved within all bacteria, the composition of the peptides does vary. Whilst Gram-negative bacteria contain the DAP-type PG described above, Gram-positive bacteria have an L-lysine (L-Lys) instead of m-DAP as the third amino acid in peptide side chain (Lys-type PG)

(Figure 1A and B). In DAP-type PG, peptide side chains are directly linked, in contrast to Lys-type PG, which can contain an interpeptide bridge of varying length and sequence, depending on the species (21). The majority of stem peptides are connected by D-Ala^4→*meso*-DAP^3 cross-links (4,3-cross-links) (16), whilst a link between two *meso*-DAP residues (3,3-cross-links) is more rare (Figure 1C) (22).

Furthermore, Gram-positive bacteria can form branched stem peptides, whose role has been associated with resistance against ß-lactam antibiotics (23) and as the attachment site of covalently linked (or associated) surface proteins (24, 25). Interestingly, these branched stem peptides are absent in the Gram-positive *Bacillus subtilis*, in which the cross-links are identical to those found in *E. coli* (26). Usually 40 to 60 % of peptides are part of cross-links in *B. subtilis* (27), *E. coli* (16), and other Gram-negative bacteria (28).

The murein sacculus is so robust that it can be isolated intact from cells. Transmission electron microscopy (TEM) and atomic force microscopy (AFM) revealed sacculi in the same shape and size as the original bacterial cells. Isolated sacculi from *E. coli* are 2-4 µm in length with a diameter between 0.5-1 µm and a PG thickness of only 6 nm (29, 30). Small-angle neutron scattering showed that PG sacculi have an uneven surface thickness, where 75-80 % of the sacculi surface is 2.5 nm thick, the rest is up to 7 nm thick. In conclusion, 75-80 % of the murein surface must be single layered (31). Despite its sturdy nature, the murein mesh is a flexible structure that can expand as well as shrink up to three-fold without fracturing (32). This observed elasticity mostly stems from the flexibility of the peptides, which under normal conditions bend back towards the glycan strand but can become straight when stretched, thus allowing the murein net to expand (33-36). According to these murein models (33, 36), the peptides extend in a helical pattern from the glycan strands, whereby 4 di-saccharide subunits would be required for one complete turn. Nuclear magnetic resonance (NMR) analysis suggested that the peptides are arranged at a 120 ° angle from each other, meaning that 3 disaccharide subunits would suffice to generate a full turn (37). Electron cryo-tomography (ECT) of sacculi from *E. coli* and *C. crescentus* revealed that glycan strands lie parallel to the cell surface, approximately perpendicular to the long axis of the cell (38).

As already indicated, PG is a 3D mesh-like macromolecule that surrounds the entire cell and is responsible for upholding cell shape and withstanding the internal turgor pressure (4). If the integrity of the murein sacculus is compromised or completely removed, the cells usually undergo immediate osmotic lysis, unless prevented by osmoprotectant additives (39). Interestingly, not all bacteria require a cell wall for viability. L-form bacteria, which are cell wall-deficient cells (40), are viable under certain conditions and are able to proliferate by membrane blebbing, tubulation, vesiculation, and fission (41-43).

1.1.2. The synthesis of the PG precursors in the cytoplasm

PG biosynthesis can be divided into two different steps, the cytoplasmic and the periplasmic stages (19). First, the PG precursor lipid II is synthesized in several steps in the cytoplasm (44) (Figure 2). The molecular precursor for the glycan backbone is fructose-6-P, which is converted to GlcNAc by GlmS, GlmM, and the bifunctional enzyme GlmU, which in the last step attaches the uridine diphosphate

(UDP) to generate UDP-GlcNAc. The second subunit of the glycan backbone is synthesized by MurA and MurB, which with the consumption of PEP and NADH transform UDP-GlcNAc into UDP-MurNAc. Next a pentapeptide side chain is attached by the Mur ligases (MurC-F) to UDP-linked MurNAc (19). In this instance, peptide bonds are generated by either ATP-dependent ligases or nonribosomal peptide bond-forming enzymes under ATP hydrolysis. After the initial attachment of L-Ala to UDP-MurNAc by MurC, MurD adds the D-Glu (generated by the glutamate racemase MurI), followed by the addition of *meso*-DAP (or L-Lys) by MurE. The Ala racemases Alr or DadX produce D-Ala, which is dimerized by the D-Ala–D-Ala ligase Ddl before it is attached to the growing peptide chain by MurF. The product of the reaction is attached to bactoprenol (undecaprenyl-PP) by the transferase MraY, yielding lipid I. Lipid II is generated by the attachment of UDP-GlcNAc to lipid I by the *N*-Acetylglucosaminyl transferase MurG (45). Lipid II is flipped across the cytoplasmic membrane into the periplasm by an integral membrane protein, which was speculated to be either RodA (46) or FtsW (47, 48); however, currently MurJ seems to be the most likely candidate (49). During the attachment of the lipid II molecule to the existing PG mesh, the bactoprenol is detached and recycled within the inner membrane by the undecaprenyl-pyrophosphate phosphatase UppP and flipped back towards the cytoplasm by a yet unknown mechanism (50).

1.1.3. The polymerization of PG in the periplasm

To polymerize glycan chains, a ß-1,4-glycosidic bond between the GlcNAc of lipid II and the MurNAc of the nascent PG chain is catalysed by transglycosylases (GTases) and the glycan strands are connected at their stem peptides by transpeptidases (TPases) (19) (Figure 2), also known as penicillin-binding proteins (PBPs) (51). PG synthases can be divided into three types: bifunctional GTases-TPases (class A PBPs), monofunctional TPases (class B PBPs), and monofunctional GTases (19). *E. coli* possesses three bifunctional synthases (PBP1A, PBP1B, and PBP1C), one GTase (MtgA), and two monofunctional TPases (PBP2 and PBP3).

A common feature of all PBPs is an N-terminal membrane anchor with their TPases and other domains facing into the periplasm. All PBPs have a penicillin-binding (PB) domain, which consists of three highly conserved motifs with one motif harbouring the active site serine (Ser) residue required for TPase activity. Only monofunctional GTases like MtgA do not contain a PB domain. Class A PBPs have a non-PB domain consisting of 5 conserved motifs that are responsible for the specific GTase activity of these enzymes. On the other hand, the non-PB domain of Class B PBPs only contains 3 conserved motifs (52, 53), which might increase the internal protein stability and promote the multimerisation of these enzymes (54, 55).

In *E. coli* the enzymes with the highest murein synthesis activity are the two class A PBPs PBP1A and PBP1B. Cells are viable in the absence of either enzyme, yet a double deletion of both genes is lethal (56, 57). It appears that both PBPs have distinct cellular functions as they do not form heterodimers (only homodimers) and single deletion mutants react differently to the presence of ß-lactam antibiotics or the absence of other class B PBPs (58-61). A further indication for their distinct function is

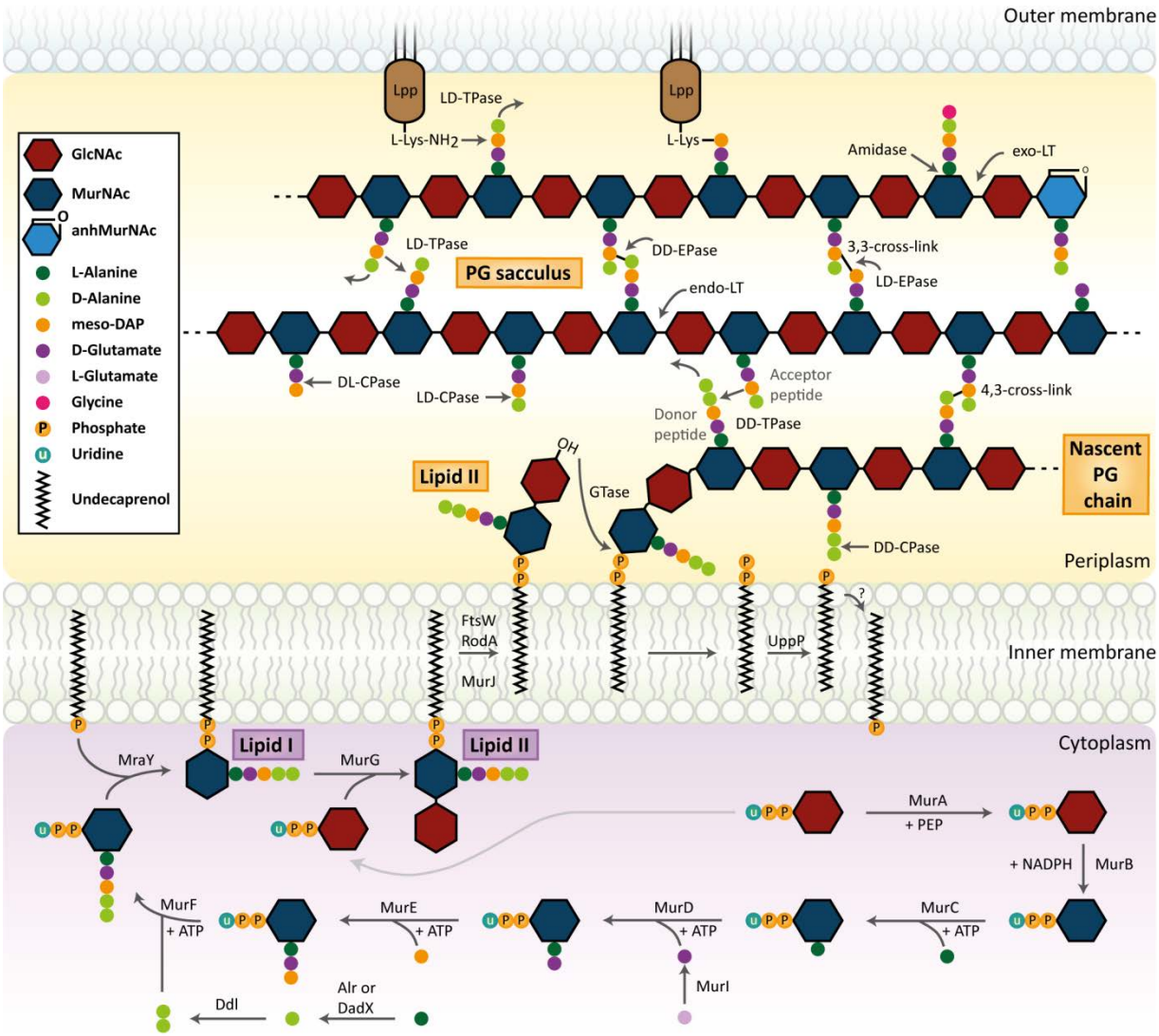

Figure 2. Summary of the peptidoglycan biosynthesis pathway in *E. coli*. The synthesis and attachment of new PG subunits into the existing PG mesh. All known synthetic and hydrolytic enzymes are indicated. The PG precursors lipid I and lipid II are synthesized in the cytoplasm and linked to undecaprenol before being flipped into the periplasm by presumably FtsW, RodA, or most likely MurJ. The polymerization of the glycan chain is catalysed by a glycosyltransferase (GTase) whilst a transpeptidases (TPase) cross-links the stem peptide by a 4,3-cross-link to the established PG layer. LD-transpeptidases catalyse the formation of 3,3-crosslinks between stem peptides and attach the PG strands to Lpp, which anchors the PG mesh to the outer membrane. The stem peptides are clipped by DD-, LD-, and DL-carboxypeptidases (CPases) and crosslinks are cleaved by the DD- and LD-endopeptidases (EPases). Amidases remove the complete stem peptide from the MurNAc. The glycan backbone is cleaved by *exo*- or *endo*-specific lytic transglycosylases (LTs), generating 1,6-anhydro-*N*-acetyl-muramic acid (anhMurNAc) residues at the terminal end of PG strands. See text for more detailed description. Abbreviations: Alr, Ala racemase, biosynthetic; DadX, Ala racemase, catabolic; DdlA, D-Ala–D-Ala ligase A; GlcNAc, N-acetylglucosamine; *meso*-DAP, *meso*-diaminopimelic acid; MraY, UDP-MurNAc-pentapeptide phosphotransferase; MurA, UDP-GlcNAc enolpyruvyl trans-ferase; MurB, UDP-MurNAc dehydrogenase; MurC, UDP-MurNAc–L-Ala ligase; MurD, UDP-MurNAc-L-Ala–D-Glu ligase; MurE, UDP-MurNAc-L-Ala-D-Glu–*meso*-Dap ligase; MurF, UDP-MurNAc-tripeptide–D-alanyl-D-Ala ligase; MurG, UDP-GlcNAc-undecaprenoyl-pyrophosphoryl-MurNAc-pentapeptide transferase; MurI, Glu racemase; NADPH, nicotinamide adenine di-nucleotide phosphate; PEP, phosphoenolpyruvate. Adapted from Typas *et al.*, 2012 (2).

their differential requirement for specific outer-membrane-anchored lipoproteins (LpoA and LpoB, respectively) to stimulate their activity (62, 63). For effective TPase-mediated cross-linking, both PBP1A and PBP1B require ongoing GTase activity (64, 65). Additionally, in its dimeric form the glycan

polymerization activity of PBP1B is increased (65). *E. coli*'s third class A PBP, PBP1C, is non-essential and cannot compensate for the loss of both PBP1A and PBP1B (66), and speculations have arisen that it might not have TPase activity at all (66). In *C. crescentus* the class A PBPs PbpY and PbpX are recruited to the cell division site and interact with other divisome components, whilst PbpC localizes to the stalked pole. The class A PBPs in *C. crescentus* are in part highly redundant and at least one PBP is required for viability (with the exception of PbpZ) (67).

The two class B PBPs of *E. coli* seem to have more specified functions than their class A counterparts. PBP2 is essential for cell elongation and PBP3 (also known as FtsI) is essential for cell division (68). PBP2 localizes to the lateral cell wall and to midcell only during the early stages of division, indicating its more prominent role during cell elongation (69). PBP3 localizes to the septum at the division site (70), where it interacts with PBP1B (65).

As a monofunctional GTases with only glycan polymerization but no peptide cross-linking activity, MtgA is not considered a PBP (71). Deletion of the *mtgA* gene in species such as *E. coli* (66), *Haemophilus influenzae* (72), and *Brucella abortus* (73) causes no defects under laboratory conditions. MtgA from *S. aureus* (also known as Mgt) becomes vital in the absence of PBP2 (74). Apart from this MtgA is speculated to have a role in cell division as it localizes to the cell division site in *E. coli*; however, its precise role remains unclear (75).

In general, most TPases are predominantly D,D-transpeptidases (DDT) that catalyse D-Ala^4→*meso*-DAP^3 cross-links (4,3-cross-links) (16). However, seldom a link between two *meso*-DAP residues (3,3-cross-links) is catalysed by specialized L,D-transpeptidases (LDT), which are resistant to ß-lactam antibiotics (22). In *E. coli* during exponential growth the abundance of 3,3-cross-links amounts to 2-10 %, which can more than double in the stationary phase (5, 15, 16). In Mycobacteria, the function of LDTs contributes significantly to cell wall integrity (76). In rare cases like in the plant pathogen *Agrobacterium tumefaciens* and the related *Sinorhizobium meliloti* more than 50 *%* of all cross-links are generated by LDTs (77). Furthermore, in *A. tumefaciens* one of the 14 LDT homologues localizes to the growth pole, indicating a potential role for LDTs during polar growth (78). In *E. coli*, the main function of LDTs is to attach Lpp to the peptidoglycan (79).

1.1.4. The cleavage of PG in the periplasm

In order for cells to grow and divide, PG has to be continuously remodelled, whereby cleavage of the existing PG mesh is a prerequisite for the insertion of new PG strands and successful cell separation (5). If new glycan strands were added without any cleavage of the existing PG net, the murein layer would merely thicken but the glycan polymers would not be extended. In order to promote murein extension the insertion of new PG subunits should always be accompanied by the hydrolysis of the old murein layer (80). The degradation of PG is accomplished by an array of specialized murein hydrolases that cleave the covalent bonds in the murein backbone, including lytic transglycosylases, peptidases, and amidases (81). These hydrolytic enzymes are also referred to as autolysins as they have the ability to lyse the cell in which they are produced. In Gram-negative bacteria autolysins are located in the periplasm, whereas in Gram-positive bacteria they are anchored in the cell wall (26).

Amidases cleave the peptide side chains from the glycan backbone (82), while lytic transglycosylases cleave the MurNAc-ß-1,4-GlcNAc glycosidic bond, generating 1,6-anhydro-muropeptides, which are recycled to synthesize new PG (13, 83). Peptidases degrade the peptide cross-links between glycan chains (81). In *E. coli* more than 35 PG-specific autolysins have been identified (84).

1.1.4.1. N-Acetylmuramyl-L-alanine amidases

The peptide side chains are removed via amidases from the glycan backbone. *N*-Acetylmuramyl-L-alanine amidases specifically cleave the amide bond between the D-lactoyl moiety of the MurNAc and the L-Ala of the peptide side chain. The catalytic domains responsible for this hydrolysis are Ami_3 (84) and CHAP (cysteine, histidine-dependent amidohydrolases/peptidases) (85, 86). *E. coli* possesses five characterized amidases, AmiA, AmiB, AmiC, AmiD, and AmpD (87). The amidases AmiABC are characterized by an Amidase_3 domain (88) and localize in the periplasm (89). AmiD is a membrane-bound lipoprotein with an Amidase_2 domain (90). AmpD also has an Amidase_2 domain but it is a soluble cytoplasmic enzyme (91). The major role of AmiABC is the cleavage of septal PG during cell division (87). Both AmiB and AmiC localize to the division site whilst AimA is mainly diffuse throughout the periplasm (89, 92). Deletion of two or more amidases causes the formation of chains of connected cells (93), whereas the overexpression of either AmiB or AmiC leads to cell lysis (87). AmpD has a remarkable specific activity against anhMurNAc containing muropeptides (91, 94) and in the absence of AmpD, anhMurNAc species accumulate, indicating a role for AmpD in the PG recycling pathway (95). Similar to AmpD, AmiD also has a specific activity against anhMurNAc–L-Ala bonds; however, it is also active against MurNAc–L-Ala (88, 90). Interestingly, the domain architecture of both AmpD and AmiD is reminiscent of Zn^{2+} metallopeptidases (96, 97). In *E. coli*, AmiD and AmpD are the only amidases active against anhMurNAc moieties (90). Amidases with a CHAP domain have been recently postulated to play a role in cell division in *S. aureus* and *Streptococcus pneumoniae* (98, 99). Overall, amidases have been implicated to play an important role in cell division in *E. coli* (87), *B. subtilis* (100), *Vibrio cholera* (101), *P. aeruginosa* (102), *S. aureus* (99), and *S. pneumoniae* (98).

1.1.4.2. Endo- and carboxypeptidases

Peptidases cleave the amide bond between amino acids in the stem peptide. In general, exopeptidases remove amino acids at the terminus of a peptide chain, whereby aminopeptidase cleave at the amino end of a peptide and carboxypeptidases (CPs) at the carboxylic end. On the other hand, endopeptidases (EPs) cleave the amide bond between non-terminal amino acids. The specificity of the enzymes is highlighted by including in its name the stereochemistry of the two amino acids between which the cleavage site is located (81).

In *E. coli* there are over two dozen peptidases that contribute to the hydrolysis of the peptide bonds present in the murein sacculus (84). DD-CPs remove the terminal Ala^5 from newly synthesized PG, generating a tetrapeptide side chain. LD-CP will generate tripeptides, which can be further cleaved to dipeptides by DL-CP (19). As the deactivation of these enzymes causes morphological defects in *E. coli*, *Helicobacter pylori*, and *Campylobacter jejuni*, it has been postulated that these CPs might regulate the incorporation of new PG subunits based on the availability of donor and acceptor peptides accessible for TPases (103-105).

These enzymes are also referred to as low molecular weight PBPs, since akin to TPases they can also bind penicillin (106). *E. coli* has three DD-CPs, PBP5, PBP6, and PBP6B, which all contribute to the correct orientation of the Z-ring, and their absence causes asymmetric cell division and branching (107). The major DD-CP PBP5 (encoded by *dacA*) localizes to the lateral cell wall and the division site, where it participates significantly in the maintenance of cell diameter and shape (107, 108). The LD-CP LdcA is essential during the onset of the stationary phase and localizes in the cytoplasm, where it plays a role in PG recycling (109).

DD-EPs hydrolyse the D-Ala–*meso*-DAP cross-link that joins the peptide side chains of muropeptide subunits (81). The membrane-associated PBP4 and PBP7 are both DD-EPs, although PBP4 has additional DD-CP activity. In the absence of PBP4 and PBP7, the cell division defect of an amidase deletion strain is elevated (110). PBP7 is not only involved in septum cleavage and biofilm formation (2), but together with its proteolysed form, PBP8, it stabilizes and stimulates that activity of the lytic transglycosylases Slt70 (see below) (111). MepA is a periplasmic DD/LD-EP that is insensitive to penicillin (112, 113) and contributes to septum cleavage together with PBP4 and PBP7 (93, 110).

Another widely distributed group of endopeptidases are the lysostaphin-like metalloproteases (LytM factors), which belong to the family of M23 zinc-metallopeptidases. LytM factors were first described in Gram-positive Staphylococci and Enterococci were they cleave the penta-glycine bridges in murein (114-118). LytM factors cleave the crosslinks between murein stem peptides. However, they seem to have a broad cleavage specificity which includes the hydrolysis of L-Ala–D-Glu (119) and Gly–Gly (120) bonds. The catalytic domain of LytM factors includes the typical M23 metalloprotease metal binding site with two conserved motifs, HXXXD and HXH (121), which was first identified in lysostaphin from *S. aureus* (122). Based on motif similarities, LytM factors belong to the LAS (lysostaphin-type enzymes, D-Ala–D-Ala metallopeptidases and sonic hedgehog) enzymes (117). LytM factors have been attributed a role in cell division in *E. coli* (123), *B. subtilis* (114), *P. aeruginosa* (102), *V. cholera* (101), and *H. influenzae* (124). The LytM factors EnvC, NlpD, YgeR, and YebA are known to be involved in cell division in *E. coli* (123). Interestingly, not all enzymes seem to have proteolytic activity based on mutations within the conserved metal-binding site. Both EnvC and NlpD have incomplete catalytic domains and have been shown to regulate the activity of amidases, where EnvC specifically regulates the activity of AmiAB and NlpD activates AmiC at mid cell (92). Some LytM factors are endowed with LysM domains which act as PG binding domains (125). The LytM factor DipM, which has four LysM domains, localizes to the division site and plays a substantial role during cell division in *C. crescentus* (126-128). LytM factors are not solely involved in cell division but also contribute to pathogenesis in *H. pylori* (129), *Neisseria gonorrhoeae* (130), *Yersinia pestis* (122), and *H. influenzae* (124).

An additional superfamily of cell-wall hydrolases present in numerous bacterial lineages are NlpC/P60 domain proteins. The catalytic triad of these enzymes (Cys, His, and a polar residue (His/Gln/Asn)) is reminiscent of that found in papain-like thiol peptidases and are often fused to an SH3 domain, which acts as a PG recognition module (131-133). These enzymes typically cleave the bond between D-Glu and *meso*-DAP and thus belong to the DL-EP II (120). In *E. coli* the three redundant EPases MepS, MepM, and MepH (formerly Spr, YebA, and YdhO) are important for growth as a strain deleted of all

three genes is unable to incorporate new PG subunits, which swiftly leads to cell lysis (134, 135). Similarly in *B. subtilis*, the two redundant EPs LytE and CwlO are essential for cell wall synthesis and cell elongation (136).

1.1.4.3. Glycosidases

In *E. coli* there are two sets of PG glycosidases that cleave within the glycan backbone: *N*-acetylglucosamidases that cleave the GlcNAc-ß-1,4-MurNAc glycosidic bond and *N*-acetylmuramidases that cleave the MurNAc-ß-1,4-GlcNAc glycosidic bond (84). The non-essential NagZ protein is the only *N*-acetylglucosamidases in *E. coli* (137). NagZ localizes in the cytoplasm (138) and plays a role in PG recycling (95).

The *N*-acetylmuramidases can be divided into two subgroups according to their terminal processing of MurNAc; lysozymes produce terminally reduced MurNAc whilst lytic transglycosylases (LTs) produce anhMurNAc (13). *E. coli* has 7 LTs: the soluble LT Slt70 and the OM-anchored MltA, MltB, MltC, MltD, MltE (also known as EmtA), and MltF (13). In contrast to lysozyme, LTs are not considered hydrolases as they lack the conserved catalytic aspartate (which is present in lysozyme) and therefore do not require H_2O for substrate cleavage (13). The substrate specificity varies amongst the LTs. Slt70 can only cleave glycan strands with stem peptides but not glycan strands lacking peptides, whilst MltA is able to cleave either (139).

The mechanism of insertion of new glycan strands into the existing PG mesh is still ambiguous. During septation/cytokinesis, glycan chains are only cross-linked to newly synthesized glycan chains, one third of which is degraded again. The excess PG is rapidly removed from the division plane during septation/cytokinesis to ensure proper separation of daughter cells (140). This observation is consistent with the '3 for 1 model' (5), which proposes that for the insertion of three new glycan strands one is removed. So far it is unclear whether this model is applicable for lateral cell wall elongation, where peptide cross-links are formed between old and newly inserted glycan strands (95, 140-142).

1.2. The bacterial cytoskeleton

The cytoskeleton plays a major role in the temporal and spatial organization of cells. Cytoskeletal elements are involved in vital functions, including cell division, cell morphogenesis, chromosome partitioning, and cell motility (143). Nowadays it is established that prokaryotes, similar to eukaryotes, have a cytoskeleton. Counterparts of tubulin, actin, and intermediate filament proteins have been identified based on their structural and biochemical properties rather than sequence homology. A short overview of the bacterial cytoskeleton is given in Figure 3. In addition to homologues of canonical eukaryotic cytoskeletal proteins, recent studies identified more proteins that are unique to the prokaryotic cytoskeleton (143). Before delving into greater detail, what are the requirements for a protein to be considered cytoskeletal? Cabeen and Jacobs-Wagner propose three criteria that must be fulfilled: First, the protein must form polymers *in vivo* at its native cellular level. Second, *in vitro* studies of the purified protein should confirm the polymer-forming properties of the protein under

appropriate physiological conditions. Lastly, the resulting polymer should have a relevant function or confer mechanical properties *in vivo* (143). This chapter will give a short introduction into the major bacterial cytoskeletal elements, with a focus on the actin homologue MreB and the bacteria-specific bactofilins.

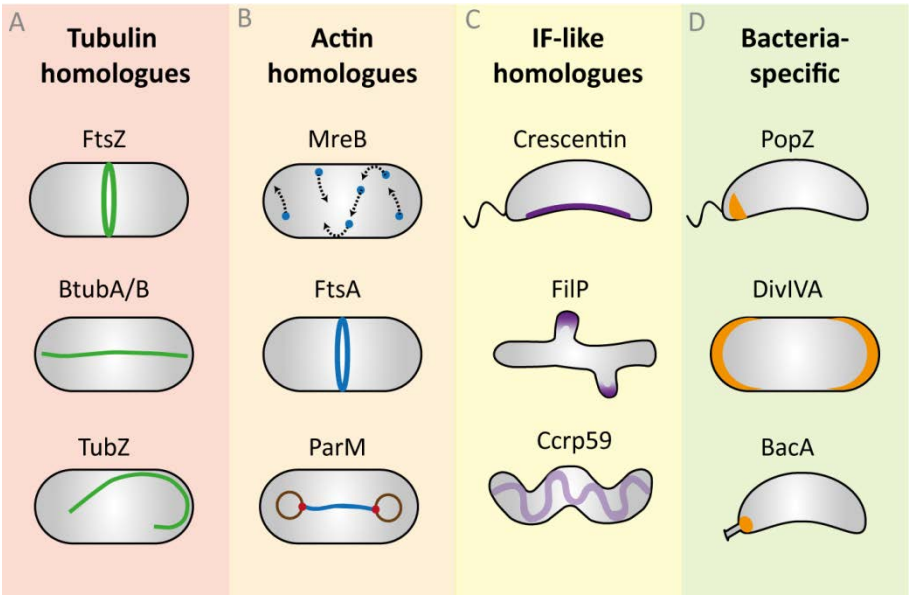

Figure 3. Schematic depicting the localization of different bacterial cytoskeletal elements. A) Tubulin homologues: FtsZ forms a ring-like structure at the division site in *E. coli* (144); BtubA/B from *Prosthecobacter* form tube-like filaments which reach from pole to pole when expressed in *E. coli* (145, 146); TubZ forms long filaments that curve at the cell pole in *B. thuringiensis* (147); **B)** Actin homologues: MreB dynamically localizes in discrete patches which mostly arrange in a helical-like pattern in *B. subtilis* (reviewed in (148)); FtsA co-localizes with FtsZ at the division site in *E. coli* (119, 149); ParM forms long filaments to segregate plasmids in *E. coli* (150); **C)** IF-like homologues: Crescentin forms an inert polymer at the inner curvature of *C. crescentus* (151); FilP forms growth-dependent gradients at the apical pole of *Streptomyces coelicolor* (152); Ccrp59 localizes in stationary discrete foci in a patchy pattern reminiscent of a helical organization in *H. pylori* (153); **D)** Bacteria-specific cytoskeletal proteins: PopZ localizes to the stalked pole in swarmer cells and to both poles in stalked cells of *C. crescentus* (154); DivIVA assembles at negatively curved membranes in *B. subtilis* (155, 156); BacA localizes at the stalked pole in *C. crescentus* (157).

1.2.1. FtsZ and other tubulin homologues

In eukaryotes, microtubules fulfil essential functions such as the segregation of chromosomes, they act as components of flagella and cilia, and form tracks for intracellular transport (143). The first prokaryotic cytoskeletal component to be discovered was the tubulin homologue FtsZ (158). In most bacteria FtsZ is an essential cell division protein (159). It has structural similarity to tubulin, though their sequence conservation is less than 10 % (160). Purified FtsZ can polymerize into head-to-tail protofilaments which can be straight, curved, or ring-shaped. This self-assembly is only possible in the presence of GTP (161-164). Furthermore, single filaments can bundle together to form sheets and tubular structures in the presence of multivalent cations or crowding agents (165-169). FtsZ does not seem to form microtubule-like structures; nonetheless, the subunit arrangement of FtsZ proto-filaments strongly resembles that of tubulin (170).

The major function of FtsZ, after polymerizing into a ring-like structure (Figure 3A), called the Z-ring, is to act as a scaffold for proteins involved in cell division (144, 171). The Z-ring is responsible for the recruitment and thus the correct positioning of enzymes involved in cell wall biogenesis and constriction (172). Previously, it was assumed that FtsZ formed one continuous ring around the cell, which upon constriction generated the necessary force to achieve cell constriction (173). More recent studies postulate that the Z-ring is an open structure consisting of several loosely assembled arched protofilaments that slide into close proximity to close the Z-ring during cell division (173). Another study from *C. crescentus* indicates that repeated cycles of GTP hydrolysis cause an increase in protofilament bending, which in the end leads to Z-ring constriction (174). For a long time it was thought that GTP hydrolysis alone might drive cell invagination (173). According to recent studies it is most likely that constriction during cell invagination is driven by PG synthesis during cytokinesis and that GTP hydrolysis plays a lesser role (175). As FtsZ is essential for cell division in most bacteria, they have developed elaborate systems to ensure the correct positioning of the Z-ring (176).

In prokaryotes, tubulin homologues are not restricted to FtsZ alone. Amongst the Verrucomicrobia, species like *Prosthecobacter*, possess two genes closely related to tubulin, termed *btubA* and *btubB* (bacterial tubulin A/B) that lie an operon (177). The crystal structure of heterodimeric BtubA/B revealed a very close resemblance to tubulin (178). In the presence of GTP, collectively BtubA/B can form structures similar to double-walled tubules that are made up of 24 nm wide filament bundles. However, alone BtubA is unable to polymerize whilst BtubB forms 35-36 nm wide rings (145). It has been postulated that BtubA/B heterodimer formation is crucial for filament establishment (179). When the Btub pair was heterologously expressed in *E. coli*, long filamentous structures were observed that reached from pole to pole (Figure 3A) (145). Since then, ECT revealed that BtubA/B form microtubule-like structures in *Prosthecobacter*, which have been termed “bacterial microtubules” (146). In essence, the bacterial tubulins are assumed to be ancient tubulin genes passed on via horizontal gene transfer from a primitive eukaryotic cell to a bacterium (180).

Another interesting tubulin homologue is TubZ, which belongs to the subgroup of tubulin/FtsZ-like proteins and, as its hybrid name already indicates, it combines conserved sequence residues of both tubulin and FtsZ (147). TubZ proteins are involved in the type III plasmid partitioning system (181) and seem to be mainly encoded by large plasmids as well as selected bacteriophages of *Bacillus* and *Clostridium* species (147, 182, 183). In *B. thuringiensis*, TubZ forms long, partially curved filaments that travel around within the cell (Figure 3A) (147). Due to their treadmilling activity, which is required for plasmid stability (184), TubZ filaments present an efficient plasmid partitioning system (147). Recently, a bacteriophage-encoded tubulin-like protein, PhuZ, was discovered to form spindle-like filaments with dynamic instability to position the phage DNA at midcell (185, 186).

1.2.2. MreB and other actin homologues

The existence of bacterial actin homologues was predicted by a bioinformatics search, which compared the structure of three functionally different ATPases, actin, sugar kinase, and Hsp70. This search lead to the identification of five common ATPase motifs, which first revealed MreB, ParM, and FtsA (187).

In eukaryotes actin is an essential component of the cytoskeleton as it helps maintain the structure of the nucleus and is vital for muscle contractions. The first protein to be recognized as a bacterial actin homologue and analysed as such was MreB (187, 188). Although MreB shows no sequence homology to eukaryotic actin, their crystal structures are remarkably similar (189). MreB1 from *Thermotoga maritima* assembles into filaments in the presence of ATP or GTP and does not require magnesium (189). EM revealed that akin to actin double filaments (190), MreB also forms right-handed filaments, which are either straight or curved and can even form crystalline sheets under low-salt conditions (189). The assembly of MreB is promoted in the presence of divalent cations but inhibited by monovalent salts (191). When MreB assembles in the presence of divalent cations, the filamentous polymers generated are larger and stiffer than those of single actin filaments, indicating that MreB forms filament bundles or sheets as previously observed with TEM (189, 191, 192). MreB from *T. maritima* can bind directly to the membrane via a membrane insertion loop whilst MreB from *E. coli* associates to the membrane by an N-terminal amphipathic helix (193). Most recent *in vitro* studies on MreB from *T. maritima* demonstrated that its membrane association has a large impact on its polymerization dynamics and that MreB from *C. crescentus* can form antiparallel filaments under suitable conditions (193, 194).

MreB was first discovered as a rod-shape determining factor in *E. coli* (195) and since has proven to be essential for the maintenance of cell shape in most non-spherical bacteria. The MreB-encoding gene is absent in spherical bacteria, whilst it is present in most non-spherical bacteria (196). In general, Gram-negative bacteria encode one *mreB* gene, whilst some Gram-positive species encode several MreB paralogues. The Gram-positive *B. subtilis* has three MreB paralogues: MreB, Mbl (MreB-like protein) and MreBH (MreB homologue) (197-200). Exceptions to this generalization are the Gram-negatives *Rhizobium* and *Agrobacterium* as well as the Gram-positive *Actinobacteria*, which are rod-shaped but lack a recognizable *mreB* gene. A common feature of these species is their growth from one cell pole (77, 196).

MreB and its isoforms typically localize in a helical-like structure along the lateral sides of the cell or in a Z-ring-dependent manner at mid-cell and are associated with the inner membrane (188, 201, 202). The main function of MreB seems to be the spatial and temporal coordination of PG synthesis and degradation (203, 204). Nonetheless, the general understanding of the interplay between bacterial cytoskeletal elements and the peptidoglycan biosynthesis machinery is still largely unresolved (see section 1.3 for more detail) (2).

Previous reports have claimed that *B. subtilis* MreB and Mbl, and *E. coli* MreB form continuous membrane-associated helical filaments along the complete long cell axis (188, 205, 206). Functional GFP fusions to all three MreB paralogues showed a helical-like arrangement in *B. subtilis*, confirming the helix as the preferred arrangement of MreB and its paralogues. Furthermore, time-lapse microscopy revealed that both MreB and Mbl are highly dynamic with filament bundles making a full rotation in 50-60 s around the diameter of the cell (201). Thus the theory developed that MreB would not only act as a mechanical structure to uphold cell shape but actively participate in shaping the cell

by guiding the cell wall machinery (196, 207). With the development of new microscopy techniques in the last couple of years, the view on MreB's function and precise localization has been challenged.

The first doubts about the existence of continuous MreB filaments emerged when ECT was unable to show long helical filaments in rod-shaped bacteria. Instead cytoplasmic MreB filaments were found and it was postulated that rather than forming a rigid scaffold MreB might form dynamic complexes (208). Later in the same year the existence of dynamic MreB patches was confirmed by state of the art microscopy methods including total internal reflection fluorescence (TIRF) microscopy, which enabled a better spatiotemporal resolution of MreB *in vivo* (209-211). In essence, the new data confirmed that MreB undergoes dynamic, circumferential (not helical) movement, which is dependent on peptidoglycan biosynthesis and not driven by actin-like polymer dynamics (209-211).

Nevertheless, most recent work anew supports the existence of long, partially helical MreB filaments. It was revealed that MreB polymers are composed of antiparallel protofilaments, which enable it to bind intimately to the membrane (193, 194). This firm association between MreB and the inner membrane might be one of the reasons why so far large MreB filaments have remained undetected by ECT (148, 208). Furthermore, the localization pattern of MreB has been re-evaluated using a new generation of super-resolution microscopy techniques. Using structured illumination microscopy (SIM), stimulation emission depletion (STED) microscopy, and TIRF-SIM, the existence of extended filaments with circumferential motion along the long axis of the cell was confirmed (Figure 3B) (212, 213).

The possible role of MreB in cell shape and cell wall biogenesis is detailed in section 1.3.1. Previous studies in different species showed that MreB is not solely required for the maintenance of cell shape but also affects other aspects of cellular differentiation. In *C. crescentus*, it appears to participate in polar stalk elongation (214, 215). In *Myxococcus xanthus* by contrast, MreB is required for adventurous as well as social motility (216) and MreB also plays a role in spore differentiation and germination (217). MreB also appears to play a role in type-IV pilus localization and pilus-driven cell motility in *Pseudomonas aeruginosa* (218). In the actinomycete *Streptomyces coelicolor*, MreB is involved in spore formation but not necessary for vegetative growth (219). The inactivation of MreB in *H. pylori* causes a growth defect and abnormal nucleoid morphology (153). Furthermore, MreB filaments organize unique membrane regions with increased fluidity that are important for overall lipid homeostasis as well as membrane protein localization in *B. subtilis* (220). Nevertheless, there are still many controversies on the precise function and intracellular localization of MreB. Consequently the analysis of MreB still remains an active field of research.

Another member of the actin/sugar kinase/Hsp70 superfamily is the cell division protein FtsA (187), even though its fold slightly deviates from the canonical actin fold due to the addition and deletion of a subdomain (221). Similar to MreB, FtsA can form actin-like filaments (222) that are membrane-associated due to a conserved amphipathic helix at its C-terminus (223, 224). FtsA localizes in a ring-like structure at the future division site (Figure 3B) (225-227), where it directly interacts with FtsZ and acts as a tether for FtsZ (72, 224). Together FtsA and ZipA (another cell division protein) play a crucial part in the recruitment of downstream division proteins as well as the stabilization of the Z-ring (228).

However, prokaryotic actin homologues are not only involved in the maintenance of cell shape and cell division. ECT of *Magnetospirillum magnetotacticum* revealed that MamK, a distant homologue of both actin and MreB, forms linear filamentous structures that are vital for the proper positioning of magnetosomes (229).

Apart from MreB, FtsA, and MamK, most actin homologues are encoded by plasmids and also take part in their segregation (143). The best studied of these is ParM, which is encoded by the *par* locus of the R1 plasmid from *E. coli* (230). The crystal structure of ParM is very similar to that of actin (231); nonetheless it forms left-handed double helical filaments (75). Together with ParR and the *parC* (*parS*) DNA sequence, ParM is part of a three-component plasmid partitioning system (232). Only when bound to ParR/*parC* can ParM form stable filaments, which then further polymerize to push plasmids apart (233). On their own, ParM filaments are dynamically instable (233), which explains why *in vivo* ParM filaments are always associated with plasmids at both ends (Figure 3B) (150). This polymerization behaviour in the presence of a stabilizing substrate at one end of a filament is reminiscent of the action of formins on eukaryotic actin (234, 235).

In recent years, several new distinct bacterial actin families have been identified. Amongst them are AlfA (actin like filament A), which has sequence similarities to MreB, ParM, and actin, and several ALPs (actin like proteins) (236). These proteins were found encoded on various plasmids and responsible for their segregation (236, 237).

1.2.3. Crescentin and other intermediate filament-like proteins

Although the function of IF proteins differs vastly, they share a number of key characteristics. All eukaryotic IF proteins have a tripartite domain organization with a central coiled-coil-forming rod domain, which is split into four coiled-coil subdomains separated by linkers. The central domain is flanked by variable N-terminal head and C-terminal tail regions (151, 238). Thus, IF proteins are a subgroup of coiled-coil-rich proteins (CCRPs). *In vitro*, IFs can self-assemble into apolar filaments in the absence of nucleotides or cofactors. Even though IFs are flexible, they are very resistant to mechanical forces such as pulling. Therefore, IFs appear to mainly perform mechanical functions in bacteria (143).

The first prokaryotic IF homologue to be identified and characterized was crescentin from *C. crescentus* (151). Crescentin and other IF homologues, akin to eukaryotic IFs, are characterised by several coiled-coil domains (151). Purified crescentin is able to polymerize into IF-like filaments *in vitro* (151). Upon addition of 5-10 mM Mg^{2+} crescentin filaments bundle and make tight networks (239).

Crescentin polymerizes along the cytoplasmic membrane of the inner cell curvature and forms a stable, rigid structure (Figure 3C) (151). Hence cell wall growth is more abundant on one side of the cell due to the constriction of crescentin on the other side, which provides *C. crescentus* with its characteristic curvature (240). In the absence of crescentin, *C. crescentus* cells become straight (151). *In vivo*, crescentin filaments are exceptionally stable and no fluorescence recovery could be observed

during FRAP (fluorescence recovery after photobleaching) experiments. Whole-cell bleaching revealed that newly synthesized crescentin subunits are incorporated along the complete length of the existing filament (241), which is also characteristics of eukaryotic IFs (242). When expresses heterologously in *E. coli*, crescentin is able to induce cell curvature (240). The membrane association of crescentin is directly dependent on MreB (241).

Crescentin co-localizes with the essential CTP synthase CtpS, which is a bifunctional cytoskeletal metabolic enzyme producing the nucleotide cytidine triphosphate (CTP) (243, 244). CtpS can self-assemble without additional co-factors and independent of its enzyme activity into long filaments. These filaments are formed independently of crescentin and are recruited to the inner curvature of the *C. crescentus* cell by crescentin. CtpS polymers can perturb the assembly of crescentin. As the overexpression of CtpS causes cells to straighten and depletion of CtpS induces hypercurvature, it is conceivable that CtpS regulates cell shape by affecting the polymerization dynamics of crescentin. The CtpS homologue in *E. coli* (also known as PyrG) shows similar filament assembly properties as observed for CtpS from *C. crescentus*. Even though *E. coli* lacks crescentin and is rod-shaped, its CtpS homologue is still able to complement the enzymatic and structural function of CtpS from *C. crescentus*. Possibly, polymerization emerged as an allosteric regulatory mechanism for the enzymatic activity of CtpS. It is probable that *C. crescentus* adapted this feature of CtpS to serve as a regulatory component for the maintenance of cell morphology (243).

1.2.4. Coiled-coil rich proteins

Recently, a large group of IF-like polymer-forming proteins have been identified that do not share sequence homology to crescentin or eukaryotic IF proteins that are known as coiled-coil-rich proteins (CCRPs). As their name already indicates, these proteins contain several coiled-coil domains, although they do not possess the typical domain architecture of eukaryotic IF proteins (245-247). Many of these CCRPs have been shown to influence cell shape by providing mechanical stability to the cells (248).

One of the first filament-forming CCRPs to be discovered was FilP from the polarly growing species *S. coelicolor*. FilP, short for filament forming protein, forms extensive filamentous structures *in vivo* that line the cell envelope throughout growing hyphae and are most pronounced in the apical region (Figure 3C) (152). Furthermore, FilP forms apical growth-dependent gradients whose formation depends on DivIVA (152), which is a further CCRP and the main component of the polarisome complex in Actinobacteria (see section 1.2.5) (249). Cells lacking FilP do not only have growth and germination defects but also have irregular, gnarled hyphae (247). FilP is required to ensure the stability and flexibility of the hyphal cell wall by providing mechanical support (152). Another filament forming CCRP, Scy, is also recruited by DivIVA to the apical polarisome where it interacts with FilP (250). A *scy* null-mutant strain has severe morphological defects; however, FilP is still able to form apical gradients (152). Furthermore, Scy recruits the chromosome partitioning ATPase ParA to the growing tip of the hyphae, where ParA in concert with ParB promotes chromosome segregation (251). Thus, the interplay of various CCRPs is required for regular growth and morphogenesis in *S. coelicolor* (252).

Another CCRP required for the maintenance of cell shape is RsmP (rod-shaped morphology protein) from *Corynebacterium glutamicum,* which belongs to the polarly growing Actinobacteria that lack MreB (246, 253). RsmP was first identified as one of several proteins that were upregulated in a DivIVA-depleted strain. Like other CCRPs, RsmP forms long nucleotide-independent polymers *in vivo* and *in vitro*, which can associate into higher-order bundles (246). In the absence of RsmP, the cells lose their typical rod-shape to form coccoids, which is reminiscent of cells depleted of DivIVA (246, 253). *In vitro*, RsmP is phosphorylated at specific serine (Ser) and threonine (Thr) residues in the head and tail regions by the Ser/Thr protein kinases PknA and, to a lesser extent, by PknL (246). This post-translational modification of the head and tail regions is characteristic for some eukaryotic IFs, where it serves to regulate their assembly and function (254). Interestingly, phosphorylation of RsmP has a negative effect on filament formation *in vivo*. In short, RsmP seems to play a key role in maintaining the rod-shaped morphology in *C. glutamicum* and therefore might have taken the place of MreB (246).

In the spiral-shaped human pathogen *H. pylori*, four CCRPs, Ccrp58, Ccrp59, Ccrp1142, and Ccrp1143, act in concert to uphold correct cell morphology and motility. All four proteins are able to polymerize in a nucleotide-independent manner, generating filaments with a diameter close to ~10 nm (153, 255). Ccrp59 localizes statically in distinct foci in a patchy pattern along the long-axis of the cell, indicating the possibility of a helical organization (Figure 3C) (153). Deletion of Ccrp59 leads to a complete loss of helical shape, whilst the single deletion of the other CCRPs results in less drastic morphological changes (153, 255). The mechanism by which CCRPs contribute to proper cell shape in *H. pylori* still remains to be determined.

1.2.5. Bacteria-specific cytoskeletal proteins

The term “cytoskeletal” was first coined to describe long filamentous structures in eukaryotes; however, not all bacterial homologues, including MreB and FtsA, form lengthy visible structures *in vivo*. Consequently, filament formation is not a prerequisite for proteins to be part of the bacterial cytoskeleton (256). Hence, bacteria-specific scaffold-forming proteins like DivIVA and PopZ, which oligomerize *in vitro* and form large assemblies *in vivo*, are also considered members of the bacterial cytoskeleton (248).

DivIVA is widely conserved amongst Gram-positive bacteria and acts as a polar scaffolding protein (257). DivIVA homologues are characterized by two coiled-coil domains divided by a flexible linker region and flanked by short unstructured regions (258). In *B. subtilis*, DivIVA dimers assembly into “doggy-bone” structures that oligomerize end-to-end into ordered two dimensional lattice-like structures (259). DivIVA preferentially accumulates at sites of strong negative membrane curvature, like the cell poles and the cell division septum (Figure 3D) (155, 156). At the septum, DivIVA recruits MinCDJ to prevent premature reinitiation of cytokinesis at the new cell poles (260, 261). During sporulation, polar DivIVA recruits the DNA-binding protein RacA to the prespore in order to ensure chromosome attachment (262, 263). In *S. coelicolor*, DivIVA has a paramount function in tip extension and branching (249, 264). Recent studies showed that DivIVA directs the subpolar addition of new cell

wall material in mycobacteria (265). In *C. glutamicum*, DivIVA associates with ParB to anchor the chromosomal origin region to the cell pole (266).

Most Gram-negative Alphaproteobacteria possess PopZ, which is a protein functionally similar to DivIVA (154, 267). In contrast, PopZ does not contain any coiled-coil regions but instead has a central unstructured proline-rich region flanked by conserved α-helical structures (268). Even though there is no evolutionary link between PopZ and DivIVA, PopZ also assembles into filamentous oligomers that form a gel-like matrix, which creates a ribosome- and DNA-free region at the cell poles (154, 268, 269). In *C. crescentus*, PopZ localizes dynamically to the cell poles (Figure 3D) and, similar to DivIVA, interacts with ParB to tether the origin region to the pole. Additionally, PopZ interacts with ParA to facilitate proper chromosome segregation (154). It also positions the two membrane-bound histidine kinases CckA and DivJ, which play a decisive role in cell cycle regulation and stalk formation (269, 270). Unlike DivIVA, the accumulation of PopZ at the poles seems to be independent of membrane curvature and most likely relates to the protein's preference of nucleoid-free regions (269, 271). However, the mechanism of PopZ assembly is not fully understood.

1.2.6. Bactofilins, limited to bacteria but divers in function

The first bactofilin to be characterized was from *Proteus mirabilis*, which was identified during a transposon insertion screen. Cells with an insertion in the *ccmA* gene, which stands for curved cell morphology, were unable to swarm, which was attributed to the elongated and irregularly curved morphology of the mutant (272). The conclusion that bactofilins are a new class of proteins, that are widely distributed among bacteria and feature many cytoskeletal characteristics came only with the characterization of BacA from *C. crescentus* (157).

C. crescentus has two bactofilin paralogues termed BacA and BacB, which are small (~20 kDa) soluble proteins characterized by a conserved bactofilin (formerly DUF583) domain flanked by proline-rich regions (157). Both BacA and BacB localize to the stalked pole in a cell-cycle-dependent manner (Figure 3D), whilst they remain diffuse in swarmer cells (Figure 4A). The two bactofilins form a sheet-like polymer that lines the inner membrane at the stalked cell pole and *in vitro* bactofilins can spontaneously organize nucleotide-independently into rod-, ribbon-, or sheet-like assemblies (Figure 4A) (157, 273). The bactofilin copolymers are assumed to play a role in stalk biogenesis as they recruit the PG synthase PbpC to the stalked pole (Figure 4B) (157). Additionally, PbpC recruits and tethers the stalk-specific membrane protein StpX to the stalked pole, where StpX is required for stalk elongation under nutrient-limiting conditions (274, 275). In the absence of BacA stalk length is reduced by approximately 45 %, whilst the absence of BacB and PbpC caused less pronounced changes in stalk length. If overproduced, the bactofilins produce long filamentous structures that cause cell shape defects and hypercurvature. These findings indicate that bactofilins play a role in stalk biogenesis in *C. crescentus* (157, 276).

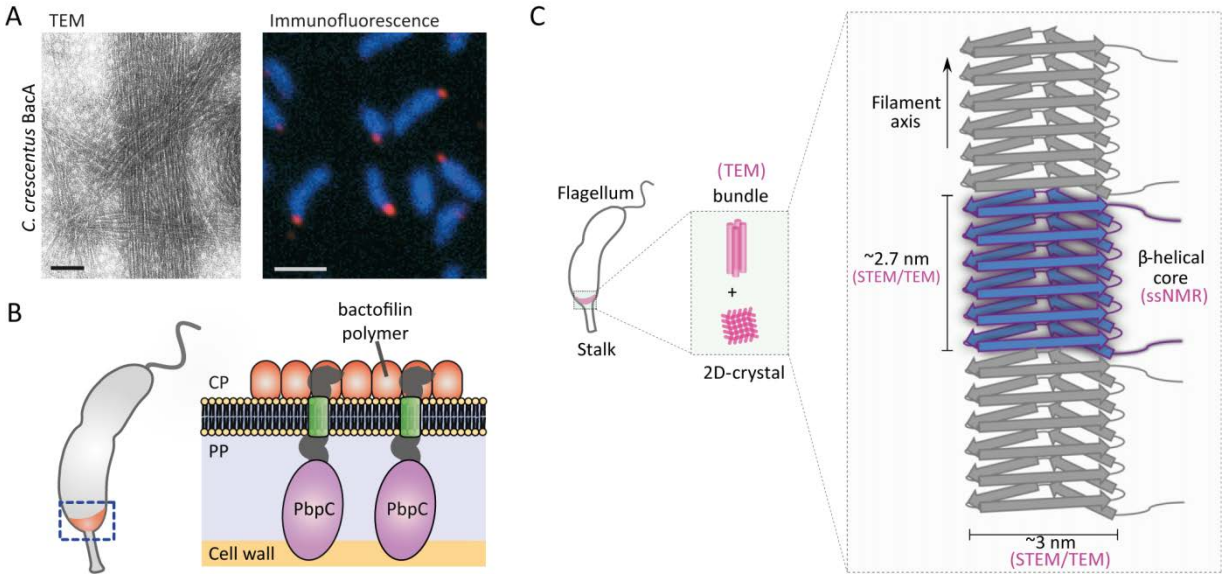

Figure 4. Filament structure and subcellular localization of BacA in *C. crescentus*. A) Left panel: TEM image of negatively stained BacA filaments from *C. crescentus*. Scale bar, 75 nm. Right panel: subcellular localization of BacA in *C. crescentus* determined immunofluorescence microscopy. BacA is visible in red, the DAPI stained chromosome is visible in blue. Scale bar, 2 µm. **B)** Cartoon depicting the subcellular localization of BacA (red) in *C. crescentus* and its interaction with the integral PG synthase PBPC. The hatched box indicates the region of the cell displayed on the right. Abbreviations: CP, cytoplasm; PP, periplasm. Images taken from Lin and Thanbichler, 2013 (277). **C)** Cartoon representing the filament structure of BacA. Structural parameters were determined as indicated. Image taken from Vasa *et al*., 2014 (273).

Despite the lack of evolutionary relationship, the bactofilin paralogues BacA and BacB from *C. crescentus* resemble the protein localization factors DivIVA from *B. subtilis* (155, 259) as well as PopZ from *C. crescentus* (154, 269) in their ability to form polarly localized, membrane-associated polymers (157).

Using solid state nuclear magnetic resonance (NMR) analysis, the atomic structure of the bactofilin domain (residues 37 to 139) from *C. crescentus* BacA could be resolved. Its core is composed of 18 rigid β-strands and flexible N- and C-terminal regions (Figure 4C). Overall a β-helical fold was suggested for BacA (273). Further analysis revealed that BacA forms a right-handed β-helix consisting of six windings with a triangular hydrophobic core (278). Notably, this is the first instance a right-handed β-helical fold has been attributed to a cytoskeletal protein. How the structure of BacA relates to its function as a scaffold remains to be determined.

Bactofilins are involved in diverse cellular processes. *Myxococcus xanthus* has four bactofilin homologues, BacMNOP, of which BacM is relevant for cell morphology and cell wall stability (157, 279). In the absence of BacM, the otherwise rod-shaped cells develop kinks and become more sensitive towards cell-wall-targeting antibiotics. Purified BacM forms 3 nm wide filaments, which assemble into larger chains that form helical-like cables throughout the cell whilst a small subpopulation form lateral rod-like structures at one pole. BacM exists as a 150 amino acid full-length protein as well as an N-terminally processed version, which is 27 amino acids shorter. Interestingly, isolated fibres only consisted of the shorter BacM version, indicating that BacM is processed before or during polymerization (279).

Additional studies showed that BacP plays a vital role in establishing cell polarity in *M. xanthus* (280). For motility *M. xanthus* uses type IV (T4) pili, which are assembled at the leading pole and have to be delocalized and reassembled at the other pole during directional reversals (281). Polymeric BacP localizes in the subpolar regions of both poles. The small GTPase SofG and the T4 pili motor ATPases PilB and PilT are recruited to one of these clusters and eventually localized to the pole. In a further step, the two motor ATPases are distributed to opposite poles by another small GTPase, MglA. Thus, BacP plays an important role in the establishment of cell polarity during motility in *M. xanthus* (280).

Together with BacN and BacO, BacP is also responsible for the maintenance of the chromosome segregation machinery in *M. xanthus*. BacNOP form a co-polymer at the polar to subpolar region that recruits ParA and ParB, which are both essential for chromosome segregation in *M. xanthus* (282). The interaction between BacNOP and ParA/B seems to be mediated by BadA (also known as PadC), which is a ParB-like nuclease. Taken together, Bactofilins act as a polar landmark to organise chromosome segregation in concert with BadA in *M. xanthus* (277).

In *B. subtilis*, the two bactofilin paralogues BacE and BacF are essential for motility. In the absence of BacEF, cells lose their swimming motility as they no longer make flagella. It appears that in the absence of BacEF, flagellar hook assembly and flagellar filament assembly are abolished whilst the flagellar basal body is correctly assembled. The N-terminal fusion of BacE localizes in discrete foci along the membrane, whilst some of the fusion proteins diffuse freely within the cytosol. On the other hand, N-terminally tagged BacF forms distinct membrane-associated foci reminiscent of flagellar proteins (283). With the help of G-STED (gated stimulated emission depletion) microscopy, the structure of BacF was revealed to be more round than filamentous. Only when overexpressed did the bactofilins form long filamentous structures. When expressed heterologously in S2 Schneider cells, BacE associated with the membrane and formed filaments on its own, whilst BacF failed to form filaments but instead assembled into foci. Expressed simultaneously, the proteins formed extensive filaments, indicating that BacE and BacF likely act in concert. Time-lapse experiments revealed that whilst BacE co-localizes dynamically with flagellar basal bodies, BacF statically localizes to a subset of basal bodies. Taken together, bactofilins in *B. subtilis* form partially dynamic filamentous structures that are vital for swimming motility (283).

The establishment of helical cell shape in *H. pylori* depends on its sole bactofilin homologue CcmA (284). In the absence of CcmA, the cells lose their characteristic helical shape and form slightly curved or straight cells. How CcmA contributes to cell shape is unclear. Experimental evidence indicates that CcmA and the three LytM-domain peptidases Csd1-3 act in concert to generate the helical shape of *H. pylori* by the hydrolysis of PG along certain points of the long axis of the cell, which results in a shift of the cell wall into its helical confirmation (284). Assuming that CcmA forms polymers akin to its other bactofilin counterparts, it might act as a membrane-associated scaffold for the (in)direct positioning of Csd1-3 (277).

In *Shewanella oneidensis*, the bactofilin homologue localizes to the division plane and is thus thought to play a role in cell division (157). In summary, bactofilins preform a wide range of functions within

various bacterial species, which include cell motility, cell shape, chromosome segregation and possibly even cell division. The extent to which bactofilins are scaffolds for coordinating PG synthesis and hydrolysis remains an active field of research and will be further addressed in this study.

1.3. PG incorporation during cell growth and cell division

Generally, growth can be divided into the two distinct stages of cell elongation and cell division. PG biogenesis is orchestrated by a conserved and highly sophisticated machinery that has to be tightly regulated in order to maintain cell shape and facilitate cell division (2). The specific enzymes that play a determining part in the organisation during each stage are detailed below.

1.3.1. Growing along with the elongasome

Before cells proliferate they increase in size. In most rod-shaped bacteria, dispersed PG insertion along the lateral cell wall is essential for growth and cell elongation (2). During elongation, the coordination of PG incorporation is thought to be mainly mediated by the polymer-forming actin homologue MreB (Figure 5). MreB is vital for the elongation of rod-shaped bacteria, and its depletion or inactivation causes a swift stop in cell elongation, which leads to an increase in cell diameter up to the formation of spheres (285-287).

MreB is tethered to the inner membrane by either RodZ (288-290) or via an N-terminal amphipathic helix (193), where it also associates directly or indirectly with the inner-membrane protein RodA (215, 291-296) and the conserved inner-membrane proteins MreC and MreD (292, 297). In all probability MreB is involved in directly or indirectly recruiting and/or positioning components of the PG biosynthesis machinery (207, 298, 299). Together, MreBCD, RodA, and PBP2 form the so-called elongasome complex, which facilitates the insertion of new PG in a helical manner during cell elongation (292, 293). MreB interacts with the lipid II synthases MraY and MurG (300). Indirectly, MreB is also most likely responsible for the localization of PBP1A (2, 300), which together with its activator LpoA localizes in distinct foci to the sidewall (62, 63, 301). Additionally, PBP1A directly interacts with PBP2, which stimulates the GTase activity of PBP1A as well as the TPase activity of PBP2, leading to an increased attachment of new PG (301).

Previously it was thought that the motion generated by MreB polymerization guided the elongasome along a circumferential path (302-304). However, when the ATPase cycle of MreB was perturbed by the MreB inhibitor A22 or by mutation of the *mreB* gene, the motion of MreB remained unaffected (209, 210). On the other hand, the depletion or antibiotic-mediated inhibition of PBP2 in *E. coli* and PBP2A and PBPH in *B. subtilis* abolished MreB filament movement. These results indicate that the movement of the elongasome is driven by the ongoing PG synthesis (209-211). A recent study revealed that MreB rotation depends on its interaction with RodZ, which directly or indirectly connects MreB to the PG synthesis machinery. Notably, MreB rotation is not required for rod shape determination under standard laboratory conditions; nevertheless it remains essential to uphold cell shape under conditions of cell wall stress (296).

1.3.2. Splitting with the divisome

At the onset of cell division, the tubulin homologue FtsZ takes over the control of the PG machinery and thus specifies and coordinates preseptal growth and septum formation (zonal growth) at the division plane (172). The protein complex that assembles around FtsZ and promotes cell separation is referred to as the divisome (305). In *E. coli* the assembly of the divisome can be divided into two steps, the recruitment of the early and the late divisome (306).

In the first assembly stage of the divisome, FtsZ localizes to the future cell division site along with FtsA and ZipA, which are essential for Z-ring stability (224, 307). Furthermore the non-essential ZapABCD proteins also associate with the Z-ring, whereby ZapA and ZapD directly interact with FtsZ to promote Z-ring stability (308-310) with the assistance of ZapB (311) and ZapC (308). The last member of the early divisome is the ATP-binding cassette (ABC) transporter homologue FtsEX, with the ATP-binding protein FtsE binding directly to FtsZ (312-314).

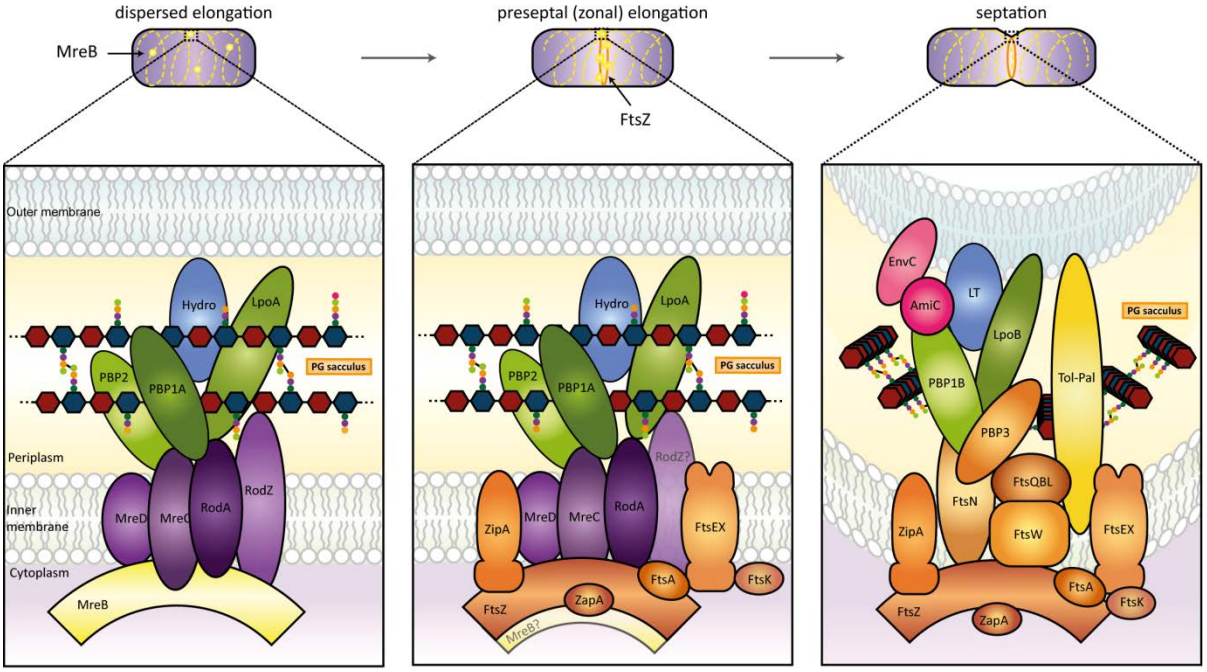

Figure 5. The cell cycle-specific composition of the PG biosynthesis complex in *E. coli*. The first panel on the left depicts the elongasome complex during lateral (dispersed) elongation. During this stage, MreB and its associated protein (MreCD, RodAZ) recruit the PG synthases PBP1A (along with its activator LpoA) and PBP2, as well as still-unknown hydrolases (Hydro) to the elongasome. The second panel shows pre-septal growth, during which FtsZ (and possibly MreB) guides the PG-remodelling complex. During pre-septal growth, the first part of the divisome is already assembled (FtsA, ZipA, ZapA, FtsEX, FtsK, and possibly contains some MreB-associated proteins as well). The last panel depicts the mature divisome, which is solely guided by FtsZ and contains all essential proteins for cell division. At this late stage, the PG-remodelling complex contains the PG synthases PBP1B and PBP3, the amidase AmiC with its regulator EnvC and lytic transglycosylases (LT) along with the Tol-Pal complex for constriction of the outer membrane. Based on Typas *et al.*, 2012 (2).

In some species like *E. coli* and *C. crescentus*, an FtsZ-dependent (pre-septal) growth phase at midcell occurs before the actual onset of cell division (Figure 5). In contrast to *E. coli*, pre-septal growth contributes significantly to cell elongation in *C. crescentus* (315, 316). During this stage the lipid II synthase MurG is recruited to midcell presumably along with PG synthases (19, 298, 315), excluding

PBP3 (316). Furthermore, studies in *E. coli* and *C. crescentus* suggest a potential involvement of MreB in preseptal growth (202, 317).

The second step of divisome maturation includes the independent recruitment of the essential proteins FtsK, FtsQ, FtsL, FtsB, FtsW, PBP3 (FtsI), and FtsN, whereby most proteins seem to arrive at the future division site simultaneously (Figure 5) (306, 318). During this second recruitment phase PBP2 leaves the division site (69). Other non-essential proteins of the late divisome include the PG synthase PBP1B (71) along with its regulator LpoB (63) and the hydrolases AmiB and AmiC (89, 92) accompanied by their regulators EnvC and NlpD (123). PBP1B localizes to the division site in a PBP3-dependent manner (71), whereas PBP3 is recruited to the divisome by the integral membrane protein FtsW (319), which also interacts with PBP1B (320). In the absence of PBP1B, the elongasome synthase PBP1A localizes to midcell and participates in cytokinesis (301). PBP3 also interacts with the DNA-translocase FtsK (321, 322) as well as the bitopic membrane protein FtsN (323, 324), which also interacts with PBP1B and stimulates its activity (324). It is still unclear how the force necessary to achieve constriction is generated; the most recent speculations include a combined action of FtsZ and PG biogenesis (175). Additional hydrolases at the division site presumably include the LTs Slt70, MltA, and the DD-EP PBP7/8 (111, 325). In *C. crescentus* the LytM peptidase DipM also participates in cell division (126-128).

Additionally, in Gram-negative species the invagination of the outer membrane during septation is facilitated by the Tol-Pal complex, which also localizes to the division septum (326). The Tol-Pal complex is essential in *C. crescentus* (327), but not in *E. coli* (63).

1.3.3. Establishing rod-shape and alternative growth modes

For cells to successfully maintain their morphology and effectively proliferate, the interplay between PG synthesis and degradation must be spatiotemporally tightly regulated (5). After successful cell separation, PG synthesis is redirected to the lateral cell wall once again (202). In most cases symmetric cell wall synthesis leads to the production of two equally sized daughter cells where both have an old and a new pole (328).

As already indicated, PG insertion in most rod-shaped bacteria, such as *E. coli* and *B. subtilis*, occurs in a dispersed manner along the complete cell (316, 329-333). Zonal PG insertion is only observed during septum formation (172) and, if present, during the pre-septal elongation phase before the onset of septation (Figure 6) (316).

Nevertheless, there are alternative ways the PG biosynthesis machinery can be guided in rod-shaped bacteria that lack MreB. In the rod-shaped Actinobacteria, such as *Corynebacterium*, *Mycobacterium* and *Streptomyces*, DivIVA determines cell polarity by accumulating at negatively curved membranes, where it recruits PG biogenesis-relevant enzymes. Thus the cells elongate by polar growth (249, 257, 334). Interestingly, the PG along the side walls seems to stay inert (196, 335).

The Alphaproteobacteria offer a wide range of alternative ways for growth and cell division (336). Polar growth can be found in some rod-shaped Alphaproteobacteria, which reproduce by budding, a

process in which the offspring is generated exclusively from new cell material at one pole of the cell (337). Amongst the members of the Rhizobiales, the *Rhizobiaceae* and *Brucellaceae* are believed to proliferate by budding (77). Interestingly, genomes of bacteria of these genera lack the operon encoding MreBCD, RodA and PBP2 (196, 338). The absence of these conserved proteins indicates that cell growth is mediated by a so far unknown mechanism.

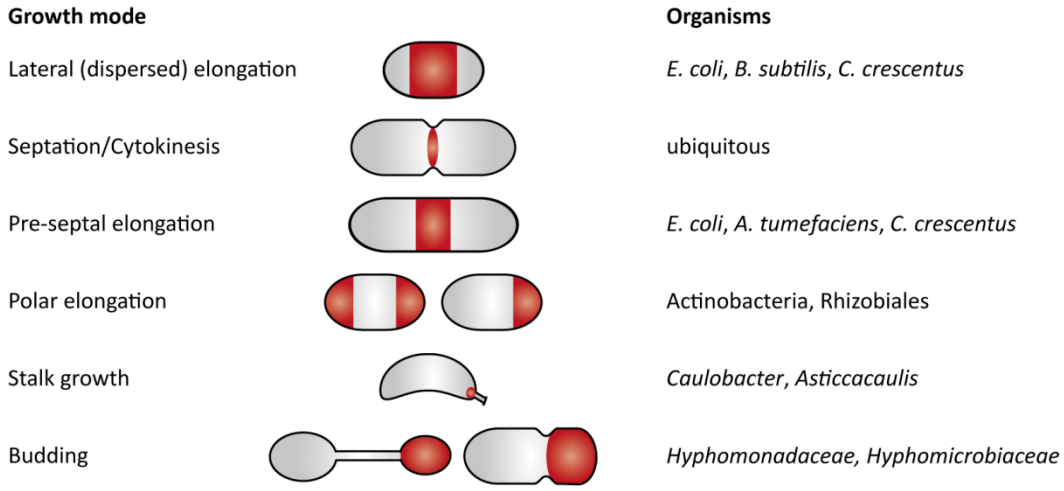

Figure 6. Growth modes in rod-shaped bacteria. The various growth regions of different bacterial species are schematically depicted in red. Adapted from Randich and Brun, 2015 (276).

Another form of polar growth is the generation of a cellular extension at one cell pole (339). The well-studied *C. crescentus* is a model organism for asymmetric binary fission, which arises from the cell cycle-dependent formation of a stalk at the old cell pole (Figure 7C). In *C. crescentus* the stalk functions as an adhesive structure that is not part of the cell body as it is compartmentalised by crossbands, thus the stalk does not contain any DNA and cytoplasmic proteins (340, 341). Some species of *Asticcacaulis* can even produce multiple stalks (342). It appears that in *C. crescentus* MreB together with RodA and PBP2 recruit further PG synthesis enzymes (215). The overexpression of RodZ causes the formation of multiple stalks (290). It seems that *C. crescentus* relies on the same PG biosynthetic machinery for stalk biogenesis that is responsible for cell elongation (276). At the same time the bactofilins recruit PbpC to the stalked pole, where it might act in concert with PbpX (62, 67). In the absence of bactofilins, stalk length is reduced by 45 % (157). Under phosphate limiting conditions, *C. crescentus* can elongate its stalk, whereby the surface area of the stalk is increased (343), which was thought to facilitate nutrient uptake (339, 341, 344). However, with the identification of the diffusion barrier generated by crossbands in *C. crescentus*, the nutrient scavenging properties of the stalk have been severely challenged (345).

Amongst the budding Rhizobiales, Hyphomicrobiacae, such as *Hyphomicrobium* (346) and *Rhodomicrobium* (347), combine polar stalk formation with a budding mechanism, whereby the stalk is utilized as a reproductive organelle (346). The dimorphic *Hyphomonas neptunium*, a close relative of *C. crescentus* (348, 349), also propagates by budding (350). As recently genetic tools have been established for *H. neptunium* (3), it offers a novel and intriguing system to study budding in prosthecate Alphaproteobacteria.

1.4. *Hyphomonas neptunium* as a model organism for stalked budding bacteria

Hyphomonas neptunium is a dimorphic, Gram-negative Alphaproteobacterium, which was first isolated in 1964 from a seawater sample from the harbour of Barcelona, Spain (Figure 7A). Originally, the species was described as *Hyphomicrobium neptunium* due to morphological similarities to members of the Hyphomicrobiaceae (350). Recent 23S rRNA gene sequence analysis and concatenated protein alignments support a possible reclassification to the order *Caulobacterales*. These findings are further supported by a comparative genomic analysis between *H. neptunium* and the model organism *C. crescentus* (349). Unlike *C. crescentus*, *H. neptunium* is a non-saccharolytic bacterium (350), even though it possesses all the genes required for glycolysis and the pentose phosphate pathway. In case *H. neptunium* utilise carbohydrates, it has not been observed under standard laboratory conditions (349), instead its preferred energy and carbon source are amino acids (351). *Hyphomonas* species are also capable of using pyruvate, α-ketoglutarate, fumarate, or malate as a carbon source (352).

Most Bacteria reproducing by budding, including *H. neptunium*, belong to the Alphaproteobacteria. A particular feature of cell division in prosthecate bacteria is the generation of offspring that are morphologically and physiologically different from each other. Figure 7 shows two examples of prosthecate bacterial cell division. Both *H. neptunium* and *C. crescentus* undergo morphological changes that are coupled to cell cycle progression. Based on a close phylogenetic relationship between the two species, *H. neptunium* possesses homologues of several key cell cycle regulators from *C. crescentus* (349). Nonetheless, *C. crescentus* divides by asymmetric binary fission, whilst *H. neptunium* reproduces by budding and uses its stalk as a reproductive organelle (Figure 7B and C).

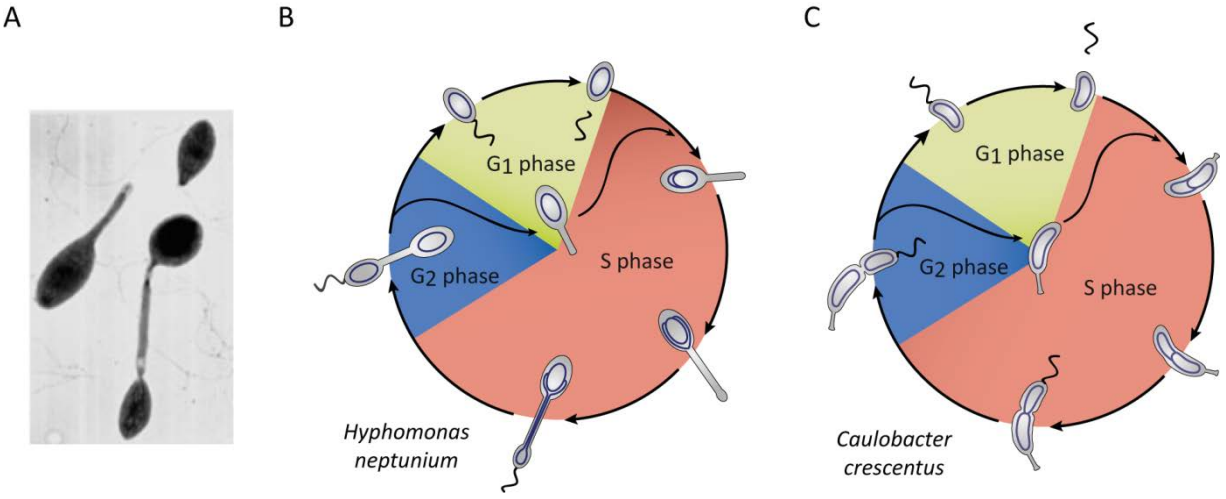

Figure 7. Comparison of *H. neptunium* and *C. crescentus* cell cycles. A) Electron microscopy image of *H. neptunium* displaying a swarmer cell (top right), a stalked cell (left) and a budding cell (right). Adapted from Wagner and Brun, 2007 (339); **B)** Life cycle of *H. neptunium* dividing by budding. **C)** Life cycle of *C. crescentus* reproducing by asymmetric binary fission (courtesy of M. Thanbichler).

At the beginning of its cell cycle, *H. neptunium* has an ovoid shaped swarmer cell that is motile due to the presence of a single polar flagellum. To reproduce, a swarmer cell must differentiate into a non-motile stalked cell. Before the onset of stalk formation, cells might adhere to a surface by producing EPS (extracellular polymeric substance (353). The transition from the swarmer to the stalked cell requires the shedding of the flagellum and the outgrowth of a stalk at the opposite pole of the cell (354). Swarmer cells are only able to replicate their chromosome when they shed their flagellum and begin to differentiate into a stalked cell (355). The mother cell uses its elongated stalk as a reproductive organelle. As the cell cycle progresses, a bud emerges at the distal pole of the stalk, which eventually expands into a flagellated swarmer cell. The cellular components required for bud formation, such as ribosomes and DNA, must be transported through the stalk of the mother cell. Pseudovesicles (356), which were thought to facilitate the transport process through the stalk, could not be confirmed by ECT (A. Briegel, unpublished). Once the bud reaches its final size and has generated a flagellum at the new pole, cell division occurs at the junction between the stalk and the bud (also referred to as the bud neck). This highly asymmetric cell division produces a motile swarmer cell and a non-motile stalked mother cell (Figure 7B). The mother cell can directly undergo another round of cell division, whereas the swarmer cell must differentiate into a stalked cell (353, 355).

The main advantage of budding is the dispersal of the new generation, whereby the competition for resources is reduced. Spatial separation is promoted by the motility of the daughter cell and the immobile sessile state of the mother cell. In short, budding represents an excellent reproduction strategy for survival in a nutrient-limited environment (357).

The best-studied budding bacteria include *Hyphomicrobium* species, such as *H. vulgare* (267), and *Rhodomicrobium* species, such as *R. vannielii* (358). Nonetheless, previous studies have not addressed the molecular mechanisms of budding. Accordingly, the molecular mechanisms and their regulators involved in budding require further investigation. Since *H. neptunium* has become genetically accessible, it can serve as a model organism for the budding process (3).

1.5. Scope

Our current knowledge of bacterial growth, cell division, and morphological differentiation is limited to *E. coli* and *B. subtilis*, which are characterized by a regular rod-shaped form and thus divide by symmetric binary fission. Research on alternatives modes of growth, division, and differentiation is mainly based on *S. coelicolor*, *C. crescentus*, and *M. xanthus*. Thus, at present our understanding of polarly growing bacteria as well as budding bacteria is still very limited due to the lack of genetic accessibility of these species. Since the dimorphic, budding Alphaproteobacterium *H. neptunium* has recently become genetically amenable, we are finally able to broaden our understanding of bacteria that utilise alternative growth and proliferation mechanisms.

The aim of my PhD project is to analyse the growth and the control of morphogenesis in *H. neptunium*. To conduct an in-depth analysis of cell morphogenesis, we will investigate the interplay between the bacterial cytoskeleton and the peptidoglycan biosynthetic machinery. We will try to

identify the factors that play a major role in the morphological transitions of *H. neptunium* as well as identify specific factors unique to the budding process. To accomplish this, we will analyse the PG composition of *H. neptunium* and identify the PG synthases and hydrolases involved in sculpting its cell wall. We will also determine the role of MreB during growth and budding. An additional focus is on understanding how bactofilins influence and control cell shape in *H. neptunium*. Overall, we strive to conduct a detailed characterization of the growth mechanisms in *H. neptunium* by which we will improve the global understanding of asymmetrically growing and budding bacteria.

2. Results

2.1. Dynamics of the peptidoglycan biogenesis machinery during budding in *H. neptunium*

Our first goal was to determine how *H. neptunium* proliferates. We wanted to elucidate how the stalk is generated and maintained during the cell cycle. We also aimed to analyse the molecular mechanism of budding at the distal end of the stalk. A global approach was started to identify novel candidates for cell wall biogenesis factors in *H. neptunium*, of which some had already been previously described in other organisms. First we pursued homologues of *C. crescentus* proteins known to partake in cell wall remodelling in *H. neptunium* using NCBI-BLAST (359). Second, we used the Pfam database (360) to search for additional proteins in *H. neptunium*, which do not have homologues in *C. crescentus*, that had specific functional domains previously described to be involved in cell wall biogenesis. The findings of this search and its subsequent results are summarized in the following sections. During this work, we gained insight into the complex growth pattern of *H. neptunium*. We could also identify some of the major components involved in the biogenesis of new cell wall material. Nevertheless, still much work remains until the intricate mechanism of budding will be fully unravelled.

2.1.1. The mother cell forms one unit with the stalk and the bud

To gain a better understanding of how *H. neptunium* cells grow and what role the stalk plays in budding of the daughter cell, electron cryo-tomography (ECT) was performed on wild-type cells (Figure 8). The advantages of ECT are that the samples are retained in their near native state as they do not require additional staining and the low electron dosage required for imaging reduces the harsh sample damage normally caused by transmission electron microscopy (TEM) (361, 362). The tomographic images clearly reveal that *H. neptunium* lacks crossbands, which are characteristic of the stalk of *C. crescentus* (Figure 8C and D) (345). Furthermore, the stalk of *C. crescentus* contains no cytoplasm (341). In *H. neptunium*, there is also no visible barrier between the stalk and the emerging daughter cell, indicating that the stalk is a true extension of the cytoplasmic compartment. The average diameter of a stalk lies between 120 - 140 nm and can reach up to 150 nm (Y.-W. Chang, private communication), which is comparable to the stalk width of *C. crescentus* (363). Like for other bacteria, the daughter cell stays connected to the mother cell via its stalk until the onset of cell division (Figure 8C, D and E). Contrary to previous observations, no pseudovesicles, which should be invaginations of the cytoplasmic membrane that are still connected to the cytoplasm of the mother cell, were observed. Previously, these pseudovesicles have been postulated to facilitate the transport of DNA and ribosomes through the stalk to the emerging bud (356). Most likely the observed pseudovesicles were an artefact generated during the fixation of cells for TEM. Previous reports also claimed that ribosomes were restricted to the mother cell and to pseudovesicles within the stalk; however, our tomographic images clearly reveal that free ribosomes are also present within the stalk.

Interestingly, in some cells we could observe a dense, filament-like structure that reached from the base of the stalk to its tip (Figure 8B). This structure was only observed in a few young stalked cells, in which the stalk just started to emerge. Regardless, the composition and function of this filament-like structure remains unclear. The tomographic images have confirmed that the stalk in *H. neptunium* is a continuous structure that is a true protrusion of the cell body and not segmented by any intracellular barriers from the mother or daughter cell, indicating a free translocation of DNA and proteins between the mother cell and the budding daughter cell.

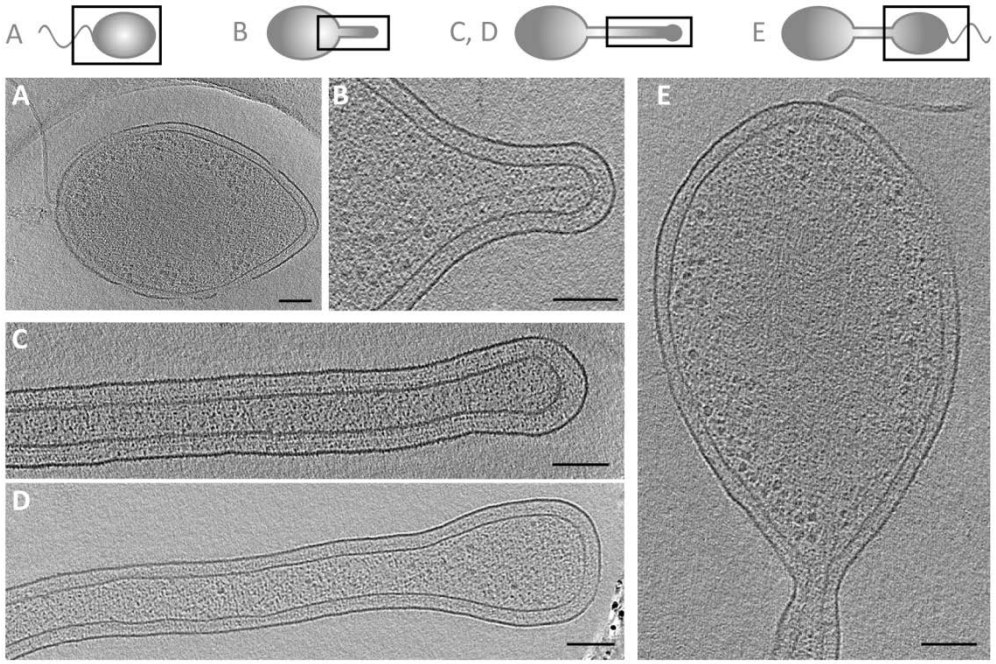

Figure 8. The mother cell forms one continuous unit with the stalk and the bud. The *H. neptunium* wild type was grown to exponential phase in MB medium and analysed by electron cryotomography. Cells and structures depicted are A) a flagellated swarmer cell, B) the stalked pole with an outgrowing stalk, C) and D) stalks with an emerging bud, and E) a flagellated daughter cell at the distal end of the stalk. Scale bar, 100 nm. Images provided by Yi-Wei Chang and Grant Jensen.

2.1.2. *H. neptunium* growth dynamics is cell cycle-dependent

In order to understand how the asymmetric morphology of *H. neptunium* is established, we first wanted to elucidate exactly in which manner *H. neptunium* cells grow and how often one cell can produce offspring. Previous reports have stated that prosthecate budding bacteria can only produce up to eight offspring before cell death (346). Tracking single cells in a microfluidic system revealed that mother cells can produce at least 30 offspring without showing any decrease in reproduction rate or morphological defects (Figure 9A and Movie S1). Based on these observations, we presume that a mother cell has the capacity to divide multiple times beyond our investigated time frame. Our results indicate that contrary to past belief, *H. neptunium* can proliferate at least up to 30 times with the potential for numerous further divisions.

Our next goal was to determine how the new daughter cell is generated at the tip of the stalk. There were two possible hypothesis: either the bud would grow out of the tip of the stalk or the tip of the

stalk would simple expand to contain the new offspring. In order to determine how *H. neptunium* proliferates, single cells were tracked in a microfluidic system (Figure 9A). The completion of a single round of the cell cycle from the swarmer cell to cell division in general approximately 180 to 210 min in this system. Once the stalk has been established, a mother cell can produce a new bud every 2 to 2.5 h (Figure 9). To assess overall cell growth, the length of the cell body, the stalk, and the bud of a single cell were measured over the course of several rounds of development. The fluctuations in compartment length over the cell cycle are characterized by periodicity, with the exception of the mother cell's body size, which stays constant throughout the course of the experiment (Figure 9B). On the other hand, the stalk grows to a certain extent until the onset of budding. Once the new daughter cell starts to increase in size, the stalk becomes shorter (Figure 9B). Our measurements indicate that the new daughter cell matures by remodelling the tip of the mother cell's stalk. It seems that during budding in *H. neptunium* the new cell compartment forms by remodelling a part of the stalk to generate the daughter cell.

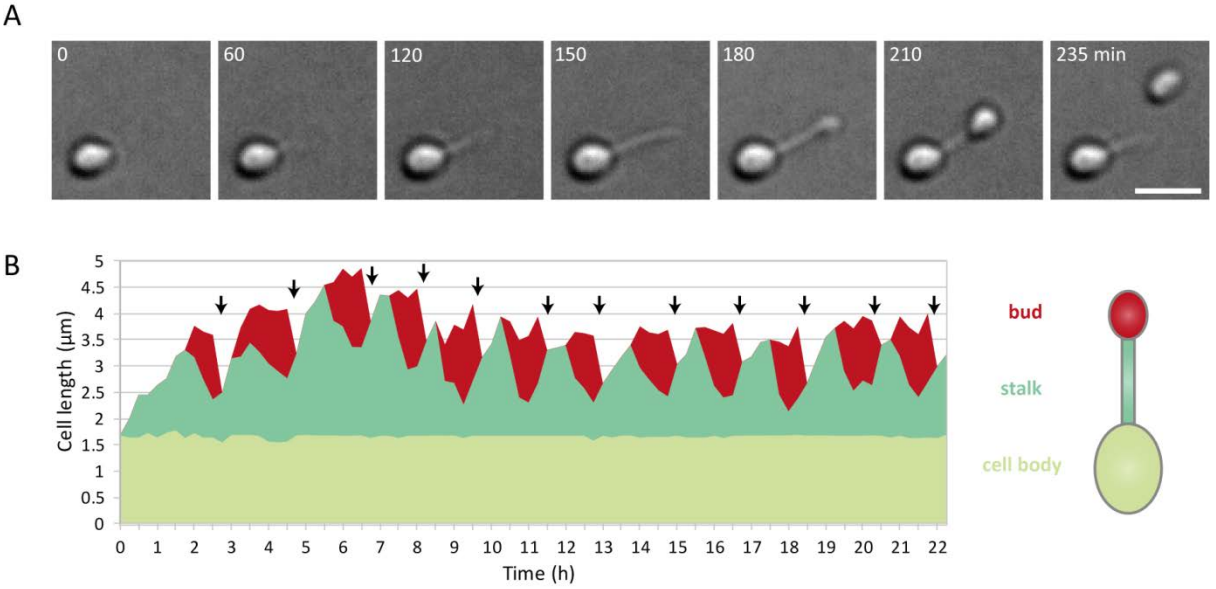

Figure 9. During budding the daughter cell grows into the stalk of *H. neptunium*. A) *H. neptunium* utilizes its stalk as a reproductive organelle. *H. neptunium* wild-type cells were grown to exponential phase in MB medium and transferred to a microfluidic system. DIC images were taken every 15 min. Scale bar, 2 µm. **B)** The emerging daughter cell remodels part of the mother cell's stalk. The *H. neptunium* wild type was grown to exponential phase in MB medium and transferred to a microfluidic system for 23 h. DIC images were taken every 15 min. Arrows indicate the first frame after a cell division event. Separate measurements were made for mother cell body, stalk and daughter cell (bud).

2.1.3. The stalk grows at the stalked pole *H. neptunium*

We know from other Alphaproteobacteria such as *C. crescentus* and *Asticcacaulis excentricus* that their stalk is synthesized at the base (315, 364, 365). One of our major goals was to clarify whether stalk growth is also initiated at the base or rather at the tip of the stalk in *H. neptunium*.

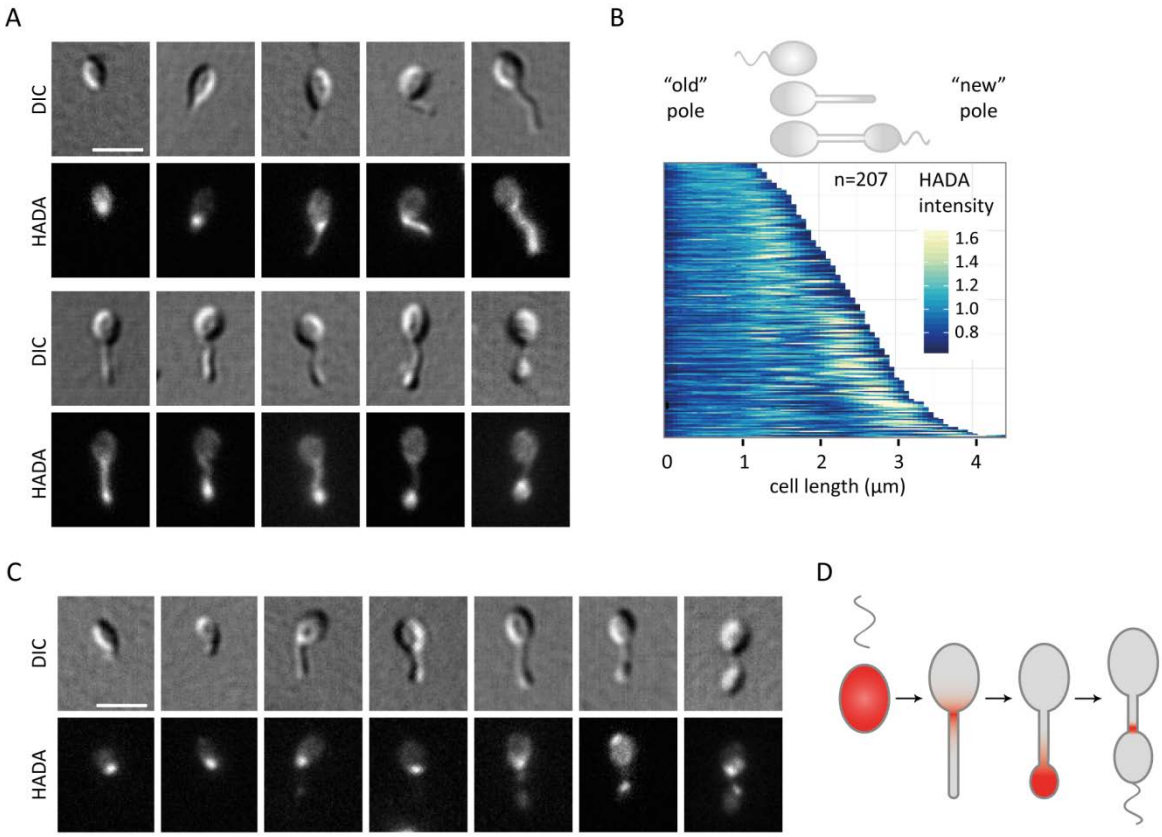

Figure 10. Cell growth is characterized by four specific growth phases in *H. neptunium*. A) Cell growth is divided onto four specific locations in *H. neptunium*. *H. neptunium* wild type was grown to exponential phase in MB medium, pulse-labelled with HADA, and imaged by DIC and fluorescence microscopy. Scale bar, 2 µm. **B)** Nascent PG incorporation in *H. neptunium*. Demograph of nascent PG insertion based on images from A). **C)** Rapid cell wall turnover in *H. neptunium*. *H. neptunium* wild type was grown to exponential phase in MB medium and incubated with 500 µM HADA for 1 h at 28 °C. Cells were washed to remove HADA and imaged 1 h after recovery by fluorescence and DIC microscopy. Scale bar, 2 µm. **D)** New PG incorporation is characterized by four specific growth phases in *H. neptunium*. Scheme is based on data from A) - C). Zones of new PG insertion are highlighted in red.

To assess where new PG is added to the cell wall, we determined the localization of nascent PG (365). To identify these sites, we used the fluorophore-labelled D-amino acid HADA, which is incorporated at the 5th (or the 4th) of the pentapeptide side chain (365). Usually soon after incorporation, the HADA at the 5th position should be removed either by TPases during crosslinking or by D-Ala–D-Ala carboxypeptidases (365). Thus, muropeptides containing HADA should only be present in the PG structure at recent sites of synthesis. Once incorporated in *H. neptunium*, the new-born swarmer cells showed a diffuse signal (Figure 10A), indicating that the cell was still increasing in size before it differentiated into a stalked cell. Once the cell reached a defined size, the signal for nascent PG synthesis was observed at the future stalked pole where is resided during stalk extension (Figure 10A). The bulk of the signal stayed at the stalked pole until the onset of budding, when a strong signal would encompass the complete daughter cell (Figure 10A). In individual cells, a strong signal was observed within the stalk, which we speculate would occur as growth at the base of the stalk transitioned to the new daughter cell, which becomes more evident in the demograph (Figure 10B). The demograph displays the intensity change of HADA staining. The cells have been arranged

according to size with the old cell pole always orientated to the left side. In rare cases, and only in late pre-divisional cells, a signal at the junction between the stalk and the daughter cell was observed, indicating the site of septal PG synthesis before cell division. These findings were confirmed by a HADA chase experiment, which also revealed the rapid turnover and relocation of HADA within the cell wall (Figure 10C). From these observations we can conclude that *H. neptunium* expands its cell body before stalk generation and that the stalk grows from the base, alike to *C. crescentus* and *A. excentricus*, until finally growth transitions to the daughter cell at the tip of the stalk.

Additionally, there seems to be a basal level of cell wall maintenance in the mother cell. Nevertheless, the major sites of peptidoglycan biogenesis are at the stalked pole and the growing bud. Our data indicate that the stalk grows at its base and not at the tip. This makes sense, if one considers that the bud grows into the stalk, it would be most difficult to regenerate the stalk if its synthesis occurred other than at its base. Overall, the generation of new cell wall material in *H. neptunium* occurs at four different sites, namely in the swarmer cell, at the stalked pole, the bud, and the future cell division site (Figure 10D).

2.1.4. Unique glycine-enriched PG composition of *H. neptunium*

To better understand the unique morphology of *H. neptunium*, isolated PG was analysed and its composition compared to that of cell walls from its close relative *C. crescentus* (348, 349). For previous analyses of isolated PG sacculi only the major peaks collected from the HPLC were analysed by mass spectrometry (MS) (67). We obtained our data by “in-line” liquid chromatography (LC) wherein LC is directly coupled to MS. Using this combined method, we could even detect PG species that are only present in low abundance and would not have been detected using the conventional HPLC methods. In total ~71.5 % of the analysed *H. neptunium* PG sample could be assigned to particular muropeptides (Table 1).

Already on first inspection, the chromatogram revealed major differences between the PG composition of *H. neptunium* and *C. crescentus* (Figure 11 and Table 1). Mainly tetra- and pentapeptides were identified in this approach, whereas no mono- and dipeptides could be detected (Table 1). In general, the amount of penta- and tetrapeptides present would depend on the overall turnover rate of PG biosynthesis (5). In *H. neptunium* ~90 % of the PG consists of tetrapeptides, which indicates that most of the PG has been processed. In most species, peptides contain D-Ala at the 4^{th} and 5^{th} position (16). Interestingly, in this analysis, only pentapeptides with a glycine at the 5^{th} position (Gly^5) were identified for *H. neptunium*, which correlates with previous reports (366). Pentapeptides with D-Ala^5 were not detected in *H. neptunium*, contrary to *C. crescentus*, which contains high amounts D-Ala^5. In general, *C. crescentus* has five times more pentapeptides than *H. neptunium*. The quantity of anhydromuropeptides is similar in both organisms. The low amount of pentapeptides in *H. neptunium* is an indication that most have been converted to tetrapeptides, hence the elevated occurrence of tetra-tetra-anhydromuropeptides. The average glycan chain length in *H. neptunium* is 11 disaccharide subunits, which is slightly longer than the glycan length of *C. crescentus* (Table 1). Except for varying tetra- and pentapeptide ratios, the average glycan chain lengths as well as the amount of cross-linked peptides are nearly identical in *H. neptunium* and *C. crescentus*. With nearly 27 % of cross-links

Table 1. Muropeptide composition of the cell wall of *H. neptunium* and *C. crescentus* [a]

Muropeptide	*H. neptunium*	*C. crescentus*
Tri/Tri without GlcNAc	0 ± 0	0,91 ± 0,76
Tetra-Tetra-Tetra-Tetra	0,73 ± 0,07	0 ± 0
Tetra-Tetra-Tetra-anhydro	1,32 ± 1,05	2,07 ± 0,65
Tetra-Tetra-Tetra	0 ± 0	1,29 ± 0,07
Tetra-Tetra-Penta-anhydro	0 ± 0	1,16 ± 0,22
Tetra-Tetra-anhydro	7,77 ± 0,33	1,71 ± 0,57
Tetra-Tetra/Tetra-Tetra-Tetra-Tetra	0 ± 0	4,70 ± 1,48
Tetra-Tetra/Tetra-Tetra-Tetra	11,06 ± 3,53	0 ± 0
Tetra-Tetra dianhydro	2,26 ± 2,49	0 ± 0
Tetra-Tetra	0,96 ± 0,23	0,52 ± 0,16
Tetra-Penta-anhydro	0 ± 0	1,10 ± 0,05
Tetra-Penta (Gly5)-anhydro	0,37 ± 0,15	1,32 ± 0,86
Tetra-Penta (Gly5)	6,79 ± 4,77	4,09 ± 0,90
Tetra-Penta	0 ± 0	4,04 ± 1,32
Tetra-anhydro	0,10 ± 0,09	3,55 ± 1,42
Tetra (Gly4)/Tetra (Gly4) without GlcNAc	0 ± 0	0,73 ± 0,67
Tetra	36,87 ± 2,48	21,07 ± 2,65
Penta-Penta-Penta/Penta	0 ± 0	10,30 ± 1,30
Penta/Penta-anhydro	0 ± 0	2,67 ± 1,94
Penta (Gly5)-Tetra-Tetra-anhydro	0 ± 0	1,39 ± 0,56
Penta (Gly5)/Penta (Gly5) without GlcNAc	2,14 ± 0,47	8,80 ± 1,35
Penta (Gly5)/Di	0 ± 0	1,01 ± 0,23
Penta (Gly5)	1,07 ± 0,32	0 ± 0
Penta	0 ± 0	0,32 ± 0,04
Other	28,58 ± 0,05	27,23 ± 7,85
all known	71,43 ± 0,07	72,78 ± 7,86
monomers (total)	56,24 ± 3,86	53,84 ± 2,73
dimers (total)	40,90 ± 2,30	23,79 ± 4,64
Trimers (total)	1,84 ± 1,47	22,37 ± 1,91
Tetramers (total)	1,02 ± 0,09	0 ± 0
tripeptides (total)	0 ± 0	1,32 ± 1,19
tetrapeptides (total)	90,50 ± 3,66	58,44 ± 2,36
pentapeptides (total)	9,50 ± 3,66	40,24 ± 1,17
chain ends (anhydros)	9,61 ± 3,97	13,61 ± 1,69
Average chain length	11,38 ± 4,70	7,41 ± 0,92
degree of cross-linkage	22,44 ± 2,20	26,81 ± 1,05
% peptides in cross-links	43,76 ± 3,86	46,16 ± 2,73

[a] To obtain muropeptides, *H. neptunium* LE670 and *C. crescentus* CBN15 were grown to exponential phase and PG was isolated from 10 mg of lyophilized cells, digested with mutanolysin, and after reduction with sodium borhydrate, muropeptides were analysed on a C18 phase column via ultra-performance liquid chromatography (UPLC) and subsequent mass spectrometry. Di, disaccharide dipeptide; Tri, disaccharide tripeptide; Tetra, disaccharide tetrapeptide; Penta, disaccharide pentapeptide; Gly5/Gly4, glycine in position 4 or 5 of a peptide side chain; anhydro, 1,6-anhydro muramic.

between muropeptides, the peptidoglycan mesh of *C. crescentus* seems to be more compact compared to *H. neptunium*, which only has 22 % of cross-linkage (Table 1). Overall, the muropeptide composition and structure of *H. neptunium* and *C. crescentus* seem fairly similar. However, the slightly reduced amount of cross-linked muropeptides and longer glycan chains could render the cell wall of *H. neptunium* more flexible, which might be an advantage during budding.

A previous study of the polarly growing Alphaproteobacterium *A. tumefaciens* suggested that LDTs, which catalyse 3,3-cross-links, play a major role in polar growth (78, 227). In our muropeptide analysis we could not identify any 3,3-cross-links or tripeptides, which we would expect to encounter as one of the first muropeptide species to elute from the column (Table 1). The lack of these muropeptide species once again indicates a high turnover of PG in *H. neptunium* as well as implies a trivial nature for the 3,3-cross-links under standard growth conditions.

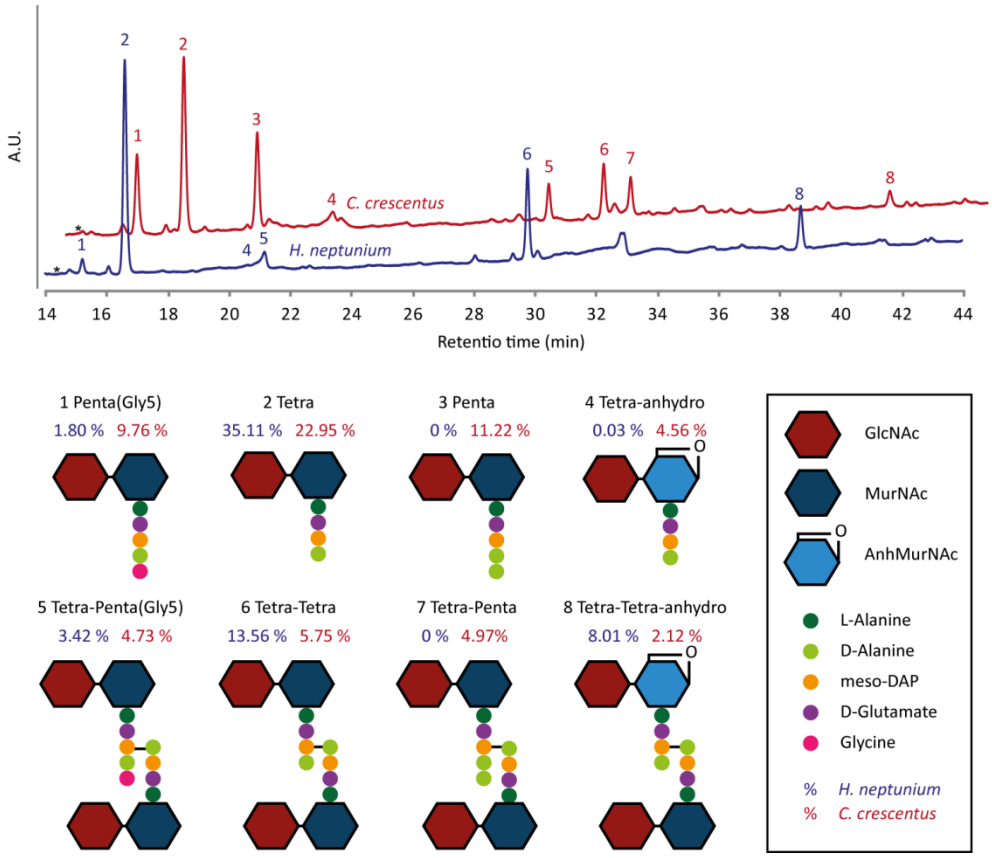

Figure 11. Peptidoglycan composition of *H. neptunium* reveals high turnover and glycine at 5th position. The *H. neptunium* wild type was grown to exponential phase in MB medium and *C. crescentus* was grown to exponential phase in PYE medium. Peptidoglycan was isolated from 10 mg of lyophilized cells, digested with mutanolysin, and analysed for muropeptide composition using ultra-performance liquid chromatography followed by mass spectrometry analysis. Percentage refers to the muropeptide content of the respective peak. Asterisks indicate the position at which tripeptides are expected to elute.

2.1.5. Redundant PG hydrolases determine cell shape

The lack of pentapeptides in *H. neptunium*'s PG profile indicates a high turnover rate of PG (5). To accomplish such a rapid, large scale reshaping of the cell wall at the sites of active growth, mainly at the stalked pole and the bud, PG hydrolases are fundamental (81). First, we decided to investigate the

D-Ala–D-Ala carboxypeptidases, which cleave the terminal 5th amino acid off the peptide side chains (5). In a bioinformatic screen, we identified three potential D-Ala–D-Ala carboxypeptidases encoded in the genome of *H. neptunium*. These are the carboxypeptidases DacB (HNE0402) (D-alanine–D-alanine carboxypeptidase), a close homologue of DacB in *E. coli*, and the *H. neptunium* specific DacH (HNE1025) and DacL (HNE1814), which are characterized by either a ß-lactamase or an S13 peptidase domain, respectively (Figure 12).

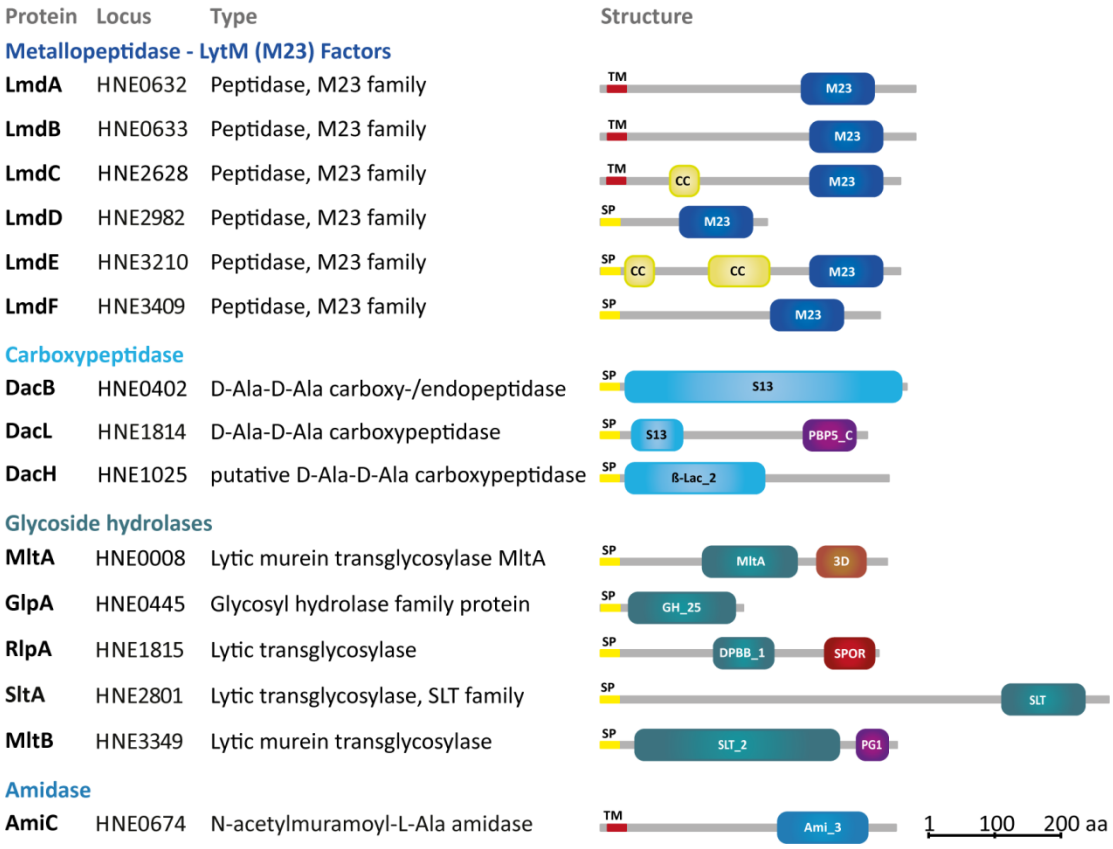

Figure 12. Schematic overview of all analysed peptidoglycan hydrolases in *H. neptunium*. Domain information was obtained from SMART (10.2015)(367, 368) Abbreviation: 3D, 3 conserved aspartate domain; Ami_3, amidase domain 3; CC, coiled-coil domain; DPBB_1, double-psi beta-barrel; GH_25, glycoside hydrolase family 25 domain; M23, LytM family Gly-Gly endopeptidase domain; MltA, lytic transglycosylase MltA domain; PBP5_C, penicillin-binding protein 5 C-terminal domain; PG1, PG-binding domain 1; TM, transmembrane domain; S13, D-Ala-D-Ala carboxypeptidase family 3 domain; SLT, soluble lytic transglycosylase domain; SLT_2, transglycosylase domain 2; SP, signal peptide; SPOR, sporulation related domain.

In a first approach, in-frame deletions were made of each carboxypeptidase gene. Only a slight stalk elongation phenotype and minimal chaining could be observed for the *ΔdacB* mutant (Figure 13A), whereas the other deletion strains had wild-type morphology (Figure S1). However, cell length measurements showed that there was only a slight elongation phenotype of the *ΔdacB* strain compared to the wild type (Figure 13B). To determine if any of the carboxypeptidases localized in the periplasm and participated in the growth of the stalk or bud, C-terminal mCherry fusions were generated and placed under the control of the copper-inducible promoter or their native promoter (3). Only the DacL-mCherry fusion, which replaced the original *dacL* gene, could be localized to the stalked pole in *H. neptunium*, whilst an additional diffuse signal was present in the complete cell

(Figure 14A). Western blot analysis revealed that the DacL-mCherry fusion was stable (data not shown). The other fusion constructs were unstable (data not shown). The growth rates of the deletion strains were close to that of the wild type (Table 18). From our observations we can conclude that the D-Ala–D-Ala carboxypeptidases in *H. neptunium* are redundant and individually only have a minor role in cell morphology.

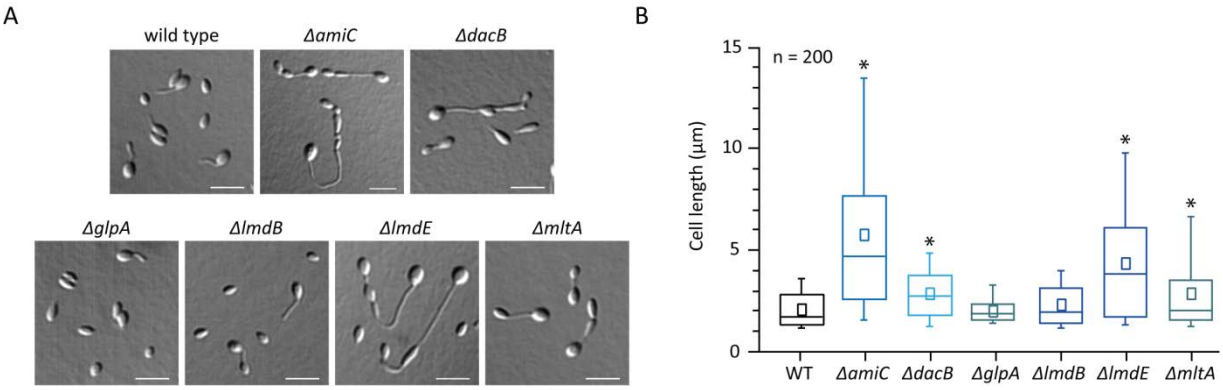

Figure 13. Deletion of peptidoglycan hydrolases causes stalk elongation and cell chaining. A) Deletion of hydrolases causes cell elongation and cell chaining. *H. neptunium* wild type and strains EC53 (*ΔlmdB*), EC90 (*ΔlmdF*), EC95 (*ΔmltA*), SR07 (*ΔglpA*), SR11 (*ΔdacB*) and SR18 (*ΔamiC*) were grown to exponential phase in MB medium and analysed by DIC microscopy. Scale bar, 3 µm. **B)** Deletion of hydrolases causes cell elongation. Cell length measurements are based on images from B). Box plots show the median and the interquartile range (box), the average value (square in box), and the 5th and 95th percentile (whiskers). Asterisk indicates a *p*-value of < 0.001 (*t*-test). Data generated in collaboration with S. Rosskopf.

A noteworthy observation from the PG analysis was the high presence of anhydromuropeptides, which is an indication for high PG turnover (5). Anhydromuropeptides are generated by lytic trans-glycosylases (TG) (13), for which we found four homologues in *H. neptunium*: MtlA (HNE0008), MltB (HNE3349), RlpA (HNE1815), and SltA (HNE2801) (Figure 12). Another glycoside hydrolase identified was GlpA (HNE0445), which belongs to the glycoside hydrolase family 25, whose members act as lysozymes. These enzymes could play a vital role in the turnover of PG and one would expect them to localize in the periplasm and sites of PG biosynthesis. Out of all deletions, only the *ΔmltA* mutant showed a slight elongation phenotype (Figure 13A and B, Figure S1). The growth rate of all deletion strains was comparable to that of the wild type (Table 18). A fusion construct for SltA was stable but localized diffusely, whilst GlpA-mCherry was unstable (data not shown). Only RlpA-mCherry expressed from its native promoter could be localized in *H. neptunium*. Unfortunately, Western blot analysis revealed that the fusion construct was largely degraded (Figure S2). Nonetheless, in a few cells RlpA mainly resided at the stalked pole, from where it moved to the tip of the stalk to finally localize in the stalk once the bud was firmly established (Figure S3A). Additional growth experiments confirmed the viability of the fusion strain (Table 19). Overall, our results indicate that the lytic TG MltA might play a role in cleaving the PG to facilitate insertion of new PG material and thus partake in establishing cell morphology in *H. neptunium*.

Since the nature of the muropeptide composition could not be entirely resolved by the enzymes analysed so far, we decided to further investigate other hydrolases in *H. neptunium*. Genome analysis revealed that *H. neptunium* only has one amidase homologue, AmiC (HNE0674), which has an Ami_3

domain and is predicted to be a periplasmic inner membrane protein (Figure 12). The deletion of *amiC* causes extensive stalk elongation and pronounced cell chaining, suggesting that is has a prominent role in cell division (Figure 13A and B). Localization studies of inducible AmiC-mCherry revealed that in swarmer cells AmiC localizes to the stalked pole (Figure 14B). In stalked and early budding cells, AmiC mostly remains at the stalked pole whilst in some cells a focus is visible within the stalk. During the final stage of budding, AmiC localizes to the future division site (Figure 14B); however, this becomes less clear in the demograph due to the differences in cell length and, as a late cell division protein (89), AmiC spends a short time at the division site, which makes its observation more rare. The chaining phenotype of the deletion mutant indicates that AmiC has a relevant function during cell division, which is strengthened by the localization of AmiC to the division site. Furthermore, the localization of AmiC to the stalked pole suggests a role in stalk biogenesis. However, the evidence of elongated stalks in the deletion mutant argues against a fundamental role of AmiC during stalk growth. Taken together our results suggest that AmiC plays a major role during cell division as well as a possible a minor role in stalk biogenesis.

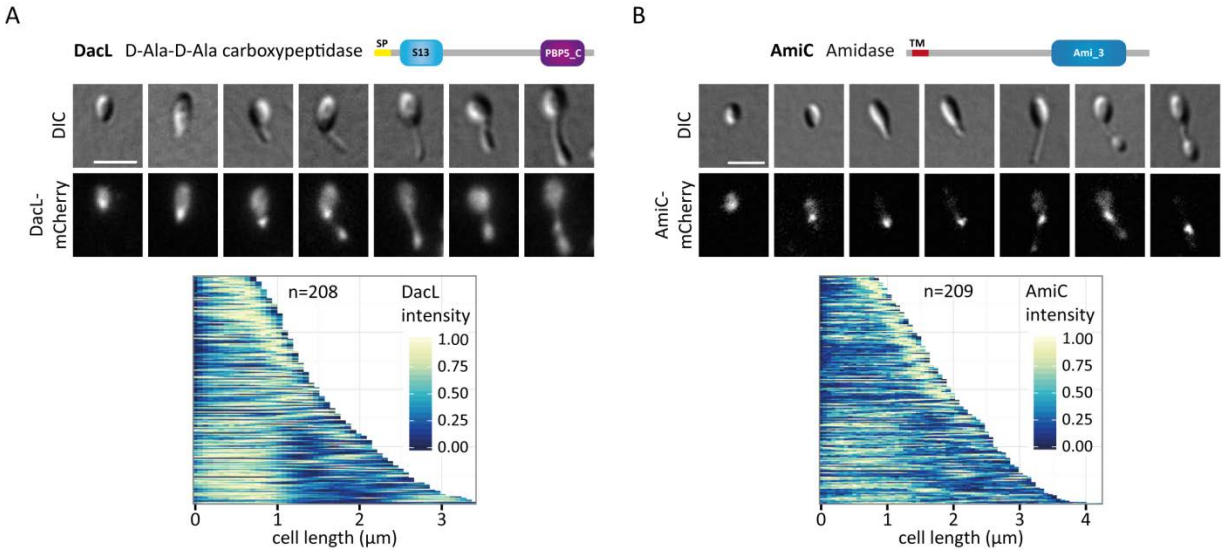

Figure 14. Peptidoglycan hydrolases DacL and AmiC localize to sites of cell wall biogenesis. A) DacL-mCherry localizes to the stalked pole. Strain SR28 (*dacL-mCherry*) was grown to exponential phase in MB medium and imaged by DIC and fluorescence microscopy. Images represent the major localization pattern and have been ordered according to their stage within the cell cycle. Scale bar, 2 µm. **B)** AmiC-mCherry localizes to the stalked pole and division site. Strain EC70 (P_{Cu}::P_{Cu} *amiC-mCherry*) was grown to exponential phase in MB medium and induced with 300 µM $CuSO_4$ 24 h and diluted to exponential phase prior to imaging with DIC and fluorescence microscopy. Images represent the major localization pattern and have been ordered according to their stage within the cell cycle. Scale bar, 2 µm. Microscopy data generated in collaboration with S. Rosskopf.

Further analysis revealed that *H. neptunium* possesses a large number of LytM domain (M23) metallopeptidases, which are known PG hydrolytic enzymes (123). The six LytM factors in *H. neptunium* named LmdA-F (LytM domain containing protein A-F) are characterized by an M23 hydrolytic domain in their C-terminal region and are predicted to localize in the periplasm either freely or bound to the inner membrane. Some proteins also contain coiled-coil regions that might act as interaction domains for other proteins (Figure 12) (369). To analyse whether these proteins might

play a dominant role in establishing cell morphology, in-frame deletion strains were constructed. With the exception of *lmdC*, all genes could be deleted. However, only the deletion of *lmdB* and *lmdE* gave rise to an obvious phenotype as reflected by elongated stalks and a slight chaining phenotype, which was more pronounced in the Δ*lmdE* mutant (Figure 13A and B). To determine if any of the Lmd peptidases localize to the site of PG biosynthesis, natively expressed C-terminal mCherry fusions were generated. For most constructs, we could only observe a diffuse periplasmic localization (with the exception of LmdE all fusions were stable; data not shown). The only exception was LmdF-mCherry, which localized at the stalked pole at the onset of stalk formation, the stalk, and the future division site (Figure S3B).

Interestingly, the conserved LytM (M23) metalloprotease metal binding sites, HxxxD and HxH, are completely absent in LmdE (Figure 15). Whilst LmdE lacks conserved catalytic residues, the LytM domain of the other LytM factors is complete (Figure 15). Previous studies in *E. coli* showed that proteins with partial LytM domains, like EnvC and NlpD, act as regulators for other enzymes (92, 116, 370), which might be the case for LmdE. Taken together it seems that LytM domain peptidases contribute to cell morphology in *H. neptunium*. However, with the exception of LmdC and LmdE, they also seem highly redundant.

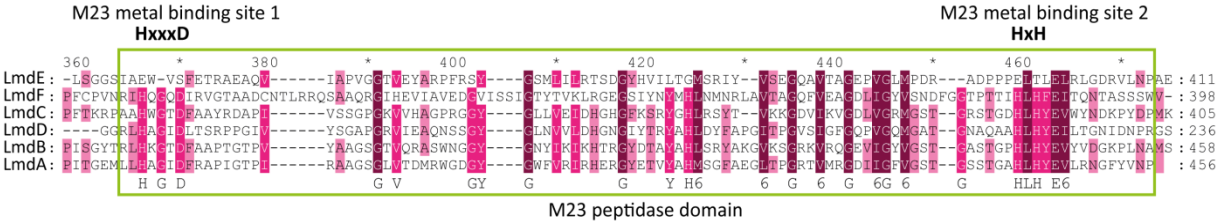

Figure 15. The LytM (M23) peptidase domain is not conserved across all Lmd peptidases in *H. neptunium*. Alignment of all M23 peptidases in *H. neptunium* was generated with Clustal Omega (04.2015) (http://www.ebi.ac.uk/Tools/msa/clustalo/). LytM (M23) domain is highlighted by a green frame. Residues in dark pink colour are highly conserved, pink indicates average conservation, and light pink indicates low conservation of residues across the aligned homologues.

Collectively, we tried to identify PG hydrolases that strongly contribute to stalk biogenesis and budding in *H. neptunium*. Most deletions did not cause a significant change in morphology or growth rate (Figure S1 and Table 18). The most important candidates seem to be AmiC and LmdE, which have the strongest deletion phenotype (Figure 13A and B). When examined for nascent PG incorporation by HADA staining, all of the deletion strains displayed a wild-type incorporation of PG (Figure S4). Overall, PG hydrolases of all classes contribute to cell growth and morphology. However, with the exception of LmdC, all hydrolases seem to be highly redundant or dispensable in *H. neptunium*.

We assume that the variable localization patterns observed for individual proteins are caused by the cell cycle-dependent differentiation process, which we are not able to detect with single-cell images. To determine the cell cycle-dependent dynamics of each hydrolase, it would be advantageous to preform time-lapse experiments. However, in all cases the signal intensity failed to be sufficient for these kinds of experiments.

2.1.6. PBPs contribute to cell growth

Another major question was how growth is localized to various sites within the cell. Could different enzymes be responsible for the growth of the mother cell, the stalk, and the bud? To gain further insights into the establishment of cell morphology and budding, the PG synthases were also analysed. The genome of *H. neptunium* encodes five PBPs, two TPases and one TGase. The PBPs identified are PBP1A (HNE1911), PBP1X (HNE0768), PBP1C (HNE3002), PBP2 (HNE2934), and PBP3 (HNE3030/FtsI) (Figure 16). The bifunctional PBPs, which have both a TPase and TGase domain, include PBP1A, PBP1X, and PBP1C. PBP1A possesses an additional PCB_OB (penicillin-binding protein oligonucleotide/oligosaccharide binding)-like domain, which has specific ligand binding properties (282, 371). The mono-functional PBPs, which only have a TPase domain, are PBP2 and PBP3. The only monosynthetic TGase identified to date is MtgA (HNE3102). All these enzymes are predicted to be periplasmic inner membrane-bound proteins (Figure 16). *H. neptunium* also codes for two LDT, LdtA (LD transpeptidase A) (HNE0929) and LdtB (HNE3551), which are characterized by a YkuD domain (Figure 16).

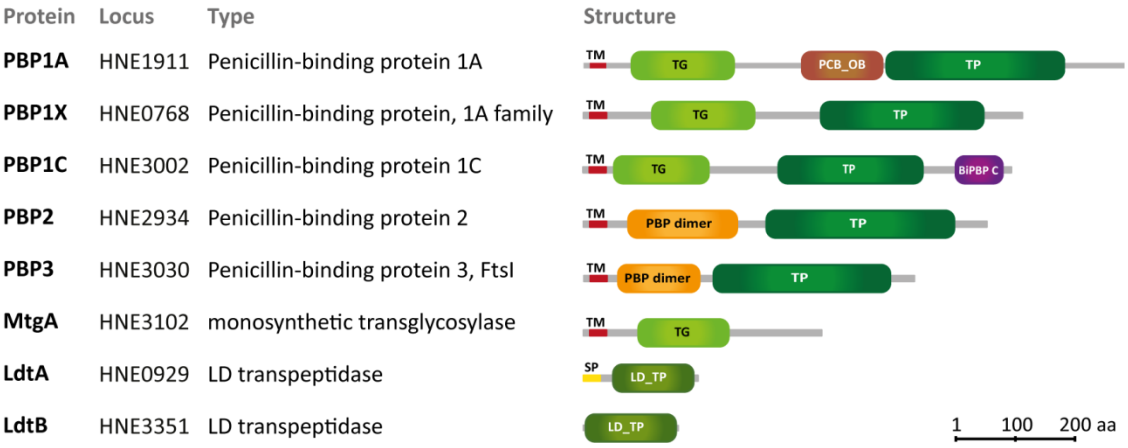

Figure 16. Schematic overview of peptidoglycan hydrolases in *H. neptunium*. Domain information was obtained from SMART (10.2015)(367, 368) Abbreviation: BiPBPC, penicillin-binding protein C-terminal domain; LD_TP, YkuD LD-transpeptidase domain; PBP dimer, penicillin-binding protein dimerization domain; PCB_OB, Penicillin-binding protein OB-like domain; TG, transglycosylase domain; TM, transmembrane domain; TP, transpeptidase domain; SP, signal peptide.

To determine which PG synthases play a vital role in cell wall biogenesis in *H. neptunium*, deletion mutants were generated. As PBP1A, PBP2, and PBP3 could not be deleted, we assume they are essential for viability. The deletion phenotype of the *Δpbp1X* deletion mutant yields a strong stalk elongation phenotype, whilst the *Δpbp1C* deletion mutant resembles the wild type (Figure 17A and B). The *Δpbp1X1C* double mutant is similar in morphology and cell length to the *Δpbp1X* single mutant (Figure 17A and B). PG incorporation was unaffected in the *Δpbp1X* and *Δpbp1X1C* deletion strains (Figure S4). Overall, there seems to be a vital set of PG synthases, consisting of PBP1A, PBP2, and PBP3, whilst PBP1X and PBP1C are dispensable for cell division and growth.

A previous study in *A. tumefaciens* suggested that LDTs play a major role in polar growth (78, 227). LDTs catalyse the link between two *meso*-DAP residues (3,3-cross-links), which in the case of *A. tumefaciens* make up more than 50 % of the peptide cross-links (77). A crucial feature of *H. neptunium*'s PG composition is the complete lack of 3,3-cross-linked peptides (Figure 11, Table 1),

even though *H. neptunium* has two LDT, LdtA and LdtB. The deletion of either the *ldtA* or the *ldtB* gene as well as the double deletion had no significant effect on the morphology (Figure 17A and B) or the growth (Table 18) of *H. neptunium*. Expressed under the control of the copper-inducible promoter and equipped with a C-terminal mCherry tag, both LdtA and LdtB showed a diffuse localization (Figure S5). Thus, under the tested conditions, LDTs do not seem to play a crucial part in polar growth and establishment of morphology in *H. neptunium*.

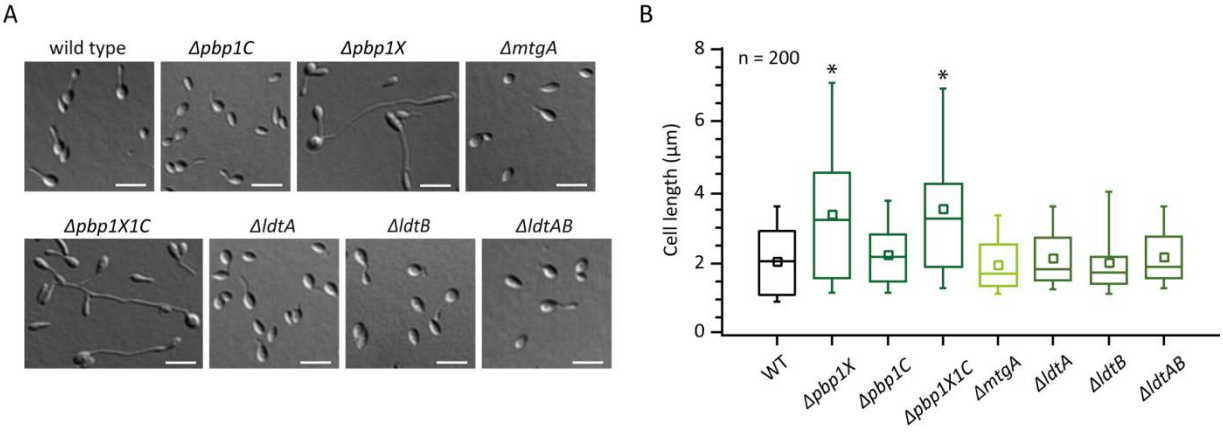

Figure 17 Deletion of peptidoglycan synthases causes stalk elongation. A) Deletion of peptidoglycan synthases causes stalk elongation. The *H. neptunium* wild type and strains CR04 (*ΔldtB*), EC26 (*Δpbp1X*), EC27 (*Δpbp1C*), EC57 (*Δpbp1XΔpbp1C*), SR31 (*ΔldtA*), and SR32 (*ΔldtAB*) were grown to exponential phase in MB medium and analysed by DIC microscopy. Scale bar, 3 µm. B) Deletion of peptidoglycan synthases causes stalk elongation. Cell length measurements are based on images from **B)** and were determined. Box plots show the median and the interquartile range (box), the average value (square in box), the 5th and 95th percentile (whiskers). Asterisk indicates a *p*-value of < 0.001 (t test). Data generated in collaboration with S. Rosskopf.

Next, the localization of the TPases PBP2 and PBP3 was investigated by generating fluorescent fusion constructs placed under the control of their native promoters. Venus-PBP2 localized to the stalked pole in swarmer cells (Figure 18A). In budding cells, PBP2 was observed within the bud and even partially within the stalk and at the future division site (Figure 18A). Venus-PBP3 (data generated by S. Eisheuer) was only observed to localize at the stalked pole and at the future division site (Figure 18B). Both fusions were functional (Figure S2) and neither strain showed any morphological abnormalities or growth defects (Table 19). Fusions of PBP1C and PBP1X localized diffusely within the cell (data not shown). PBP2 and PBP3 localize to sites of intensive PG turnover, indicating a vital role for both TPases in cell growth and morphology of *H. neptunium*.

Since the monofunctional PBPs PBP2 and PBP3 could not be deleted and we have no functional depletion system for low abundant proteins to date, we decided to inhibit various PG synthases with specific antibiotics. First, cells were treated with ampicillin to inhibit a broad range of TPases (68), which caused the majority of the cells to round up (Figure S6). Upon inhibition of PBP3 with cephalexin (68), the cells produced slightly misshaped cell bodies and extensively elongated stalks, which point to a cell division defect (Figure S6). When PBP2 was inhibited with mecillinam (68), the cell bodies increased in size and rounded up, additionally, many cell bodies appeared severely distorted (Figure S6). To inhibit all TGases, the cells were treated with moenomycin (372). Once

treated with moenomycin, the cell bodies became elongated and deformed (Figure S6). Our observations suggest that the TGase and TPase activities of PBP1A as well as the TPase activity of PBP2 and PBP3 play a vital role in cell growth and morphogenesis, whilst the mode of action of PBP1X, PBP1C, and MtgA seem to be redundant in *H. neptunium*.

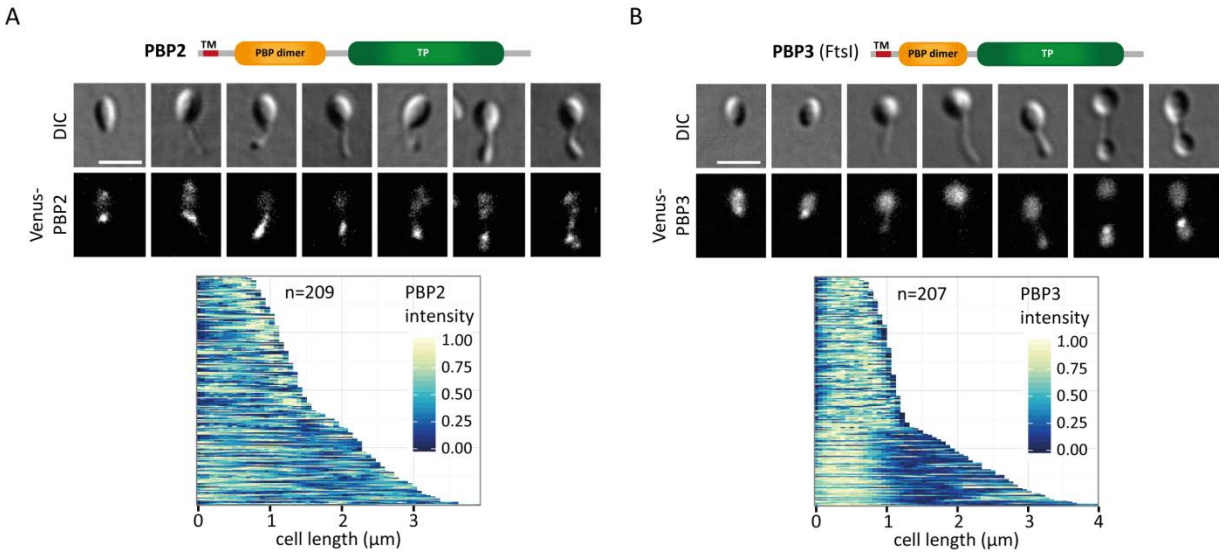

Figure 18. Penicillin-binding proteins localize to sites of cell wall biogenesis. A) Venus-PBP2 localizes to sites of nascent peptidoglycan synthesis. Strain SR14 (*venus-pbp2*) was grown to exponential phase in MB medium and imaged by DIC and fluorescence microscopy. Images represent the major localization pattern and have been ordered according to their stage within the cell cycle. Scale bar, 2 µm. **B)** Venus-PBP3 localizes to the stalked pole and the division site. Strain SE161 (*venus-pbp3*) was grown to exponential phase in MB medium and imaged by DIC and fluorescence microscopy by S. Eisheuer. Images represent the major localization pattern and have been ordered according to their stage within the cell cycle. Scale bar, 2 µm.

2.1.7. MreB and its associated proteins localize to the sites of PG synthesis

To gain insights into the coordination of the PG biogenesis enzymes, we decided to focus on MreB. In most non-spherical bacteria, the actin homologue MreB plays a pivotal role in coordinating the insertion of newt PG during lateral growth and is thus vital for the maintenance of cell shape (148, 196). Since in *H. neptunium*, unlike in the Rhizobiales (196, 338), MreB seems to be essential (as we could not generate a viable deletion mutant), we assumed that it might contribute to cell growth.

H. neptunium, similar to other Gram-negative bacteria (196), has a single MreB homologue (HNE2937), which is characterized by an MreB_Mbl domain containing two ATP binding motifs (187) (Figure 19A). To visualize MreB in *H. neptunium*, we created a strain in which the native *mreB* gene was replaced by an *mreB-mCherry* sandwich fusion (*mreB*^{SW}) at the native gene locus (Figure 19B). The mCherry fluorescent protein was inserted in an unstructured loop between Asparagine (N)227 and Glutamate (E)226, as previously accomplished in *E. coli* (Figure 19C) (288). The strain carrying this construct was viable and showed no growth defects (Table 19). In the majority of swarmer cells MreB^{SW} localized to the future stalked pole, where it also localized in most stalked cells (Figure 19D). In budding cells the signal appeared mainly diffuse within the mother cell, whilst a distinct signal was visible either in the stalk or the growing bud (Figure 19D). Individual MreB^{SW} complexes could only

seldom be resolved within the stalk and the bud due to the small size of *H. neptunium*. According to our observations, MreB preferentially localizes to the major site of PG synthesis at the stalked pole and the bud.

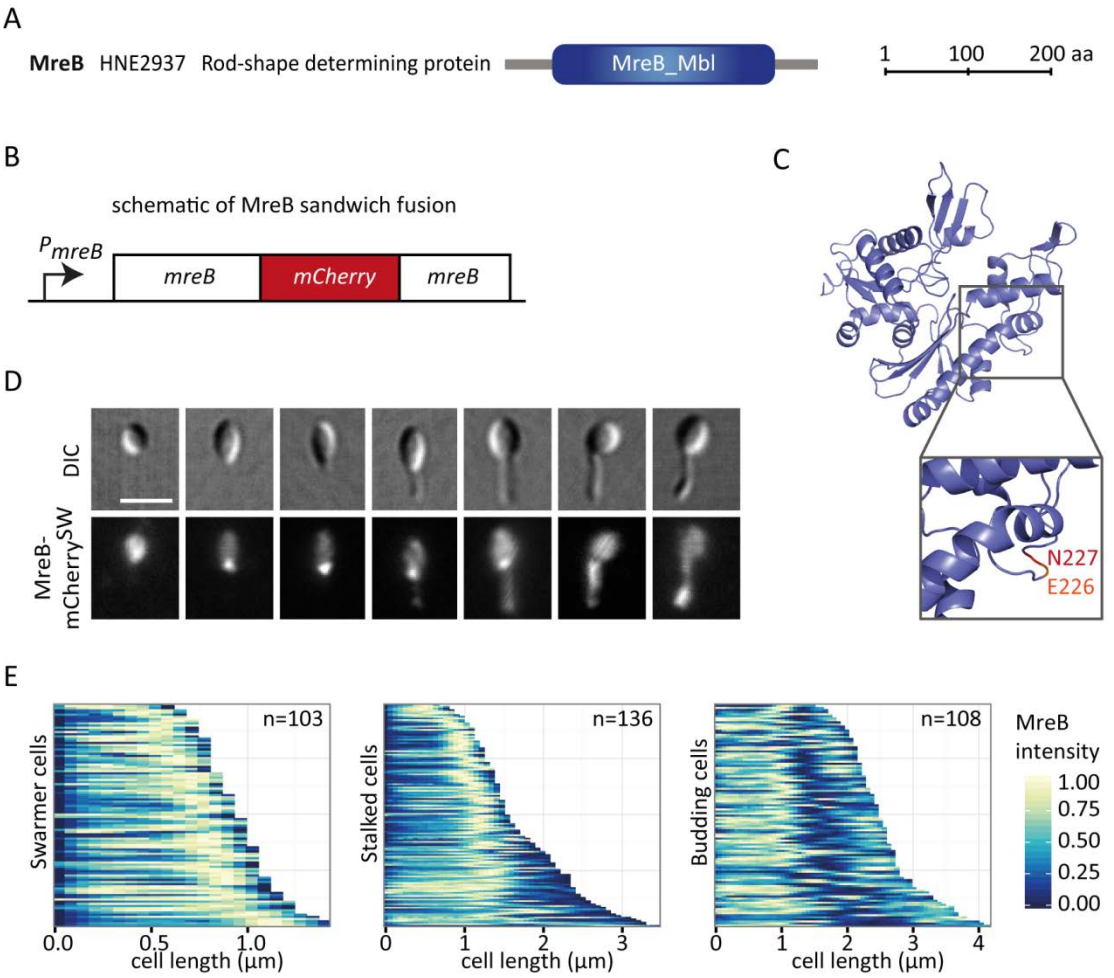

Figure 19. MreB localizes to the stalked pole, the stalk, and bud of *H. neptunium*. A) Schematic overview of MreB from *H. neptunium*. Domain information was obtained from SMART (10.2015) (367, 368). Abbreviation: MreB_Mbl, MreB/Mbl protein domain. **B)** Schematic of the native *mreB-mCherry* sandwich fusion construct. **C)** Position of the mCherry fusion within an unstructured loop of MreB. Structure of *H. neptunium* MreB (HNE2937) was generated using I-Tasser (373-375) based on $MreB_{CC}$ (PDB 4CZF) and processed with Pymol (376). **D)** $MreB^{SW}$ localizes to the stalked pole and the daughter cell. Strain EC63 (*mreB-mCherry*^{SW}) was grown to exponential phase in MB medium and imaged by DIC and fluorescence microscopy. Images represent the major localization pattern and have been ordered according to their stage within the cell cycle. Scale bar, 2 µm. **E)** Demographs of MreB-$mCherry^{SW}$ are based on images from D).

In order to validate the observed pattern for MreB, we looked at the subcellular localization of MurG and RodZ. MurG is the *N*-acetylglucosaminyl transferase that catalyses the last step in lipid II synthesis (377, 378) and was shown to interact with MreB *in vitro* (379). MurG is a cytoplasmic protein characterized by a glycosyltransferase family 28 and a glycosyltransferase family 1 domain (Figure 20A). The YFP-MurG fusion expressed from its native promoter localized in a patchy pattern within the mother cell, the stalk, and the daughter cell (Figure 20A). RodZ is a cell shape-determining factor which has been observed to link MreB to the cell wall synthesis machinery in *E. coli* (296). RodZ is a membrane protein with a helix-turn-helix domain situated in the cytoplasm and a DUF4115 domain

protruding into the periplasm (Figure 20B). Interestingly, when expressed from its native promoter, the YFP-RodZ fusion showed a clear localization at the future stalked pole in swarmer cells and early stalked cells, with some cells possessing bipolar foci (Figure 20B). In stalked cells, RodZ localized in regular patches within the stalk and later exclusively in the emerging bud (Figure 20B). Shortly before the onset of cell division, RodZ was recruited back to the stalked pole again (Figure 20B). We assume that both fusions were largely functional as they could replace the function of the essential native protein and proved stable in a Western blot analysis (Figure S2). Furthermore, both fusion strains showed growth rates and morphologies similar to that of the wild type (Table 19). According to our observations, RodZ and MreB localize to sites of new PG synthesis as determined by HADA incorporation (Figure 10A and B), which suggests that both might be part of the PG incorporating complex in *H. neptunium*.

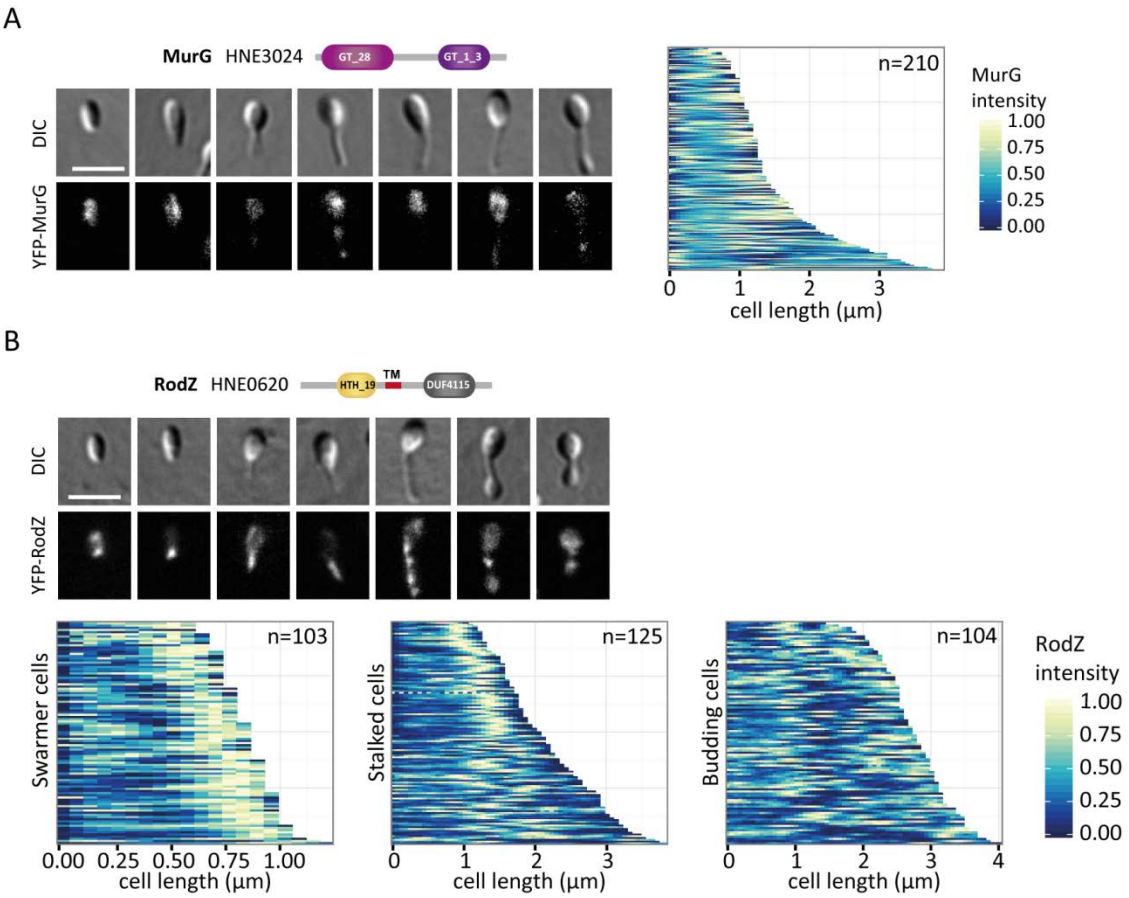

Figure 20. MurG and RodZ localize to sites of peptidoglycan turnover. A) YFP-MurG localizes in diffuse patches in *H. neptunium*. Strain EC96 (*yfp-murG*) was grown to exponential phase in MB medium and imaged by DIC and fluorescence microscopy. Images represent the major localization pattern and have been ordered according to their stage within the cell cycle. Scale bar, 2 µm. Domain information was obtained from SMART (10.2015) (367, 368). Abbreviations: GT_28 contains two domains: *Glyco_tran_28_C*, Glycosyltransferase family 28 C-terminal domain and *Glyco_transf_28*, Glycosyl-transferase family 28 N-terminal domain; *Glyco_trans_1_3*, Glycosyl-transferase family 1. **B)** YFP-RodZ localizes to the stalked pole, the stalk and, the bud. Strain EC93 (*yfp-rodZ*) was grown to exponential phase in MB medium and imaged by DIC and fluorescence microscopy. Images represent the major localization pattern and have been ordered according to their stage within the cell cycle. Scale bar, 2 µm. Domain information was obtained from SMART (10.2015) (367, 368). Abbrevi-ations: DUF4115, domain of unknown function 4115; HTH_19, helix-turn-helix domain 19; TM, transmembrane domain.time

2.1.8. MreB plays a prominent role in growth and the coordination PG insertion

So far it was not possible to delete MreB, indicating that like in many other bacteria, MreB is also essential in *H. neptunium*, even though it is not a fully rod-shaped bacterium (196). Since we could neither delete nor generate a deplete construct for MreB, we opted to inhibit the function of MreB to better understand the role its in *H. neptunium*. For this, wild type cells were treated with the MreB-inhibiting agent A22, which inhibits MreB by binding next to MreB's nucleotide-binding pocket (194, 380, 381). As observed for other bacteria (381), after treatment with A22 *H. neptunium* cells turned increasingly oval until swarmer cells became completely spherical (Figure 21A). The effect of A22 is only transient. Once A22 was removed from the media, the cells were able to regain their wild-type morphology (Figure 21A). Growth experiments with A22 showed that the increase in cell density is markedly reduced with rising A22 concentrations until growth was completely abolished (Figure 21C). Similar results were obtained for the strain harbouring the MreB-mCherry^{SW} fusion; however, when A22 was added at a later time point, growth was impaired less than compared to the wildtype (Figure S7 and Figure S10). Time lapse experiments on pads showed that once cells are placed on pads containing A22, cell growth and development are completely aborted (Figure S8). To verify our observations, we opted to use another MreB inhibitor, called MP265. In previous studies, MP265 proved to be very effective in disrupting MreB structure as well as having less secondary effects due to higher MreB-specificity (285). After treatment with MP265, the cells rounded up similar to the A22-treated cells (Figure 21B). Growth was also perturbed with increasing concentration of MP265 (Figure 21D). Interestingly, a more pronounced effect on morphology was observed when cells were treated with lower concentrations of A22 and MP265 (Figure S9). At higher concentrations, where growth was highly reduced, the cells did not undergo morphological changes (Figure S9). Taken together our observations indicate that morphological changes are most pronounced in fast growing cells and that *H. neptunium* at least partially relies on MreB for the maintenance of cell shape.

With increasing concentrations of either A22 or MP265, the average cell body length (in case of budding cells measurements were restricted to the mother cell) indicates that whilst some cells became shorter, others became longer (Figure 21E). In contrast, the average cell body width was clearly elevated after A22 or MP265 treatment (Figure 21F). These measurements demonstrate that upon the inhibition of MreB the major morphological change is the conversion of the slightly ovoid cell shape of *H. neptunium* to round spheres.

Some cells contained large PHB (poly-ß-hydroxybutyrate) granules (346), which are only formed when the cells are under prolonged stress. Many tiny, spherical cells were observed, which were smaller and rounder than normal swarmer cells (Figure 21A and B). To determine whether these small round cells were true mini-cells or only rounded swarmer cells, DAPI staining was performed, which confirmed that the spherical cells contained DNA comparable to untreated cells (Figure S11).

To resolve the effect of MreB disruption on the cell morphology of *H. neptunium*, we treated synchronized wild-type cells with A22 and monitored their development. With our current synchronization protocol we are able to enrich for swarmer cells. As development progresses, the percentage

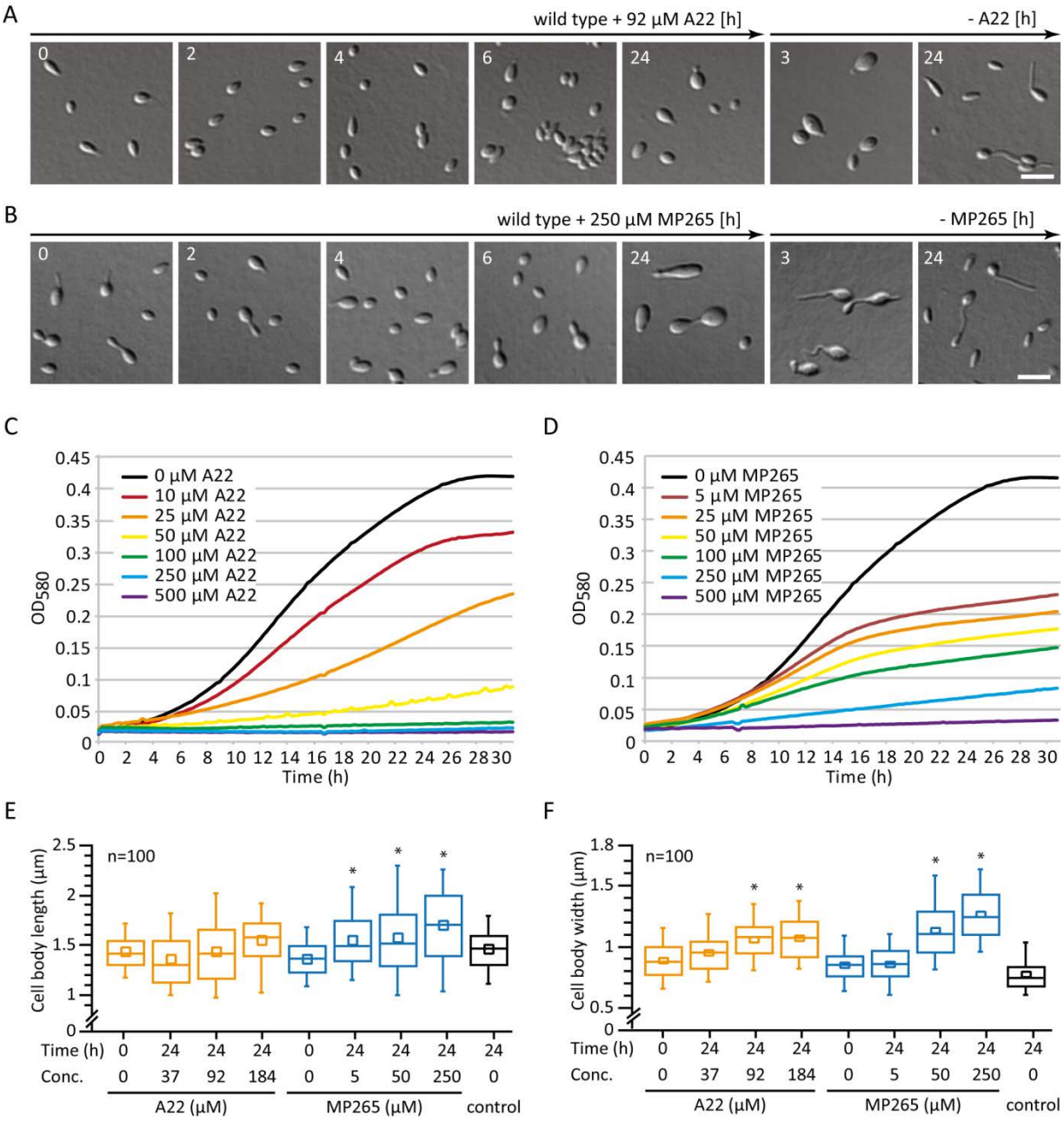

Figure 21. MreB plays a prominent role in cell growth and the control of morphology. A) MreB inhibition by A22 transiently alters cell shape. The *H. neptunium* wild type was grown to exponential phase in MB medium and treated with 92 µM A22. After 24 h, cells were washed twice with MB to remove A22 and resuspended in fresh MB medium. Cells were analysed by DIC microscopy at the indicated time points. Scale bar, 3 µm. **B)** MreB inhibition by MP265 transiently alters cell shape. The *H. neptunium* wild type was grown to exponential phase in MB medium and treated with 250 µM MP265. After 24 h, cells were washed twice with MB to remove MP265 and resuspended in fresh MB medium. Cells were analysed by DIC microscopy at the indicated time points. Scale bar, 3 µm. **C)** Inhibition of MreB causes a decline in growth. Growth experiments with *H. neptunium* wild type in the presence of varying concentration of A22 **D)** and MP265, respectively. **E)** MreB inhibition leads to the deregulation of cell length. *H. neptunium* wild type was grown to exponential phase in MB medium and treated with 37, 92 and 184 µM A22 as well as 5, 50 and 250 µM MP265 for 24 h. Cells were analysed by DIC microscopy and cell width was determined. Box plots show the median and the interquartile range (box), the average value (square in box), the 5th and 95th percentile (whiskers). Asterisk indicates a *p*-value of < 0.001 (*t*-test). **F)** MreB inhibition leads to an increase of cell width. The *H. neptunium* wild type was grown to exponential phase in MB medium and treated with 37, 92 and 184 µM A22 or 5, 50 and 250 µM MP265 for 24 h. Cells were analysed by DIC microscopy and cell width was determined. Box plots were generated as described in E).

of swarmer cells decreased as the abundance of stalked and budding cells increased (Figure S12A). Under optimal growth conditions, it takes three hours for the distribution of cell types to reach equilibrium. If wild-type cells are treated with higher concentrations of A22 immediately after synchronization, the ratio between swarmer, stalked and budding cells does not alter, indicating a stop in differentiation. A small increase in the stalked and budding population is only observed after 24 hours of incubation with A22 (Figure S12B). On the other hand, we did not observe this change after 24 hours if even higher concentrations of A22 were used (data not shown). These observations are consistent with the growth arrest observed in the presence of A22 during the growth experiments (Figure 21C).

To assess how fast the MreB-perturbing agents affect *H. neptunium*, wild-type cells were treated with A22 and MP265 during exponential growth. Once the cells were supplemented with either A22 or MP265 their growth rate noticeably declined as expected (Figure S10) (285). This observation suggests susceptibility of cells to MreB inhibiting agents is immediate even though morphological changes need several hours to manifest (Figure 21A and B).

To determine if the arrest in growth and development was caused by the displacement of MreB, the strain carrying the MreB-mCherry^{SW} fusion was treated with A22 and MP265, respectively. After already 1 hour of incubation with either MP265 or A22, most of the MreB localization pattern is lost (Figure 22A). Nonetheless, a small subpopulation of cells retained an MreB focus at the stalked pole even after 24 hours of incubation with MP265 (Figure 22B and Figure S14A). Comparable results were obtained with A22 (Figure S14B and C). The fusion tag might make MreB less susceptible to A22 and MP265, which seems unlikely as in *C. crescentus* a complete diffusion of the GFP-MreB signal was observed after treating cells for 1 h with 50 µM MP265 (285). Interestingly, wild-type cells treated with either A22 or MP265 still showed active PG incorporation, indicating that some cell wall remodelling components are still active and functional even though MreB is inhibited (Figure 22C, Figure S15). Our findings strongly suggest that the MreB and the MreB^{SW} polymers do not diffuse after inhibition but stay in their current localization. This correlates with previous findings, which have shown that A22 and MP265 both prevent the phosphate release of MreB but do not disassemble the protofilaments *in vitro*, suggesting that MreB could still be present as an inactive polymer (194). Since the predicted conformation of the ATP-binding pocket of MreB seems to be slightly different from that in *C. crescentus*, it might explain why the effect of A22 and MP265 is less pronounced in *H. neptunium* (Figure S13). Overall, it seems that as long as minimal cell growth is possible, MreB is also detectable at sites of PG turnover in *H. neptunium*.

To determine if MreB plays a crucial role in the coordination of other cell wall remodelling enzymes, strains carrying fluorescent protein fusions to various synthases and hydrolases were treated with either MP265 or A22. 5 hours after MP265 or A22 treatment, no major alterations were observed in the localization pattern of selected proteins (Figure S14). However, after 24 hours of MP265 incubation, DacL-mCherry as well as Venus-PBP2 were mostly delocalized, whilst LmdF-mCherry and YFP-RodZ seemed only mildly affected (Figure 22B). The continued localization of LmdF-mCherry and YFP-RodZ despite inhibition might be partially due the lingering presence of MreB (Figure 22B). After

24 hours of A22 treatment, the proteins showed a more diffuse localization, which might be due to an overall rounder cell shape (Figure S14C). On the other hand, a previous study demonstrated that PBP2 is only transiently associated with MreB and is active independently of MreB in *E. coli* (382). Similarly to *E. coli*, RodZ might play a role in localizing MreB and thus recruiting other morphogenetic factors (296). In *H. neptunium* this might be the case not only for PBP2 but several other PG remodelling enzymes, which assemble into dynamic complexes.

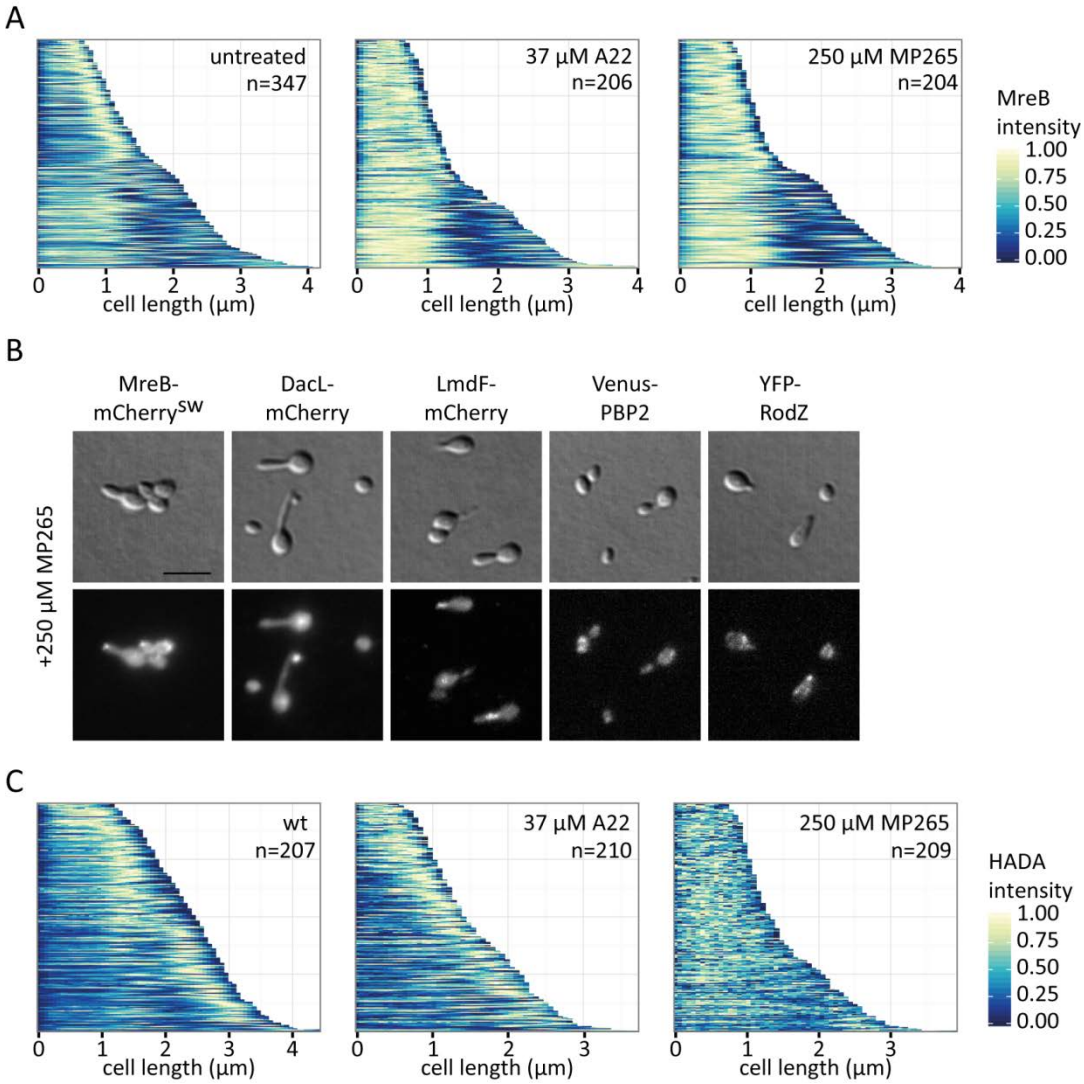

Figure 22. MreB coordinates the cell wall machinery and influences the insertion of new peptidoglycan. A) A22 and MP265 delocalize MreB. Strain EC63 (*mreB-mCherry*^{SW}) was grown to exponential phase in MB medium before treatment with 37 µM A22 and 250 µM MP265, respectively, for 1 h. Cells were imaged by DIC and fluorescence microscopy. **B)** Localization of PG remodelling enzymes is partially MreB-dependent. Strains EC63 (*mreB-mCherrySW*), SR28 (*dacL-mCherry*), SR26 (*lmdF-mCherry*), SR14 (*venus-pbp2*) and EC93 (*yfp-rodZ*) were grown to exponential phase in MB medium and treated with 250 µM MP265 for 24 h and imaged by DIC and fluorescence micros-copy. Scale bar, 3 µm. **C)** The inhibition of MreB disrupted the insertion of new peptidoglycan. The *H. neptunium* wild type was grown to exponential phase in MB medium and treated with 37 µM A22 and 250 µM MP265, respectively, for 5 h followed by a short HADA pulse and imaged by DIC and fluorescence microscopy.

Although some enzymes are still able to partially localize to sites of cell growth sites despite the inhibition of MreB, the overall incorporation of new PG is strongly affected. Even though after 5 hours of incubation with 37 µM A22 the incorporation of nascent PG seems to take place at the correct place, the cells are markedly shorter than the wild type (Figure 22C). If higher concentrations were used, like 250 µM MP265, the localized incorporation of new PG was largely abolished after 5 hours (Figure 22C). These results explain why the cells exhibit reduced growth at increasing concentrations of MreB inhibitors (Figure 21C and D). It is interesting to note that even a minimal amount of MreB at the stalked pole seems to suffice in order to support cell growth.

Overall, our results indicate that MreB is vital for cell shape in *H. neptunium*, since after disruption of MreB, cells lose their characteristic ovoid shape and become spherical. To what extent MreB plays a key role in the coordination of several cell wall biogenesis enzymes in *H. neptunium* still remains to be determined.

2.2. Morphology of *H. neptunium* relies on a coiled-coil-rich protein

We know from several bacteria that intermediate filaments (IFs) play a substantial role in establishing as well as maintaining cell morphology (248). Coiled-coil-rich proteins (CCRPs), to which also the IFs belong, are also referred to as IF-like proteins (248). In eukaryotes, intermediate filaments have vital structural functions in cell shape, internal cellular organization, and the regulation of intercellular transport (383). Recent studies have shown that CCRPs play a role in bacterial cell morphology by providing mechanical stability, for example, in *S. coelicolor*, *H. pylori*, and *C. crescentus* (151, 153, 247, 255). Bioinformatic analysis revealed that *H. neptunium* possesses a CCRP (HNE3462) (247), which also possesses the characteristic coiled-coil-rich regions and two domains of unknown function (Figure 23A). Henceforth the protein will be referred to as CCRP. In a first attempt the *ccrp* gene was deleted (Figure 23B and C). Surprisingly, the *Δccrp* deletion mutant showed a similar elongation and chaining phenotype as the *ΔamiC* deletion strain (Figure 13A and B). These observations indicate that the CCRP might play a role in cell division and maintenance of cell morphology in *H. neptunium*.

To further characterise CCRP in *H. neptunium*, we determined its localization. After an inducible C-terminal mCherry fusion proved functional (data not shown), a construct expressed from its native promoter was created, which localized to the stalked pole, in patches within the stalk and in the emerging bud (Figure 23D and F). Thus, the main function of CCRP seems to be needed at the stalked pole and within the stalk. Interestingly, a Western blot analysis revealed two distinct bands (Figure 23E). The CCRP-mCherry protein is predicted to be 126 kDa in size, which most likely corresponds to the full length CCRP-mCherry fusion protein. The observed double band in the Western blot indicates the possibility that CCRP is proteolytically processed, which most likely pertains to its function as a cytoskeletal element.

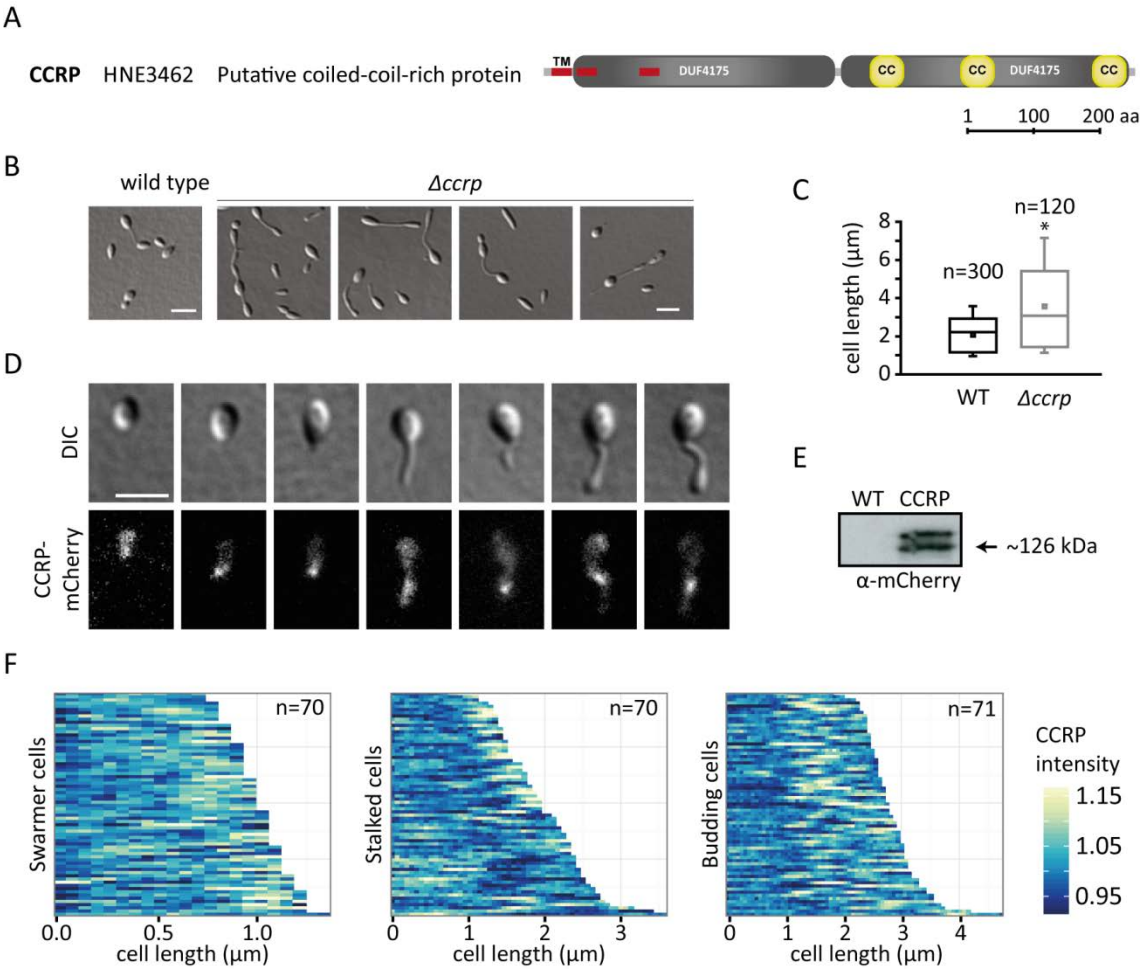

Figure 23. CCRP contributes to cell morphology in *H. neptunium*. A) CCRP consists of two domains of unknown function that include the typical coiled-coil regions of IF-like proteins. Domain information was obtained from SMART (02.2016) (367, 368) Abbreviation: CC, coiled-coil domain; DUF4175, domain of unknown function 4175; TM, transmembrane domain. **B)** Deletion of CCRP causes cell chaining and stalk elongation. The *H. neptunium* wild type and strain EC71 (*Δccrp*) were grown to exponential phase in MB medium and imaged by DIC microscopy. Scale bar, 3 µm. **C)** Deletion of CCRP causes cell chaining and stalk elongation. Cell length measurements are based on images from B) Box plots show the median and the interquartile range (box), the average value (square in box), the 5th and 95th percentile (whiskers). Asterisk indicates a *p*-value of < 0.001 (*t*-test). **D)** CCRP localizes at the stalked pole and in the stalk. Strain SR27 (*ccrp-mCherry*) was grown to exponential phase in MB medium and imaged by DIC and fluorescence microscopy by S. Rosskopf. Images represent the major localization pattern and have been ordered according to their stage within the cell cycle. Scale bar, 2 µm. **E)** CCRP is N-terminally processed. *H. neptunium* wild type and strain EC71 (*Δccrp*) were cultivated as described in B), samples were taken and subjected to immunoblot analysis using an anti-mCherry antibody. **F)** CCRP localizes sat the stalked pole and in the stalk. Demographs of CCRP-mCherry are based on images from D).

To verify the functionality of the fusion construct, the *Δccrp* deletion strain was complemented with the inducible construct. Surprisingly, before complementation this strain (SR27, *Δccrp* P_{Cu}*::*P_{Cu}*-ccrp-mCherry*) displayed wild-type morphology. However, upon induction the cells showed similar defects as the parental deletion strain (data not shown; (384)). The same effect was observed when the *Δccrp* deletion strain was complemented with untagged CCRP (data not shown; (384)). These findings indicate that the intracellular levels of CCRP are crucial for its correct function in *H. neptunium*.

Growth experiments indicate that the *Δccrp* deletion strain might have a slight growth defect (Table 18), which is hard to distinguish due to the increased biofilm formation of the strain (Table 18). DAPI staining confirmed that nucleoid distribution was not affected in the mutant (data not shown; (384)). HADA staining revealed that PG remodelling was also unaffected (Figure S4). Taken together, these results suggest that at normal intracellular levels CCRP has a minor function within the stalk, which possibly also contributes to cell division and thus influences cell morphology in *H. neptunium*.

2.3. Bactofilins control cell morphology in *H. neptunium*

In order to resolve how peptidoglycan biogenesis is coordinated in *H. neptunium*, the spatial organization of the cytoskeleton was further investigated. To complete the analysis of the bacterial cytoskeleton and its role in cell morphology, the focus was laid on the newly discovered bactofilins. Bactofilins are a novel class of bacterial cytoskeletal elements that presumably act as scaffolds for morphology-determining processes (157).

2.3.1. Bactofilins are essential to uphold cell shape

Similar to *C. crescentus*, *H. neptunium* possesses two bactofilin paralogues, BacA (HNE2629) and BacB (HNE0444), which are characterised by a bactofilin domain surrounded by proline-rich regions (Figure 24A). A first indication that bactofilins might play a role in morphogenesis was the observation that the loss of the *bacA* gene caused distorted cells with multiple and even branched stalks, which were generated all over the cell body (Figure 24B). Some cells completely omitted the stalk as reproductive organelle and instead divided by binary fission. Interestingly, the swarmer cells consistently displayed wild-type morphology. These observations imply a severe polarity defect upon the onset of differentiation in the *ΔbacA* deletion strain. In contrast, the *ΔbacB* deletion strain had no obvious phenotype (Figure 24B). To further investigate the function of both bactofilins, a *ΔbacAB* double deletion was created, which intensified the morphological defects already observed in the *ΔbacA* single deletion strain (Figure 24B). The *ΔbacA* and *ΔbacAB* deletion strains have a slightly decreased growth rate compared to the wild type, which might be due to increased biofilm formation (Table 18). Despite perturbed cell shape, the nucleoid distribution was mainly unaffected in all three deletion strains, with the exception of some cells in the *ΔbacAB* double mutant (Figure S18). As stalk formation was only compromised but not abolished in the absence of BacAB, it is probable that bactofilins play a more pronounced role in cell morphology than stalk biogenesis.

To verify the mutant phenotypes, both the Δ*bacA* single deletion strain and the Δ*bacAB* double mutant were complemented with the BacA and BacB proteins, respectively. 24 hours after inducing the expression of *bacA* from the copper locus, the majority of the Δ*bacA* deletion mutants displayed wild-type morphology (Figure S16A). Similar results were obtained for the complementation of the Δ*bacAB* double mutant with the BacA protein (data not shown). On the other hand, induction of *bacB* did not restore the wild type phenotype to either of the bactofilin deletion strains (Figure S16B, data not shown).

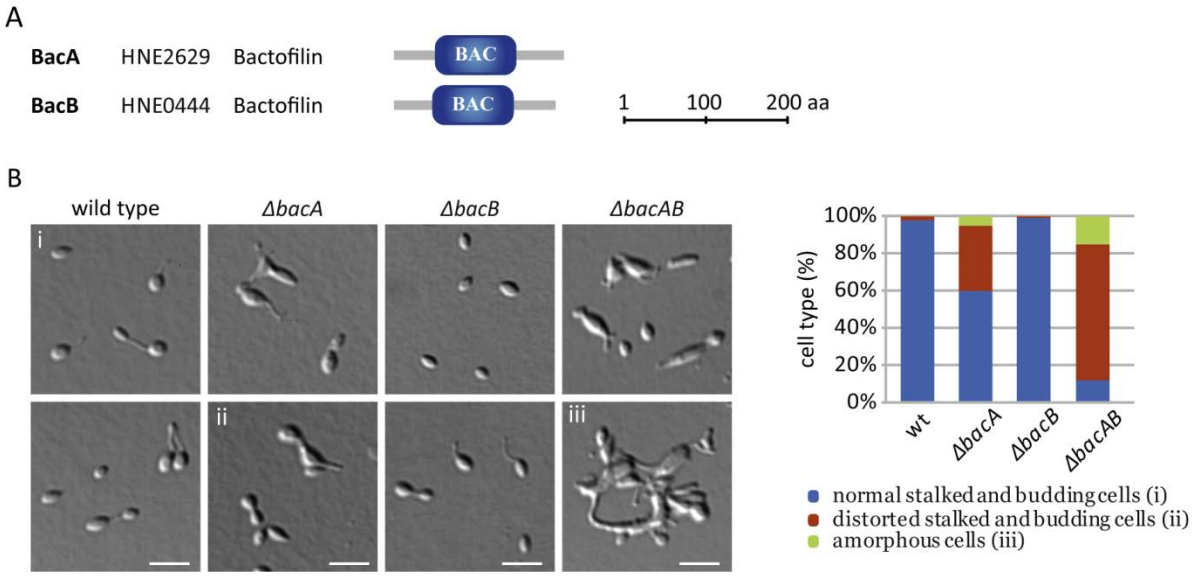

Figure 24. BacA is required for correct morphology in *H. neptunium*. A) Bactofilins are characterized by a bactofilin (DUF583) domain. Domain information was obtained from SMART (10.2015) (367, 368) Abbreviation: BAC, bactofilin domain. **B)** Deletion of BacA causes severe morphological defects. The *H. neptunium* wild type and strains EC23 (*ΔbacB*), EC28 (*ΔbacA*), and EC33 (*ΔbcaAB*) were grown to exponential phase in MB medium and analysed by DIC microscopy. Scale bar, 3 µm. 100 cells per strain were analysed for morphological defects (excluding swarmer cells).

To further characterize the bactofilins in *H. neptunium*, C-terminal fusions constructs were created and placed under the control of their native promoters. Tracking BacA-YFP in a long-term time-lapse experiment revealed that it localizes dynamically within the stalk and mainly formed a foci at the bud neck (the junction between the stalk and the bud) (Figure 25A and Movie S2). In some cases, a dual signal was observed, where BacA also localized to both ends of the stalk. In rare cases, multiple foci could be observed within the stalk that could merge and split again (data not shown). In some cases, the BacA-YFP signal was observed to split, where one signal remained at the stalked pole and the other localized at the bud neck (Figure 25A). Interestingly, BacA was always excluded from the tip of the stalk (Figure 25A). In stalked cells, BacA always localized in a sub apical manner to the end of the stalk, which in time-lapse experiments was revealed to be the incipient bud neck and thus future division site (Figure 25A). Similar observations were made for BacB-Venus, which also preferentially localized to the stalked pole and within the stalk (Figure 25B and D). Both fusion proteins appear to be largely stable when expressed from under their native promoters, whereas BacA seems to be expressed at a much higher level than BacB (Figure 25C). Localization of BacA-YFP and BacB-mCherry expressed from their native promoters showed a clear co-localization of both proteins at the stalked pole and the bud neck, indicating that both bactofilins might act in concert with each other (Figure 25E). In this strain the expression of BacB-mCherry was higher than that of the BacB-Venus (Figure 25C and F). Based on these observations, we assume that bactofilins might be involved in stalk biogenesis in *H. neptunium*.

As a side note, in the initial investigation both bactofilins were C-terminally tagged with a fluorescent protein and placed under the control of an inducible promoter. After induction, both BacA-mCherry

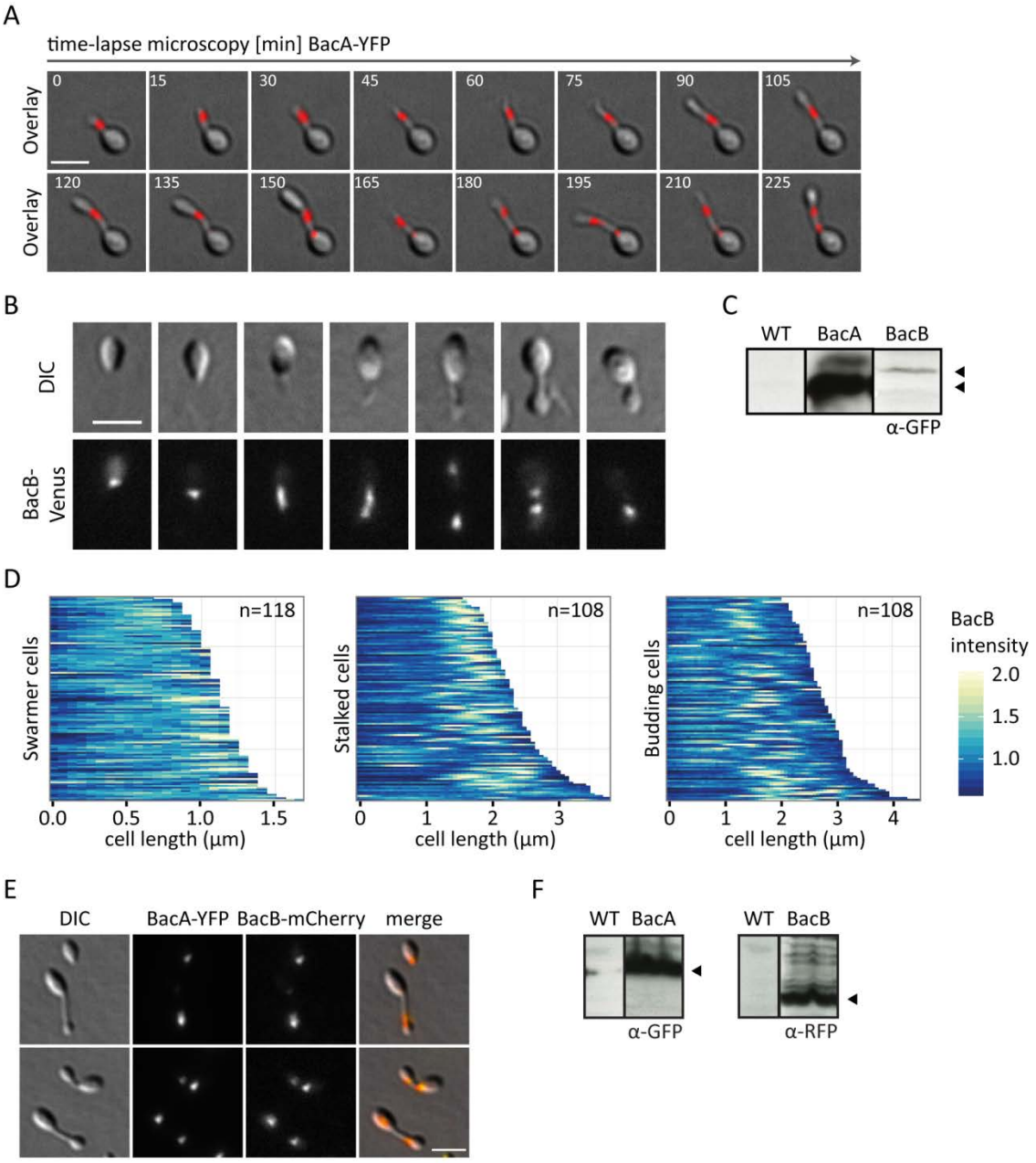

Figure 25. Bactofilins localize within the stalk and form bipolar foci. A) BacA localizes dynamically within the stalk of *H. neptunium*. Strain EC61 (*bacA-yfp*) was grown to exponential phase in MB medium, transferred into a microfluidic system and tracked by DIC and fluorescence microscopy in 15 min intervals. Scale bar, 2 µm. **B)** BacB localizes mainly at the stalked pole and within the stalk. Strain EC67 (*bacB-venus*) was grown to exponential phase in MB medium and analysed by DIC and fluorescence microscopy. Images represent the major localization pattern and have been ordered according to their stage within the cell cycle. Scale bar, 2 µm. **C)** Protein level of bactofilin fusion proteins expressed from their native promoters. The *H. neptunium* wild type, Strain EC61 (*bacA-yfp*) and EC67 (*bacB-venus*) were cultivated as described in A) and B). Samples were taken and subjected to immunoblot analysis using an anti-GFP antibody. Triangles indicate BacA-YFP (~50 kDa) and BacB-Venus (~55 kDa). **D)** BacB localizes mainly at the stalked pole and within the stalk. Demographs of BacB-Venus based on images from B). **E)** BacA and BacB co-localize at the stalked pole and within the stalk. Strain EC68 (*bacA-yfp bacB-mCherry*) was grown to exponential phase in MB medium and analysed by DIC and fluorescence microscopy. Scale bar, 2 µm. **F)** Protein level of bactofilin fusion proteins expressed from their native promoters. The *H. neptunium* wild type and strain EC68 (*bacA-yfp bacB-mCherry*) were cultivated as described in E). Samples were taken and subjected to immunoblot analysis using an anti-GFP or anti-RFP antibody, respectively. Triangles indicate BacA-YFP (~60 kD) and BacB-mCherry (~50 kDa).

and BacB-Venus localized in the complete stalk (but not the bud), indicating that internal protein levels highly affect the localization of both bactofilins (data not shown).

The modified bactofilins seem to be fully functional *in vivo* as all bactofilin fusion strains show similar growth rates as the wild type (Table 18). Nonetheless, to ensure the functionality of the BacA fusions, we complemented the *ΔbacA* single deletion strain with the BacA-mCherry fusion and the Δ*bacAB* deletion strain with the BacA-YFP fusion. After induction, both fusion proteins localized as expected and largely restored the wild-type phenotype to both deletion mutants (data not shown). These complementation assays match those conducted with the wild-type protein (Figure S16A), indicating that the BacA fusions are functional and behave as their native counterparts.

In order to clarify the recruitment of BacB, we expressed BacB-Venus under the control of the zinc-inducible promoter in the Δ*bacA* mutant background. In some cases BacB-Venus was observed to localize to the stalked pole. However, in some cells, an off-centre focus in the cell body could be observed (Figure S17A and B). Presumably BacB needs BacA for its correct localization. Taken together, these results indicate that BacA seems to have a more important role in *H. neptunium*.

2.3.2. Bactofilins are required for proper stalk maintenance

Our next goal was to verify that BacA acts as a true cytoskeletal protein in *H. neptunium*. For this reason, BacA-His_6 was purified by using Ni-NTA (nickel-nitrilotriacetic acid) agarose beads in a batch purification approach. Analysis of the purified BacA-His_6 by TEM indicated that BacA forms 2 nm wide polymers, which can bundle together to larger cables (Figure 26A and B). The TEM images confirmed that BacA can form higher-order polymers, which might act as a scaffold for biosynthetic enzymes at the stalked pole and the future division site.

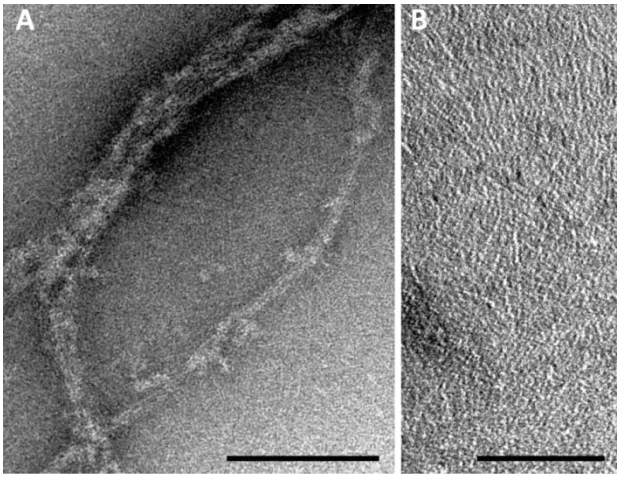

Figure 26. BacA forms thin polymers and cables *in vitro*. Transmission electron micrograph of BacA protofilament bundles (B) and single BacA protofilaments (A) formed in a low-salt buffer (10 mM HEPES/NaOH, pH 7.2,10 mM NaCl, 5 mM $MgCl_2$, 0.1 mM EDTA, 1 mM ß-mercaptoethanol). Scale bar, 100 nm. Data generated by A. Klingl.

To determine the interaction of bactofilins with each other, their localization was observed in a heterologous system. To this end, both BacA and BacB were individually as well as simultaneously expressed in *E. coli* cells. Expressed on its own, BacA-YFP formed bipolar foci (Figure 27A). BacB-CFP, on the other hand, localized in randomly positioned inclusion bodies (Figure 27B). When both bactofilins were co-expressed, they co-localized within large structures that spanned the complete cell body and seemed to be mainly associated with the cell membrane (Figure 27C). In the presence

of BacA, BacB did not form any inclusion bodies but always co-localized with BacA. In some cases both proteins localized to the lateral wall of the cell, creating a filament-like structure along its long axis (Figure 27C). Strikingly, the nucleoid of *E. coli* was largely excluded from the bactofilin clusters (Figure 27C). In essence, BacA and BacB seem to form co-polymers, which can only extend along the cell axis if both bactofilins act in concert.

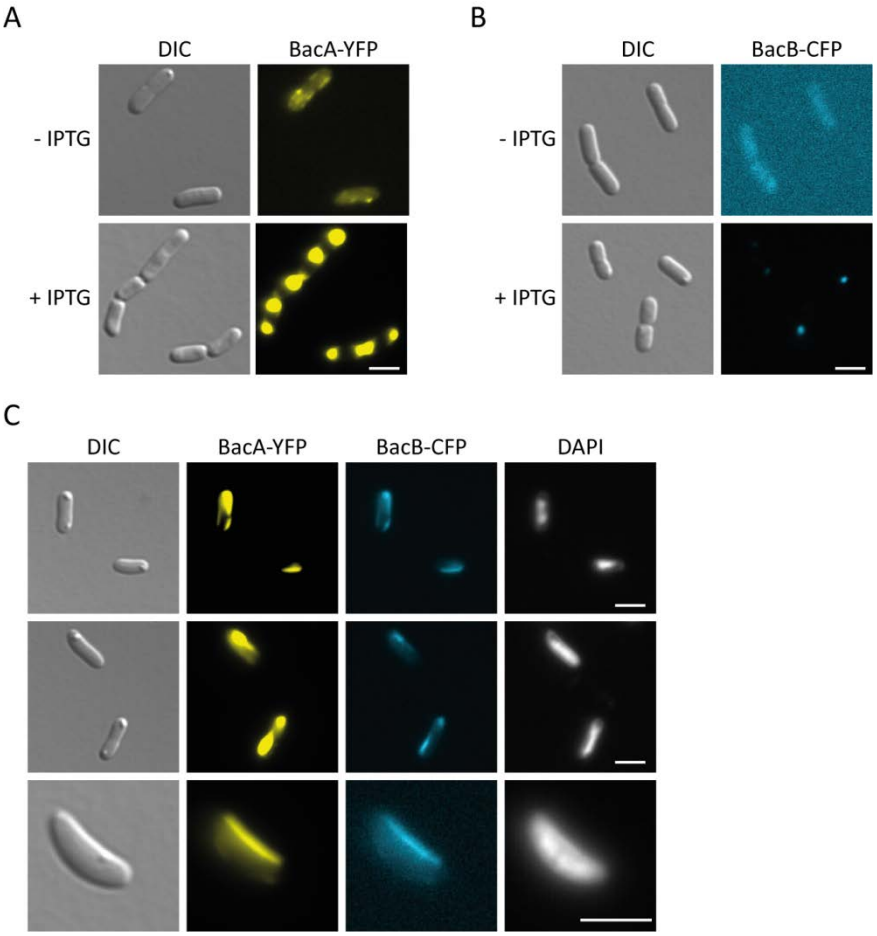

Figure 27. Bactofilins form polymer-like structures when expressed heterologous in *E.coli*. A) BacA-YFP forms bipolar loci in *E. coli*. Cells of *E. coli* BL21(DE) bearing the plasmid pEC119 (P_{T7}-*bacA-cfp*) were grown in LB with 5 % glucose to exponential phase, induced with 0.5 mM IPTG for 1 h before analysis with DIC and fluorescence microscopy. Scale bar, 3 µm. **B)** BacB-CFP forms inclusion bodies in *E.coli*. Cells of *E. coli* BL21(DE) bearing the plasmid pEC120 (P_{T7}-*bacB-yfp*) were grown in LB with 5 % glucose to exponential phase, induced with 0.5 mM IPTG for 1 h before analysis with DIC and fluorescence microscopy. Scale bar, 3 µm. **C)** BacA-YFP and BacB-mCherry form co-polymers in *E. coli*. Cells of *E. coli* BL21(DE) bearing the plasmid pEC121 (P_{T7}-*bacA-yfp* P_{T7}-*bacB-cfp*) were grown in LB with 5 % glucose to exponential phase, induced with 0.5 mM IPTG for 1 h before analysis with DIC and fluorescence microscopy. Scale bar, 3 µm.

To test whether the bactofilins play a role in cell polarity, the localization of DivJ was analysed. DivJ is a histidine kinase that is part of the phosphorelay that regulates the activation and stability of the master regulator CtrA and localizes to the old cell pole (385, 386). In *H. neptunium*, DivJ localizes to the flagellated pole, i.e. opposite of the future stalked pole (387). To assess the state of cell polarity, DivJ-Venus was expressed from under the control of its native promoter in all three bactofilin deletion mutants. In most cases, DivJ localized to the non-stalked cell pole (Figure S19). Occasionally, DivJ was observed to localize at the stalked pole or random places along the cell outline in cells which

have lost all resemblance to the wild type (Figure S19). Concluding, the absence of bactofilins does not cause a direct cell polarity defect. However, the morphological alterations caused by the absence of BacA might lead to loss of cell polarity in individual cells.

As cell polarity is established and maintained independently of bactofilins, our next goal was to determine their mode of action. To this end, we wanted to determine what causes the morphological defects in the *ΔbacAB* deletion mutants. We preformed time-lapse microscopy with the *ΔbacAB* deletion mutant, in order to observe how the morphological defects manifest. *ΔbacAB* cells budding for the first time can undergo this process without any evident alterations. However, it appears that the following cell divisions seem to cause problems. The major issue observed in the *ΔbacAB* deletion strain seems to be that the bud uncontrollably grows into the stalk so that the next round of budding is initiated within the stalk before the other daughter cell is fully budded off (Figure 28A and Movie S3). Furthermore, it appears that the cells are growing in several sites at once and as a result the cells lose their cell shape (Figure 28B, Movie S4, and Movie S5). The cells can only divide once narrow junctions are formed, which indicates that a stalk is not a prerequisite for cell division but that cell diameter plays a much more substantial role.

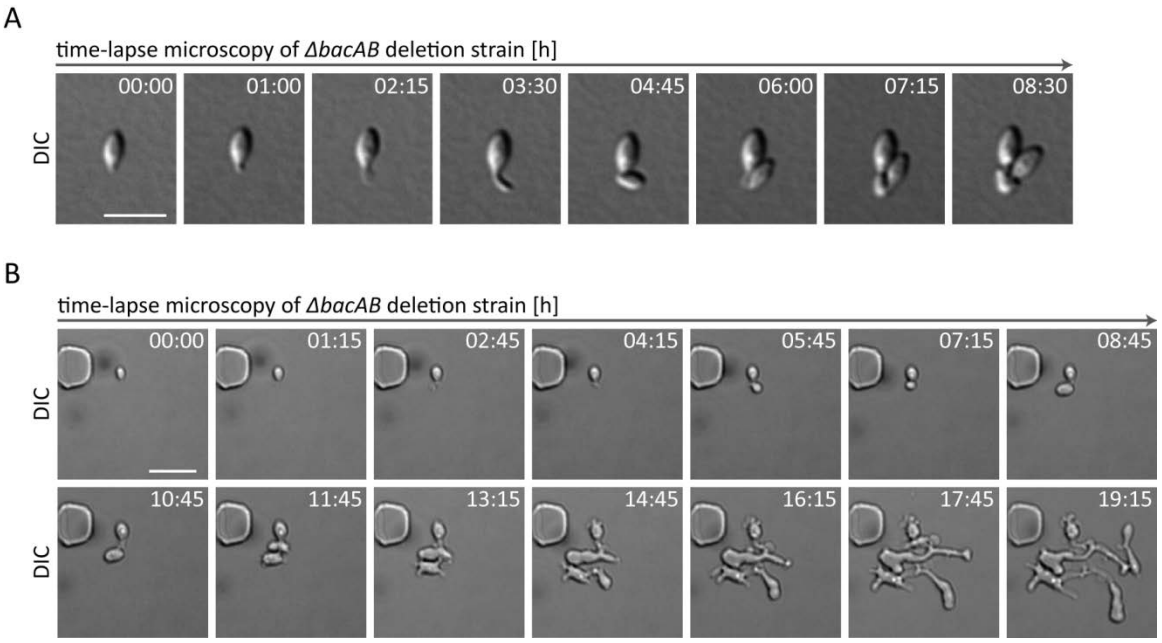

Figure 28. In the absence of bactofilins stalk integrity is lost and cell growth is deregulated. A) In the absence of bactofilins the bud fully incorporates the stalk. Strain EC33 (*ΔbacAB*) was grown to exponential phase in MB medium, transferred to 1 % MB agarose pads and tracked with DIC microscopy every 15 min. Scale bar, 3 µm. **B)** The bactofilin double deletion mutant is characterised by aberrant growth. Strain EC33 (*ΔbacAB*) was grown to exponential phase in MB medium, transferred to microfluidic system, and monitored with DIC microscopy every 15 min. Scale bar, 5 µm.

We next examined whether PG incorporation may be linked to the presence of bactofilins in *H. neptunium*. HADA staining of the *ΔbacA* and the *ΔbacAB* deletion mutants revealed that as long as cells had wild-type morphology PG incorporation occurred at the expected sites, such as the future stalked pole and the bud (Figure 29). In contrast, cells with morphological defects were integrating new PG randomly throughout the entire cell body, with only a small number of visible foci that

indicate specific growth zones (Figure 29). These observations indicate that in the absence of bactofilins PG insertion is fully functional but no longer restricted to specific growth zones, which indicates a loss in the coordination of PG incorporation. The loss of specificity in cell wall remodelling most likely leads to the significant morphological alterations observed for the bactofilin mutants.

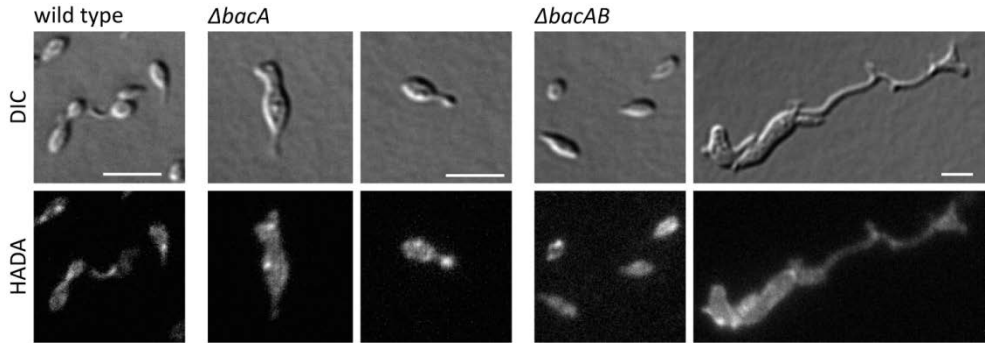

Figure 29. Peptidoglycan incorporation is disordered in the absence of bactofilins. The *H. neptunium* wildtype and strains EC23 (*ΔbacB*), EC28 (*ΔbacA*), and EC33 (*ΔbcaAB*) were grown to exponential phase in MB medium, pulse-labelled with HADA, and imaged by DIC and fluorescence microscopy. Scale bar, 3 µm.

Next, it was to be resolved if the bactofilins interacted with other cytoskeletal elements in *H. neptunium*. To test this, BacA-YFP and BacB-Venus were co-localized with the MreB-mCherry^{SW} sandwich fusion. In both cases, we could observe an occasional co-localization of both bactofilins with MreB at the stalked pole (Figure 30A and B). It still remains to be determined if both bactofilins directly or indirectly interact with MreB.

To test whether the bactofilins might act in concert with MreB, strains expressing BacA-YFP or BacB-Venus from their native locus were treated with A22. Brief incubation with A22 did not alter the localization of either bactofilin (data not shown). In cells treated with A22 for 24 hours, both bactofilins were able to localize to the stalked pole and the stalk (Figure 30E and F). However, once cells were completely spherical, neither bactofilin could localize anymore (Figure 30E and F). In summary, bactofilins do not require MreB for localization to the stalked pole, and the bud neck but appear to require a geometric cue for localization nonetheless.

To determine whether MreB acts in concert with the bactofilins, MreB-mCherry^{SW} expressed from its native promoter was localized in both the *ΔbacA* and the *ΔbacAB* deletion strains. MreB-mCherry^{SW} still localized to the stalk-like protrusions in both strains (Figure 30D). These data suggest that MreB localizes independently to the stalked pole of *H. neptunium* and even though these proteins co-localize during some stages of the cell cycle, MreB does not require the bactofilins for polar coordination (Figure 30A and B).

To gain further insights into how bactofilins are targeted to the stalked pole, BacA and BacB from *C. crescentus* (BacA$_{cc}$ and BacB$_{CC}$) were localized in *H. neptunium*. In *C. crescentus*, BacA$_{cc}$ localizes diffusely in swarmer cells until it is recruited to the stalked pole and only upon overproduction does it extend from the stalked pole into the stalk (157). BacB$_{cc}$-Venus was placed under the control of

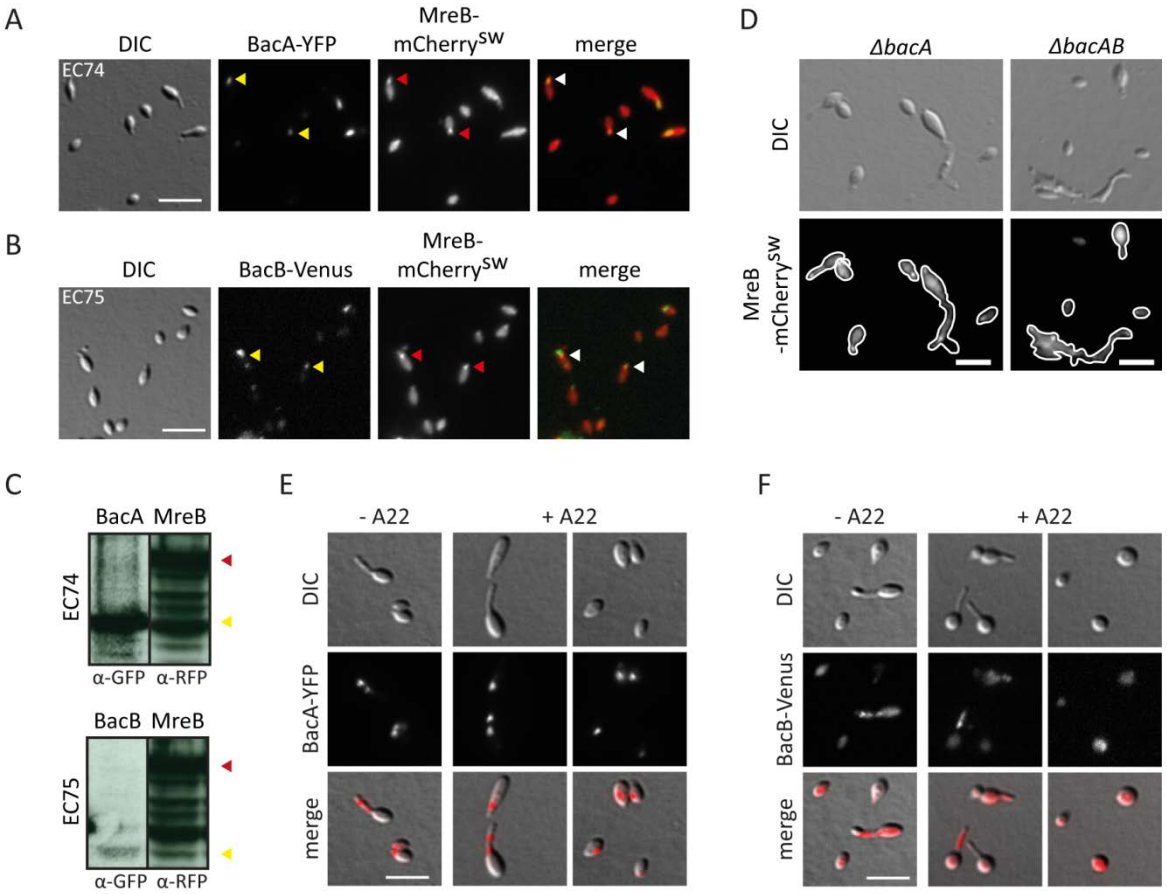

Figure 30 Localization of bactofilins relies on cell morphology whilst MreB does not require bactofilins for correct localization. A) BacA-YFP and MreB-mCherry^{SW} sporadically co-localize. Strain EC74 (*bacA-yfp mreB-mCherry*^{SW}) was grown to exponential phase in MB and visualized by DIC and fluorescence microscopy. White triangles indicated co-localization. Scale bar, 3 µm. **B)** BacB-Venus and MreB-mCherry^{SW} sporadically co-localize. Strain EC75 (*bacB-venus mreB-mCherry*^{SW}) was grown to exponential phase in MB and visualized by DIC and fluorescence microscopy. White triangles indicated co-localization. Scale bar, 3 µm. **C)** Protein levels of bactofilin and MreB fusion proteins expressed from their native promoters. Strains EC74 (*bacA-yfp mreB-mCherry*^{SW}) and EC75 (*bacB-venus mreB-mCherry*^{SW}) were grown to exponential phase in MB. Samples were taken and subjected to immunoblot analysis using an anti-GFP or anti-RFP antibody, respectively. The red triangle indicates MreB-mCherry (~72 kDa) and the yellow triangle indicates BacA-YFP (~50 kDa) and BacB-Venus (~45 kDa), respectively. **D)** In the absence of bactofilins, MreB is still able to localize to the stalked pole and the stalk. Strains EC81 (*ΔbacA mreB-mCherry*^{SW}) and EC82 (*ΔbacAB mreB-mCherry*^{SW}) were grown to exponential phase in MB and visualized by DIC and fluorescence microscopy. Scale bar, 3 µm. **E)** Upon the inhibition of MreB, BacA partially fails to localize correctly. Strain EC61 (*bacA-yfp*) was grown to exponential phase in MB medium, treated with 37 µM A22 for 24 h, and analysed by DIC and fluorescence microscopy. Scale bar, 3 µm. **F)** Upon the inhibition of MreB, BacB partially fails to localize correctly. Strain EC67 (*bacB-venus*) was grown to exponential phase in MB medium, treated with 37 µM A22 for 24 h, and analysed by DIC and fluorescence microscopy. Scale bar, 3 µm.

the copper-inducible promoter and after induction $BacB_{cc}$ localized diffusely in the cell body (data not shown). Similarly, $BacA_{cc}$-Venus was placed under the control of the copper-inducible promoter. After induction, $BacA_{cc}$ localized to the stalked pole as well as the stalk itself (Figure 31A). To exclude the possibility that $BacA_{cc}$ is targeted to the stalked pole by interaction with endogenous $BacA_{HNE}$, $BacA_{cc}$-Venus was visualized in the *ΔbacAB* mutant strain. Even though $BacA_{cc}$-Venus could not rescue the *ΔbacAB* mutant phenotype, the fusion localized to the stalked pole(s) in most pleomorphic cells (Figure 31B). Despite the analogous localization of $BacA_{cc}$ and $BacA_{HNE}$, $BacA_{cc}$ cannot fully complement the cell shape defect of either the *ΔbacA* or the *ΔbacAB* mutant (Figure 31C, D, and E).

Nonetheless, taken together, these results indicate that BacA homologues might be targeted to the stalked pole by a geometric cue (e.g. positive membrane curvature) instead of recruitment by other specific polarity factors.

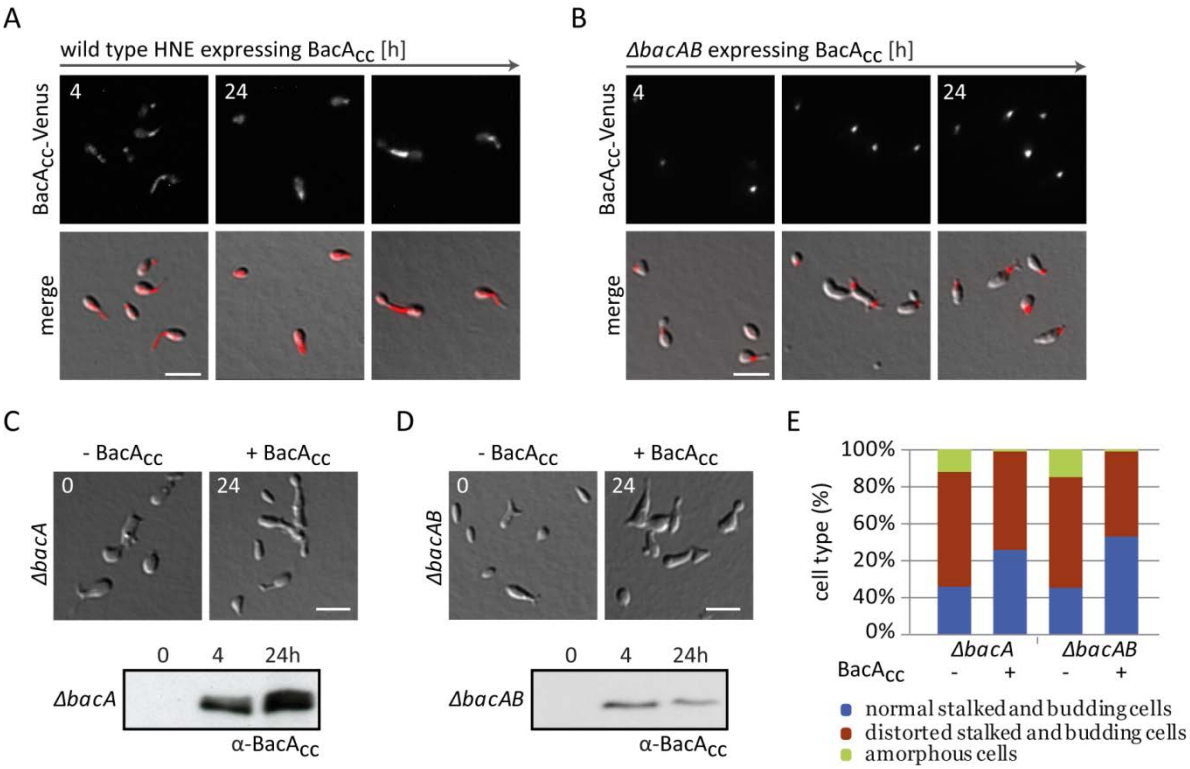

Figure 31. BacA$_{CC}$ from *C. crescentus* cannot compensate for the loss of bactofilins in *H. neptunium*. A) BacA$_{CC}$ localizes in the stalk of *H. neptunium*. Strain EC51 (*P$_{Zn}$::P$_{Zn}$-bacA$_{CC}$-venus*) was grown to exponential phase in MB, induced with 500 µM $ZnSO_4$ for 24 h, and visualized by DIC and fluorescence microscopy at the indicated time points. Scale bar, 3 µm. **B)** BacA$_{CC}$ localizes to the stalked pole in the *ΔbacAB* deletion strain. Strain EC64 (*ΔbacAB P$_{Zn}$::P$_{Zn}$-bacA$_{CC}$-venus*) was grown to exponential phase in MB, induced with 500 µM $ZnSO_4$ for 24 h, and visualized by DIC and fluorescence microscopy at the indicated time points. Scale bar, 3 µm. **C)** BacA$_{CC}$ can partially complement the *ΔbacA* deletion strain. Strain EC72 (*ΔbacA P$_{Cu}$::P$_{Cu}$-bacA$_{CC}$*) was grown to exponential phase in MB, induced with 300 µM $CuSO_4$ for 24 h, and visualized by DIC at the indicated time points. Concomitantly, samples were taken and subjected to immunoblot analysis using an anti-BacA$_{CC}$ antibody. Scale bar, 3 µm. **D)** BacA$_{CC}$ can partially complement the *ΔbacAB* deletion strain. Strain EC73 (*ΔbacAB P$_{Cu}$::P$_{Cu}$-bacA$_{CC}$*) was grown to exponential phase in MB, induced with 300 µM $CuSO_4$ for 24 h, and visualized by DIC at the indicated time points. Concomitantly, samples were taken and subjected to immunoblot analysis using an anti-BacA$_{CC}$ antibody. Scale bar, 3 µm. **E)** Quantitative analysis of the BacA$_{CC}$ complementation efficiency. For classification of cell morphologies see Figure 24B. 100 cells were quantified according to their morphological defects (excluding swarmer cells) from C) and D) prior to and after induction.

2.3.3. Finding potential interaction partners for bactofilins

Previous analyses have shown that BacA plays a vital role in the coordination of bud formation as well as cell growth. Previous studies in *C. crescentus* showed that BacA co-localizes at the stalked pole with the PG synthase PbpC (157). If BacA in *H. neptunium* also functions as a scaffold, it would most likely recruit enzymes involved in stalk biogenesis. Thus, the next step was to identify potential interaction partners for BacA.

To find interaction partners for BacA, the native *bacA* gene was replaced with a fusion encoding a C-terminally HA-tagged version, which was used for co-immunoprecipitation (Co-IP) experiments. HNE0630, which is annotated as a conserved hypothetical protein with a domain of unknown function, was identified as a potential interaction partner of BacA (Figure 32A). HNE0630 is conserved amongst Alphaproteobacteria and lies within a conserved genetic locus, which mainly consists of *prfA* and *prmC* in other species (Figure 32B). Since it was not possible to generate an in-frame deletion of HNE0630, we presume that it has an essential role in *H. neptunium*. Inducible N- and C-terminal mCherry fusions of HNE0630 were localized to the new (flagellated) pole in swarmer cells, where it remained as the cells differentiated into stalked and budding cells (Figure 32C, D and E). In accordance with this observation, it was presumed that HNE0630 might act as an inhibitor of BacA at the flagellated pole. However, we were unable to generate a fusion construct for HNE0630 expressed from under the control of its native promoter. Thus, so far the localization of HNE0630 could not be validated. In order to shed light on the role of HNE0630 in Alphaproteobacteria, we analysed its homologue in *C. crescentus*, CCNA_00920. As the deletion mutant showed no obvious phenotype and the fusion construct localized diffusely, no further conclusions could be drawn (S. Rosskopf, data not shown). In either case, the role of HNE0630 and its connection with BacA still remains unclear and is in need of further investigation.

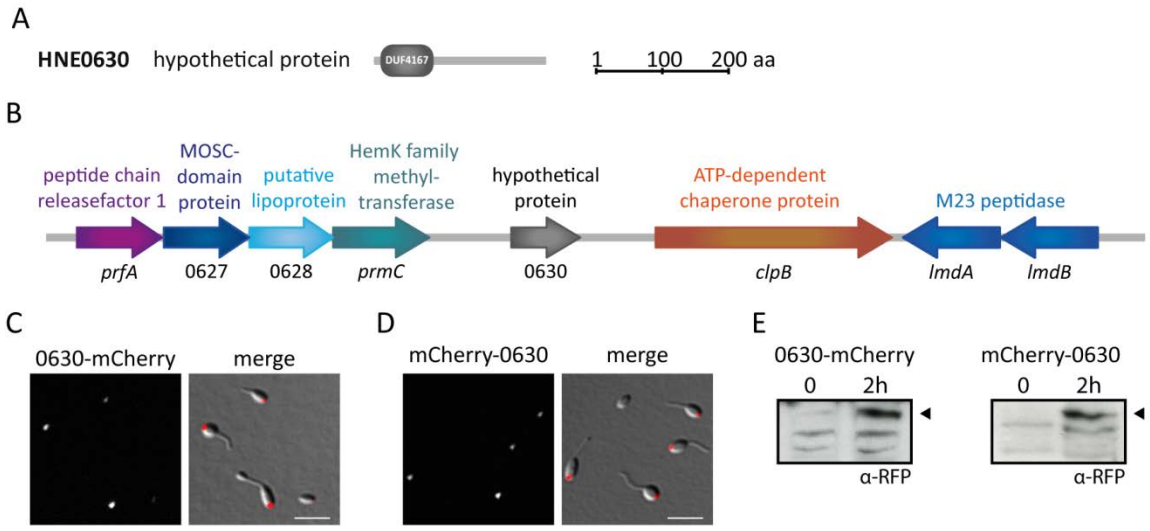

Figure 32. Potential BacA interaction partner HNE0630 localizes to the flagellated pole. A) HNE0630 is a conserved hypothetical protein with a domain of unknown function. Domain information was obtained from SMART (10.2015) (367, 368). Abbreviations: DUF4167, domain of unknown function 4167. **B)** Conserved chromosomal context of HNE0630. **C)** HNE0630-mCherry localizes to the new pole. Strain EC58 (*P_{Cu}::P_{Cu}-HNE0630-mCherry*) was grown to exponential phase in MB and, after induction with 300 µM $CuSO_4$ for 2 hours, cells were visualized by DIC and fluorescence microscopy. Scale bar, 3 µm. **D)** mCherry-HNE0630 localizes to the flagellated pole. Strain EC59 (*P_{Cu}::P_{Cu}-mCherry-HNE0630*) was grown to exponential phase in MB and after induction with 300 µM $CuSO_4$ for 2 hours, cells were visualized by DIC and fluorescence microscopy. Scale bar, 3 µm. **E)** Expression levels of HNE0630 fusion constructs under the control of P_{Cu}. Strains EC58 (*P_{Cu}::P_{Cu}-HNE0630-mCherry*) and EC59 (*P_{Cu}::P_{Cu}-mCherry-HNE0630*) were grown to exponential phase in MB. Samples for immunoblot were taken before and after induction with 300 µM $CuSO_4$ for 2 hours and probed with an anti-RFP antibody.

In order to find further potential interaction partners for BacA, the previously purified BacA-His_6 was used for affinity purification experiments. As this venture proved fruitless, specific anti-BacA antibodies were further purified and used for pull-down assays. Unfortunately, this attempt also did

not yield any further potential interaction partners. In short, apart from HNE0630, no further novel interaction partners could be identified for BacA to this date.

Since finding novel interaction partners proved to be futile, we shifted our focus on verifying interactions with already familiar proteins. It is well know from the literature that cytoskeletal elements in bacteria interact with cell wall remodelling enzymes (293). The most prominent example in case of bactofilins is BacA from *C. crescentus*, which recruits the peptidoglycan synthase PpbC to the stalked pole (157). Other examples include MreB, which is part of the elongasome as well as MreC, RodZ, and MurG (290, 292, 300). Since BacA has a role in cell morphology, it assumably would interact with cell wall remodelling enzymes in *H. neptunium*. Potential candidates, apart from BacB and MreB, might be the cell wall hydrolases LmdABC, since bactofilins are often encoded in operons with LytM hydrolases (284), which is also true for *C. crescentus* and *H. neptunium*. Additionally, LmdABC harbour a transmembrane domain, which might facilitate the interaction with BacAB in the cytoplasm (Figure 12).

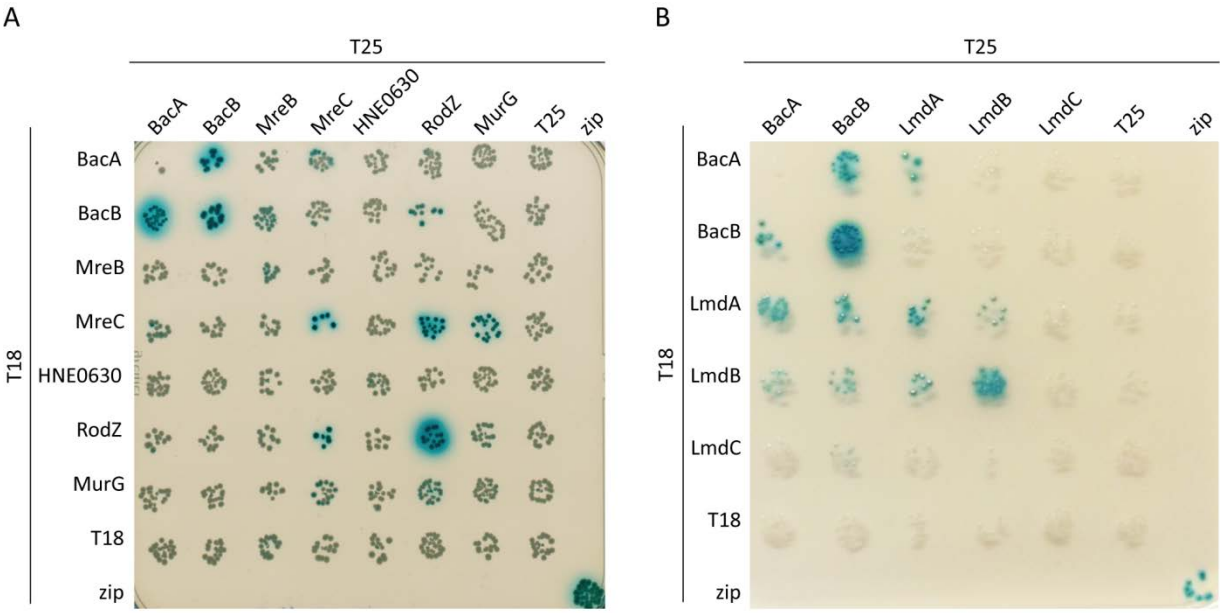

Figure 33. Bacterial two-hybrid assay to detect interaction between bactofilins and their potential interaction partners. The reporter strain *E. coli* BTH101 was transformed with pair of plasmids containing the T18 and T25 fragment of the *B. pertussis* adenylate cyclase fused proteins of interest. Untagged T18 and T25 fragments were used as negative controls whilst the GCN4 leucine zipper region (zip) was utilized as a positive control. Blue colour indicates a positive interaction. A complete list of employed plasmids can be found in Table 24. **A)** Interaction of bactofilins with components of the elongasome. **B)** Interaction of bactofilins with LytM factors (data generated by S. Kanngießer).

To validate possible interactions, bacterial-two-hybrid (BACTH) assays were conducted. In these assays, we could confirm the interaction of BacA and BacB. However, we could not observe any self-interaction for BacA as *E. coli* cells did not grow in the presence of elevated BacA levels (Figure 33A). RodZ on the other hand showed a clear self-interaction, as well as MreC (Figure 33A). Furthermore, there seems to be a strong interaction between RodZ and MreC as well as between MurG and MreC (Figure 33A). The BACTH assay also indicates a possible interaction between RodZ and BacB (Figure 33A). There was no interaction observed for either MreB or HNE0630, which might indicate that

neither fusion was functional in our assays. Generating a sandwich fusion similar to the MreB-mCherry^{SW} construct with the T18 and T25 fragment might render the assay more successful (388). Furthermore, there appears to be a strong interaction between the bactofilins and LmdA and to some extent with LmdB (Figure 33B). These results indicate a strong link between bactofilins and cell wall remodelling enzymes, which requires further validation.

3. Discussion

This work represents the first molecular study of growth and budding in *H. neptunium* and a stalked budding bacterium in general. *H. neptunium* offers an intricate study of asymmetric growth and cell division in stalked budding bacteria. A motile swarmer cell not only differentiates into a sessile, stalked cell but generates its offspring at the distal end of the stalk by budding. This work focused on identifying how *H. neptunium* maintains and alters its cell shape during its life cycle.

3.1. The advantages of budding at the distal end of a stalk

Our study showed that, like other prosthecate Alphaproteobacteria (339), *H. neptunium* also extends its stalk from its the base, where it is attached to the cell body. Using the fluorophore-labelled D-amino acid HADA, we could show that *H. neptunium* has four distinct growth phases (Figure 34). In the first and shortest phase, the swarmer cells enlarge their cell body before stalk biogenesis is initiated. In the next phase, the stalk is elongated from the base of the mother cell's body. Once the stalk has reached a critical length, the new daughter cell is generated at the tip of the stalk. In the final growth phase, which corresponds to the initiation of cell division at the bud neck, which is the site between the new daughter cell and the stalk. The separate growth phases seem to be tightly controlled as they were not observed to overlap. It seems that once the mother cell has reached a certain cell size, the circumference of the cell body is maintained and growth is focused to the stalk and the new daughter cell.

Previous reports have proposed that asymmetric cell division, especially budding, is a favourable system for the study of aging in bacteria (346, 389). In theory, the offspring is generated from newly formed material and has no old pole, in contrast to cells dividing by symmetric binary fission (389). This is also true for *H. neptunium*, as the daughter cell emerges at the distal end of the stalk. The tip of the stalk is expanded to form the new daughter cell, which consequently remodels part of the stalk to generate its cell body. However, most of the daughter cell's PG is new (Figure 34). Thus, *H. neptunium* offers an excellent system for the study of senescence, as the "old" (mother) cell and the "new" (daughter) cell are clearly distinguishable from each other. As the daughter cell is generated at the distal end of the stalk it ensures that any inclusion bodies accumulated within the mother cell are not passed on to the new generation. The clear advantage of budding at the tip of an appendage is the propagation of a new, damage-free daughter cell that does not inherit any of the mother cell's old or damaged proteins (389). This is an obvious benefit for *H. neptunium* compared to polarly growing bacteria where detrimental cellular material could still end up in the newly synthesized daughter cell.

Clearly, the mode of budding in *H. neptunium* differs from polar growth in other Alphaproteobacteria. Amongst the Rhizobilaes, the Rhizobiaceae like *A. tumefaciens* grow at one pole to produce a new daughter cell (78). In the case of *H. neptunium,* and similar to *C. crescentus*, polar growth is restricted to stalk biogenesis. In *H. neptunium* the emergence of the new daughter cell via budding is partially a

form of zonal remodelling and growth at the tip of the stalk, which occurs in a dispersed, MreB-dependent manner. In contrast to other Alphaproteobacteria, *H. neptunium* seems to utilize a combination of zonal growth coupled to subsequent polar remodelling to generate a daughter cell (Figure 34).

Why would the cell relinquish part of its own stalk? A possible explanation for this phenomenon is that it might be easier to generate a cell based upon a pre-existing PG template than to synthesize the complete structure *de novo*. However, it was recently shown that wall-less *B. subtilis* L-forms can establish a rod-shape without a pre-existing template structure (390). Nonetheless, partially incorporating already constructed parts of the stalk could accelerate the budding process as less new cell material has to be generated from scratch.

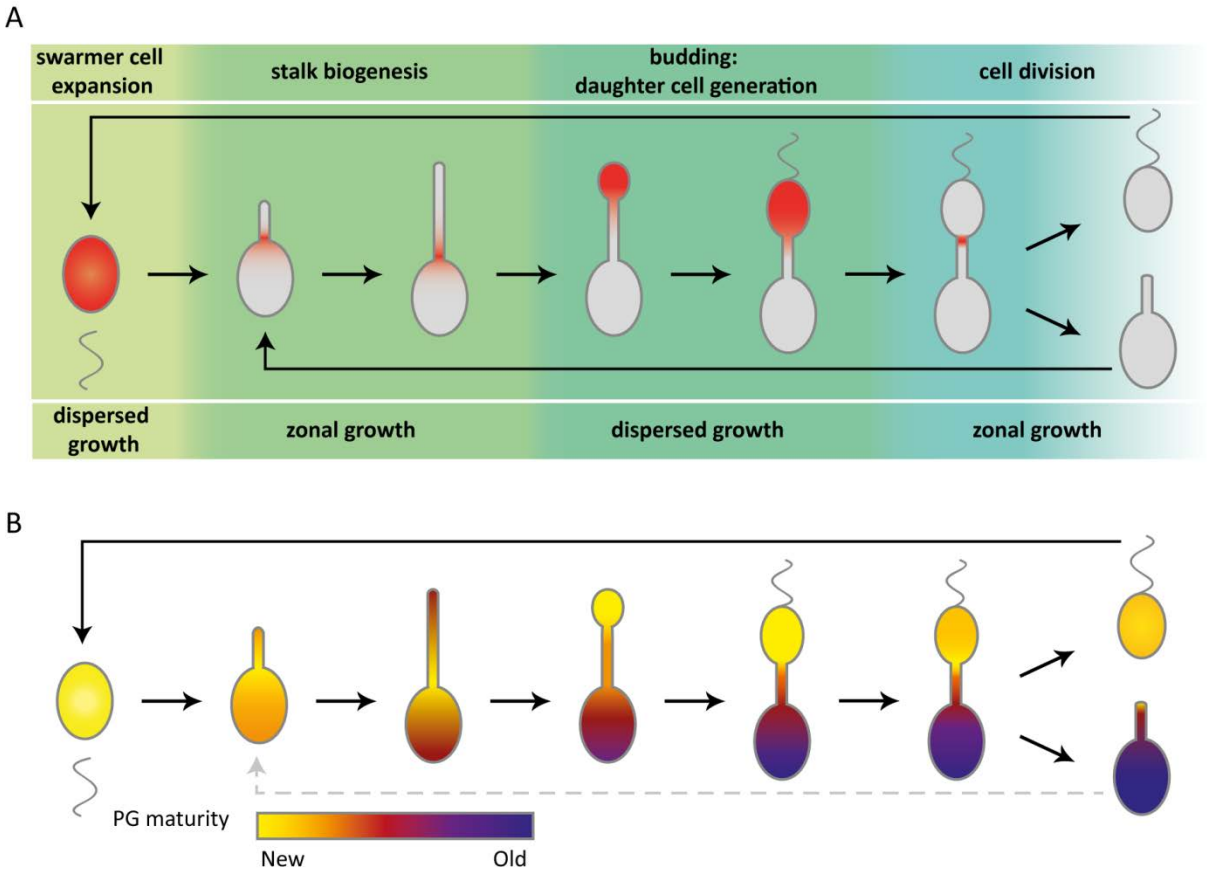

Figure 34. Cell growth is characterized by four specific growth phases in *H. neptunium*. A) In the first phase, the swarmer cells enlarge their cell body (PG incorporation is represented in red) before stalk biogenesis is initiated. In the second phase the stalk is elongated from the base of the mother cell's body. Once the stalk has reached a critical length, the new daughter cell is generated at the tip of the stalk during the third phase. In the last growth phase, the initiation of cell division between the new daughter cell and the stalk occurs. After cell division, the motile swarmer cell has to increase in size before it can further differentiate whilst the stalked mother cell reinitiates stalk biosynthesis at the stalked pole. **B)** Peptidoglycan aging in *H. neptunium* during the course of a developmental cycle. In young swarmer cells, new PG (yellow) is incorporated in a dispersed manner throughout the whole cell. As the stalk begins to develop, new PG is added at the base of the stalk. The bud is generated at the distal end of the stalk and is fully composed of new PG. In a final step, PG is added at the cell division site (the junction between the stalk and the bud) to promote constriction and subsequent cell division. Presumably, the mother cell shows minimal PG turnover after the initiation of stalk formation and thus is mainly composed of old PG (blue), which continues to age with each round of cell division (represented by dashed grey line).

3.1.1. PG biogenesis in *H. neptunium*

A striking feature of *H. neptunium* PG is that it only contains pentapeptides with a glycine at the 5th position. It is known that *C. crescentus* can incorporate glycine into its PG structure in the presence of glycine in the media, which enables nutrient-specific plasticity of the PG composition without affecting its function (391). In *H. neptunium*, the incorporation of Gly^5 could serve as a regulator for cross-linking, meaning that those stem peptides with a Gly^5 are not utilized for cross-links and thus indirectly regulate the amount of cross-linking between glycan strands. As no pentapeptides with D-Ala^5 were detected, we assume that those peptide side chains have been already utilized for cross-linking. It is highly interesting to speculate that since no pentapeptides with D-Ala^5 are detected *H. neptunium* in general would only incorporate Gly^5, although this possibility seems unlikely as all D-Ala processing enzymes (Alr, Ddl, and MurF) are present in *H. neptunium*. The overall lower abundance of pentapeptides can be explained by the high occurrence of various tetrapeptides, which are an indication of the remarkably fast PG turnover (5) in *H. neptunium*.

To determine which factors are involved in PG biosynthesis and to elucidate their role in growth and stalk biogenesis, all proteins of *H. neptunium* were screened for motifs of known cell wall remodelling enzymes. After the analysis of all known PBPs, we could confirm that as in *E. coli*, PBP2 is essential for cell elongation, and PBP3 for cell division (68). Another essential PG synthase in *H. neptunium* is PBP1A. The mixed phenotype of the other deletion mutants is due to the redundant nature of PBPs (392), which is also the case in *C. crescentus* (67). Unfortunately, the depletion of PBP2 was unsuccessful due to the leakiness of the promoter and the fact that probably only a few copies of PBP2 are required for PG synthesis (data not shown) (393).

A strong redundancy was also observed for the PG hydrolases in *H. neptunium*. With the exception of LmdC, all other hydrolases were dispensable for cell growth. The strongest phenotype was observed for the amidase AmiC, whose absence causes elongated stalks and a pronounced chaining phenotype. Our observation is comparable to those made in *E. coli*, where deletion of AmiABC also causes cell chaining (87). Amidases seem to play an eminent role in cell division rather than overall cell growth (87). The dynamic localization of many cell wall biogenesis enzymes to different growth zones (Figure 35), identified by nascent PG labelling (Figure 34), indicates that most likely a very similar set of enzymes is responsible for overall growth. Probably the same enzymes are recruited to the required growth zone and possibly activated when appropriate. The highly redundant system of PG synthases and hydrolases still requires further investigation in order to determine which family contributes chiefly to cell morphology and budding.

In *A. tumefaciens* and the related *S. meliloti* more than 50 % of all cross-links are 3,3-cross-links, which are generated by LDTs (77). It was previously observed in *A. tumefaciens* that an LDT localizes to the growing pole during unipolar growth, indicating a prominent role for LDTs in this species (78). LD-transpeptidases seem to play no relevant role in *H. neptunium* under standard conditions. The PG analysis also showed no LD-linked species. It might be that *H. neptunium* only utilizes both its LD transpeptidases under certain conditions, i.e. antibiotic stress. Recently work from our group showed that *H. neptunium* is resistant against a broad spectrum of common antibiotics (3). It will be

interesting to find out if PG alterations caused by LD-transpeptidases might prevent cell lysis under conditions of cell wall stress in *H. neptunium*.

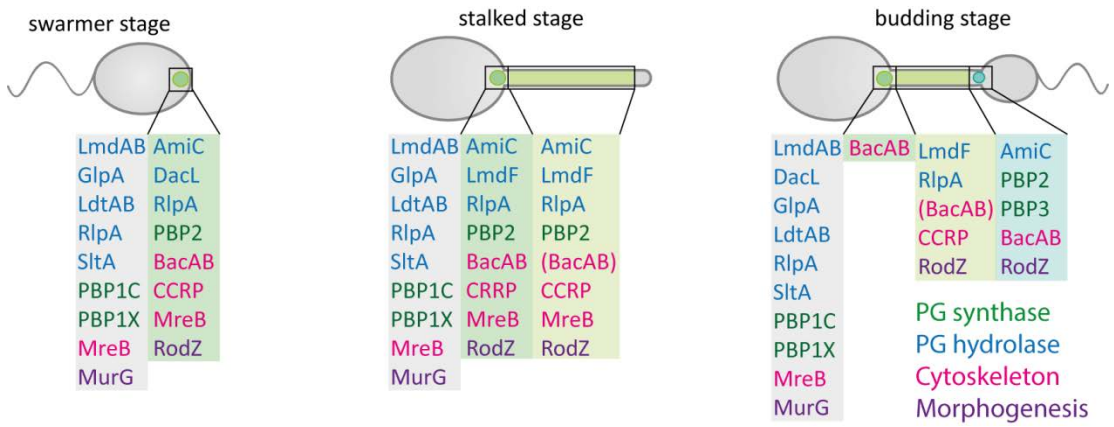

Figure 35. Localization scheme of peptidoglycan-remodelling enzymes and morphogenesis factors during the *H. neptunium* cell cycle. In swarmer cells many of the PG remodelling enzymes and cytoskeletal as well as morphological factors localize to the future stalked ("new") pole (green). In stalked cells, most proteins exhibit the same localization pattern as before, with the addition that some proteins also localize within the stalk either as distinct foci or within the complete stalk (light green). During budding a number of proteins localizes to the future division site (light blue). RodZ, BacA, and BacB can be present as multiple foci within the stalk. Certain proteins remain diffuse over the complete course of the cell cycle (grey). Proteins like DacL localize in during the swarmer stage but become diffuse once the stalk is generated. Some proteins, like MreB and RlpA, are observed to localize as distinct foci whilst exhibiting a high background fluorescence (which is considered as a diffuse localization pattern). The affiliation of the individual proteins is indicated by colour; green represents PG synthases; blue denotes PG hydrolases; pink represents cytoskeletal elements; purple specifies morpho-genesis factors. For more detail see results section.

3.1.2. MreB and its role in growth and morphology

In non-spherical bacteria, the actin homologue MreB is essential for cell shape (196). Our experiments with A22 and MP265 imply that MreB is important for growth and might influence several PG remodelling enzymes. In the case of *H. neptunium*, MreB seems to play a more vital role in cell growth, differentiation, and budding rather than merely maintenance of cell shape. Although cell width is evidently altered in the presence of the MreB inhibiting agents A22 and MP265 (Figure 21F), cell growth is only abolished at high concentrations (Figure 21C and D). Interestingly, minimal perturbation of MreB's function is enough for cells to lose their cell shape. For morphological defects to truly manifest, cells require active cell growth, which does not occur at high concentrations of either A22 or MP265. If MreB movement is truly driven by TPase activity (209-211), then PG insertion might be able to continue without accompanying MreB dynamics for a certain time. Moreover, MreB is not directly required for PBP activity (63, 296). This might explain why we still detected PG incorporation in the presence of A22 and MP265 (Figure S15). On the other hand, the *H. neptunium* MreB polymers might be less affected by A22 and MP265 than those of *C. crescentus* MreB due to the predicted minimal differences within their ATP-binding pockets (Figure S13).

Direct interaction partners still need to be determined to fully understand MreB's mode of action. The MreB construct generated for BATCH was presumably non-functional, which explains why there

was no interaction observed for MreB. Since MreB forms polymers, we would expect it to self-interact (207) and as MreB is also part of the elongasome, we would also expect MreB to interact with RodZ (388), MreC (292), and possibly MurG (300). Additionally, several other PG remodelling enzymes have a localization pattern comparable to that of MreB (Figure 35) and thus might also directly or indirectly (as known for PBP2 (296)) interact with MreB. Further interaction partners could be obtained with Co-IP experiments. Possibly super-resolution microscopy might lead the way into further understanding MreB's role in budding in *H. neptunium*. Furthermore, it is conceivable that apart from MreB and FtsZ other cytoskeletal elements that localize to the stalked pole and within the stalk, such as CCRPs and bactofilins (Figure 35), contribute to the spatiotemporal control of *H. neptunium*'s unique cell morphology.

3.2. Coiled-Coil-Rich Proteins

Coiled-coil-rich proteins (CCRPs) are referred to as intermediate filaments-like proteins (248). Recent studies have shown that CCRPs play a role in bacterial cell morphology by providing mechanical stability, for example, in *S. coelicolor*, *H. pylori*, and *C. crescentus* (151, 153, 247, 255). CCRP in *H. neptunium* localizes at the stalked pole, within the stalk, and the bud neck, and if the *ccrp* gene is deleted (Figure 23), the mutant shows a similar elongation and chaining phenotype as the *ΔamiC* deletion strain (Figure 14), but also morphological defects similar to the *ΔbacA* deletion strain (Figure 24). Consequently, the CCRP homologue in *H. neptunium*, as in to other organisms (279, 284), has a role in cell morphogenesis and possibly cell division.

It remains to be determined if the CCRP from *H. neptunium* can polymerize into filaments and form higher-order structures *in vivo* and *in vitro*. A first attempt to characterize CCRP as a new cyto-skeletal element in *H. neptunium* would be to purify the protein and analyse it for multimerisation by TEM. Since no extended fluorescent signals have been observed for CCRP in *H. neptunium*, but rather single, distinct foci, it is unlikely that CCRP would form extensive long filaments alike to crescentin in *C. crescentus* (151). If CCRP formed polymers, most likely the structure would be similar to the matrix-like network observed for DivIVA in *B. subtilis* (259) and PopZ in *C. crescentus* (154).

The yet unknown mode of action of CCRP in *H. neptunium* clearly indicates a protein level-dependent mechanism. When crescentin is overexpressed, *C. crescentus* becomes hypercurved (151). Similarly, *H. neptunium*'s cell shape becomes altered when CCRP is overproduced (data not shown). Furthermore, CCRP seems to be N-terminally processed in *H. neptunium in vivo* (Figure 23). It will be interesting to determine how CCRP and its subsequent processing influences cell morphology in *H. neptunium*.

3.3. Staying in shape with bactofilins

Bactofilins are a novel class of bacterial cytoskeletal elements that might act as a scaffold for morphology-determining processes, play a role in motility, chromosome segregation, and cell division (157, 277, 279, 280, 283). Localization experiments indicate that the two bactofilin paralogues BacA

and BacB mainly co-localize at the stalked pole and the bud neck in *H. neptunium*. By having placed both bactofilin fusion constructs under the control of their native promoters, we exclude excess production of the proteins and subsequent mislocalization due to overexpression.

To confirm that BacA is truly a cytoskeletal element that can form polymers in the absence of nucleotides, we purified BacA-His_6 by Ni-NTA affinity chromatography and visualized the untreated protein by TEM. In the electron micrographs we could see that BacA forms thin polymers with 2 nm diameter, which can bundle into larger filaments (Figure 27). It will be interesting to observe these higher-order filaments after we have enriched for them by high speed ultra-centrifugation. In summary, BacA seems to be a true cytoskeletal element in *H. neptunium*.

3.3.1. BacA as the stalk-defining bactofilin in *H. neptunium*

Deletion, complementation, and localization experiments revealed that BacA plays a prominent role in establishing cell shape, and thus BacA seems to be the major bactofilin in *H. neptunium*. The localization of BacA at the stalked pole implies a role in stalk biogenesis similar to what was previously observed in *C. crescentus* (157). Motility seems unaffected by the absence of either bactofilin, implying a different function than in *B. subtilis* (283). A role for BacA in chromosome segregation seems unlikely, since chromosome segregation and positioning is unaffected in the *ΔbacAB* deletion strain (394). In *H. neptunium* BacA also has no role in establishing cell polarity. Thus, BacA has other cellular functions than BacNOP from *M. xanthus* (277, 280). BacA seems to be vital for cell shape, similar to BacM in *M. xanthus* (279) and CcmA in *H. pylori* (284). Interestingly, BacA localizes to the future division site, similar to the bactofilin homologue in *S. oneidensis* (157). Nonetheless, cells are able to undergo division in the absence of BacA in *H. neptunium*. Thus, the analysis of BacA in *H. neptunium* once again proved that bactofilins have a broad range of species-specific functions.

To elucidate the reason for the morphological defects in the *ΔbacAB* deletion mutant, we tracked its morphological development by time-lapse microscopy. Astonishingly, newly developed stalked cells were able to undergo two to three cell divisions without any morphological impairment. The major alteration of cell shape began with the loss of the stalk as a reproductive organelle, which becomes completely remodelled into the growing bud and is not regenerated (Figure 28). Once the stalk structure is lost, cell growth is no more localized at the stalked pole but seems to occur randomly throughout the cell. Experiments with HADA confirmed that the incorporation of new PG in the *ΔbacA* deletion mutants is no longer confined to specific zones but is spread around the entire cell (Figure 29). Interestingly, the *ΔbacAB* deletion strain can divide without the use of its stalk, it merely requires narrow enough regions for the formation of a functional Z-ring, which might occur less frequently as more FtsZ has to accumulate (which might be more difficult since FtsZ is spread in a larger volume and might localize at multiple sites). This is an indication that the ancestor of *H. neptunium* divided by binary fission and that the stalk as a reproductive organelle was acquired at a later time.

Microscopic analyses have indicated a possible co-localization of both bactofilins with MreB (Figure 30). However, localization experiments in the presence of A22 indicated that bactofilins might act independently of MreB, as in the case of *C. crescentus* (157). Vice versa, the localization of MreB seems to be independent of both bactofilins. Nonetheless, we cannot exclude a potential (transient or indirect) interaction of these cytoskeletal elements at the stalked pole.

These observations led us to pursue interaction partners for BacA, to specify its intracellular function and possible role as a scaffold structure. To identify potential interaction partners of BacA, we performed co-immunoprecipitation (Co-IP) analyses. As a potential interaction partner for BacA, we found HNE0630, which is a conserved hypothetical protein with a domain of unknown function that is widely conserved among Alphaproteobacteria. Interestingly, HNE0630 lies upstream of the two LytM factor-encoding genes *lmdAB*. As attempts to delete HNE0630 have failed, we presume that it plays a vital role in *H. neptunium*. Localization of inducible N- or C-terminally tagged HNE0630 showed that it localizes at the pole opposite of the stalk in both the mother cell and the bud. Thus, the localization of HNE0630 and the bactofilins seem to exclude each other. The interaction between BacA and HNE0630 still requires further biochemical confirmation. If the interaction between these two candidates is proven to be valid, HNE0630 might act as an inhibitor of bactofilin polymer assembly at the non-stalked pole.

Since several attempts with various Co-IP protocols, Co-IP with BacA-specific antibodies, and affinity purification experiments with BacA-His_6 have not yielded any promising interaction partners, we have tried to detect potential interaction partners with BATCH. This approach has produced promising results. We could show that there is a strong interaction between BacA and BacB as well as a strong self-interaction of BacB (Figure 32A). Even though it was not possible to show a positive self-interaction of BacA (since it seems that *E. coli* has a low tolerance level for BacA), we could show that there seems to be a strong connection between BacAB and the LytM factors LmdAB (Figure 32B). These findings offer the first indication that LmdAB may be involved in stalk biogenesis and maintenance of cell shape. However, the roles of LmdAB are redundant as the *ΔlmdABF* deletion mutant has no phenotype (S. Rosskop, personal communication).

At this point it is interesting to note that BacA lies downstream of and is likely co-transcribed with the gene for the LytM factor LmdC. Intriguingly, LmdC is so far the only hydrolase in *H. neptunium* that could not be deleted. Attempts to delete *bacA* and *lmdC* simultaneously have also been fruitless. It appears that LmdC might play a crucial role in PG degradation and may interact with BacA. The genetic co-occurrence of a bactofilin gene overlapping with a LytM factor-encoding gene seems to be conserved in proteobacteria and is also present in *C. crescentus*. In the case of *H. pylori*, the bactofilin homologue *ccmA* lies directly downstream of the LytM factor-encoding genes *csd1* and *csd2*, and experimental data indicate an interplay between these proteins in establishing cell shape (105, 284). This might very well be the case for BacAB and LmdABC. However, more experimental proof is required in order to determine the roles of LmdABC and their connection to BacA in *H. neptunium*.

Still the question remains how BacA finds the future stalked pole if it is not guided by other cytoskeletal elements? Could BacA be the first protein to localize at the future stalked pole and recruit factors necessary for stalk biogenesis and budding? This notion is plausible, since previous studies in *B. subtilis* identified DivIVA as the first protein to localize at the pole of the pre-spore and thus recruit proteins necessary for chromosome incorporation into the spore (262, 263). DivIVA is targeted to the cell pole by negative membrane curvature (156, 395). On the other hand, SpoVM from *B. subtilis* is targeted to the outer membrane of the spore by positive membrane curvature (396). It is likely that BacA might be targeted to the future stalked pole by membrane curvature. We obtained a first indication for the recruitment by a geometric cue when we localized *C. crescentus* $BacA_{cc}$ to the stalked pole and the stalk of *H. neptunium*. This finding is highly interesting as in *H. neptunium* the stalk is at the new pole, whereas it emerges from the old pole in *C. crescentus*. It would also be very interesting to see whether *H. neptunium* BacA could localize to the stalked pole in *C. crescentus*. To test whether BacA can align to curved membranes, purified BacA would have to be mixed with liposomes and then analyse for attachment to the positively or negatively curved surface of the liposomes. This type of *in vitro* experiment could successfully show that DivIVA is recruited by negative membrane curvature (156). Presumably, BacA is recruited to the future stalked pole by a factor that localizes at the "new" pole, where it recognizes the unique PG structure at the site of the last cell division (397). For this to apply, the factor would have to have a special periplasmic PG-binding domain, which recognizes the PG at the "scar" of the last cell division, and a cytoplasmic part, which could interact with BacA. Future research will have to test the existence of such a protein in *H. neptunium*.

Time-lapse microscopy implies that BacA plays a dynamic part within the stalk (Figure 25A). It is of great interest to determine if BacA truly is a dynamic protein, which seems unlikely due to its nucleotide-independent polymerization and because none of the other analysed bactofilin homologues have been reported to behave dynamically. The observed dynamics of BacA possibly arise from stalk biogenesis. Since the fluorescent signal for BacA-YFP was uncommonly stable (more than 40 h during repeated imaging, data not shown), there must be a very dynamic exchange of filaments within the BacA polymer, which could be tested by fluorescence recovery after photobleaching (FRAP) experiments.

Clearly, bactofilins play a prominent role in the maintenance of cell shape in *H. neptunium*. Nonetheless, the precise mode of action of bactofilins remains mysterious. Presumably, bactofilins act as a landmark for stalk biogenesis as well as a boundary for the bud compartment. It remains to be determined if BacA acts as a scaffold for cell wall remodelling enzymes, like the LytM factors, or if BacA would limit the access of these enzymes, thereby preventing the complete remodelling of the stalk by the bud. Future research will have to focus on elucidating the mode of action by which BacA influences stalk biogenesis, stalk stability, and overall cell morphology.

3.3.2. The role of BacB

In *H. neptunium* the role of BacB seems to be quite cryptic. Just like BacA, BacB localizes to the stalked pole and the bud neck; however, the deletion of the *bacB* gene has no effect on cell

morphology or cell growth (Figure 24 and Table 18). Additionally, the protein levels of BacB are not always as high as those of BacA (Figure 25). At first glance the existence of BacB seems to be insignificant. However, the heterologous expression experiments of both bactofilins in *E. coli* have shed new light onto the possible function of BacB. Expressed on its own, BacB forms inclusion bodies, whilst BacA forms bipolar foci. Strikingly, it is only in the presence of BacB that BacA can form filament-like structures which span the long axis of the cell (Figure 27). This is in accordance with the polymerization properties of the tubulin homologues BtubA and BtubB from *Prosthecobacter*, wherein both proteins are needed to make long filaments and bundles (145, 179). A similar polymerization behaviour was observed for BacE and BacF from *B. subtilis*, wherein both proteins are required to make extensive elongated filaments (283). From purification experiments, we now that BacA can form polymers without BacB. In a BacAB co-polymer, BacB might induce conformational changes, which might enables longer filaments or enhance the mechanical stability of the polymer (273, 277).

Deletion of the *bacB* gene does not cause the same morphological changes seen for the deletion of the *bacA* gene, as most likely the BacA polymers can correctly perform their allocated function without the assistance of BacB. We only see BacA assemble into discrete foci at the stalked pole and the bud neck, so most likely long filaments are not necessary for the correct function of BacA and thus BacB is most likely not involved in generating longer BacAB polymers. More likely, BacA and BacB have distinct interaction partners, of which those of BacA play a more critical role in ensuing proper cell growth and morphology.

Although BacB on its own cannot complement the deletion defects of the *ΔbacA* and the *ΔbacAB* deletion mutants, it can nonetheless localize to the stalk-like structures formed by these mutants. Since the morphological defects of the *ΔbacAB* strain are more pronounced than that of the *ΔbacA* single mutant, this indicates that BacB must be able to fulfil some function in the absence of BacA. Possibly, low concentrations of BacB at its correct position are enough to partially co-ordinate cell wall biosynthetic enzymes and thus ensure a minimal amount of order.

3.4. Concluding remarks about cell shape and budding

In summary, this work compromises the identification and detailed analysis of factors that are required for growth and establishment of cell morphology in *H. neptunium*. Overall we can conclude that cell asymmetry and polar growth are more complex than previously thought. *H. neptunium* does not show the typical signs of polarly growing bacteria as there is no outgrowth of a new daughter cell. Instead, *H. neptunium* proliferates by polar remodelling of its stalk, which occurs in a dispersed manner, whilst stalk biogenesis is a locally restricted form of polar growth. Thus, the polar growth observed in *A. tumefaciens* and *H. neptunium* seems to be based on different molecular mechanisms, which most likely have evolved differently.

Even though basic aspects of PG remodelling seem to be conserved in *H. neptunium*, critical features, like the prominent role of bactofilins, are unique. The organization as well as the coordination of budding still remains largely unresolved. It will be an important aspect of subsequent research to

elucidate the growth complexes involved in cell growth, stalk biogenesis, and budding in *H. neptunium* and other budding bacteria. Furthermore, the exact mechanism that determines bud size in *H. neptunium* and the role MreB and bactofilins play in this process still remains to be clarified. Further studies will give insight into the growth and establishment of morphology in bacteria proliferating by alternative mechanisms of cell division.

4. Materials and Methods

4.1. Materials

4.1.1. Source of used reagents and enzymes

All chemicals used in this study were obtained from Amersham (UK), Applichem (Germany), Ambion (USA), Becton Dickinson (USA), Bioline (Germany), Carl-Roth (Germany), Difco (Spain), Fermentas (Germany), GE Healthcare (Germany), Invitrogen (Germany), Merck (Germany), PerkinElmer (USA), peqlab (USA), Promega (USA), Sigma-Aldrich (USA), Thermo Scientific (USA) and Qiagen (Germany).

All enzymes were obtained from New England Biolabs (NEB, USA) or Fermentas (Canada). KOD Hot Start Polymerase (Merck, Germany) or BioMix™Red (Bioline, Germany) were used for PCR reactions. Specific chemicals are detailed in the text.

4.1.2. Buffers and solutions

Standard buffers and solutions were prepared as described by Ausubel (398) and Sambrook (399). Special buffers and solutions are listed in the respective method section. All buffers were prepared with de-ionized water (Purelab Ultra water purification system, Elga).

4.1.3. Media

All media were autoclaved at 120 °C for 20 min at 2 bar. For solid media, 1.5% (w/v) agar was added to the medium prior to autoclaving. To dissolve essential components MB media was boiled for 1 min prior to autoclaving and filter-sterilized using bottle top filters (Sarstedt, Germany, pore size 0.2 µm). Media additives such as antibiotics, heavy-metals and carbohydrates were filter-sterilized (Sarstedt, Germany, pore size 0.22 µm) and added to the medium (~ 60 °C) after autoclaving. The concentration of respective additives is listed in Table 2 and Table 3.

MB (Marine Broth, Difco™, USA)
0.5 % (w/v) Bacto™Peptone
0.1 % (w/v) Bacto™Yeast extract
0.4 mM Fe(III) citrate
333 mM NaCl
62 mM $MgCl_2$
27 mM $MgSO_4$
16 mM $CaCl_2$
7.4 mM KCl
1.9 mM Na_2CO_3
672 µM KBr
215 µM $SrCl_2$
356 µM H_3BO_3
33 µM Na_2SiO_3
57 µM NaF
20 µM $(NH_4)NO_3$
56 µM Na_2HPO_4

PYE (peptone-yeast-extract)
0.2 % (w/v) Bacto™Peptone
0.1 % (w/v) Yeast extract
1 mM $MgSO_4$
0.5 mM $CaCl_2$

LB (Luria-Bertani, Miller)
1.0 % (w/v) Tryptone
0.5 % (w/v) Yeast extract
1.0 % (w/v) NaCl

SB (Super Broth)
3.5% (w/v) Tryptone
2% (w/v) yeast extract
0.5% (w/v) NaCl

Table 2. Used antibiotics

Antibiotic	Stock solution (mg/mL)	Final concentration (µg/mL)			
		E. coli liquid	*E. coli* solid	*H. neptunium* liquid	*H. neptunium* solid
Ampicillin	100	200	200	-	-
Chloramphenicol	10	20	30	-	-
Gentamicin	1	15	20	-	-
Kanamycin	20	30	50	100	200
Rifampicin	10/0.5	25	50	1	2
Streptomycin	10	30	30	-	-

Table 3. Used additives

carbohydrates	stock concentration	final concentration
A22	37 mM	37 µM
Copper sulfate	20 mM	300 µM
Glucose	40 % (w/v)	0.5 % (w/v)
IPTG	1 M	0.5 mM
MP265	50 mM	250 µM
Sucrose	-	3 % (w/v)
Xgal	10 mg/mL	80 µg/mL
Zinc sulfate	1 M	500 µM

4.1.4. Oligonucleotides and plasmids

Oligonucleotides for molecular cloning were designed using GeneTool Lite 1.0 (BioTools Inc., Canada) as well as Vector NTI Advance™ 11 (Invitrogen, Germany) and synthesized by either Eurofins MWG Operon (Germany) or SIGMA-Aldrich (Germany). A complete list of oligonucleotides (Table 25, Table 26 and Table 27) and plasmids (Table 22, Table 23 and Table 24) used in this study can be found in the appendix.

4.2. Microbiological and cell biological methods

4.2.1. Cultivation of *E. coli*

E. coli was cultivated either in liquid LB or SB medium (shaking at 210 rpm) or on LB agar plates at 37°C. When *E. coli* was under selection, liquid and solid media were supplemented with the required antibiotics (Table 2) and other additives (Table 3).

When testing for protein-protein interactions, *E. coli* BTH101 derivatives were grown at 28 °C on MacConkey agar plates supplemented with 50 µg/mL kanamycin, 200 µg/mL ampicillin, and 30 µg/mL streptomycin or on LB agar plates supplemented with 80 µg/mL Xgal, 50 µg/mL kanamycin, 200 µg/mL ampicillin, 30 µg/mL Streptomycin, and 250 µM IPTG.

4.2.2. Cultivation of *H. neptunium*

H. neptunium was cultivated either in liquid MB medium in baffled flasks (shaking at 180 rpm) or on MB agar plates at 28 °C. When *H. neptunium* was under selection, liquid and solid media were supplemented with the required antibiotics (Table 2) and other additives (Table 3).

4.2.3. Cultivation of *C. crescentus*

C. crescentus was cultivated either in liquid PYE (shaking at 210 rpm) or on PYE agar plates at 28 °C.

4.2.4. Storage of bacteria

For long-term storage, bacterial overnight cultures were supplemented with 10 % (v/v) DMSO (dimethyl sulfoxide) and stored at -80 °C.

4.2.5. Determination of cell densities

The optical density (OD_{600}) of a bacterial culture was determined photometrically using an Ultrospec™ 10 Cell Density Meter (GE Healthcare, Germany) at a wavelength of 600 nm. The corresponding culture medium was used as a blank.

4.2.6. Growth curves

H. neptunium strains were grown in MB to exponential/stationary phase for 2 days, diluted 1:10, and cultivated further overnight. The main cultures were inoculated to an OD_{600} of 0.01 in a 24-well plate (Becton Dickinson Labware, USA), incubated at 28 °C shaking while cell growth was monitored at OD_{580} for 31 h every 15 min using a Tecan infinity M200Pro plate reader (Tecan Group Ltd., Switzerland). Growth rates were calculated using a modified solver spreadsheet.

4.2.7. Biofilm assay

The biofilm assay is based on the staining of extracellular polysaccharides with crystal violet as previously described by Strepanović (400). Immediately after the completion of a growth experiment as described above, each well of the culture plate was incubated with 70 µL of 0.5 % (w/v) crystal

violet (Roth, Germany) solution for 5 min at RT. The wells were washed twice with 1 mL dd H_2O for 10 min. The supernatant was carefully extracted via suction, so as not to disturb the biofilm. To determine biofilm formation, the wells were incubated with 1 mL 100 % ethanol for 5 min to release bound crystal violet, which was subsequently measured at a wavelength of 580 nm using the Tecan infinity M200Pro plate reader (Tecan Group Ltd., Switzerland).

4.2.8. Synchronization

For the synchronization (selective enrichment of small swarmer cells by filtration) of *H. neptunium*, a protocol previously reported (353, 401) was adapted and further developed by W. Strobel (402).

H. neptunium was grown in 10 mL MB in a 100 mL baffled flask at 28 °C until the culture reached stationary phase (2 days). On the morning before the day of the synchronization, 300 mL MB in a 1000 mL baffled flask were inoculated from the pre-culture such as to achieve an OD_{600} of 0.6 at the desired starting point of the synchronization procedure the next day. Before synchronization, all equipment and solutions were pre-cooled to 4 °C. Once the culture had reached the desired OD_{600} of 0.6, the cells were continuously kept on ice during the whole synchronization procedure. If the OD_{600} of the culture was above 0.6 the culture was diluted accordingly with MB and incubated at least two more hours until the culture reached an OD_{600} of 0.6. Once the culture reached an OD_{600} of 0.6, it was transferred into a pre-cooled GS-3 centrifuge tube and centrifuged for 15 min with 3,000 x g and 4 °C in a Sorvall GS-3 rotor. After centrifugation the supernatant was discarded. The cell pellet was gently resuspended in 100 mL ice-cold 1x phosphate buffered saline (PBS) (137 mM NaCl, 2.7mM KCl, 10 mM Na_2HPO_4, 2 mM KH_2PO_4). The cells were filtered through a 1.2 µm pore size filter membrane (Millipore) in 50 mL steps using a 90 mm filtration unit (Millipore). The filtrate was collected in a 1 L pre-cooled filtering flask. The cells were filtered a second time through a 0.8 µm pore size filter membrane (Millipore) using a 45 mm filtration unit (Millipore). The filtrate was collected in a 250 mL pre-cooled filtering flask. The swarmer cells were transferred into a pre-cooled Sorvall GS-3 tube and pelleted by centrifugation for 15 min with 3,000 x g and 4 °C in a Sorvall GS-3 rotor. After centrifugation, the supernatant was discarded and the swarmer cells were resuspended in 20 mL pre-warmed MB. The OD_{600} of the cells was adjusted to 0.3-0.4 by addition of MB. The cells were transferred into a 250 mL baffled flask. At selected time points the cells were visualized under the microscope on 1 % agarose pads. To determine the efficiency of the synchronization, between 120-210 cells were counted and sorted into the three different cell categories: swarmer cells, stalked cells and budding cells.

A maxi-synchronization was achieved by tripling the initial volume of the culture. In this case, all other volumes were adjusted accordingly.

Small filtration equipment:	1x vacuum filtering flask 250 mL
(Millipore, Germany)	1x silicone stopper with a fritted base
	1x aluminium spring clamp
	1x glass funnel 250 mL
	0.8 µm nitrocellulose membranes, 47 mm diameter

Large filtration equipment: (Millipore, Germany)	1x vacuum base (1 L) and cap, 90 mm diameter 1x stainless steel screen, PTFE-coated, 90 mm diameter 1x gasket, PTFE 1x spring clamp, anodized aluminium 1x funnel, 1 L, 90 mm diameter, ground glass seal 1.2 µm nitrocellulose membranes, 90 mm diameter

4.3. Microscopic methods

The quality of a bacterial culture was assessed with a Axiostar plus (Zeiss, Germany) equipped with a Plan-Apochromat 100x/1.25 oil Ph3 objective (Zeiss, Germany). Mid-exponentially growing cells were imaged with a Zeiss Observer.Z1 (Zeiss, Germany). Differential interference contrast (DIC) images were acquired using a Plan-Apochromat 100x/1.46 oil DIC objective (Zeiss, Germany). Phase contrast (Ph3) images were obtained with a Plan-Apochromat 100x/1.40 oil Ph3 M27 objective (Zeiss, Germany). Fluorescence images were taken with an X-Cite® 120PC metal halide light source (EXFO, Canada) in combination with ET-DAPI (also for HADA), ET-CFP (CFP), ET-YFP (eYFP), or ET-TexasRed (mCherry) filter sets (Chroma, USA). When appropriate immersion oil (Immersol® 518F, Zeiss, Germany) was used. Images were processed with MetaMorph® 7.7.0.0 (Universal Imaging Group) and Adobe® Illustrator® CS5® (USA). Cell length measurements were made by utilizing the MetaMorph® region measurement function.

The synthesis of inducible fluorescent protein fusion proteins was activated in *H. neptunium* and *E. coli* by the addition of the appropriate inducer (Table 3). Depending on the construct, cells were induced between 1-24 h before imaging.

4.3.1. Nucleoid staining

Mid-exponentially growing *H. neptunium* and *E. coli* cells were incubated with 1.5 µg/mL DAPI (4', 6-diamidino-2-phenylindole) for 15 min at RT in the dark.

4.3.2. Labelling peptidoglycan of live bacteria through fluorescent D-amino acids (FDAAs)

250 µL of mid-exponentially growing *H. neptunium* cells were mixed with 1.25 µL 100 mM HADA (hydroxy coumarin-carbonyl-amino-D-alanine) and incubated shaking (180 rpm) for 9 min at 28 °C, after which 100 % ice-cold ethanol was added to a concentration of 35 %. Cells were incubated for 20 min on ice in the dark, washed thrice with 1x PBS (137 mM NaCl, 2.7 mM KCl, 10 mM Na_2HPO_4, 2 mM KH_2PO_4) (centrifugation for 2 min at 9,000 rpm), and resuspended in 100 µL 1x PBS prior to imaging.

4.3.3. Time-lapse microscopy on pads

To monitor the spatiotemporal localization dynamics of fluorescent protein fusions, early exponential cells were immobilized on 1 % MB agar pads. The cover-slide was sealed with VLAP (vaseline, lanolin

and paraffin at a 1:1:1 ratio) to protected the cells from dehydration. Images were taken at the indicated time points.

4.3.4. Time-lapse microscopy in the microfluidic system

Microfluidic experiments were carried out using B04A microfluidic plates (Millipore) with a F84 manifold coupled to an ONIX EV262 Microfluidic System (CellASIC, USA). Before usage, the chamber was washed with PBS buffer for at least 30 min. Early exponential cells were loaded according to the manufacturer's instructions and kept under constant medium flow (0.4 µl/h). Images were taken at the indicated time points.

4.3.5. Transmission electron microscopy

Electron micrographs of purified BacA-His_6 were taken in collaboration with Dr. A. Klingl (at the Dept. of Biology, FB17, Philipps University and *LOEWE Center for Synthetic Microbiology*, Germany). Prior to sample preparation, thawed purified BacA-His_6 was dialyzed against low-salt buffer (50 mM HEPES, pH 7.2, 10 mM NaCl, 5 mM $MgCl_2$, 0.1 mM EDTA, 1 mM ß-mercaptoethanol) for at least 16 h. The protein was spotted onto carbon-coated grids and allowed to settle for 2 min. The grids were blotted dry, stained with 1:2 diluted supernatant of saturated 2 % uranyl acetate (in H_20) for 1 min, dried and imaged using a Zeiss CEM902 electron microscope, operated at 80 kV and equipped with a 2048x2048 pixel CCD camera. Image processing was carried out using Adobe® Photoshop® CS2 and Adobe® Illustrator® CS5 (Adobe Systems).

4.4. Molecular biology methods

4.4.1. Isolation of microbial DNA

Plasmid DNA from *E. coli* was isolated using GenElute™ Plasmid Kit (SIGMA-Aldrich, Germany) following the manufacturer's instructions. Chromosomal DNA from *H. neptunium* and *C. crescentus* was obtained using the illustra™ bacteria genomicPrep Mini Spin Kit (GE Healthcare, Germany) according to the manufacturer's instructions.

4.4.2. DNA sequencing

DNA sequencing was performed by Eurofins MWG Operon (Germany). In general, 50-100 ng of DNA products were provided along with suitable oligonucleotides. Sequencing results were analysed using Vector NTI Advance™ 11 (Invitrogen, Germany), GeneTool Lite 1.0 (BioTools, Canada) and SnapGene® 2.8.1 (GSL Biotech LL, USA).

4.4.3. Polymerase Chain Reaction (PCR)

To amplify template DNA for subsequent cloning, KOD Hot Start DNA Polymerase (Merck, Germany) was used. All components (Table 4) were combined and the respective PCR programme (Table 5 and Table 6) was applied using a BioRad C1000™ thermal cycler. PCR amplicons were purified using the PCR Clean Up Kit (Sigma, USA).

Table 4. KOD Polymerase standard reaction mix

Component	Volume
10x KOD Hot Start Polymerase buffer	5 µL
dNTPs (2 mM each)	5 µL
25 mM MgSO4	2 µL
DMSO	2.5 µL
forward primer (100 µM)	0.25 µL
reverse primer (100 µM)	0.25 µL
KOD Hot Start DNA Polymerase (1U/µl)	1 µL
template DNA (genomic) (23 ng/µL)	1 µL
H_2O	33 µL

Table 5. KOD Polymerase standard reaction cycle

Step	Temperature	Duration
1. Initial denaturation	94°C	2 min
2. Denaturation	94 °C	0.5 min
3. Primer annealing	depending on primer 60-65°C	0.5 min
4. Elongation	72°C	1 min per 1 kb
Repetition of steps 2-4 for 25-30 cycles		
5. Final elongation	72 °C	5 min
6. Pause	4 °C	∞

Table 6. KOD Polymerase extension overlap reaction cycle

Step	Temperature	Duration
1. Initial denaturation	94°C	2 min
2. Denaturation	94 °C	0.55 min
3. Primer annealing	depending on primer 60-65°C	0.7 min
4. Elongation	72°C	1 min per 1 kb
Repetition of steps 2-4 for 25-30 cycles		
5. Final elongation	72 °C	10 min
6. Pause	4 °C	∞

Correct plasmid uptake by *E. coli* or correct DNA integration into *H. neptunium* was confirmed by colony PCR using the BioMix Red™ reaction mix (Table 7) and respective reaction cycle (Table 9) in a BioRad C1000TM thermal cycler. Prior to colony PCR, *H. neptunium* cells were resuspended in 50 µL H_2O, lysed at 95 °C for 10 minutes, centrifuged and 2 µL of the supernatant were used as template for a colony PCR reaction. In case product amplification failed with KOD polymerase, BioMix Red was used to amplify DNA fragments for cloning (Table 8).

Table 7. BioMix Red™ standard reaction mix for colony PCR

Component	Volume	
	E. coli	*H. neptunium*
BioMix Red™ (Bioline, Germany)	5 µL	5 µL
DMSO	0.5 µL	0.5 µL
forward primer (100 µM)	0.05 µL	0.05 µL
reverse primer (100 µM)	0.05 µL	0.05 µL
template	colony	2 µL
H_2O	4.4 µL	2.4 µL

Table 8. BioMix Red™ standard reaction mix for product amplification

Component	Volume
BioMix Red™ (Bioline, Germany)	25 µL
DMSO	2.5 µL
forward primer (100 µM)	0.25 µL
reverse primer (100 µM)	0.25 µL
template	0.5-1.0 µL
H_2O	ad 50 µL

Table 9. BioMix Red™ standard reaction cycle for cloning

Step	Temperature	Duration
1. Initial denaturation	95 °C	2 min
2. Denaturation	95 °C	2 min
3. Primer annealing	depending on primer 60-65°C	0.5 min
4. Elongation	72 °C	0.5 min per 1 kb
Repetition of steps 2-4 for 30-35 cycles		
5. Final elongation	72 °C	4 min
6. Pause	4 °C	∞

4.4.4. Restriction digestion (also blunt ending and PNK) and ligation of DNA fragments

The digestion of DNA was performed as suggested by the manufacturer (Table 10) using the recommended buffer (NEB, USA). Samples were incubated at 37 °C for 2 h or overnight. FastDigest™ was performed as suggested by the manufacturer (Table 11), whereby samples were incubated for 30 min to 2 h at 37 °C. After the restriction digest, the samples were purified using the PCR Clean-up Kit (Sigma, USA).

Table 10. Restriction digest standard reaction mix

Component	Digestion of vector DNA	Digestion of insert
10 x buffer (NEB, USA)	10 µL	50 µL
10 mg/mL BSA (NEB, USA)	1 µL	1 µL
template DNA	10 µL	50 µL
restriction enzyme(s) (10 U/µL)	0.5-1.5 µL each	0.5-1.5 µL each
SAP (1 U/µL) (Fermentas, Canada)	1 µL	-
De-ionized water	ad 100 µL	ad 100 µL

Table 11. Restriction digest FastDigest™ reaction mix

Component	Digestion of vector DNA	Digestion of insert
10 x buffer (Fermentas, Canada)	5 µL	10 µL
template DNA	10 µL	50 µL
restriction enzyme(s) (10 U/µL)	1 µL each	1 µL each
SAP (1 U/µL) (Fermentas, Canada)	1 µL	-
De-ionized water	ad 50 µL	ad 100 µL

The blunting ending of plasmids and PCR products was performed using T4 DNA polymerase (Thermo Scientific, USA) as suggested by the manufacturer (Table 12) for 5 min at RT. The reaction was purified using the PCR Clean-up Kit (Sigma, USA).

Table 12. Blunting of 5‘- or 3‘-overhang standard reaction mix

Component	Volume
5x reaction buffer (Thermo Scientific, USA)	4 µL
linear dsDNA or PCR product	2-10 µL
dNTP Mix (2 mM)	2 µL
T4 DNA polymerase (Thermo Scientific, USA)	1 µL
De-ionized water	ad 20 µL

The phosphorylation of PCR products was performed using T4 polynucleotide kinase (Fermentas, Canada) as suggested by the manufacturer (Table 13) at 37 °C for 20 min. The reaction was purified using the PCR Clean-up Kit (Sigma, USA).

Table 13. Phosphorylation standard reaction mix concentration

Component	Volume
10x T4 polynucleotide kinase buffer A (Fermentas, Canada)	2 µL
linear dsDNA (1-20 pmol) or oligonucleotide (10-50 pmol)	2-10 µL
ATP (10 mM)	2 µL
T4 polynucleotide kinase (Fermentas, Canada)	1 µL
De-ionized water	ad 20 µL

T4 DNA Ligase (Fermentas, Canada) was used following the manufacturer's instructions (Table 14). Reactions were performed for 20 min up to 2 h at RT or overnight at 4 °C.

Table 14. Ligation standard reaction mixture

Component	Volume
5x Rapid Ligation Buffer (Fermentas, Canada)	4 µL
Plasmid DNA	50 ng
Insert DNA	2x molecule number of vector
T4 DNA Ligase (5 U/µL) (Fermentas, Canada)	1 µL
De-ionized water	ad 20 µL

4.4.5. Agarose gel electrophoresis

To separate DNA fragments according to their size, 1 % (w/v) agarose gels were prepared. Agarose was dissolved in 0.5 x TAE buffer (20 mM Tris/HCl, pH 8, 0.175 % acetic acid, 0.5 mM EDTA, pH 8) and ethidium bromide was added to a final concentration of 0.005 %. After solidification, gels were submerged in 0.5 x TAE running buffer and run at a constant voltage of 160 V. The GeneRuler™ 1 kb ladder (Fermentas, Canada) was used as a size standard. PCR products, generated using BioMix Red™, were loaded directly onto the agarose gel. Other DNA samples were mixed prior to loading with 6 x DNA loading dye (Fermentas, Canada). DNA fragments were visualized with UV-light using a UV-Transilluminator (UVP-BioDoc-IT™ Imaging System, UniEquip, Germany). DNA products of interest were excised and purified using the GenElute™ Gel Extraction Kit (SIGMA-Aldrich, Germany).

4.4.6. Plasmid construction

Plasmids were designed *in silico* using either Vector NTI Advance™ 11 (Invitrogen, Germany) or SnapGene® 2.8.1 (GSL Biotech LL, USA). A complete list of all generated plasmids can be found in Table 23 and Table 24 in the Appendix section.

4.4.6.4. Plasmid for the expression of N- and C- terminal fusion in *H. neptunium*

To generate fusion proteins with either N- or C-terminal fusions to mCherry, Venus or YFP expressed under the control of P_{Cu} or P_{Zn}.

pEC48 was constructed by amplification of *mreB* from LE670 chromosomal DNA using oligos oE123 and oEC124, digestion of the PCR product with KpnI and NheI, and ligation of the fragment with pNPTS138 cut with KpnI and NheI.

pEC59 was constructed by amplification of *bacB* from LE670 chromosomal DNA using oligos SW186 and oEC151, digestion of the PCR product with NdeI and KpnI, and ligation of the fragment with pZVENC-2 cut with NdeI and KpnI.

pEC70 was constructed by amplification of *bacB* from LE670 chromosomal DNA using oligos SW186 and oEC151, digestion of the PCR product with NdeI and KpnI, and ligation of the fragment with pCCHYC-3 cut with NdeI and KpnI.

pEC80 was constructed by amplification of $bacA_{CC}$ from CBN15 chromosomal DNA using oligos MT743 and MT744, digestion of the PCR product with NdeI and SacI, and ligation of the fragment with pZVENC-2 cut with NdeI and SacI.

pEC91 was constructed by amplification of HNE0630 from LE670 chromosomal DNA using oligos oEC191 and oEC192, digestion of the PCR product with NdeI and KpnI, and ligation of the fragment with pCCHYC-3 cut with NdeI and KpnI.

pEC92 was constructed by amplification of HNE0630 from LE670 chromosomal DNA using oligos oEC193 and oEC194, digestion of the PCR product with NdeI and KpnI, and ligation of the fragment with pCCHYN-3 cut with NdeI and KpnI.

pEC94 was constructed by amplification of *bacB* from LE670 chromosomal DNA using oligos SW186 and oEC151, digestion of the PCR product with NdeI and KpnI, and ligation of the fragment with pCCHYC-3 cut with NdeI and KpnI.

pEC115 was constructed by amplification of *amiC* from LE670 chromosomal DNA using oligos oEC157 and SS271, digestion of the PCR product with NdeI and KpnI, and ligation of the fragment with pCCHYC-2 cut with NdeI and KpnI.

4.4.6.5. Plasmids for the construction of markerless deletions or insertions in *H. neptunium*

pEC22 was constructed by amplifying the flanking regions of *pbp1X* from LE670 chromosomal DNA using oligos oEC33 and oEC34 (upstream) and oEC35 and oEC36 (downstream). The upstream fragment was digested with PstI and HindIII, the downstream fragment with HindIII and NheI. The fragments were ligated with pNPTS138 cut with PstI and NheI.

pEC23 was constructed by amplifying the flanking regions of *pbp1A* from LE670 chromosomal DNA using oligos oEC37 and oEC38 (upstream) and oEC38 and oEC40 (downstream). The upstream fragment was digested with PstI and HindIII, the downstream fragment with HindIII and NheI. The fragments were ligated with pNPTS138 cut with PstI and NheI.

pEC25 was constructed by amplifying the flanking regions of *pbp1A* from LE670 chromosomal DNA using oligos oEC45 and oEC46 (upstream) and oEC47 and oEC48 (downstream). The upstream fragment was digested with EcoRI and HindIII, the downstream fragment with HindIII and NheI. The fragments were ligated with pNPTS138 cut with EcoRI and NheI.

pEC26 was constructed by amplifying the flanking regions of *pbp1C* from LE670 chromosomal DNA using oligos oEC49 and oEC50 (upstream) and oEC51 and oEC52 (downstream). The upstream frag-

ment was digested with EcoRI and HindIII, downstream fragment with HindIII and NheI. The fragments were ligated with pNPTS138 cut with EcoRI and NheI.

pEC28 was constructed by amplifying the flanking regions of *sltA* from LE670 chromosomal DNA using oligos oEC55 and oEC56 (upstream) and oEC57 and oEC58 (downstream). The upstream fragment was digested with HindIII and NheI, downstream fragment with NheI and EcoRI. The fragments were ligated with pNPTS138 cut with HindIII and EcoRI.

pEC29 was constructed by amplifying the flanking regions of *bacB* from LE670 chromosomal DNA using oligos oEC67 and oEC68 (upstream) and oEC69 and oEC70 (downstream). The upstream fragment was digested with EcoRI and HindIII, downstream fragment with HindIII and NheI. The fragments were ligated with pNPTS138 cut with EcoRI and NheI.

pEC31 was constructed by amplifying the flanking regions of *lmdC* from LE670 chromosomal DNA using oligos oEC80 and oEC81 (upstream) and oEC82 and oEC83 (downstream). The upstream fragment was digested with HindIII and EcoRI, the downstream fragment with EcoRI and NheI. The fragments were ligated with pNPTS138 cut with HindIII and NheI.

pEC32 was constructed by amplifying the flanking regions of *bacA* from LE670 chromosomal DNA using oligos oEC41 and oEC79 (upstream) and oEC43 and oEC44 (downstream). The upstream fragment was digested with BamHI and HindIII, the downstream fragment with BamHI and NheI. The fragments were ligated with pNPTS138 cut with HindIII and NheI.

pEC34 was constructed by amplifying the flanking regions of *lmdA* from LE670 chromosomal DNA using oligos oEC84 and oEC85 (upstream) and oEC86 and oEC87 (downstream). The upstream fragment was digested with BamHI and HindIII, the downstream fragment with BamHI and NheI. The fragments were ligated with pNPTS138 cut with HindIII and NheI.

pEC35 was constructed by amplifying the flanking regions of *lmdB* from LE670 chromosomal DNA using oligos oEC88 and oEC89 (upstream) and oEC90 and oEC91 (downstream). The upstream fragment was digested with PstI and HindIII, downstream fragment with HindIII and NheI. The fragments were ligated with pNPTS138 cut with PstI and NheI.

pEC37 was constructed by amplifying the flanking regions of *mreB* from LE670 chromosomal DNA using oligos oEC104 and oEC105 (upstream) and oEC106 and oEC107 (downstream). The upstream fragment was digested with PstI and HindIII, the downstream fragment with HindIII and NheI. The fragments were ligated with pNPTS138 cut with PstI and NheI.

pEC38 was constructed by amplifying the flanking regions of *lmdD* from LE670 chromosomal DNA using oligos oEC92 and oEC93 (upstream) and oEC94 and oEC95 (downstream). The upstream fragment was digested with PstI and HindIII, the downstream fragment with HindIII and NheI. The fragments were ligated with pNPTS138 cut with PstI and NheI.

pEC39 was constructed by amplifying the flanking regions of *lmdE* from LE670 chromosomal DNA using oligos oEC96 and oEC97 (upstream) and oEC98 and oEC99. The upstream fragment was digested with EcoRI and HindIII, downstream fragment with HindIII and NheI. The fragments were ligated with pNPTS138 cut with EcoRI and NheI.

pEC62 was constructed by amplifying *bacA-HA* from LE670 chromosomal DNA using oligos oEC160 and oEC161 and digested with KpnI and NheI before ligation with pNPTS138 cut with KpnI and NheI.

pEC64 was constructed by amplifying the flanking regions of *dacL* from LE670 chromosomal DNA using oligos oEC137 and oEC138 (upstream) and oEC139 and oEC140 (downstream). The upstream fragment was digested with PstI and EcoRI, the downstream fragment with EcoRI and NheI. The fragments were ligated with pNPTS138 cut with PstI and NheI.

pEC65 was constructed by amplifying the flanking regions of *lmdA* from LE670 chromosomal DNA using oligos oEC295 and oEC142 (upstream) and oEC143 and oEC296 (downstream). The upstream fragment was digested with HindIII and EcoRI, the downstream fragment with EcoRI and NheI. The fragments were ligated with pNPTS138 cut with HindIII and NheI.

pEC74 was constructed by amplifying two fragments for extension overlap PCR using oligos oEC160 and oEC179 (template pSW56) and oEC178 and oEC44 (LE670 chromosomal DNA). Both fragments were used as templates for extension-overlap PCR to generate a *bacA-yfp-downstream* fragment using oligos oEC160 and oEC44. The amplicon was digested with HindIII and NheI and ligated with pNPTS138 cut with HindIII and NheI.

pEC75 was constructed by amplifying two fragments for extension overlap PCR using oligos oEC171 and oEC181 (template pEC59) and oEC180 and oEC67 (LE670 chromosomal DNA). Both fragments were used as templates for extension-overlap PCR to generate a *bacB-venus-downstream* fragment using oligos oEC171 and oEC67. A new *bacB-venus-downstream* fragment was generated using oligos oEC228 and oEC229. The amplicon was digested with HindIII and NheI and ligated with pNPTS138 cut with HindIII and NheI.

pEC76 was constructed by amplifying two fragments for extension overlap PCR using oligos oEC171 and oEC181 (template pEC94) and oEC180 and oEC67 (LE670 chromosomal DNA). Both fragments were used as templates for extension-overlap PCR to generate a *bacB-mCherry-downstream* fragment using oligos oEC171 and oEC67. A new *bacB-mCherry-downstream* fragment was generated using oligos oEC228 and oEC229. The amplicon was digested with HindIII and NheI and ligated with pNPTS138 cut with HindIII and NheI.

pEC87 was constructed by amplifying three fragments for extension overlap PCR using oligos oEC182 and oEC184 (template pEC48), oEC183 and oEC186 (template pCCHYC-2), oEC185 and oEC124 (template pEC48). All three fragments were used as templates for extension-overlap PCR to generate an *mreB-mCherry-mreB* fragment using oligos oEC182 and oEC124. The amplicon was digested with HindIII and NheI and ligated with pNPTS138 cut with HindIII and NheI.

pEC93 was constructed by amplifying the flanking regions of HNE0630 from LE670 chromosomal DNA using oligos oEC195 and oEC195 (upstream) and oEC296 and oEC297 (downstream). The upstream fragment was digested with HindIII and BamHI, the downstream fragment with BamHI and NheI. The fragments were ligated with pNPTS138 cut with HindIII and NheI.

pEC106 was constructed by amplifying the flanking regions of *ccrp* for extension overlap PCR from LE670 chromosomal DNA using oligos oEC222 and oEC223 (upstream) and oEC224 and oEC225 (downstream). Both fragments were used as templates for extension-overlap PCR with oligos oEC222 and oEC225. The fragment was digested with HindIII and NheI and ligated with pNPTS138 cut with HindIII and NheI.

pEC126 was constructed by amplifying the flanking regions of *lmdF* from LE670 chromosomal DNA using oligos oEC289 and oEC290 (upstream) and oEC291 and oEC292 (downstream). The upstream fragment was digested with HindIII and BamHI, the downstream fragment with BamHI and NheI. The fragments were ligated with pNPTS138 cut with HindIII and NheI.

pEC128 was constructed by amplifying three fragments for extension overlap PCR using oligos oEC260 and oEC261 (template LE670 chrom. DNA), oEC262 and oEC263 (template pCYFPN-2), and oEC264 and oEC265 (template LE670 chrom. DNA). All three fragments were used as templates for extension-overlap PCR to generate an *upstream-yfp-murG* fragment using oligos oEC260 and oEC265. The amplicon was digested with HindIII and NheI and ligated with pNPTS138 cut with HindIII and NheI.

pEC129 was constructed by amplifying three fragments for extension overlap PCR using oligos oEC244 and oEC245 (template LE670 chrom. DNA), oEC246 and oEC247 (template pCYFPC-2), and oEC248 and oEC249 (template LE670 chrom. DNA). All three fragments were used as templates for extension-overlap PCR to generate an *upstream-yfp-rodZ* fragment using oligos oEC244 and oEC249. The amplicon was digested with HindIII and NheI and ligated with pNPTS138 cut with HindIII and NheI.

pEC157 was constructed by amplifying the flanking regions of *mltA* from LE670 chromosomal DNA using oligos oEC313 and oEC314 (upstream) and oEC315 and oEC316 (downstream). The upstream fragment was digested with HindIII and BamHI, the downstream fragment with BamHI and NheI. The fragments were ligated with pNPTS138 cut with HindIII and NheI.

pEC172 was constructed by amplifying the upstream flanking region of *rlpA* from LE670 chromosomal DNA using oligos oEC326 and oEC327. The template for the downstream region was amplified from LE670 chromosomal DNA using oligos oEC326 and oE331, which was used as a template to amplify the downstream flank using oligos oEC328 and oEC329. The upstream fragment was digested with HindIII and BamHI, the downstream fragment with BamHI and NheI. The fragments were ligated with pNPTS138 cut with HindIII and NheI.

pEC173 was constructed by amplifying the flanking regions of *ftsI* from LE670 chromosomal DNA using oligos oEC332 and oEC333 (upstream) and oEC334 and oEC335 (downstream). The upstream

fragment was digested with HindIII and BamHI, the downstream fragment with BamHI and NheI. The fragments were ligated with pNPTS138 cut with HindIII and NheI.

pEC174 was constructed by amplifying the flanking regions of *ldtA* from LE670 chromosomal DNA using oligos oEC338 and oEC339 (upstream) and oEC340 and oEC341 (downstream). The upstream fragment was digested with BamHI and KpnI, the downstream fragment with KpnI and NheI. The fragments were ligated with pNPTS138 cut with BamHI and NheI.

4.4.6.6. Plasmids for complementation of in-frame deletion mutants of *H. neptunium*

pEC60 was constructed by amplification of *bacA* from LE670 chromosomal DNA using oligos SW112 and oEC159, digestion of the PCR product with NdeI and KpnI, and ligation of the fragment with pCVENC-3 cut with NdeI and KpnI.

pEC61 was constructed by amplification of *bacB* from LE670 chromosomal DNA using oligos SW186 and oEC158, digestion of the PCR product with NdeI and KpnI, and ligation of the fragment with pCVENC-2 cut with NdeI and KpnI.

pEC103 was constructed by amplification of $bacA_{CC}$ from CBN15 chromosomal DNA using oligos MT743 and MT745, digestion of the PCR product with NdeI and KpnI, and ligation of the fragment with pCCHYC-2 cut with NdeI and KpnI.

4.4.6.7. Plasmids for co-localization and bacterial two-hybrid analysis in *E. coli*

A complete list of all plasmids generated for bacterial two-hybrid can be found in Table 24in the Appendix section.

pEC119 was constructed by amplification of *bacA-yfp* from pEC74 using oligos oEC238 and oEC170, digestion of the PCR product with PciI and BamHI, and ligation of the fragment with pRSFDuet-1 cut with NcoI and BamHI.

pEC120 was constructed by amplification of *bacB-cfp* from pEC70 using oligos SW186 and oEC242, digestion of the PCR product with NdeI and MfeI, and ligation of the fragment with pRSFDuet-1 cut with NdeI and MfeI.

pEC121 was constructed by amplification of *bacB-cfp* from pEC70 using oligos SW186 and oEC242, digestion of the PCR product with NdeI and MfeI, and ligation of the fragment with pEC120 cut with NdeI and MfeI.

pEC131 was constructed by amplification of *bacA* from LE670 chromosomal DNA using oligos oEC276 and SW113, digestion of the PCR product with EcoRI and KpnI, and ligation of the fragment with pKNT25 cut with EcoRI and KpnI.

pEC132 was constructed by amplification of *bacA* from LE670 chromosomal DNA using oligos oEC276 and SW113, digestion of the PCR product with EcoRI and KpnI, and ligation of the fragment with pUT18 cut with EcoRI and KpnI.

pEC133 was constructed by amplification of *bacB* from LE670 chromosomal DNA using oligos oEC277 and SW187, digestion of the PCR product with EcoRI and KpnI, and ligation of the fragment with pKNT25 cut with EcoRI and KpnI.

pEC134 was constructed by amplification of *bacB* from LE670 chromosomal DNA using oligos oEC277 and SW187, digestion of the PCR product with EcoRI and KpnI, and ligation of the fragment with pUT18 cut with EcoRI and KpnI.

pEC135 was constructed by amplification of *mreB* from LE670 chromosomal DNA using oligos oEC278 and oEC132, digestion of the PCR product with BamHI and KpnI, and ligation of the fragment with pKT25 cut with BamHI and KpnI.

pEC136 was constructed by amplification of *mreB* from LE670 chromosomal DNA using oligos oEC278 and oEC132, digestion of the PCR product with BamHI and KpnI, and ligation of the fragment with pUT18C cut with BamHI and KpnI.

pEC137 was constructed by amplification of *mreC* from LE670 chromosomal DNA using oligos oEC285 and oEC286, digestion of the PCR product with BamHI and KpnI, and ligation of the fragment with pKT25 cut with BamHI and KpnI.

pEC138 was constructed by amplification of *mreC* from LE670 chromosomal DNA using oligos oEC285 and oEC286, digestion of the PCR product with BamHI and KpnI, and ligation of the fragment with pUT18C cut with BamHI and KpnI.

pEC139 was constructed by amplification of HNE0630 from LE670 chromosomal DNA using oligos oEC279 and oEC280, digestion of the PCR product with BamHI and KpnI, and ligation of the fragment with pKNT25 cut with BamHI and KpnI.

pEC140 was constructed by amplification of HNE0630 from LE670 chromosomal DNA using oligos oEC279 and oEC280, digestion of the PCR product with BamHI and KpnI, and ligation of the fragment with pUT18 cut with BamHI and KpnI.

pEC141 was constructed by amplification of *rodZ* from LE670 chromosomal DNA using oligos oEC281 and oEC282, digestion of the PCR product with BamHI and KpnI, and ligation of the fragment with pKNT25 cut with BamHI and KpnI.

pEC142 was constructed by amplification of *rodZ* from LE670 chromosomal DNA using oligos oEC281 and oEC282, digestion of the PCR product with BamHI and KpnI, and ligation of the fragment with pUT18 cut with BamHI and KpnI.

pEC143 was constructed by amplification of *murG* from LE670 chromosomal DNA using oligos oEC283 and oEC284, digestion of the PCR product with BamHI and KpnI, and ligation of the fragment with pKNT25 cut with BamHI and KpnI.

pEC144 was constructed by amplification of *murG* from LE670 chromosomal DNA using oligos oEC283 and oEC284, digestion of the PCR product with BamHI and KpnI, and ligation of the fragment with pUT18 cut with BamHI and KpnI.

pEC145 was constructed by amplification of *lmdA* from LE670 chromosomal DNA using oligos oEC306 and oEC307, digestion of the PCR product with BamHI and KpnI, and ligation of the fragment with pKT25 cut with BamHI and KpnI.

pEC146 was constructed by amplification of *lmdA* from LE670 chromosomal DNA using oligos oEC306 and oEC307, digestion of the PCR product with BamHI and KpnI, and ligation of the fragment with pUT18C cut with BamHI and KpnI.

pEC147 was constructed by amplification of *lmdB* from LE670 chromosomal DNA using oligos oEC308 and oEC309, digestion of the PCR product with BamHI and KpnI, and ligation of the fragment with pKT25 cut with BamHI and KpnI.

pEC148 was constructed by amplification of *lmdB* from LE670 chromosomal DNA using oligos oEC308 and oEC309, digestion of the PCR product with BamHI and KpnI, and ligation of the fragment with pKT25 cut with BamHI and KpnI.

4.4.6.8. Plasmids for expression in *E. coli*

For the overexpression and purification of BacA-His_6 from *E. coli* Rosetta 2(DE3)/pLysS, **pEC86** was constructed by amplification of *bacA* from LE670 chromosomal DNA using oligos SW112 and SW113, digestion of the PCR product with NdeI and EcoRI, and ligation of the fragment with pET21a(+) cut with NdeI and EcoRI.

4.4.7. Preparation and transformation of chemically competent *E. coli*

To generate chemically competent *E. coli* TOP10 cells, 10 mL LB medium supplemented with streptomycin was inoculated from an *E. coli* TOP10 cryo-culture and incubated at 37 °C overnight. The following morning 250 mL LB medium were inoculated with 2.5 mL of pre-culture and cultivated to an OD_{600} of 0.6. The cells were transferred to pre-cooled 250 mL GS-3 tubes, incubated on ice for 10 min, and harvested by centrifugation using a Sorvall GS-3 rotor (Thermo Fisher, USA) at 3,000 x g and 4 °C for 10 min. The supernatant was discarded and the pellet was resuspended in 15 mL ice-cold 0.1 M $CaCl_2$ solution and transferred in pre-cooled SS34 tubes. The cells were then incubated on ice for 30 min and collected by centrifugation with an SS34 rotor (Thermo Fisher, USA) at 3,000 x g and 4 °C for 10 min. The pellet was gently resuspended in 4 mL pre-cooled 0.1 M $CaCl_2$ containing 15 % glycerol. Aliquots of 140 µL in Eppendorf tubes were snap-frozen in liquid nitrogen and stored at -80 °C.

To transform chemically competent *E. coli* TOP10, cells was thawed on ice and mixed with 10 µL of a ligation reaction or 10 ng of bacterial two-hybrid plasmids and incubated 20 min on ice. After a heat-shock at 42 °C for 90 s, the cells were incubated again on ice for 2 min and added to 500 µL LB. The cells were incubated for 60 min at 37 °C before 200 µL of the cell suspension were spread onto a LB

agar plate supplemented with the appropriate antibiotics. Plates were incubated at 37 °C until single colonies appeared. For the generation and transformation of competent *E. coli* WM3064 cells, 300 µM diaminopimelic acid (DAP) was added to the LB medium and agar.

Chemically competent *E. coli* BTH101 were thawed in ice, 15 µL of cells were co-transformed in a µltraAmp™ 96-well semi-skirted PCR plate (Sorenson BioScience,) with 1 µL of each 10 ng/µL plasmid and 3 µL H_2O. After incubation on ice for 1 h, cells were heat-shocked for 30 s at 42 °C in a water bath and incubated on ice for another 20 min. The cells were added to 80 µL of LB medium supplemented with 0.5 % glucose and incubated for 1 h at 37 °C. For further procedure see section 4.4.8.

4.4.8. Bacterial Adenylate Cyclase Two Hybrid (BACTH) Assay

BACTH analysis was performed essentially as described previously (403). To detect protein-protein interactions, the adenylate cyclase-deficient *E. coli* strain BTH101 was co-transformed with plasmids encoding the proteins of interest fused to either the T25 or the T18 fragment of *Bordetella pertussis* adenylate cyclase. After transformation, cells were transferred into a 96-well tissue culture plate (Sarstedt, Germany), added 100 µL LB medium supplemented with 0.5 % glucose, 100 µg/mL kanamycin, 400 µg/mL ampicillin, 60 µg/mL streptomycin, and incubated for 3-5 h at 37 °C. To detect protein-protein interactions, 5 µL were spotted in duplicates onto LB agar plates supplemented with 50 µg/mL kanamycin, 200 µg/mL ampicillin, 30 µg/mL streptomycin, 250 µm IPTG, and 0.5 % glucose, and incubated for 36 h at 28 °C. To intensify the colour, plates were incubated at RT and later at 4 °C.

4.4.9. Conjugation of *H. neptunium*

Conjugation as used to integrate plasmids of interest via single homologous recombination into *H. neptunium*. *E. coli* WM3064 cells (donor strain) harbouring the plasmid of interest were grown to stationary phase in liquid LB medium supplemented with the appropriate antibiotic and 300 µM DAP. *H. neptunium* (recipient strain) was also grown to stationary phase in MB medium for 2-3 days. 1 mL of the *E. coli* WM3064 culture and 2 mL of the *H. neptunium* culture were pelleted for 2 min at 9,000 rpm and washed with 1 mL MB medium supplemented with 300 µM DAP and resuspended in 100 µL MB medium supplemented with 300 µM DAP. The combined cultures were spotted onto an MB agar plate supplemented only with 300 µM DAP. After 24 h of growth at 28 °C, the cells were removed, resuspended in 1 mL plain MB medium and then washed twice with MB medium (2 min, 7,000 rpm). 200 µL of the suspension (undiluted and 1:10 dilution) were plated on MB agar supplemented with the appropriate antibiotic and grown at 28 °C until single colonies appeared (5-7 days).

For double homologous recombination, *H. neptunium* cells were transformed by conjugation as described above. Positive clones were verified by colony PCR and grown for 24 h in MB medium. 200 µL of a 1:200 dilution were plated on MB agar supplemented with 3 % sucrose and incubated at 28 °C for 5-7 days. Single clones were restreaked in parallel onto MB agar supplemented with 3 % sucrose and MB agar supplemented with the appropriate antibiotic. After 48 h of growth, colony PCR was performed on clones which grew on MB sucrose agar plates but not on the antibiotic supplemented plate.

4.4.10. Lyophilization of cells for PG analysis

250 mL of a *H. neptunium* LE670 and *C. crescentus* CBN15 culture of OD600 of 0.7 were harvested for 10 min at 7,000 x g at 4 °C. Cells were resuspended in 1 mL de-ionized H_2O and boiled for 10 min at 100 °C. Cell lysates were transferred into a 15 mL falcon tube, snap-frozen horizontally in liquid nitrogen and stored at -80 °C till lyophilisation at 0.1 mbar at -55 °C using the single-stage cooling system freeze dryer Alpha 1-4 (Christ, Germany).

4.4.11. Peptidoglycan muropeptide analysis

Lyophilized cell lysates of *H. neptunium* LE670 and *C. crescentus* CBN15 were prepared as described above and sent to ANASYN Dr. Gökay (Germany) for analysis.

4.5. Biochemical methods

4.5.1. SDS-Polyacryl gel electrophoresis (SDS-PAGE)

Protein samples were electrophoretically separated utilizing the principles of the discontinuous method described by Laemmli (404). To prepare cell lysate samples were harvesting cells at 14,680 rpm for 2 min and resuspended in 2x sodium dodecyl sulfate (SDS) sample buffer (125 mM Tris, 20 % (w/v) glycerol, 2 % (w/v) SDS, 200 mM dithiothreitol, 0.05 % bromophenol blue, pH 6.8) to a theoretical OD_{600} of 1. The samples were boiled at 95 °C for 10 min prior to loading onto an SDS gel consisting of a 5 % stacking gel and an 11 % resolving gel (Table 15). PageRuler™ Prestained Protein ladder (Fermentas, Canada) was used as a protein molecular weight standard. Electrophoresis was performed in SDS running buffer (25 mM Tris Base, 192 mM glycine, 0.1 % (w/v) SDS) at 15-30 mA per gel using a PerfectBlue™ Twin S system (Peqlab, USA).

To visualize proteins after electrophoresis, the SDS gel was either stained with Coomassie blue (40 % methanol, 10 % acidic acid, 0.1 % (w/v) Brilliant Blue R 250) for 10 min followed with destaining in a solution of 20 % ethanol and 10 % acidic acid or Coomassie blue (10 % acidic acid, 0.1 % (w/v) Brilliant Blue G 250) for 10 min followed with destaining in water. For specific protein detection, SDS-PAGE gels were subjected to immunoblot analysis (section 4.5.2).

Table 15. Composition of SDS-PAGE gels

Component	5 % stacking gel (2.5 mL)	11 % resolving gel (5 mL)
Aqua dest.	1.43 mL	1.9 mL
500 mM Tris Base (pH 6.8), 0.4 % (w/v) SDS	625 µL	-
1.5 M Tris Base (pH 8.8), 0.4 % (w/v) SDS	-	1.25 mL
30 % Rotiphorese® NR-Acrylamide/Bis- (29:1)	417 µL	1.9 mL
TEMED (N,N,N',N'-Tetramethylethylenediamine)	1.9 mL	3 µL
10 % (w/v) APS (Ammonium persulfate)	25 µL	40 µL

4.5.2. Immunoblot analysis

For immunoblot analysis, proteins were first resolved in an 11 % acrylamide gel as described above and transferred onto a polyvinylidene fluoride (PVDF) membrane (Millipore, USA) by semi-dry transfer using the PerfectBlue™ Semi-Dry-Elektro Blotter (peqlab, USA). The PVDF membrane was rinsed for 15 s in 100 % methanol, washed for 2 min in de-ionized water, and equilibrated for at least 5 min in Western blot transfer buffer (25 mM Tris base, 1.92 M glycine, 10 % methanol). Proteins were transferred with the PerfectBlue™ Wet Blotting System (VWR Peqlab, USA) from the gel to the membrane with 2 mA/cm² for 1-2 h. Proteins larger than 100 kDa were transferred from the gel onto a PVDF membrane by wet tank transfer using the Perfect-Blue™ Wet Blotting Systems (Peqlab, USA). The PVDF membrane was treated as above. Proteins were transferred from the gel to the membrane at 4 °C as indicated in Table 16.

Table 16. Power supply settings for PerfectBlue™ Wet Blotting Systems

PerfectBlue™ Web S		PerfectBlue™ Web M	
overnight	1 h	overnight	1 h
10-40 V	50-100 V	25-40 V	50-60 V
40-80 mA	200-400 mA	80-160 mA	200-250 mA

After transfer, the membrane was blocked in TBST buffer (10 mM Tris Base, 150 mM NaCl, 0.1 % (w/v) Tween20, pH 7.5) containing 2.5 % (w/v) non-fat dry milk on a shaker for 1 h at RT or overnight at 4 °C. Proteins were detected by protein-specific antibodies or anti-sera as shown in Table 17. After blocking, the membrane was incubated on a shaker at RT for 1-2 h in TBST buffer with 2.5 % (w/v) non-fat dry milk and the appropriate primary antibody. Membranes were washed trice with 1 x TBST for 5 min prior to incubation at RT for 1-2 h with the secondary antibody (HRP-labelled anti rabbit IgG) dissolved in 1 x TBST containing 2.5 % (w/v) non-fat dry milk. After five 5 min wash steps in 1 x TBST, visualization of proteins was performed using the Western Lightening™ Chemiluminescence Reagent Plus kit (PerkinElmer, USA) according to the manufacturer's instructions. The membrane was exposed to Amersham Hyperfilm™ ECL-Chemiluminenscence films (GE Healthcare, Germany) and chemiluminescence was detected with a LAS-4000 Luminescent Image Analyzer (Fujifilm, Germany).

In order to reuse a probed membrane for further immunoblot analysis, the antibodies were removed by incubation of the membrane in 15 mL Restore™ Plus Western Blot Stripping Buffer (Thermo Fischer, USA) for 1 h at RT. Before blocking with TBST containing 2.5 % (w/v) non-fat dry milk, the membrane was washed twice with TBST for 10 min. Immunoblot analysis was carried out as described above.

Table 17. Antibodies used in this study

Antibody	Dilution	Comment/reference
Primary antibodies (rabbit)		
α-HA	1:8 000	Millipore, Germany
α -BacA (serum)	1:10 000	This study
α -$BacA_{CC}$	1:10 000	Kühn, 2011 (157)
α -mCherry	1:10 000	BioVision, USA
α -RFP (serum)	1:10 000	Chen, 2005 (405)
α -GFP (works also anti-YFP, anti-CFP, and anti-Venus)	1:10 000	Sigma-Aldrich, Germany
Secondary antibodies		
HRP-labelled anti rabbit IgG (goat)	1:20 000	PerkinElmer, USA

To ensure correct loading of the cell lysate, the membrane was incubated in amido black (40 % methanol (v/v), 10 % acetic acid (v/v), 0.1 % amido black 10B (w/v)) for 1 min and destained with water until protein bands were clearly visible.

4.5.3. Protein purification

To overproduce His-tagged BacA, *E. coli* strain Rosetta(DE3)/pLysS (Invitrogen) was transformed with pEC86 (*bacA-his*$_6$) and grown to an OD_{600} of 1.0 in LB medium at 37 °C. IPTG was added to a final concentration of 0.5 mM and incubation was continued for 3 h. Cells were harvested by centrifugation for 10 min at 7,500 x g and 4 °C, washed in 1/10 Vol lysis buffer (50 mM NaH_2PO_4, 300 mM NaCl, 10 mM imidazole, adjusted to pH 8.0 with NaOH) and frozen in liquid nitrogen. Cells were resuspended in 2 mL per g wet cell extract lysis buffer containing 100 µg/mL PMSF, 10 µg/mL DNase I, 1 mM ß-mercaptoethanol and lysed by three passages through a French press at 16,000 psi. The suspension was centrifuged for 30 min at 30,000 x g at 4 °C. The cleared lysate was mixed with 8 mL Ni-NTA agarose beads (Qiagen) that were equilibrated with wash buffer (50 mM NaH_2PO_4, 300 mM NaCl, 20 mM imidazole, 1 mM ß-mercaptoethanol, adjusted to pH 8.0 with NaOH) and incubated under gentle agitation for 1 h at 4 °C. The Ni-NTA beads with the bound protein were collected by centrifu-gation for 5 min at 2,000 x g at 4 °C and washed four times in 65 mL wash buffer for 15 min at 4 °C. The bound protein was eluted twice in 24 mL elution buffer (50 mM NaH_2PO_4, 300 mM NaCl, 250 mM imidazole, 1 mM ß-mercaptoethanol, adjusted to pH 8.0 with NaOH) for 15 min under gentle agitation at 4 °C.

All fractions were analysed by SDS-PAGE and the two elution fractions were pooled. The flow-through after incubation with the Ni-NTA agarose beads contained so much protein that the purification step was repeated as above. The second batch of purified His-tagged BacA was dialysed against in 10 L FPLC (fast protein liquid chromatography) buffer (50 mM sodium phosphate buffer, pH7.0, 5 mM $MgCl_2$, 0.1 mM EDTA, 1 mM ß-mercaptoethanol) for at least 16 h at 4 °C. Precipitates were removed by centrifu-gation for 20 min at 30,000 x g at 4 °C. The supernatant was loaded on a HiPrep™ 16/10 SP FF cation exchange column (GE Healthcare, Germany) of the ÄKTA Purifier.10 system (GE Healthcare, Germany) equilibrated with FPLC buffer containing 50 mM NaCl. The column was washed with 75 mL FPLC buffer containing 50 mM NaCl prior to elution with 250 mL of a linear NaCl gradient (50-500 mM in FPLC buffer), collecting 2 mL fractions. The fractions were analysed by SDS-PAGE, and fractions containing the protein of interest were pooled.

Both protein solutions were dialysed against 10 L dialysis buffer (50 mM HEPES, pH 7.2, 50 mM NaCl, 5 mM $MgCl_2$, 0.1 mM EDTA, 10 % glycerol, 1 mM ß-mercaptoethanol) for at least 16 h at 4 °C, aliquoted, snap frozen in liquid nitrogen, and stored at -80 °C.

Protein concentrations were measured with the RotiNanoquant reagent (Carl-Roth, Germany), based on a modified Bradford assay (406, 407). The protein was concentrated by centrifugation in an Amicon Ultra centrifugal tube (Amicon, USA) for 10 min at 7,500 x g and 4 °C.

4.5.4. Antibody synthesis

Purified BacA-His_6 was sent for antibody generation according to the company's instructions (Eurogentec, Belgium).

4.5.5. Co-immunoprecipitation and mass-spectroscopy

For co-immunoprecipitation of BacA-HA, *H. neptunium* strain EC47 and LE670 (negative control) were grown in 1000 mL MB to mid-exponential phase (OD_{600} of 0.6). *Para*-formaldehyde (in 1 x PBS, pH 7.4) at a final concentration of 0.6 % was used to cross-link proteins for 20 min at 37 °C. The reaction was quenched by the addition of 125 mM glycine (1 x PBS, pH 7.4) for 5 min at RT. Cells were harvested by centrifugation for 10 min at 3,000 x g at 4 °C and washed twice with wash buffer I (50 nM $NaPO_4$, pH7.4, 5 mM $MgCl_2$). The cells were washed once with 20 mL Co-IP buffer (20 mM HEPES, pH7.4, 100 mM NaCl, 20 % glycerol, 0.5 % Triton X-100), resuspended in 10 mL Co-IP buffer supplemented with 10 mM $MgCl_2$, 10 mg/mL lysozyme, 5 µg/mL DNaseI, and 100 µg/mL phenylmethylsulfonyl-fluorid (PMSF), and incubated on ice for 30 min. Cells were disrupted by three passages through a French press at 16,000 psi and cell debris was removed by centrifugation for 10 min at 3,000 x g at 4 °C. 500 µL aliquots of the clear lysate were snap-frozen and stored at -80 °C.

To precipitate BacA-HA, 80 µl EZview™ Red Anti-HA Affinity Gel (SIGMA-Aldrich, Germany) were equilibrated with Co-IP buffer according to the manufacturer's instructions, mixed with 2 mL cell lysate, and then incubated overnight on a rotary shaker at 4 °C. The affinity gel-sample complexes were pelleted for 1 min at 8,000 x g at 4 °C and washed twice with 750 µL Co-IP buffer for 5 min at 4 °C, thrice with wash buffer II (50 mM Tris/HCl, pH 7.5, 150 mM NaCl, 1 mM EDTA, 0.5 % Triton X-100) and thrice with wash buffer III (100 mM Tris/HCl, pH 8, 750 mM NaCl, 1 mM EDTA, 0.05 % Triton X-100). Precipitated proteins were eluted from the affinity gel by boiling at 95 °C for 20 min in 100 µL 2 x SDS sample buffer. Samples were run approx. 1 cm into an 11 % resolving SDS gel (Table 15), excised, and submitted to mass spectroscopic analysis.

4.6. Bioinformatic methods

All DNA and protein sequences were obtained from either the NCBI database at http://www.ncbi.nlm.nih.gov/ (October 2010 - 2016) (408), the JCVI CMR database at http://cmr.jcvi.org/cgi-bin/CMR/CmrHomePage.cgi (October 2010) (J. Craig Venter Institute), or the KEGG database at http://www.genome.jp/kegg/ (2013-2016) (Kanehisa Laboratories). The identification of proteins sharing functional domains was done by using the Pfam database (Trust Sanger Institute) at http://pfam.sanger.ac.uk/ (November 2010 - 2016) (409, 410). Structural predicttions for proteins were made using PSIPRED (protein structure prediction server, UCL) at http://bioinf.cs.ucl.ac.uk/psipred/ (February 2011) (411, 412). Simple schematics depicting protein domain structures were drawn with the help of SMART (Simple Modular Architecture Research Tool at http://smart.embl-heidelberg.de/smart/set_mode.cgi?NORMAL=1 (February 2011 - 2016) (367, 413). The TOPCONS web ser-ver was used for combined membrane protein topology and signal peptide prediction (2014 -

2016) (414). Protein structures were model with I-Tasser (373-375) and processed with Pymol 1.8 (376). Box plots were generated using QtiPlot 0.9.8.7. Demographs prepared with Fiji and R x64 3.1.1.

5. Appendix

5.1. Supplemental figures

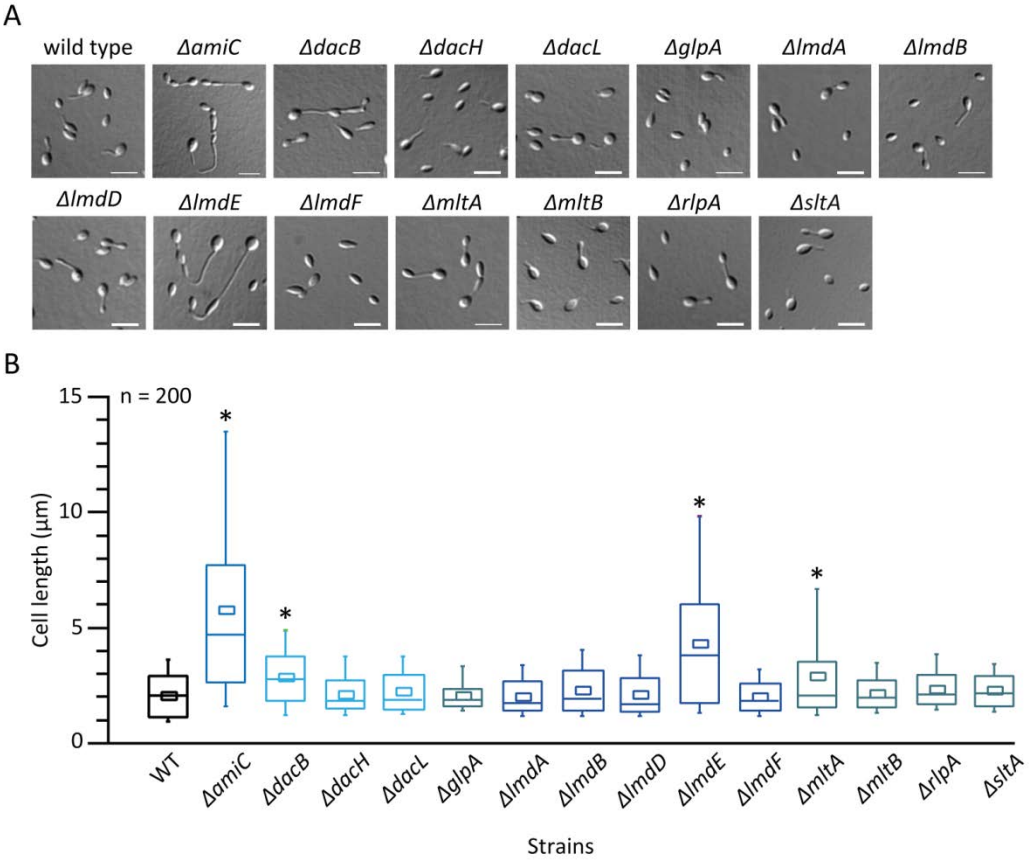

Figure S1. Overview of the phenotypes of all autolysin deletion mutants in *H. neptunium.* A) Deletion of autolysins causes a cell elongation and cell chaining phenotpye. The *H. neptunium* wild type and strains EC21 (*ΔsltA*), EC36 (*ΔlmdA*), EC38 (*ΔlmdD*), EC39 (*ΔlmdE*), EC46 (*ΔdacL*), EC53 (*ΔlmdB*), EC90 (*ΔlmdF*), EC95 (*ΔmltA*), SR07 (*ΔglpA*), SR08 (Δ*dacH*), SR11 (Δ*dacB*), SR18 (Δ*amiC*), SR20 (Δ*mltB*) and SR33 (Δ*rlpA*) were grown to exponential phase in MB medium and analysed by DIC microscopy. Scale bar, 3 µm. **B)** Deletion of autolysins causes stalk elongation and cell chaining. Cell length measurements are based on images from A). Box plots show the median and the interquartile range (box), the average value (square in box), the 5th and 95th percentile (whiskers), outliers are excluded. Asterisk indicates a *p*-value of < 0.001 (*t*-test). Data generated in collaboration with S. Rosskopf.

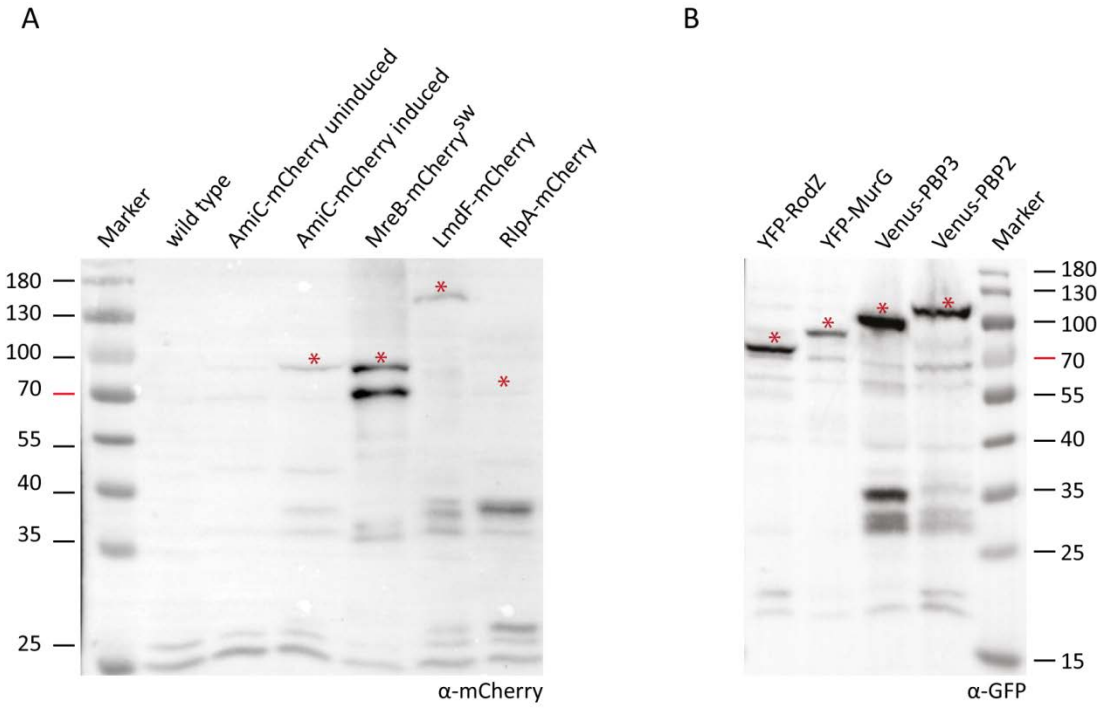

Figure S2. Stability of fusion protein constructs. A) The *H. neptunium* wild type and strains EC63 (*mreB-mCherry*^{SW}), EC70 (P_{Cu}::P_{Cu}-*amiC-mCherry*), SR26 (*lmdF-mCherry*), SR28 (*dacL-mCherry*) and SR38 (*rlpA-mCherry*) were grown to exponential phase in MB medium and EC70 was induced with 300 µM $CuSO_4$ for 24 h prior to analysis. An anti-mCherry antibody was used for immunodetection. **B)** Strains EC93 (*yfp-rodZ*), EC96 (*yfp-murG*), SE161 (*venus- pbp3*), and SR14 (*venus-pbp2*) were grown to exponential phase in MB medium. An anti-GFP antibody was used for immunodetection. Asterisks indicate the stable fusion protein. Data generated in collaboration with S. Rosskopf.

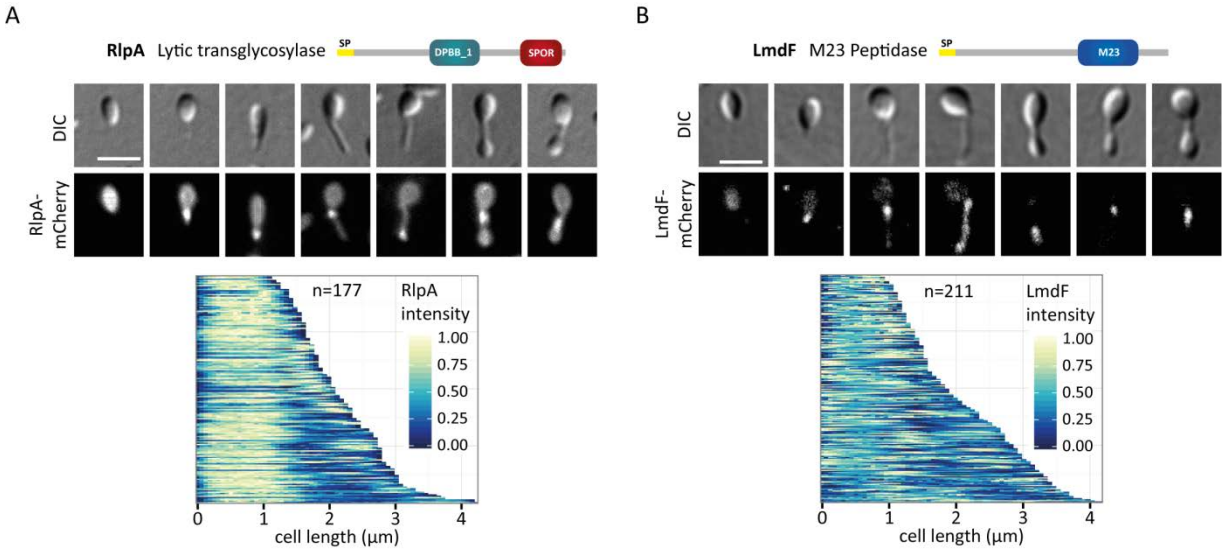

Figure S3. Peptidoglycan hydrolases RlpA and LmdF localize to sites of cell wall biogenesis. A) RlpA-mCherry localizes to the stalked pole and the stalk. Strain SR38 (*rlpA-mCherry*) was grown to exponential phase in MB medium and imaged by DIC and fluorescence microscopy. Scale bar, 2 µm. **B)** LmdF-mCherry localizes to sites of cell growth in *H. neptunium*. Strain SR26 (*lmdF-mCherry*) was grown to exponential phase in MB medium and imaged by DIC and fluorescence microscopy. Scale bar, 2 µm. Microscopy data generated in collaboration with S. Rosskopf.

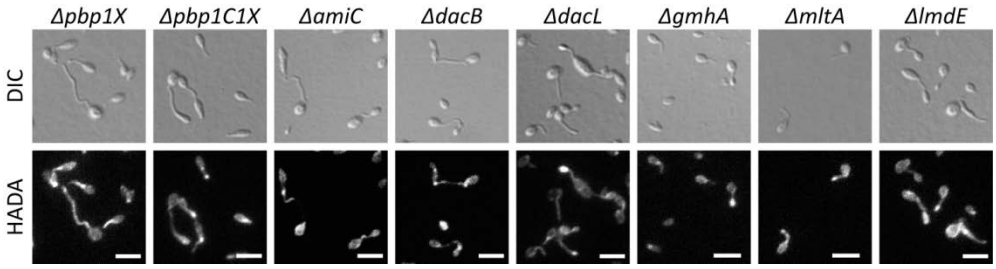

Figure S4. Peptidoglycan incorporation is unaffected in deletion mutants with a pronounced morphological phenotype in *H. neptunium*. The *H. neptunium* wild type and strains EC26 (*Δpbp1X*), EC39 (*ΔlmdE*), EC46 (*ΔdacL*), EC57 (*Δpbp1CΔpbp1X*), EC95 (*ΔmltA*), SR07 (*ΔglpA*), SR11 (*ΔdacB*), and SR18 (*ΔamiC*) were grown to exponential phase in MB medium, pulse-labelled with HADA, and imaged by DIC and fluorescence microscopy. Scale bar, 3 µm. Data generated by S. Rosskopf (384).

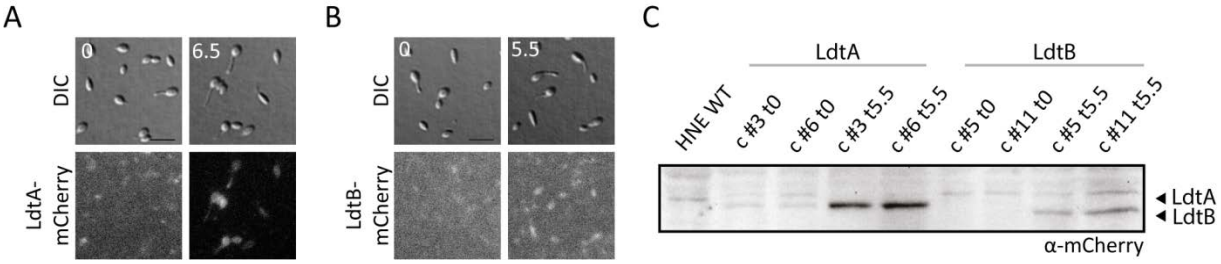

Figure S5. LdtA-mCherry and LdtB-mCherry localize diffusely in *H. neptunium*. A) LdtA-mCherry localizes diffusely. CR01 (*ΔldtA*) was grown to exponential phase in MB medium and induced with 300 µM $CuSO_4$ for 6.5 h prior to imaging with DIC and fluorescence microscopy. Scale bar, 3 µm. **B)** LdtB-mCherry localizes diffusely. CR02 (*ΔldtB*) was grown to exponential phase in MB medium and induced with 300 µM $CuSO_4$ for 5.5 h prior to imaging with DIC and fluorescence microscopy. Scale bar, 3 µm. **C)** Expression levels of LdtA-mCherry and LdtB-mCherry under the control of P_{Cu}. Cells of strains CR01 (*ΔldtA*) clone 3 and 6, and CR02 (*ΔldtB*) clone 5 and 11 were induced with 300 µM $CuSO_4$ and analysed as described in A) and B), respectively, using an anti-mCherry antibody for immunodetection. Data generated by C. Regh (415).

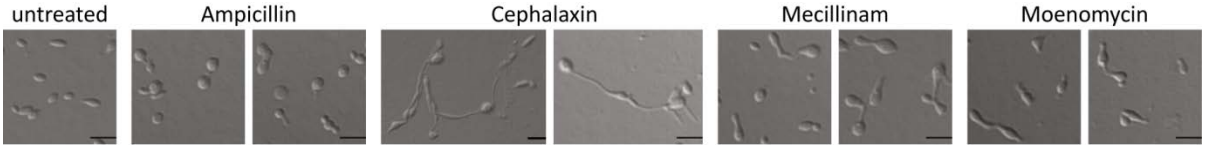

Figure S6. Inhibition of PBPs causes stalk elongation and loss of cell shape. The *H. neptunium* wild type was grown to exponential phase in MB medium and incubated overnight with 50 µg/mL ampicillin, 40 µg/mL cephalexin, 30 µg/mL mecillinam, or 50 µg/mL moenomycin, respectively. Cells were analysed by DIC microscopy. Scale bar, 3 µm. Data generated by S. Rosskopf

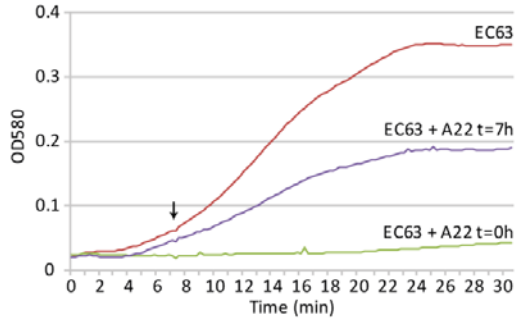

Figure S7. A22 immediately impairs growth of *H. neptunium* . Strain EC63 (*mreB-mCherry*^{SW}) was grown to exponential phase in MB medium and a growth assay was carried out as described in materials and methods. One sample was supplemented with 37 µM A22 at the onset of the experiment, whilst another sample was supplemented with 37 µM A22 7 h (indicated by black arrow) after the start of the assay.

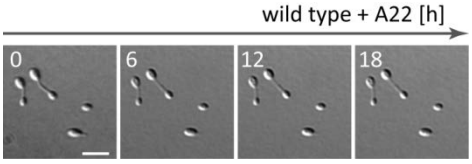

Figure S8. A22 completely blocks the growth of *H. neptunium* on agarose pads. The *H. neptunium* wild type was grown to exponential phase in MB medium and placed on an agarose pad containing 37 µM A22. The cells were followed with DIC time lapse microscopy for 18 h. Scale bar, 3 µm.

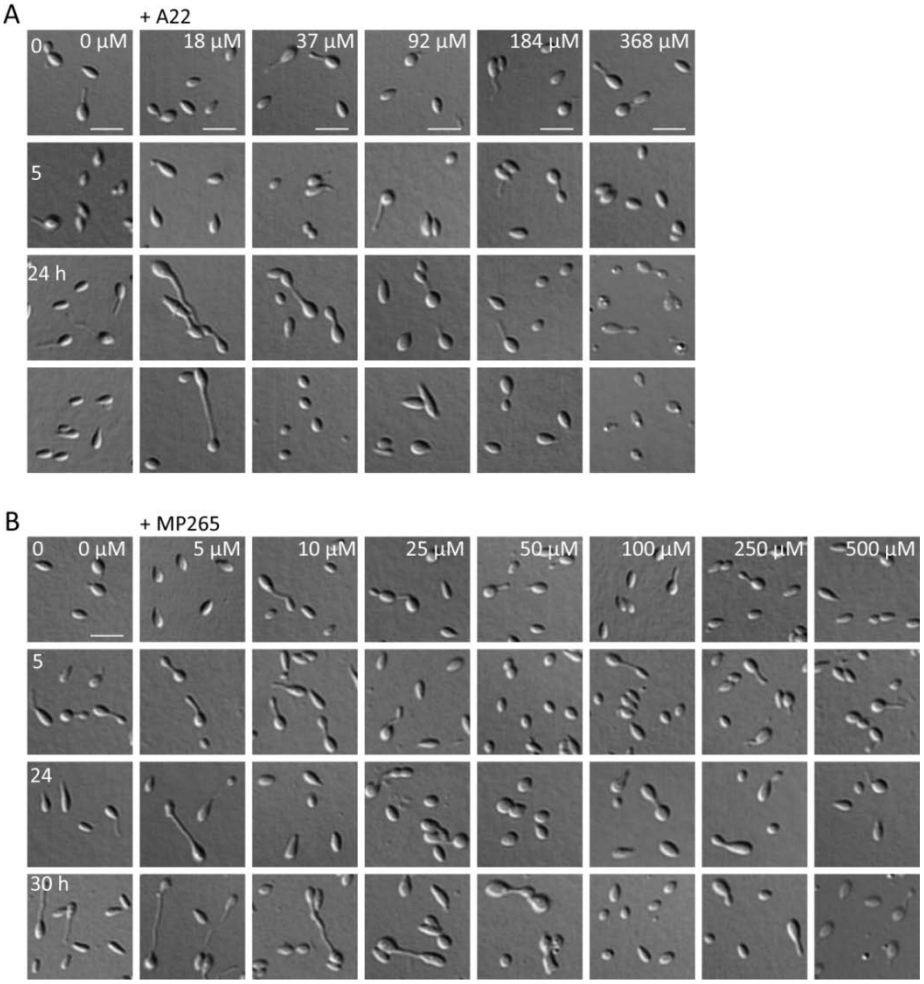

Figure S9. Cell morphology is preferentially lost during inhibition of MreB at low concentrations of A22 or MP265. A) Lower concentrations of A22 have greater effects on cell shape in *H. neptunium*. The *H. neptunium* wild type was grown to exponential phase in MB medium and treated with 18, 37, 92, 184, and 368 µM A22. DMSO was used as a control. Cells were analysed by DIC microscopy after 5, 24, and 30 h. Scale bar, 3 µm. **B)** Lower concentrations of MP265 have greater effects on cell shape in *H. neptunium*. The *H. neptunium* wild type was grown to exponential phase in MB medium and treated with 5, 10, 25, 50, 100, 250, and 500 µM MP265. DMSO was used as a control. Cells were analysed by DIC microscopy after 5, 24, and 30 h. Scale bar, 3 µm.

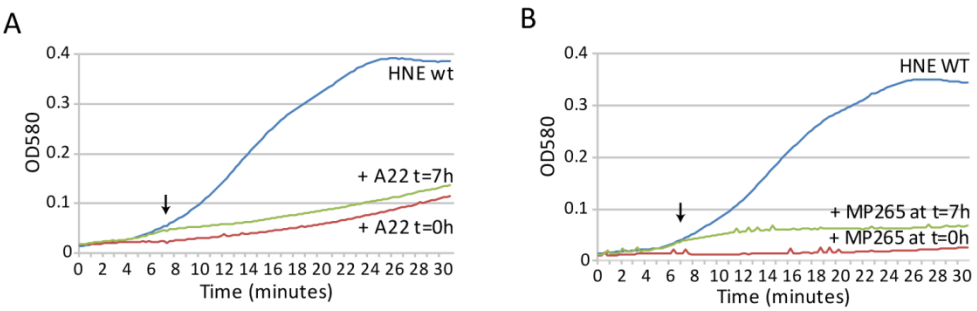

Figure S10. A22 and MP265 substantially impair growth of *H. neptunium.* A) A22 inhibits growth of *H. neptunium*. The *H. neptunium* wild type was grown to exponential phase in MB medium and a growth assay was carried out as described in materials and methods. One sample was supplemented with 37 µM A22 at the onset of the experiment, whilst another sample was supplemented with 37 µM A22 7 h (indicated by black arrow) after the start of the assay. **B)** MP265 inhibits growth of *H. neptunium*. The *H. neptunium* wild type was grown to exponential phase in MB medium and growth assay was carried out as described in materials and methods. One sample was supplemented with 250 µM MP265 at the onset of the experiment, whilst another sample was supplemented with 250 µM MP265 A22 7 h (indicated by black arrow) after the start of the assay.

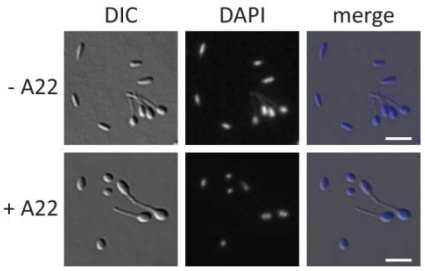

Figure S11. A22-induced spherical *H. neptunium* cells contain DNA. The *H. neptunium* wild type was grown to exponential phase in MB, synchronized and treated with 37 µM (10 µg/mL) A22 or 10 µg/mL DMSO, respectively, for 24 h. To determine nucleoid distribution, both cultures were incubated with 1.5 µg/mL DAPI for 15 min at RT in the dark and analysed by DIC and fluorescence microscopy. Scale bar, 3 µm.

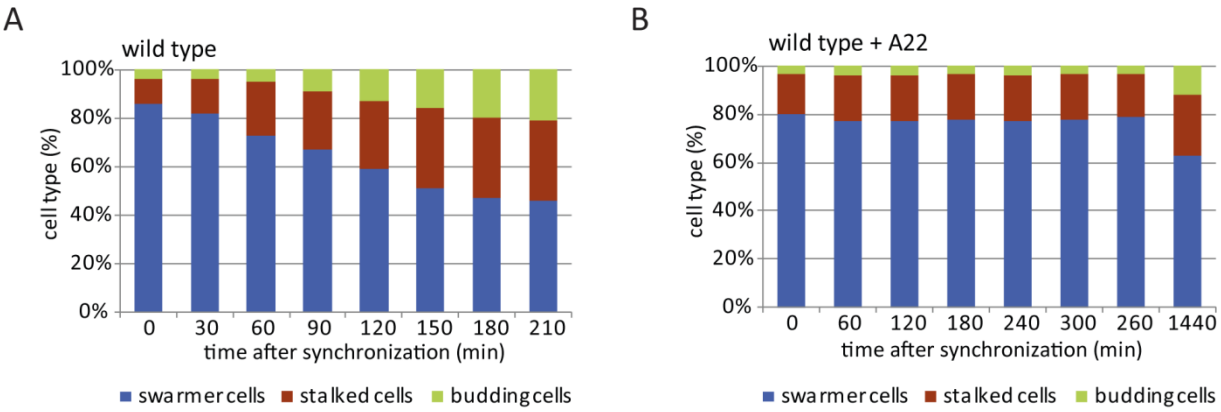

Figure S12. Inhibition of MreB prevents cell growth and thus leads to a stop in cell differentiation. A) Quantification of cell types after synchronization of wild-type cells. The *H. neptunium* wild type was grown to exponential phase in MB, synchronized, and visualized at the indicated time points by DIC microscopy. Quantifications are based on 210 cells per time point. **B)** Quantification of cell types after synchronization of wild-type cells and treatment with A22. The *H. neptunium* wild type was grown to exponential phase in MB, synchronized, treated with 92 µM (25 µg/mL) A22, and visualized at the indicated time points by DIC microscopy. Quantifications are based on 210 cells per time point.

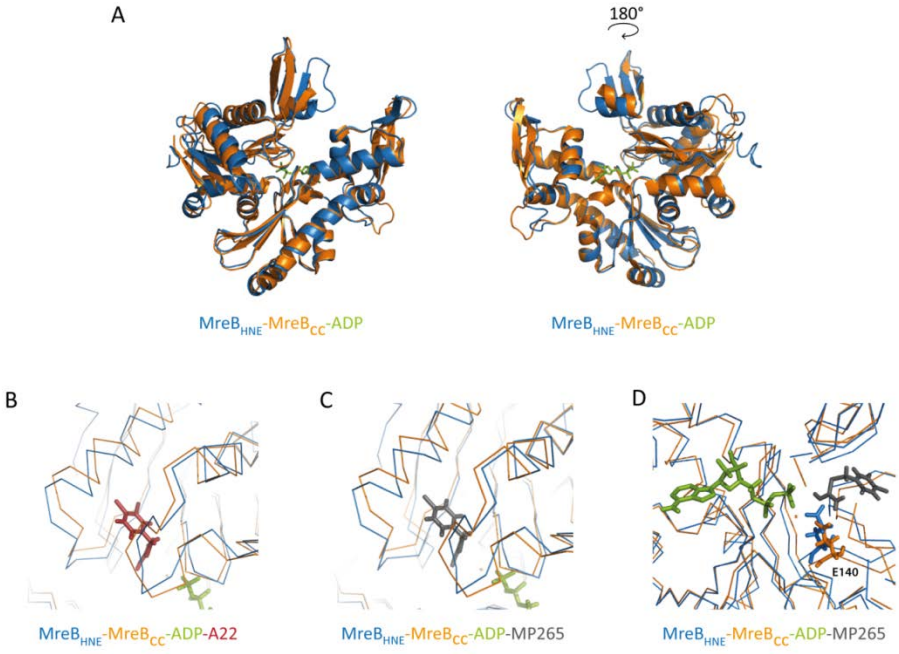

Figure S13. Structure of *H. neptunium* MreB. The structure of *H. neptunium* MreB (HNE2937) was modelled using I-Tasser (373-375) based on MreB$_{CC}$ (PDB 4CZF) and processed with Pymol (376). Structures of MreB$_{CC}$ were solved by the Löwe laboratory (194). **A)** Superposition of ADP-bound (green) MreB$_{HNE}$ (blue) and MreB$_{CC}$ (orange). **B)** Superposition of the MreB ATP-binding pocket with ADP-bound (green) MreB$_{HNE}$ (blue) and MreB$_{CC}$ (orange) in complex with A22 (red) (PDB 4CZG). **C)** Superposition of the MreB ATP-binding pocket with ADP-bound (green) MreB$_{HNE}$ (blue) and MreB$_{CC}$ (orange) in complex with MP265 (grey) (PDB 4CZH). **D)** Superposition of the MreB ATP-binding pocket with ADP-bound (green) MreB$_{HNE}$ (blue) and MreB$_{CC}$ (orange) in complex with MP265 (grey). The inhibitor MP265 binds to the catalytic residue E140 (depicted in orange (MreB$_{CC}$) and blue (MreB$_{HNE}$) sticks) and to the gamma phosphate of ADP (PDB 4CZH) (194).

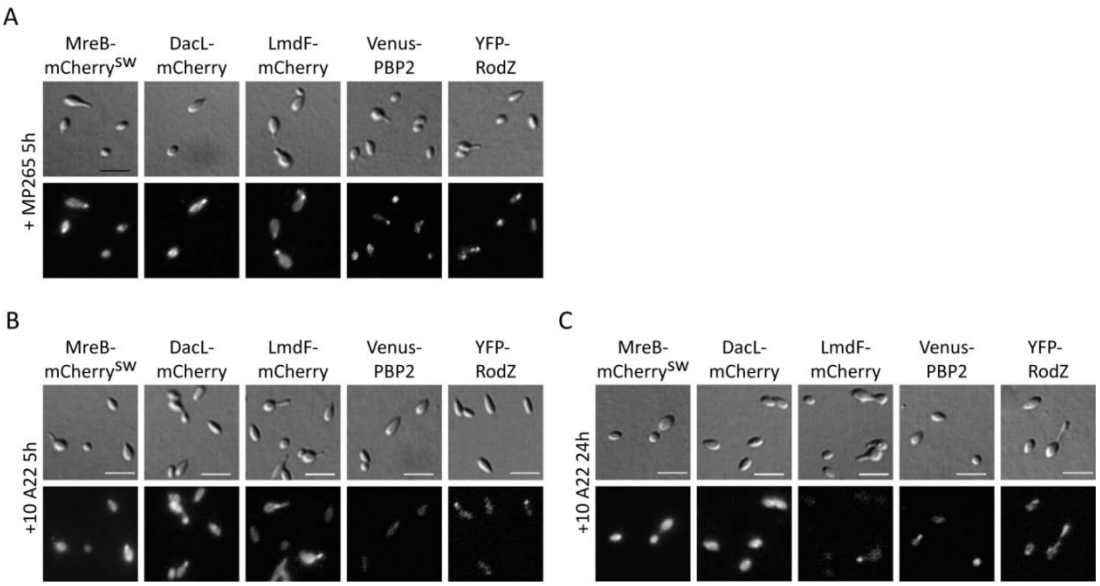

Figure S14. Localization of PG-remodelling enzymes is partially MreB-dependent. A) The localization PG-remodelling enzymes is unaffected by treatment with MP265 for 5 h. Strains EC63 (*mreB-mCherry*^{SW}), SR28 (*dacL-mCherry*), SR26 (*lmdF-mCherry*), SR38 (*rlpA-mCherry*), SR14 (*venus-pbp2*), and EC93 (*yfp-rodZ*) were grown to exponential phase in MB medium, treated with 250 µM MP265 for 5 h, and imaged by DIC and fluorescence microscopy. Scale bar, 3 µm. **B)** The localization PG-remodelling enzymes becomes slightly diffuse when treated with A22 for 5 h. Strains EC63 (*mreB-mCherry*^{SW}), SR28 (*dacL-mCherry*), SR26 (*lmdF-mCherry*), SR38 (*rlpA-mCherry*), SR14 (*venus-pbp2*), and EC93 (*yfp-rodZ*) were grown to

exponential phase in MB medium, treated with 37 µM A22 for 5 h, and imaged by DIC and fluorescence microscopy. Scale bar, 3 µm**. C)** The localization PG-remodelling enzymes becomes increasingly diffuse when treated with A22 for 24 h. Strains EC63 (*mreB-mCherry*^{SW}), SR28 (*dacL-mCherry*), SR26 (*lmdF-mCherry*), SR38 (*rlpA-mCherry*), SR14 (*venus-pbp2*), and EC93 (*yfp-rodZ*) were grown to exponential phase in MB medium, treated with 37 µM for 24 h, and imaged by DIC and fluorescence microscopy. Scale bar, 3 µm.

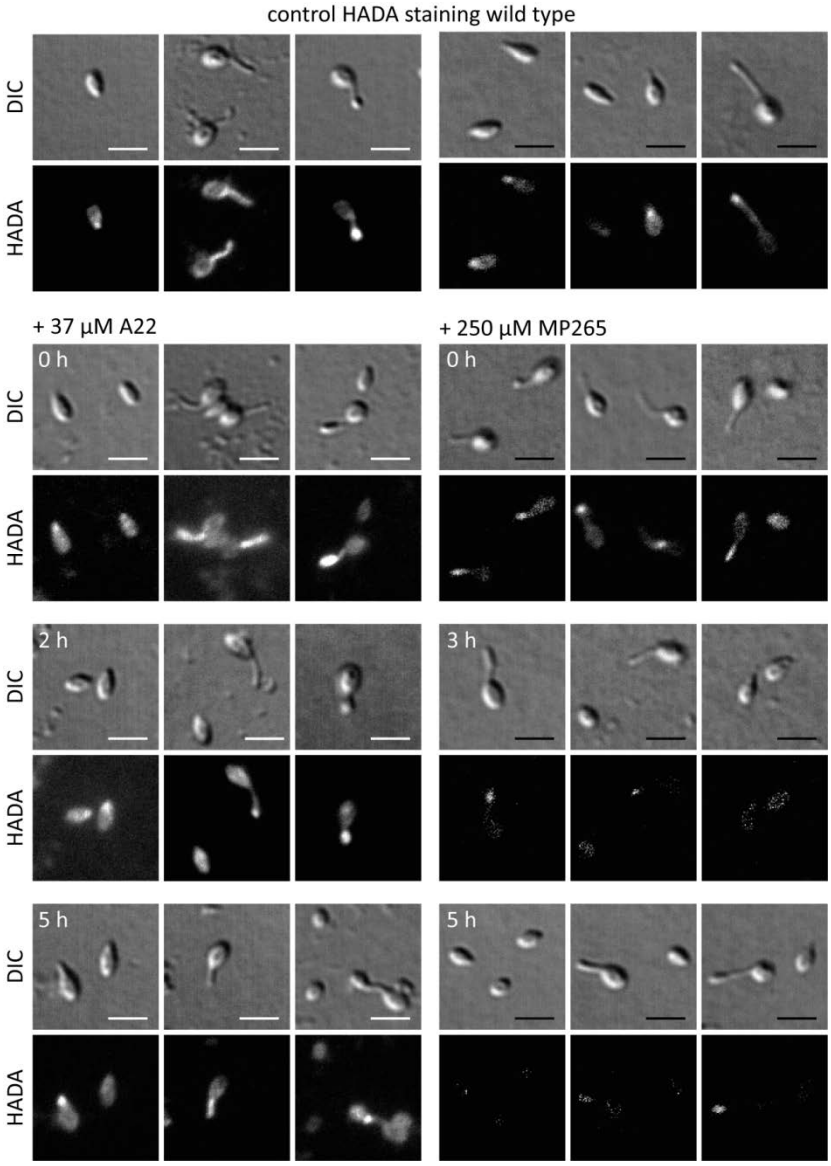

Figure S15. Peptidoglycan is still incorporated in the presence of A22 and MP265. A) Peptidoglycan is still incorporated in the presence of A22. The *H. neptunium* wild type was grown to exponential phase in MB medium and treated with 37 µM A22. Immediately after the addition of A22 as well as 2 and 5 h later the cells were pulse-labelled with HADA and imaged by DIC and fluorescence microscopy. Scale bar, 2 µm. **B)** Peptidoglycan is still incorporated in the presence of MP265. The *H. neptunium* wild type was grown to exponential phase in MB medium and treated with 250 µM MP265. Immediately after the addition of MP265 as well as 2 and 5 h later the cells were pulse-labelled with HADA and imaged by DIC and fluorescence microscopy. Scale bar, 3 µm

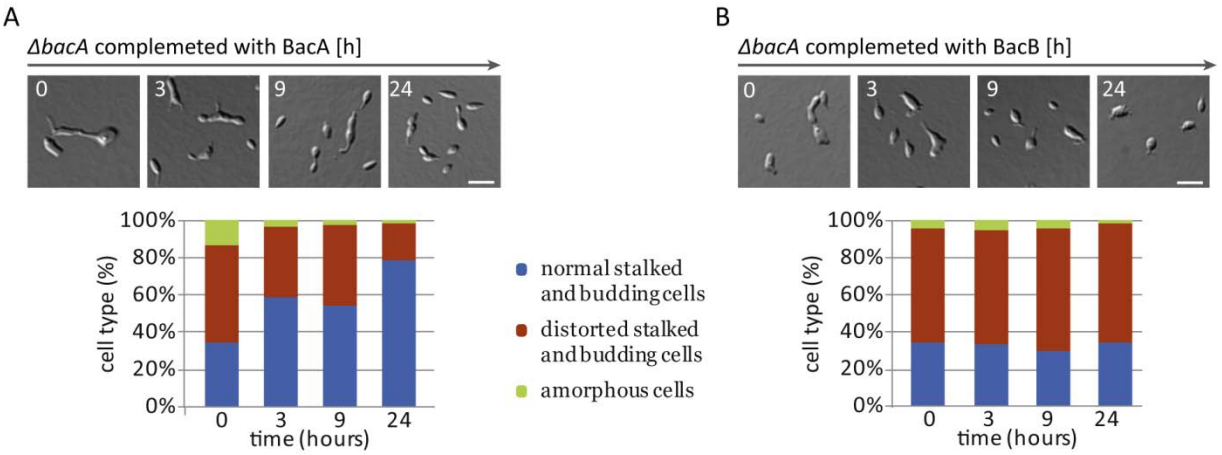

Figure S16. Elevated BacB levels cannot complement the *ΔbacA* mutant. A) Inducible expression of BacA can alleviate the phenotype of the *ΔbacA* deletion strain. Strain EC41 (*ΔbacA* P_{Cu}::P_{Cu}-*bacA*) was grown to exponential phase in MB, induced with 300 µM $CuSO_4$, and monitored at the indicated time points by DIC microscopy. Scale bar, 3 µm. 100 cells per time point were quantified according to their morphological defects (excluding swarmer cells). **B)** Inducible expression of BacB is unable to complement the phenotype of the *ΔbacA* deletion strain. Strain EC43 (*ΔbacA* P_{Zn}::P_{Zn}-*bacB*) was grown to exponential phase in MB, induced with 500 µM $ZnSO_4$ and monitored at the indicated time points by DIC microscopy. Scale bar, 3 µm. 100 cells per time point were classified according to their morphological defects (excluding swarmer cells).

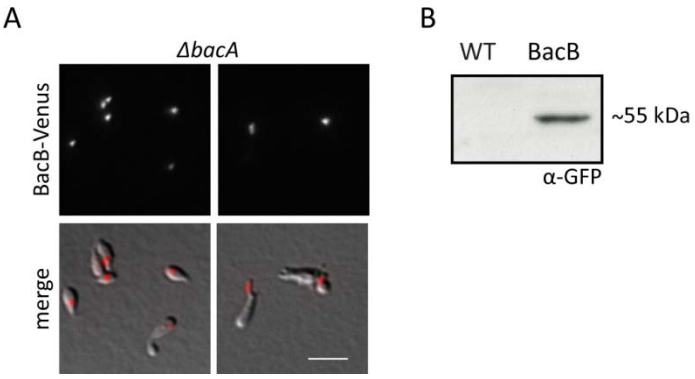

Figure S17. BacB requires BacA for correct localization in swarmer cells. A) Strain EC60 (*ΔbacA* P_{Zn}::P_{Zn}-*bacB-venus*) was grown to exponential phase in MB, induced with 500 µM $ZnSO_4$ for 4 h, and visualized by DIC and fluorescence microscopy. Scale bar, 3 µm. **B)** Expression level of BacB-Venus under the control of the P_{Zn} in the *ΔbacA* deletion strain. The *H. neptunium* wild type and strain EC60 (*ΔbacA* P_{Zn}::P_{Zn}-*bacB-venus*) were cultivated and induced as described in A). Additionally samples were taken and subjected to immunoblot analysis using an anti-GFP antibody.

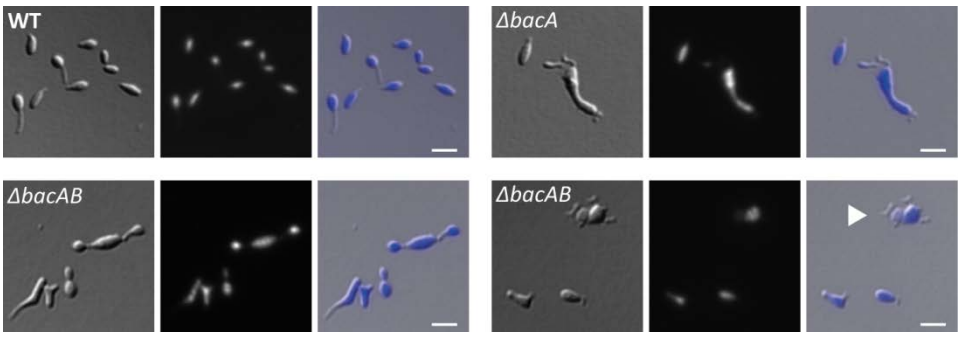

Figure S18. Nucleoid distribution is largely unaffected in the bactofilin deletion mutants. The *H. neptunium* wild type and strains EC23 (*ΔbacB*), EC28 (*ΔbacA*), and EC33 (*ΔbcaAB*) were grown to exponential phase in MB medium, incubated with 1.5 µg/mL DAPI for 15 min at RT in the dark, and analysed by DIC and fluorescence microscopy. White arrow indicates anucleated cell compartment. Scale bar, 3 µm.

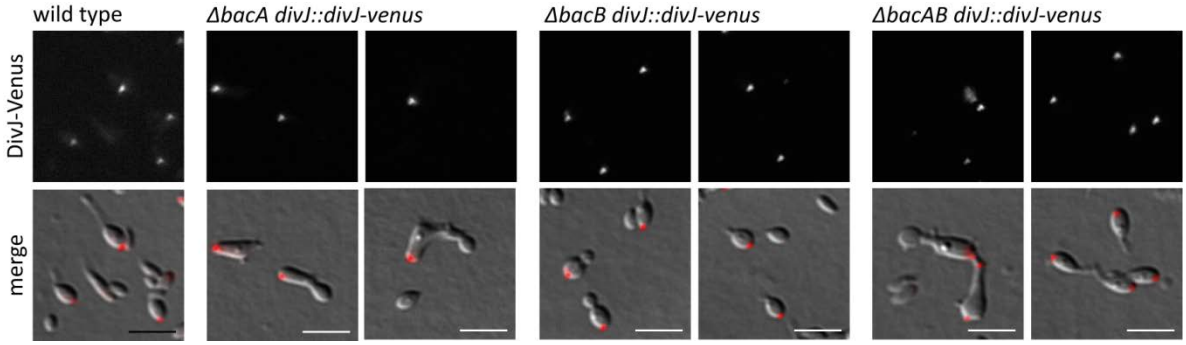

Figure S19. Cell polarity is maintained in the bactofilin deletion mutants. The *H. neptunium* wild type and strains EC86 (*ΔbacB divJ::divJ-venus*), EC87 (*ΔbacA divJ::divJ-venus*), and EC88 (*ΔbacAB divJ::divJ-venus*) were grown to exponential phase in MB medium and analysed by DIC and fluorescence microscopy. Scale bar, 3 µm.

5.2. Supplemental tables

Table 18. Growth rates of all deletion strains

Strain	Genotype	Growth rate compared to wt (%)	Biofilm (%)
LE670	Wild type	100	100
CR04	LE670 *ΔldtB*	93	97
EC21	LE670 *Δslt*	104	105
EC23	LE670 *ΔbacB*	96	0
EC26	LE670 *Δpbp1X*	104	3
EC27	LE670 *Δpbp1C*	104	1
EC28	LE670 *ΔbacA*	76	120
EC33	LE670 *ΔbacAB*	71	111
EC36	LE670 *ΔlmdA*	104	1
EC38	LE670 *ΔlmdD*	104	0
EC39	LE670 *ΔlmdE*	115	0
EC46	LE670 *ΔdacL*	115	0
EC53	LE670 *ΔlmdB*	115	1
EC57	LE670 *Δpbp1C1X*	92	6
EC71	LE670 *Δccrp*	82	127
EC89	LE670 *ΔmtgA*	100	105
EC90	LE670 *ΔlmdF*	100	103
EC95	LE670 *ΔmltA*	110	108
SR07	LE670 *ΔglpA*	98	147
SR08	LE670 *ΔdacH*	98	129
SR11	LE670 *ΔdacB*	98	189
SR18	LE670 *ΔamiC*	98	1
SR20	LE670 *ΔmltB*	100	90
SR31	LE670 *ΔldtA*	93	95
SR32	LE670 *ΔldtAB*	93	104
SR33	LE370 *ΔrlpA*	93	99

Table 19. Growth rates of all fusion strains

Strain	Genotype	Growth rate compared to wt (%)	Biofilm (%)
EC61	LE670 *bacA-yfp*	92	99
EC63	LE670 *mreB-mCherry*^{SW}	107	166
EC67	LE670 *bacB-venus*	112	72
EC68	LE670 *bacA-yfp bacB-mCherry*	90	113
EC70	LE670 P_{Cu}::P_{Cu}-*HNE0674 (amiC)-mCherry*	107	70
EC74	LE670 *bacA-yfp mreB-mCherry*^{SW}	118	113
EC75	LE670 *bacB-venus mreB-mCherry*^{SW}	101	71
EC76	LE670 *bacB-mCherry*	102	86
EC93	LE670 *yfp-rodZ*	107	162
EC96	LE670 *yfp-murG*	107	172
SE161	LE670 *venus-pbp3 (ftsI)*	107	-1
SR14	LE670 *venus-pbp2*	114	133
SR26	LE670 *lmdF-mCherry*	114	0
SR28	LE670 *dacL-mCherry*	114	124
SR38	LE670 *rlpA::rlpA-mCherry*	110	180

Table 20. *E. coli* strains used in this study

Strains	Genotype/description	References
BL21(DE3)	F$^-$ *ompT hsdS*$_B$ ($r_B^- m_B^-$) *gal dcm* (DE3); protein overproduction strain	Invitrogen
BTH101	*F*$^-$ *cya*-99 *araD*139 *galE*15 *galK*16 *rpsL*1 (StrR) *hsdR*2 *mcrA*1 *mcrB*1 cya; BACTH reporter strain	Euromedex, France
Rosetta™2(DE3)/pLysS	F$^-$ *ompT hsdS*$_B$ ($r_B^- m_B^-$) *gal dcm* (DE3) pLysSRARE2 (CamR); protein overproduction strain	Novagen®, Germany
TOP10	F$^-$ *mcr*A Δ(*mrr-hsd*RMS-*mcr*BC) Φ80*lac*ZΔM15 Δ*lac*X74 *rec*A1 *ara*D139 Δ(*ara leu*) 7697 *gal*U *gal*K *rps*L (Str^R) *end*A1 *nup*G	Invitrogen
WM6034	*thrB1*004 *pro thi rpsL hsdS lacZ*ΔM15 RP4–1360 Δ(*araBAD)567 ΔdapA*1341::[*erm pir*(wt)]	W. Metcalf (unpublished)
XL1-Blue	*recA*1 *endA*1 *gyrA*96 *thi*-1 *hsdR*17 *supE*44 *relA*1 *lac* [F´ *proAB lacI*qZΔ*M15* Tn*10* (TetR)]; cloning strain	Agilent Technologies, USA

Table 21. *H. neptunium* and *C. crescentus* strains used in this study

Strains	Genotype/description	Construction	References
LE670	*H. neptunium* wild type	ATCC 15444	E. Leifson, 1964 (350)
CB15N	*C. crescentus* wild type	Synchronizable derivate	Evinger, 1977 (416)
CR01	LE670 P_{Cu}::P_{Cu}-HNE0929 (*ldtA*)-*mCherry*	Integration of pCR01 in LE670	C. Regh, 2015 (415)
CR02	LE670 P_{Cu}::P_{Cu}-HNE3551 (*ldtB*)-*mCherry*	Integration of pCR02 in LE670	C. Regh, 2015 (415)
CR04	LE670 *ΔldtB*	In-frame deletion of *ldtB* in LE670 using pCR04	C. Regh, 2015 (415)
EC21	LE670 ΔHNE2801 (*sltA*)	In-frame deletion of *slt* in LE670 using pEC28	E. Cserti, 2011 (417)
EC23	LE670 ΔHNE0444 (*bacB*)	In-frame deletion of *bacB* in LE670 using pEC29	E. Cserti, 2011 (417)
EC26	LE670 ΔHNE0768 *(pbp1X)*	In-frame deletion of *pbp1X* in LE670 using pEC22	This study
EC27	LE670 ΔHNE3002 *(pbp1C)*	In-frame deletion of *pbp1C* in LE670 using pEC26	This study
EC28	LE670 ΔHNE2629 (*bacA*)	In-frame deletion of *bacA* in LE670 using pEC32	This study
EC33	LE670 *ΔbacA ΔbacB*	In-frame deletion of *bacB* in EC28 using pEC29	This study
EC36	LE670 ΔHNE0632 (*lmdA*)	In-frame deletion of *lmdA* in LE670 using pEC34	This study
EC38	LE670 ΔHNE2982 (*lmdD*)	In-frame deletion of *lmdD* in LE670 using pEC38	This study

Table 21. *H. neptunium* and *C. crescentus* strains used in this study (continued)

EC39	LE670 ΔHNE3210 (*lmdE*)	In-frame deletion of *lmdE* in LE670 using pEC39	This study
EC41	EC28 P_{Cu}::P_{Cu}-*bacA*	Integration of pEC60 into EC28	This study
EC43	EC28 P_{Zn}::P_{Zn}-*bacB*	Integration of pEC61 into EC28	This study
EC46	LE670 ΔHNE1814 (*dacL*)	In-frame deletion of *dacL* in LE670 using pEC64	This study
EC47	LE670 *bacA-HA*	Gene replacement in LE670 using pEC62	This study
EC51	LE670 P_{Zn}::P_{Zn}-CC1873 (*bacA*$_{CC}$)-*venus*	Integration of pEC80 into LE670	This study
EC53	LE670 ΔHNE0633 *(lmdB)*	In-frame deletion of *lmdB* in LE670 using pEC35	This study
EC57	LE670 *Δpbp1X Δpbp1C*	In-frame deletion of *pbp1C* in EC26 using pEC26	This study
EC58	LE670 P_{Cu}::P_{Cu}-HNE0630-*mCherry*	Integration of pEC91 into LE670	This study
EC59	LE670 P_{Cu}::P_{Cu}-*mCherry*-HNE0630	Integration of pEC92 into LE670	This study
EC60	EC28 P_{Zn}::P_{Zn}-*bacB-venus*	Integration of pEC59 into EC28	This study
EC61	LE670 *bacA-yfp*	Gene replacement in LE670 using pEC74	This study
EC63	LE670 *mreB-mCherry*^{SW}	Gene replacement in LE670 using pEC87	This study
EC64	EC33 P_{Zn}::P_{Zn}-*bacA*$_{CC}$-*venus*	Integration of pEC80 into EC33	This study
EC67	LE670 *bacB-venus*	Gene replacement in LE670 using pEC75	This study
EC68	LE670 *bacA-yfp*	Gene replacement in EC61 using pEC76	This study
EC70	LE670 P_{Cu}::P_{Cu}-HNE0674 (*amiC*)-*mCherry*	Integration of pEC115 in LE670	This study
EC71	LE670 ΔHNE3462 (*ccrp*)	In-frame deletion of *ccrp* in LE670 using pEC106	This study
EC72	EC28 P_{Cu}::P_{Cu}-*bacA*$_{CC}$	Integration of pEC108 into EC28	This study
EC73	EC33 P_{Cu}::P_{Cu}-*bacA*$_{CC}$	Integration of pEC108 into EC33	This study
EC74	EC63 *bacA-yfp*	Gene replacement in EC63 using pEC74	This study
EC75	EC63 *bacB-venus*	Gene replacement in EC63 using pEC75	This study
EC81	EC28 *mreB-mCherry*^{SW}	Gene replacement in EC28 using pEC87	This study
EC82	EC33 *mreB-mCherry*^{SW}	Gene replacement in EC33 using pEC87	This study
EC86	EC23 *divJ::divJ* (HNE0764)-*venus*	Integration of pOL1 in EC23	This study
EC87	EC28 *divJ::divJ-venus*	Integration of pOL1 in EC28	This study
EC88	EC33 *divJ::divJ-venus*	Integration of pOL1 in EC33	This study
EC89	LE670 ΔHNE3102 (*mtgA*)	In-frame deletion of *mtgA* in LE670 using pEC65	This study
EC90	LE670 ΔHNE3409 (*lmdF*)	In-frame deletion of *lmdF* in LE670 using pEC126	This study
EC93	LE670 *yfp*-HNE0620 (*rodZ*)	Gene replacement in LE670 using pEC129	This study
EC95	LE670 ΔHNE0008 (*mltA*)	In-frame deletion of *mltA* in LE670 using pEC157	This study
EC96	LE670 *yfp*-HNE3024 (*murG*)	Gene replacement in LE670 using pEC128	This study
SE161	LE670 *venus*-HNE3030 (*pbp3/ftsI*)	Gene replacement in LE670 using pSE68	S. Eisheuer, 2016 (418)
SR07	*LE670 ΔHNE0445 (glpA)*	In-frame deletion of *glpA* in LE670 using pSR02	S. Rosskopf, 2014 (384)
SR08	LE670 ΔHNE1025 (*dacH*)	In-frame deletion of *dacH* in LE670 using pSR03	S. Rosskopf, 2014 (384)
SR11	LE670 ΔHNE0402 (*dacB*)	In-frame deletion of *dacB* in LE670 using pSR01	S. Rosskopf, 2014 (384)
SR14	LE670 *venus*-HNE2934 (*pbp2*)	Gene replacement in LE670 using pSR06	S. Rosskopf, 2014 (384)
SR18	LE670 *ΔamiC*	In-frame deletion of *amiC* in LE670 using pSR22	S. Rosskopf, 2014 (384)
SR20	LE670 ΔHNE3349 (*mltB*)	In-frame deletion of *mltB* in LE670 using pSR19	S. Rosskopf, 2014 (384)
SR24	LE670 *lmdB-mCherry*	Gene replacement in LE670 using pSR13	S. Rosskopf, 2014
SR26	LE670 *lmdF-mCherry*	Gene replacement in LE670 using pSR17	S. Rosskopf, 2014
SR27	LE670 *ccrp-mCherry*	Gene replacement in LE670 using pSR20	S. Rosskopf, 2014
SR28	LE670 *dacL-mCherry*	Gene replacement in LE670 using pSR38	S. Rosskopf, 2014
SR31	LE670 *ΔldtA*	In-frame deletion of *ldtA* in LE670 using pEC174	S. Rosskopf (384)
SR32	LE670 *ΔldtA ΔldtB*	In-frame deletion of *ldtA* in CR04 using pEC174	S. Rosskopf (384)
SR33	LE670 *Δ*HNE1815 (*rlpA*)	In-frame deletion of *rlpA* in LE670 using pEC172	S. Rosskopf (384)
SR38	LE670 *rlpA::rlpA-mCherry*	Integration of pSR47 in LE670	S. Rosskopf

Table 22. General plasmids used in this study

Plasmids	Description	References
pCCFPC-3	Integration plasmid to construct C-terminal fusion to cfp under the control of P_{Cu}, Kan^R	Jung, 2014 (3)
pCCFPN-2	Integration plasmid to construct N-terminal fusion to *cfp* under the control of P_{Cu}, Kan^R	Jung, 2014 (3)
pCCHYC-2	Integration plasmid to construct C-terminal fusion to *mCherry* under the control of P_{Cu}, Kan^R	Jung, 2014 (3)
pCCHYC-3	Integration plasmid to construct C-terminal fusion to *mCherry* under the control of P_{Cu}, Rif^R	Jung, 2014 (3)
pCCHYN-3	Integration plasmid to construct N-terminal fusion to *mCherry* under the control of P_{Cu}, Rif^R	Jung, 2014 (3)
pCHYC-2	Integration plasmid to construct C-terminal fusion to mCherry at the site of interest, Kan^R	Thanbichler, 2007 (419)
pCVENC-2	Integration plasmid to construct C-terminal fusion to *venus* under the control of P_{Cu}, Kan^R	Jung, 2014 (3)
pCVENN-3	Integration plasmid to construct N-terminal fusion to *venus* under the control of P_{Cu}, Rif^R	Jung, 2014 (3)
pCYFPC-2	Integration plasmid to construct C-terminal fusion to *yfp* under the control of P_{Cu}, Kan^R	Jung, 2014 (3)
pCYFPN-2	Integration plasmid to construct N-terminal fusion to *yfp* under the control of P_{Cu}, Kan^R	Jung, 2014 (3)
pET21a(+)	Plasmid for overexpression of C-terminally His_6-tagged proteins under the control of P_{T7}, Amp^R	Novagen®, Germany
pKNT18	Plasmid for constructing fusions to the N-terminal end of T25 fragment, Kan^R	Karimova, 1998 (403)
pKT18	Plasmid for constructing fusions to the C-terminal end of T25 fragment, Kan^R	Karimova, 1998 (403)
pKT18-zip	Derivative of pKT in which the leucine zipper of GCN4 is fused in-frame to the T25 fragment	Karimova, 1998 (403)
pNPTS138	*sacB*-containing suicide vector used for double homologous recombination, Kan^R	M.R. Alley, unpublished
pRSFDuet-1	Plasmid for the coexpression of target genes under the control of P_{T7}, Kan^R	Novagen®, Germany
pUT18	Plasmid for constructing fusions to the N-terminal end of T18 fragment, Amp^R	Karimova, 1998 (403)
pUT18C	Plasmid for constructing fusions to the C-terminal end of T18 fragment, Amp^R	Karimova, 1998 (403)
pUT18C-zip	Derivative of pUT18C in which the leucine zipper of GCN4 is fused in-frame to the T18 fragment	Karimova, 1998 (403)
pZVENN-2	Integration plasmid to construct N-terminal fusion to *venus* under the control of P_{Zn}, Kan^R	Jung, 2014 (3)

Table 23. Complete list of plasmids generated for *H. neptunium* used in this study

Plasmid	Description	References
pCR01	pCCHYC-2 harbouring *ldtA*	C. Regh, 2015 (415)
pCR02	pCCHYC-2 harbouring *ldtB*	C. Regh, 2015 (415)
pCR04	pNPTS135 derivate for generating in-frame deletion of *ldtB*	C. Regh, 2015 (415)
pEC22	pNPTS135 derivate for generating in-frame deletion of *pbp1X*	E. Cserti, 2011 (417)
pEC23	pNPTS135 derivate for generating in-frame deletion of *pbp1C*	E. Cserti, 2011 (417)
pEC25	pNPTS135 derivate for generating in-frame deletion of *pbp1A*	E. Cserti, 2011 (417)
pEC26	pNPTS135 derivate for generating in-frame deletion of *pbp2*	E. Cserti, 2011 (417)
pEC28	pNPTS135 derivate for generating in-frame deletion of *sltA*	E. Cserti, 2011 (417)
pEC29	pNPTS135 derivate for generating in-frame deletion of *bacB*	E. Cserti, 2011 (417)
pEC31	pNPTS135 derivate for generating in-frame deletion of *lmdC*	This study
pEC32	pNPTS135 derivate for generating in-frame deletion of *bacA*	This study
pEC34	pNPTS135 derivate for generating in-frame deletion of *lmdA*	This study
pEC35	pNPTS135 derivate for generating in-frame deletion of *lmdB*	This study
pEC37	pNPTS135 derivate for generating in-frame deletion of *mreB*	This study

Table 23. Complete list of plasmids generated for *H. neptunium* used in this study (continued)

pEC38	pNPTS135 derivate for generating in-frame deletion of *lmdD*	This study
pEC39	pNPTS135 derivate for generating in-frame deletion of *lmdE*	This study
pEC48	pCCHYC-2 harbouring *mreB*	This study
pEC59	pZVENC-2 harbouring *bacB*	This study
pEC60	pCVENC-3 harbouring *bacA stop*	This study
pEC61	pZVENC-2 harbouring *bacB stop*	This study
pEC62	pNPTS135 derivate for gene replacement of *bacA*	This study
pEC64	pNPTS135 derivate for generating in-frame deletion of *dacL*	This study
pEC65	pNPTS135 derivate for generating in-frame deletion of *mtgA*	This study
pEC70	pCCHYC-3 harbouring *bacB*	This study
pEC74	pNPTS135 derivate for gene replacement of *bacA*	This study
pEC75	pNPTS135 derivate for gene replacement of *bacB*	This study
pEC76	pNPTS135 derivate for gene replacement of *bacB*	This study
pEC80	pZVENC-2 harbouring $bacA_{CC}$	This study
pEC86	pET28a(+) harbouring *bacA*	This study
pEC87	pNPTS135 derivate for gene replacement of *mreB*	This study
pEC91	pCCHYC-2 harbouring HNE0630	This study
pEC92	pCCHYN-2 harbouring HNE0630	This study
pEC93	pNPTS135 derivate for generating in-frame deletion of HNE0630	This study
pEC94	pCCHYC-3 harbouring *bacB*	This study
pEC103	pCCHYC-2 harbouring $bacA_{CC}$	This study
pEC106	pNPTS135 derivate for gene replacement of *ccrp*	This study
pEC115	pCCHYC-2 harbouring *amiC*	This study
pEC126	pNPTS135 derivate for generating in-frame deletion of *lmdF*	This study
pEC128	pNPTS135 derivate for gene replacement of *murG*	This study
pEC129	pNPTS135 derivate for gene replacement of *rodZ*	This study
pEC157	pNPTS135 derivate for generating in-frame deletion of *mltA*	This study
pEC172	pNPTS135 derivate for generating in-frame deletion of *rlpA*	This study
pEC173	pNPTS135 derivate for generating in-frame deletion of *ftsI*	This study
pEC174	pNPTS135 derivate for generating in-frame deletion of *ldtA*	This study
pOL1	pVENC-2 harbouring the last 607 bp of *divJ*	O. Leicht, 2010 (387)
pSE68	pNPTS135 derivate for gene replacement of *ftsI*	S. Eisheuer, 2016 (418)
pSR01	pNPTS135 derivate for generating in-frame deletion of *dacB*	S. Rosskopf, 2014 (384)
pSR02	pNPTS135 derivate for generating in-frame deletion of *glpA*	S. Rosskopf, 2014 (384)
pSR03	pNPTS135 derivate for generating in-frame deletion of *dacH*	S. Rosskopf, 2014 (384)
pSR06	pNPTS135 derivate for gene replacement of *pbp2*	S. Rosskopf, 2014 (384)
pSR17	pNPTS135 derivate for gene replacement of *lmdF*	S. Rosskopf, 2014 (384)
pSR19	pNPTS135 derivate for gene replacement of *mltB*	S. Rosskopf, 2014 (384)
pSR20	pNPTS135 derivate for gene replacement of *ccrp*	S. Rosskopf, 2014 (384)
pSR22	pNPTS135 derivate for generating in-frame deletion of *amiC*	S. Rosskopf, 2014 (384)
pSR38	pNPTS135 derivate for gene replacement of *dacL*	S. Rosskopf, 2014 (384)
pSR47	pCHY-2 harbouring *rlpA*	S. Rosskopf
pSW56	pYFPC-2 harbouring *bacA*	S. Wick

Table 24. Complete list of plasmids generated for *E.coli* used in this study

Plasmid	Description	Purpose	References
pEC119	pRSFDuet-1 harbouring *bacA*	Localization	This study
pEC120	pRSFDuet-1 harbouring *bacB*	Localization	This study
pEC121	pRSFDuet-1 harbouring *bacA* and *bacB*	Localization	This study
pEC131	pKNT25 harbouring *bacA*	BATCH	This study
pEC132	pUT18 harbouring *bacA*	BATCH	This study
pEC133	pKNT25 harbouring *bacB*	BATCH	This study
pEC134	pUT18 harbouring *bacB*	BATCH	This study
pEC135	pKT25 harbouring *mreB*	BATCH	This study
pEC136	pUT18C harbouring *mreB*	BATCH	This study
pEC137	pKT25 harbouring *mreC*	BATCH	This study
pEC138	pUT18C harbouring *mreC*	BATCH	This study
pEC139	pKNT25 harbouring HNE0630	BATCH	This study
pEC140	pUT18 harbouring HNE0630	BATCH	This study
pEC141	pKT25 harbouring *rodZ*	BATCH	This study
pEC142	pUT18Charbouring *rodZ*	BATCH	This study
pEC143	pKNT25 harbouring *murG*	BATCH	This study
pEC144	pUT18 harbouring *murG*	BATCH	This study
pEC145	pKT25 harbouring *lmdA*	BATCH	This study
pEC146	pUT18C harbouring *lmdA*	BATCH	This study
pEC147	pKT25 harbouring *lmdB*	BATCH	This study
pEC148	pUT18C harbouring *lmdB*	BATCH	This study

Table 25. Oligonucleotides used for PCR amplification. Restriction sites are indicated in bold.

Name	Designation	Sequence (5´ → 3´)
oEC33	HNE_0768_del1	TAT**CTGCAG**CACGAAGCCCGGCATGTCCTCAT
oEC34	HNE_0768_del2	TAT**AAGCTT**GGGTGAAGGCACCCGCTGGTATA
oEC35	HNE_0768_del3	ATAT**AAGCTT**CAGGCGGAATAGGCCAAAGAACAG
oEC36	HNE_0768_del4	ATAT**GCTAGC**GCTATGCGTGGCGATGGCGGACCT
oEC37	HNE_1911_del1	AAA**CTGCAG**CGCGCCGATGAGGGTTACCGTGTCC
oEC38	HNE_1911_del2	AAA**AAGCTT**TGTCATCTGCAAACCTTGCGGCGAA
oEC39	HNE_1911_del3	ATAT**AAGCTT**GACGTCTTCTAGCGCGACAAACG
oEC40	HNE_1911_del4	ATATGCTAGCCCGCCTTCGCCTGCATTGATCTG
oEC41	HNE_2629_del1	TAT**GAATTC**TCGGCGGAGATCAGTCCTTCATGAC
oEC43	HNE_2629_del3	TTTT**AAGCTT**CCGCCGAGCTGATCGCGCGAGGGTC
oEC44	HNE_2629_del4	TTTT**GCTAGC**ACGCGCTTGTCTGCTTCGAGGTTCA
oEC45	HNE_2934_del1	TTTG**AATTC**GAGCGGCCATTGAGCGGCATCATAC
oEC46	HNE_2934_del2	TTT**AAGCTT**CCGGCATGAGCCGGGACGGCTTTAC
oEC47	HNE_2934_del3	TTTT**AAGCTT**CCGGCTCATGTCGTCTGCCCTGATG
oEC48	HNE_2934_del4	TTTT**GCTAGC**GCCCAGCGCGCGGCTCGCCTTT
oEC49	HNE_3002_del1	AAA**GAATTC**GGATCAATGCCGCGAATGAAGTGGG
oEC50	HNE_3002_del2	TTT**AAGCTT**GACCCCGCCTGACGCCCGGTCTG
oEC51	HNE_3002_del3	TTTT**AAGCTT**GCGTTTCGGCACGGACTGGCCC
oEC52	HNE_3002_del4	TTTT**GCTAGC**GCGCTTCCTCGGCATGGACGGC
oEC55	HNE_2801_del1	ATAT**AAGCTT**TATAAAGCACCACGGGCAGGGCGAC

Table 25. Oligonucleotides used for PCR amplification (continued)

oEC56	HNE_2801_del2	ATAT**GCTAGC**AATCCGGAGCATGGTTCGGCT
oEC57	HNE_2801_del3	ATAT**GCTAGC**GGCCGCCGCTGACCGGAAGTGTC
oEC58	HNE_2801_del4	ATAT**GAATTC**GTAAGCACGCCAATGGTCGCCGA
oEC67	HNE_0444_del1	AAA**GAATTC**CAGGCCGAACTCGCCATCGAAAAGG
oEC68	HNE_0444_del2	TAT**AAGCTT**ACAGCCGTCTAGTTGTTCTGCAGG
oEC69	HNE_0444_del3	TAT**AAGCTT**ATCTGCTGCCATCCGCGTGTCTCCC
oEC70	HNE_0444_del4	TTTT**GCTAGC**CAGTTGTGCGCGTGTTCGAGATCG
oEC79	HNE_2629_del2 new	TAT**AAGCTT**GTTATTCTTTGTGAACATGTTTGCC
oEC80	HNE_2628_del1	TAT**GAATTC**TCGTTCTGGGCGTGTCGCGCGATTC
oEC81	HNE_2628_del2	TAT**AAGCTT**CTTTAAGGTTGGCACTCCACTTCGC
oEC82	HNE_2628_del3	TAT**AAGCTT**GGCAAACATGTTCACAAAGAATAAC
oEC83	HNE_2628_del4	TATA**GCTAGC**CGGCGTGCCCGAAGCGAGCGACGAG
oEC84	HNE_0632_del1	TAT**AAGCTT**GGTGTCCGAGCAGGCCCGCGAGCAT
oEC85	HNE_0632_del2	ATA**GGATCC**AACTCCGCCCGGATGGCAAACGCCC
oEC86	HNE_0632_del3	ATA**GGATCC**GACAGGAATCCGAGGCAGCTTTCGC
oEC87	HNE_0632_del4	TTTT**GCTAGC**GACACCGCCTATGCCCACCTCTCGC
oEC88	0633_del1new	TAT**CTGCAG**GGCGCAGGCGCTGGCCCCGCGTGGG
oEC89	HNE_0633_del2	TAT**GAATTC**CCGCGTGAAGCAACGCCCGTAAGCC
oEC90	HNE_0633_del3	TAT**GAATTC**GGTTGCCGGGGCGATGGGAAGGTCG
oEC91	HNE_0633_del4	TTTT**GCTAGC**CTTCCTGGGCCTCTGCGGGCACATC
oEC92	HNE_2982_del1	TAT**CTGCAG**TCTATCAGGAAGACGGCAAGGTTTG
oEC93	HNE_2982_del2	TAT**AAGCTT**CCCTATGAAGGGGCGTTGCAGGCCG
oEC94	HNE_2982_del3	TAT**AAGCTT**GGCCGCGAGCGCAAGAGCAATCGCC
oEC95	HNE_2982_del4	TTTT**GCTAGC**CATTCTTCCCAAGCCCGGCATTGAC
oEC96	HNE_3210_del1	TAT**GAATTC**GGCCGTTGATCTCGGTGATATAGTC
oEC97	HNE_3210_del2	TAT**AAGCTT**CTTAATCCTGCAGAGTGGTTGTCGC
oEC98	HNE_3210_del3	TAT**AAGCTT**AGGGCGGAAAAAGCGCATGCGCGGA
oEC99	HNE_3210_del4	TTTT**GCTAGC**GGGCGTTGGCGTTGGGTGGCGCTTG
oEC104	HNE_2937_del1	TAT**CTGCAG**ACGCCCTGCATTTCGCCGGCATTGG
oEC105	HNE_2937_del2	TAT**AAGCTT**AAAATGAAAAGCGTCCTCTGCCCGG
oEC106	HNE_2937_del3	TAT**AAGCTT**TGTGGACAACAGGCCGAGGAGGCTA
oEC107	HNE_2937_del4	TTTT**GCTAGC**GCGTCCTGGAGATTTGCAGCGCCGG
oEC123	2937_for	TTT**GGTACC**ATGATCGGTAGCCTCCTCGGCCTG
oEC124	2937_rev	TTTT**GCTAGC**TCAGACTTCCGGGCAGAGGACGC
oEC132	HNE_2937_dep_rev	ATA**GGTACC**TCAGACTTCCGGGCAGAGGACGC
oEC137	HNE_1814_del1	TAT**CTGCAG**GCTTTTGGTCTGCGCTCGAACGTG
oEC138	HNE_1814_del2	ATAT**GAATTC**GTTCGCACGTTTATTTCCAGCAGC
oEC139	HNE_1814_del3	ATAT**GAATTC**GAGCGCTCCGAGGGTCAGTAGGGC
oEC140	HNE_1814_del4	TATA**GCTAGC**CGTGTCGGCGCCGGTTGCTGC
oEC142	HNE_3102_del2	ATAT**GAATTC**GTAGGCGGGGGCGGAGGAGTTCATG
oEC143	HNE_3102_del3	ATAT**GAATTC**CCACCGGCCCCACAGAACTCCGCC
oEC151	HNE_0444_rev	TATA**GGTACC**GACGGCTGTGCTGGCCGGCGGCTC
oEC157	HNE_0674_for	TATA**CATATG**GGCACTCAACGCCCGTCTCATAC
oEC158	0444_comp_rev	TATA**GGTACC**CTAGACGGCTGTGCTGGCCGGCGG
oEC159	2629_comp_rev	TATA**GGTACC**TCAGCTCGGCGGCGAGGAACTCGAG
oEC160	HNE_2629_HA_for	TAT**AAGCTT**ATGTTCACAAAGAATAACAAAACCCCAGC
oEC161	HNE_2629_HA_rev	ATA**GGATCC**CTAAGCGTAGTCTGGGACGTCGTATGGGTAGCTCGGCGGCGAGGAACTCGAG
oEC170	mCherry/venus_rev	ATA**GGATCC**TTACTTGTACAGCTCGTCCAT
oEC171	HNE_0444_for2	TAT**AAGCTT**ATGGCAGCAGATAAGGCAAGGGAACCG
oEC178	2629-FP_eol_for	TGGACGAGCTGTACAAGTAACCGCCGAGCTGATCGCGCGA

Table 25. Oligonucleotides used for PCR amplification (continued)

oEC179	2629-FP_eol_rev	TCGCGCGATCAGCTCGGCGGTTACTTGTACAGCTCGTCCA
oEC180	0444-FP_eol_for	TGGACGAGCTGTACAAGTAATTGTTCTGCAGGTTGCGCAGAC
oEC181	0444-FP_eol_rev	GTCTGCGCAACCTGCAGAACAATTACTTGTACAGCTCGTCCA
oEC182	2937_for2	TAT**AAGCTT**ATGATCGGTAGCCTCCTCGGCCTG
oEC183	2937-SF-eol-for	CCGCGATGCCGCCTGAAAGCGGATCGAGCATGGTGAGCAAGGGCGAGGAG
oEC184	2937-SF-eol-rev	CTCCTCGCCCTTGCTCACCATGCTCGATCCGCTTTCAGGCGGCATCGCGG
oEC185	2937-SF-eol-for2	GGACGAGCTGTACAAGTCTGGTGCACCGGGTAACGGCACCGGCATGGCGC
oEC186	2937-SF-eol-rev2	GCGCCATGCCGGTGCCGTTACCCGGTGCACCAGACTTGTACAGCTCGTCC
oEC191	HNE_0630_for	TATA**CATATG**AAACGCTCACGCGGGCGC
oEC192	HNE_0630_rev	TTT**GGTACC**GTCTGTCGTCTCGGTGGAGGCG
oEC193	HNE_0630_for2	TTT**GGTACC**ATGAAACGCTCACGCGGGCGC
oEC194	HNE_0630_rev2	TATA**GCTAGC**TCAGTCTGTCGTCTCGGTGGAG
oEC195	HNE_0630_del1	TAT**AAGCTT**GCGCGCTCGATGGCGGGGCGGACGG
oEC196	HNE_0630_del2	ATA**GGATCC**GCCTGAGCGTCTGTTGCGCCCGCGT
oEC197	HNE_0630_del3	ATA**GGATCC**GTTGAAGAAGGCGCCTCCACCGAGA
oEC198	HNE_0630_del4	TATA**GCTAGC**CGTCCTGGAAGAGTTTGGCGCCCGC
oEC222	HNE_3462_del1	TTT**AAGCTT**TGAGAGGGCAGGGGCATGAT
oEC223	HNE_3462_del2	AGACGCCGCAGGTATTCGCGCTTCCCCAGCGTGTTCAGGC
oEC224	HNE_3462_del3	GCCTGAACACGCTGGGGAAGCGCGAATACCTGCGGCGTCT
oEC225	HNE_3462_del4	TATA**GCTAGCC**GGGCCGACTTCGATCAGAC
oEC228	HNE_0444_for3	TATA**GCTAGC**ATGGCAGCAGATAAGGCAAGGGAACCG
oEC229	0444_del1_extra	TTT**AAGCTT**CAGGCCGAACTCGCCATCGAAAAGG
oEC238	HNE_2629_for3	CGC**ACATGT**TCACAAAGAATAACAAAACCCCAGC
oEC242	ecfp_rev2	TAT**CAATTG**TTACTTGTACAGCTCGTC
oEC244	HNE_0620_eol_for	TATA**GCTAGC**CGCGCTCGACCATAAAGGT
oEC245	HNE_0620_eol_rev	TCCTCGCCCTTGCTCACCATATTCTACCAGTCACTTCGAC
oEC246	HNE_0620_eol_for2	GTCGAAGTGACTGGTAGAATATGGTGAGCAAGGGCGAGGA
oEC247	HNE_0620_eol_rev2	TGGGTCATGTTGTGTGCCATATGCATATTAATTAAGGCGC
oEC248	HNE_0620_eol_for3	GCGCCTTAATTAATATGCATATGGCACACAACATGACCCA
oEC249	HNE_0620_eol_rev3	TTT**AAGCTT**CGGCCAGTGTGCGGCTGAG
oEC260	HNE_3024_eol_for	TATA**GCTAGC**GCCTTTCCGGCTCTGGCGG
oEC261	HNE_3024_eol_rev	TCCGGAGCTCGAGATCTTAATAGTTCTGCGATCCTTTCGG
oEC262	HNE_3024_eol_for2	CCGAAAGGATCGCAGAACTATTAAGATCTCGAGCTCCGGA
oEC263	HNE_3024_eol_rev2	GGCAATGAAAGCAGACTTGCGGATCATAGTTCTGCGATCCTTTCCTTGTACAGCTCGTCCA
oEC264	HNE_3024_eol_for3	TGGACGAGCTGTACAAGGAAAGGATCGCAGAACTATGATCCGCAAGTCTGCTTTCATTGCC
oEC265	HNE_3024_eol_rev3	TTT**AAGCTT**GCCCGCGCCATCCAGCAGG
oEC276	HNE_2629_b2h_f	GCG**GGTACC**TATGTTCACAAAGAATAACAAAACCCCAGC
oEC277	HNE_0444_b2h_f	GCG**GGTACC**TATGGCAGCAGATAAGGCAAGGGAACCG
oEC278	HNE_2937_b2h_f	TTT**GGATCC**TATGATCGGTAGCCTCCTCGGCCTG
oEC279	HNE_0630_b2h_f	TTT**GGATCC**AATGAAACGCTCACGCGGGCGC
oEC280	HNE_0630_b2h_r	TTT**GGTACC**CGGTCTGTCGTCTCGGTGGAGGCG
oEC281	HNE_0620_b2h_f	TTT**GGATCC**AATGGCACACAACATGACCC
oEC282	HNE_0620_b2h_r	GCG**GGTACC**TCAGGGTGTCGCTGGTTCG
oEC283	HNE_3024_b2h_f	TTT**GGATCC**TATGGCTGACACCGGGACTG
oEC284	HNE_3024_b2h_r	CGC**GGTACC**CGTAGTTCTGCGATCCTTTCG
oEC285	HNE_2936_b2h_f	TTT**GGATCC**TATGGCGCGCTTCGGGCCAACAG
oEC286	HNE_2936_b2h_r	CGC**GGTACC**TTATTGGCCCTCCTGCGGCGGGATG
oEC289	HNE_3409_del1new	TTT**AAGCTT**CCCGGCCAGAAGGACACAAAATGAG
oEC290	HNE_3409_del2new	ATA**GGATCC**GGATAGTCCGATGGCGGATAAGCGT
oEC291	HNE_3409_del3new	ATA**GGATCC**TGGGTCATCCCCGAAGGCTACGAGA
oEC292	HNE_3409_del4new	TATA**GCTAGC**CGCGCTGTATATGCCGCCGGC

Table 25. Oligonucleotides used for PCR amplification (continued)

oEC295	HNE_3102_del1new	TTT**AAGCTT**GGGCCGCCACACAAACCTCGTCAGC
oEC296	HNE_3102_del4new	TATA**GCTAGC**GCAGGCGCTCATCGAGGCTGACC
oEC306	HNE_0632_b2h_for	TTT**GGATCC**TATGAAACGGACGCGAAAGCTGCCTC
oEC307	HNE_0632_b2h_rev	CGC**GGTACC**TCAAGGCGCCGGGGCGTTTGCC
oEC308	HNE_0633_b2h_for	TTT**GGATCC**TATGACCCAGGACGACCTTCCCATCG
oEC309	HNE_0633_b2h_rev	CGC**GGTACC**TCAGGGGCTTACGGGCGTTGCTTC
oEC313	HNE_0008_del1	TTT**AAGCTT**AGGATTTCGCCGCCAACATGTC
oEC314	HNE_0008_del2	TTT**GGATCC**AAGGGCGGAAAACAGGAGAGCA
oEC315	HNE_0008_del3	TTT**GGATCC**GTCGCCGCGCGCACGCCTGCGCC
oEC316	HNE_0008_del4	TATAGCTAGCCAAGGACACGGCAGACGAGTAC
oEC326	HNE_1815_del1	TTT**AAGCTT**GAACAGTATGCGATGGAAAAT
oEC327	HNE_1815_del2	TTT**GGATCC**CCGGCCAACAAAAGTCGAACG
oEC328	HNE_1815_del3	TTT**GGATCC**GGCACGGCGGACGGCCGGATC
oEC329	HNE_1815_del4	TATA**GCTAGC**CGTCATCTTGGCGAGCCGGGC
oEC331	1815_del_check_rev	GAAGATTCCAGATGCCCCGTC
oEC332	HNE_3030_del1	TTT**AAGCTT**GGCTGGTGGTGGTGACGTTCC
oEC333	HNE_3030_del2	TTT**GGATCC**CCCGACGAGCCGTGTACGATC
oEC334	HNE_3030_del3	TTT**GGATCC**CCGTTGCTTGAGGTCGATCCG
oEC335	HNE_3030_del4	TATA**GCTAGC**CCGGAAGAGGCGCACCTTGGC
oEC338	HNE_0929_del1	TTT**GGATCC**CGCAAGCGTCAGCAGCAACAG
oEC339	HNE_0929_del2	CGC**GGTACC**AAAGAGCAGAAGAAACAGGGT
oEC340	HNE_0929_del3	CGC**GGTACC**GTCCCGGAAGGAACCTTCCTG
oEC341	HNE_0929_del4	TATA**GCTAGC**CCGGCCTGCATATCCTCGTTG
MT743	CC1873-uni	TATATATA**CATATG**TTCAGCAAGCAAGCTAAATCGAACAACAAG
MT744	CC1873-rev	TA**GAGCTC**CGCCGGCGCTCTTGGCGATCGCCAGA
MT745	CC1873-rev2	TAGAGCTC**GGTACC**TTAGCCGGCGCTCTTGGCGATCG
oSS271	HNE_0674-rev	AT**GGTACC**TTGGGACGCGAGGCGGAGATCCTG
SW112	HNE2629-for	TTAA**CATATG**TTCACAAAGAATAACAAAACCCCAGCGGC
SW113	HNE2629-rev	TA**GAATTC**GAGCTCGGCGGCGAGGAACTCGAGATG
SW186	HNE0444-for	TATATA**CATATG**GCAGCAGATAAGGCAAGGGAACCG
SW187	HNE0444-rev	TATATA**GAATTC**GAGACGGCTGTGCTGGCCG

Restriction sites are indicated in bold.

Table 26. Specific oligonucleotides used to verify genotype of strains

Name	Designation	Sequence (5´ → 3´)
oEC59	1911_delcheck_for	GGTCGCGAAGGCCGGGTGAATGAAG
oEC60	1911_delcheck_rev	GCGGCGCAGGATGGAGGCCCAGTCC
oEC61	2629_delcheck_for	GCGCCCGCGGTGTTCTGGAGCTGAC
oEC62	2629_delcheck_rev	CGGATCGGCCAAGCCCGGTTTGAAC
oEC63	2801_delcheck_for	GATAGCTCACCCGGTCCATGTCGCC
oEC64	2801_delcheck_rev	GCACGGGAGTATACCAGCGCAGGAT
oEC65	2934_delcheck_for	CGCGGTGAGCGCCAGGGCGGTCGAC
oEC66	2934_delcheck_rev	CCATCAACGGCGCCATCAACGACCC
oEC71	0444_delcheck_for	CCCACAAGGAAAAGGAGACCTGAC
oEC72	0444_delcheck_rev	CATGGAAGGCCGGGGTTGTGTAG
oEC73	0768_delcheck_for	TTCGTGAAAGGGCAGGGCTGAGC
oEC74	0768_delcheck_rev2	CCATTCCCAACCGCCGCGCCTTT
oEC75	3002_delcheck_for	GCGCTGGGCACCGGACAGGGTCTC
oEC76	3002_delcheck_rev	CGGGGAGACTCCGCTGTTCCGCAC
oEC109	2628_delcheck_for	ATGCGGGCAAGTATCTGGTG
oEC110	2628_delcheck_rev	GGCAGAAAATCCACCGGCGT

Table 26. Specific oligonucleotides used to verify genotype of strains (continued)

oEC111	0632_delcheck_for	CAGGGCCGCACGGTGGATTT
oEC112	0632_delcheck_rev	CTGACTTTGCCGCCCCCACC
oEC113	0633_delcheck_for	GGCGCTGACACCGGCAAGGC
oEC114	0663_delcheck_rev	CGTGCCGCGCATTTCCAGAC
oEC115	2982_delcheck_for	TGATGGCGAGGTGCAGCGTG
oEC116	2982_delcheck_rev	GCCAAAGCCAGACCATGAGC
oEC117	3210_delcheck_for	GACCTGGAATGGATCAACGC
oEC118	3210_delcheck_rev	CCGACCCGGAAACCCGTATC
oEC121	2937_delcheck_for	GGCGGCTGGAATAATCACTG
oEC122	2937_delcheck_rev	ATGACAAGTTTGGCTATGGC
oEC147	1814_delcheck_for	TTTCCACGCGGCATCGAGCACCTG
oEC148	1814_delcheck_rev	GCCCCGCGCCTGTCGTTGCCACCC
oEC149	3102_delcheck_for	AGACGCGCCCGAGCCCGACCATTG
oEC150	3102_delcheck_rev	CGCCGAACGCTCTGCCTTTGCCCT
oEC201	0630_delcheck_for	TGGCAGGGCTGGGAAAACGCA
oEC202	0630_delcheck_rev	GTTCTTCAGCACGTCCGCCGC
oEC226	3462_del_check_for	GCATTCAGGTCGTCGGCGTC
oEC227	3462_del_check_rev	GCCACTGGTCCCGCCCACAT
oEC250	HNE_0620_check_for	GCGTGCTGGACCGGGCGGC
oEC251	HNE_0620_check_rev	GCTCGATATTGCGCCAGGG
oEC266	HNE_3024_check_for	GCATGACACTGCCTTTTGT
oEC267	HNE_3024_check_rev	GGTGACGATGGCACAGGTC
oEC274	HNE_0008_check_for	GGGCGCCTGCCTGCGAAGC
oEC275	HNE_0008_check_rev	TCGGCACGACCAAATCGAC
oEC293	3409_delcheck_f_new	CTGTCCGGCGCCAGCTATTCGGGC
oEC294	3409_delcheck_r_new	GCGGGCCTCTGGTCGCGCGCCACG
oEC297	3102_delcheck_f_new	CAAACAGCTCGCTGGCGAAGTAG
oEC298	3102_delcheck_r_new	GCGGCCCTCGTCAAGGACAGGAC
oEC317	0008_del_check_for	CTCTGTAGTTAGGGTCCCGCGCC
oEC318	0008_del_check_rev	CAGATCGAGCTGGATGAAGTGAT
oEC330	1815_del_check_for	GATTGGAATAACGGCCGAAGG
oEC330	1815_del_check_for	GATTGGAATAACGGCCGAAGG
oEC331	1815_del_check_rev	GAAGATTCCAGATGCCCCGTC
oEC331	1815_del_check_rev	GAAGATTCCAGATGCCCCGTC
oEC336	3030_del_check_for	GAGGAAGCTGTGGGCGGACGG
oEC337	3030_del_check_rev	GCCGAACGACACCACCTGCAG
oEC342	0929_del_check_for	GAAAGAAAATGCCGAGCGCCAGCG
oEC343	0929_del_check_rev	GCAGAGGGAGCGGAAAGCCAC
MT98	HA-1	ATGTACCCATACGACGTCCCAGACTACGCTTCG
MT169	HA tag-2	CTACCATGGAAGCGTAGTCTGGGACGTCGTATGGGTA

Table 27. Common oligonucleotides used for colony PCR and sequencing

Name	Sequence (5´ → 3´)
eCFP-1	GTTTACGTCGCCGTCCAGCTCGAC
eCFP-2	ATGGTCCTGCTGGAGTTCGTGACC
Duet1-MCSI-fw	GGATCTCGACGCTCTCCCTTATGC
Duet1-MCSII-fw	TTGTACACGGCCGCATAATCG
Duet1-MCSI-rev	GATTATGCGGCCGTGTACAATACG
IntSpec-1 (RecUni-1)	ATGCCGTTTGTGATGGCTTCCATGTCG
M13for	GCCAGGGTTTTCCCAGTCACGA
M13rev	GAGCGGATAACAATTTCACACAGG
mCherry-down	GGCGCCTACAACGTCAACATCAAGTTGG
mCherry-up	CTCGCCCTCGCCCTCGATCTCGAAC
P2372_check_fwd	CGCGGGCGATGTTGAGGAAGTTCTG
pCop1486_check_for	CCCCTTATCATCCAGACCAGCTACG
pCop1486_check_rev	GGCTTTTGATTTTTTGACGTCGAG
pCop1486_out_for	CGAAGTCCGCCGTGGCCGAG
pET-for	CACGATGCGTCCGGCGTAGAGGATC
pET-rev	CCTTTCAGCAAAAAACCCCTCAAGACCCG
pKNT25-for	CCCAGGCTTTACACTTTATGCTTCC
pKNT25-rev	GTTTTTTTCCTTCGCCACGGCCTTG
pKT25-for	CACTGACGGCGGATATCGACATGTT
pKT25-rev	CCGCCGGACATCAGCGCCATTC
pUT18C-for	CGGCGTGCCGAGCGGACGTTCG
pUT18C-rev	TCAGCGGGTGTTGGCGGGTGTC
pUT18-for	CCAGGCTTTACACTTTATGCTTCC
pUT18-rev	GACGCGCCTCGGTGCCCACTGC
RecZn-2	AGGCAACCAGCACGAACGCCAGC
REV-uni	GGGGATGTGCTGCAAGGCGATTAAGTTG
T7 rev	GCTAGTTATTGCTCAGCGG

5.3. Supplemental Movies

Movie S1. Time-lapse series showing the developmental cycle of *H. neptunium*. The *H. neptunium* wild type was grown to exponential phase in MB medium, transferred to microfluidic system. DIC images were taken every 15 min. Scale bar, 2 µm.

Movie S2. Time-lapse series following the localization of BacA-YFP in *H. neptunium*. Strain EC61 (*bacA-yfp*) was grown to exponential phase in MB medium, transferred into a microfluidic system, and tracked by DIC and fluorescence microscopy in 15 min intervals. Scale bar, 2 µm.

Movie S3. Time-lapse series showing the bud fully incorporating the stalk in the bactofilin double deletion mutant. Strain EC33 (*ΔbacAB*) was grown to exponential phase in MB medium, transferred to 1 % MB agarose pads, and tracked with DIC microscopy every 15 min. Scale bar, 3 µm.

Movie S4. Time-lapse series showing the aberrant growth of the bactofilin double deletion mutant. Strain EC33 (*ΔbacAB*) was grown to exponential phase in MB medium, transferred to microfluidic system, and tracked with DIC microscopy every 15 min. Scale bar, 5 µm.

Movie S5. Time-lapse series showing the aberrant growth of the bactofilin double deletion mutant. Strain EC33 (*ΔbacAB*) was grown to exponential phase in MB medium, transferred to 1 % MB agarose pads, and tracked with DIC microscopy every 15 min. Scale bar, 3 µm.

References

1. **Young KD.** 2006. The selective value of bacterial shape. Microbiol Mol Biol Rev **70:**660-703.
2. **Typas A, Banzhaf M, Gross CA, Vollmer W.** 2012. From the regulation of peptidoglycan synthesis to bacterial growth and morphology. Nat Rev Microbiol **10:**123-136.
3. **Jung A, Eisheuer S, Cserti E, Leicht O, Strobel W, Möll A, Schlimpert S, Kühn J, Thanbichler M.** 2015. Molecular toolbox for genetic manipulation of the stalked budding bacterium *Hyphomonas neptunium*. Appl Environ Microbiol **81:**736-744.
4. **Vollmer W, Blanot D, de Pedro MA.** 2008. Peptidoglycan structure and architecture. FEMS Microbiol Rev **32:**149-167.
5. **Höltje JV.** 1998. Growth of the stress-bearing and shape-maintaining murein sacculus of *Escherichia coli*. Microbiol Mol Biol Rev **62:**181-203.
6. **Schleifer KH, Kandler O.** 1972. Peptidoglycan types of bacterial cell walls and their taxonomic implications. Bacteriol Rev **36:**407-477.
7. **Mitchell P.** 1961. Approaches to the analysis of specific membrane transport. Academic Press, New York.
8. **Vollmer W, Seligman SJ.** 2010. Architecture of peptidoglycan: more data and more models. Trends Microbiol **18:**59-66.
9. **Braun V.** 1975. Covalent lipoprotein from the outer membrane of *Escherichia coli*. Biochim Biophys Acta **415:**335-377.
10. **Yem DW, Wu HC.** 1978. Physiological characterization of an *Escherichia coli* mutant altered in the structure of murein lipoprotein. J Bacteriol **133:**1419-1426.
11. **Kamio Y, Nikaido H.** 1976. Outer membrane of *Salmonella typhimurium*: accessibility of phospholipid head groups to phospholipase c and cyanogen bromide activated dextran in the external medium. Biochemistry **15:**2561-2570.
12. **Neuhaus FC, Baddiley J.** 2003. A continuum of anionic charge: structures and functions of D-alanyl-teichoic acids in gram-positive bacteria. Microbiol Mol Biol Rev **67:**686-723.
13. **Höltje JV, Mirelman D, Sharon N, Schwarz U.** 1975. Novel type of murein transglycosylase in *Escherichia coli*. J Bacteriol **124:**1067-1076.
14. **Bera A, Herbert S, Jakob A, Vollmer W, Gotz F.** 2005. Why are pathogenic staphylococci so lysozyme resistant? The peptidoglycan O-acetyltransferase OatA is the major determinant for lysozyme resistance of *Staphylococcus aureus*. Mol Microbiol **55:**778-787.
15. **Glauner B.** 1988. Separation and quantification of muropeptides with high-performance liquid chromatography. Anal Biochem **172:**451-464.
16. **Glauner B, Holtje JV, Schwarz U.** 1988. The composition of the murein of *Escherichia coli*. J Biol Chem **263:**10088-10095.
17. **Hayhurst EJ, Kailas L, Hobbs JK, Foster SJ.** 2008. Cell wall peptidoglycan architecture in *Bacillus subtilis*. Proc Natl Acad Sci U S A **105:**14603-14608.
18. **Boneca IG, Huang ZH, Gage DA, Tomasz A.** 2000. Characterization of *Staphylococcus aureus* cell wall glycan strands, evidence for a new beta-N-acetylglucosaminidase activity. J Biol Chem **275:**9910-9918.
19. **Vollmer W, Bertsche U.** 2008. Murein (peptidoglycan) structure, architecture and biosynthesis in *Escherichia coli*. Biochim Biophys Acta **1778:**1714-1734.
20. **Markiewicz Z, Glauner B, Schwarz U.** 1983. Murein structure and lack of DD- and LD-carboxypeptidase activities in *Caulobacter crescentus*. J Bacteriol **156:**649-655.
21. **Royet J, Dziarski R.** 2007. Peptidoglycan recognition proteins: pleiotropic sensors and effectors of antimicrobial defences. Nat Rev Microbiol **5:**264-277.

22. **Mainardi JL, Fourgeaud M, Hugonnet JE, Dubost L, Brouard JP, Ouazzani J, Rice LB, Gutmann L, Arthur M.** 2005. A novel peptidoglycan cross-linking enzyme for a beta-lactam-resistant transpeptidation pathway. J Biol Chem **280:**38146-38152.
23. **Chambers HF.** 2003. Solving staphylococcal resistance to beta-lactams. Trends Microbiol **11:**145-148.
24. **Dramsi S, Magnet S, Davison S, Arthur M.** 2008. Covalent attachment of proteins to peptidoglycan. FEMS Microbiol Rev **32:**307-320.
25. **Fischetti VA, Pancholi V, Schneewind O.** 1990. Conservation of a hexapeptide sequence in the anchor region of surface proteins from gram-positive cocci. Mol Microbiol **4:**1603-1605.
26. **Silhavy TJ, Kahne D, Walker S.** 2010. The bacterial cell envelope. Cold Spring Harb Perspect Biol **2:**a000414.
27. **Atrih A, Bacher G, Allmaier G, Williamson MP, Foster SJ.** 1999. Analysis of peptidoglycan structure from vegetative cells of *Bacillus subtilis* 168 and role of PBP 5 in peptidoglycan maturation. J Bacteriol **181:**3956-3966.
28. **Quintela JC, Caparros M, de Pedro MA.** 1995. Variability of peptidoglycan structural parameters in gram-negative bacteria. FEMS Microbiol Lett **125:**95-100.
29. **Matias VR, Al-Amoudi A, Dubochet J, Beveridge TJ.** 2003. Cryo-transmission electron microscopy of frozen-hydrated sections of *Escherichia coli* and *Pseudomonas aeruginosa*. J Bacteriol **185:**6112-6118.
30. **Yao X, Jericho M, Pink D, Beveridge T.** 1999. Thickness and elasticity of gram-negative murein sacculi measured by atomic force microscopy. J Bacteriol **181:**6865-6875.
31. **Labischinski H, Goodell EW, Goodell A, Hochberg ML.** 1991. Direct proof of a "more-than-single-layered" peptidoglycan architecture of *Escherichia coli* W7: a neutron small-angle scattering study. J Bacteriol **173:**751-756.
32. **Koch AL, Woeste S.** 1992. Elasticity of the sacculus of *Escherichia coli*. J Bacteriol **174:**4811-4819.
33. **Barnickel G, Labischinski H, Bradaczek H, Giesbrecht P.** 1979. Conformational energy calculation on the peptide part of murein. Eur J Biochem **95:**157-165.
34. **Oldmixon EH, Glauser S, Higgins ML.** 1974. Two proposed general configurations for bacterial cell wall peptidoglycans shown by space-filling molecular models. Biopolymers **13:**2037-2060.
35. **Virudachalam R, Rao VSR.** 1979. Theoretical studies on peptidoglycans: II. Conformation of the dissaccharide-peptide subunit and the three-dimensional structure of peptidoglycan. Biopolymers **18:**571-589.
36. **Labischinski H, Barnickel G, Naumann D, Keller P.** 1985. Conformational and topological aspects of the three-dimensional architecture of bacterial peptidoglycan. Ann Inst Pasteur Microbiol **136A:**45-50.
37. **Meroueh SO, Bencze KZ, Hesek D, Lee M, Fisher JF, Stemmler TL, Mobashery S.** 2006. Three-dimensional structure of the bacterial cell wall peptidoglycan. Proc Natl Acad Sci U S A **103:**4404-4409.
38. **Gan L, Chen S, Jensen GJ.** 2008. Molecular organization of Gram-negative peptidoglycan. Proc Natl Acad Sci U S A **105:**18953-18957.
39. **Zinder ND, Arndt WF.** 1956. Production of Protoplasts of *Escherichia coli* by Lysozyme Treatment. Proc Natl Acad Sci U S A **42:**586-590.
40. **Klieneberger E.** 1935. The natural occurrence of pleuropneumonia-like organisms in apparent symbiosis with *Streptobacillus moniliformis* and other bacteria. J Pathol Bacteriol **40:**93–105.
41. **Leaver M, Dominguez-Cuevas P, Coxhead JM, Daniel RA, Errington J.** 2009. Life without a wall or division machine in *Bacillus subtilis*. Nature **457:**849-853.
42. **Mercier R, Dominguez-Cuevas P, Errington J.** 2012. Crucial role for membrane fluidity in proliferation of primitive cells. Cell Rep **1:**417-423.

43. **Mercier R, Kawai Y, Errington J.** 2014. General principles for the formation and proliferation of a wall-free (L-form) state in bacteria. Elife **3**.
44. **Bouhss A, Trunkfield AE, Bugg TD, Mengin-Lecreulx D.** 2008. The biosynthesis of peptidoglycan lipid-linked intermediates. FEMS Microbiol Rev **32:**208-233.
45. **van Heijenoort J.** 2001. Formation of the glycan chains in the synthesis of bacterial peptidoglycan. Glycobiology **11:**25R-36R.
46. **Ikeda M, Sato T, Wachi M, Jung HK, Ishino F, Kobayashi Y, Matsuhashi M.** 1989. Structural similarity among *Escherichia coli* FtsW and RodA proteins and *Bacillus subtilis* SpoVE protein, which function in cell division, cell elongation, and spore formation, respectively. J Bacteriol **171:**6375-6378.
47. **Khattar MM, Addinall SG, Stedul KH, Boyle DS, Lutkenhaus J, Donachie WD.** 1997. Two polypeptide products of the *Escherichia coli* cell division gene *ftsW* and a possible role for FtsW in FtsZ function. J Bacteriol **179:**784-793.
48. **Mohammadi T, van Dam V, Sijbrandi R, Vernet T, Zapun A, Bouhss A, Diepeveen-de Bruin M, Nguyen-Disteche M, de Kruijff B, Breukink E.** 2011. Identification of FtsW as a transporter of lipid-linked cell wall precursors across the membrane. EMBO J **30:**1425-1432.
49. **Sham LT, Butler EK, Lebar MD, Kahne D, Bernhardt TG, Ruiz N.** 2014. Bacterial cell wall. MurJ is the flippase of lipid-linked precursors for peptidoglycan biogenesis. Science **345:**220-222.
50. **El Ghachi M, Bouhss A, Blanot D, Mengin-Lecreulx D.** 2004. The bacA gene of *Escherichia coli* encodes an undecaprenyl pyrophosphate phosphatase activity. J Biol Chem **279:**30106-30113.
51. **Suginaka H, Blumberg PM, Strominger JL.** 1972. Multiple penicillin-binding components in *Bacillus subtilis*, *Bacillus cereus*, *Staphylococcus aureus*, and *Escherichia coli*. J Biol Chem **247:**5279-5288.
52. **Goffin C, Ghuysen JM.** 1998. Multimodular penicillin-binding proteins: an enigmatic family of orthologs and paralogs. Microbiol Mol Biol Rev **62:**1079-1093.
53. **Goffin C, Ghuysen JM.** 2002. Biochemistry and comparative genomics of SxxK superfamily acyltransferases offer a clue to the mycobacterial paradox: presence of penicillin-susceptible target proteins versus lack of efficiency of penicillin as therapeutic agent. Microbiol Mol Biol Rev **66:**702-738, table of contents.
54. **Ghuysen JM, Charlier P, Coyette J, Duez C, Fonze E, Fraipont C, Goffin C, Joris B, Nguyen-Disteche M.** 1996. Penicillin and beyond: evolution, protein fold, multimodular polypeptides, and multiprotein complexes. Microb Drug Resist **2:**163-175.
55. **Goffin C, Fraipont C, Ayala J, Terrak M, Nguyen-Disteche M, Ghuysen JM.** 1996. The non-penicillin-binding module of the tripartite penicillin-binding protein 3 of *Escherichia coli* is required for folding and/or stability of the penicillin-binding module and the membrane-anchoring module confers cell septation activity on the folded structure. J Bacteriol **178:**5402-5409.
56. **Spratt BG, Jobanputra V.** 1977. Mutants of *Escherichia coli* which lack a component of penicillin-binding protein 1 are viable. FEBS Lett **79:**374-378.
57. **Suzuki H, Nishimura Y, Hirota Y.** 1978. On the process of cellular division in *Escherichia coli*: a series of mutants of *E. coli* altered in the penicillin-binding proteins. Proc Natl Acad Sci U S A **75:**664-668.
58. **Yousif SY, Broome-Smith JK, Spratt BG.** 1985. Lysis of *Escherichia coli* by beta-lactam antibiotics: deletion analysis of the role of penicillin-binding proteins 1A and 1B. J Gen Microbiol **131:**2839-2845.
59. **Garcia del Portillo F, de Pedro MA.** 1990. Differential effect of mutational impairment of penicillin-binding proteins 1A and 1B on *Escherichia coli* strains harboring thermosensitive mutations in the cell division genes *ftsA*, *ftsQ*, *ftsZ*, and *pbpB*. J Bacteriol **172:**5863-5870.

60. **Charpentier X, Chalut C, Remy MH, Masson JM.** 2002. Penicillin-binding proteins 1a and 1b form independent dimers in *Escherichia coli*. J Bacteriol **184:**3749-3752.
61. **Zijderveld CA, Aarsman ME, den Blaauwen T, Nanninga N.** 1991. Penicillin-binding protein 1B of *Escherichia coli* exists in dimeric forms. J Bacteriol **173:**5740-5746.
62. **Paradis-Bleau C, Markovski M, Uehara T, Lupoli TJ, Walker S, Kahne DE, Bernhardt TG.** 2010. Lipoprotein cofactors located in the outer membrane activate bacterial cell wall polymerases. Cell **143:**1110-1120.
63. **Typas A, Banzhaf M, van den Berg van Saparoea B, Verheul J, Biboy J, Nichols RJ, Zietek M, Beilharz K, Kannenberg K, von Rechenberg M, Breukink E, den Blaauwen T, Gross CA, Vollmer W.** 2010. Regulation of peptidoglycan synthesis by outer-membrane proteins. Cell **143:**1097-1109.
64. **Born P, Breukink E, Vollmer W.** 2006. In vitro synthesis of cross-linked murein and its attachment to sacculi by PBP1A from *Escherichia coli*. J Biol Chem **281:**26985-26993.
65. **Bertsche U, Breukink E, Kast T, Vollmer W.** 2005. In vitro murein peptidoglycan synthesis by dimers of the bifunctional transglycosylase-transpeptidase PBP1B from *Escherichia coli*. J Biol Chem **280:**38096-38101.
66. **Schiffer G, Holtje JV.** 1999. Cloning and characterization of PBP 1C, a third member of the multimodular class A penicillin-binding proteins of *Escherichia coli*. J Biol Chem **274:**32031-32039.
67. **Strobel W, Moll A, Kiekebusch D, Klein KE, Thanbichler M.** 2014. Function and localization dynamics of bifunctional penicillin-binding proteins in *Caulobacter crescentus*. J Bacteriol **196:**1627-1639.
68. **Spratt BG.** 1975. Distinct penicillin binding proteins involved in the division, elongation, and shape of *Escherichia coli* K12. Proc Natl Acad Sci U S A **72:**2999-3003.
69. **Den Blaauwen T, Aarsman ME, Vischer NO, Nanninga N.** 2003. Penicillin-binding protein PBP2 of *Escherichia coli* localizes preferentially in the lateral wall and at mid-cell in comparison with the old cell pole. Mol Microbiol **47:**539-547.
70. **Weiss DS, Pogliano K, Carson M, Guzman LM, Fraipont C, Nguyen-Disteche M, Losick R, Beckwith J.** 1997. Localization of the *Escherichia coli* cell division protein Ftsl (PBP3) to the division site and cell pole. Mol Microbiol **25:**671-681.
71. **Bertsche U, Kast T, Wolf B, Fraipont C, Aarsman ME, Kannenberg K, von Rechenberg M, Nguyen-Disteche M, den Blaauwen T, Holtje JV, Vollmer W.** 2006. Interaction between two murein (peptidoglycan) synthases, PBP3 and PBP1B, in *Escherichia coli*. Mol Microbiol **61:**675-690.
72. **Wang X, Huang J, Mukherjee A, Cao C, Lutkenhaus J.** 1997. Analysis of the interaction of FtsZ with itself, GTP, and FtsA. J Bacteriol **179:**5551-5559.
73. **Canavessi AM, Harms J, de Leon Gatti N, Splitter GA.** 2004. The role of integrase/recombinase xerD and monofunctional biosynthesis peptidoglycan transglycosylase genes in the pathogenicity of *Brucella abortus* infection in vitro and in vivo. Microb Pathog **37:**241-251.
74. **Reed P, Veiga H, Jorge AM, Terrak M, Pinho MG.** 2011. Monofunctional transglycosylases are not essential for *Staphylococcus aureus* cell wall synthesis. J Bacteriol **193:**2549-2556.
75. **Derouaux A, Wolf B, Fraipont C, Breukink E, Nguyen-Disteche M, Terrak M.** 2008. The monofunctional glycosyltransferase of *Escherichia coli* localizes to the cell division site and interacts with penicillin-binding protein 3, FtsW, and FtsN. J Bacteriol **190:**1831-1834.
76. **Sanders AN, Wright LF, Pavelka MS, Jr.** 2014. Genetic characterization of mycobacterial L,D-transpeptidases. Microbiology **160:**1795-1806.

77. **Brown PJ, de Pedro MA, Kysela DT, Van der Henst C, Kim J, De Bolle X, Fuqua C, Brun YV.** 2012. Polar growth in the Alphaproteobacterial order Rhizobiales. Proc Natl Acad Sci U S A **109:**1697-1701.
78. **Cameron TA, Anderson-Furgeson J, Zupan JR, Zik JJ, Zambryski PC.** 2014. Peptidoglycan synthesis machinery in *Agrobacterium tumefaciens* during unipolar growth and cell division. MBio **5:**e01219-01214.
79. **Magnet S, Dubost L, Marie A, Arthur M, Gutmann L.** 2008. Identification of the L,D-transpeptidases for peptidoglycan cross-linking in *Escherichia coli*. J Bacteriol **190:**4782-4785.
80. **Koch AL.** 1990. Additional arguments for the key role of "smart" autolysins in the enlargement of the wall of gram-negative bacteria. Res Microbiol **141:**529-541.
81. **Höltje JV.** 1995. From growth to autolysis: the murein hydrolases in *Escherichia coli*. Arch Microbiol **164:**243-254.
82. **Van Heijenoort Y, Van Heijenoort J.** 1971. Study of the N-acetylmuramyl-L-alanine amidase activity in *Escherichia coli*. FEBS Lett **15:**137-141.
83. **Scheurwater E, Reid CW, Clarke AJ.** 2008. Lytic transglycosylases: bacterial space-making autolysins. Int J Biochem Cell Biol **40:**586-591.
84. **van Heijenoort J.** 2011. Peptidoglycan hydrolases of *Escherichia coli*. Microbiol Mol Biol Rev **75:**636-663.
85. **Rigden DJ, Jedrzejas MJ, Galperin MY.** 2003. Amidase domains from bacterial and phage autolysins define a family of gamma-D,L-glutamate-specific amidohydrolases. Trends Biochem Sci **28:**230-234.
86. **Bateman A, Rawlings ND.** 2003. The CHAP domain: a large family of amidases including GSP amidase and peptidoglycan hydrolases. Trends Biochem Sci **28:**234-237.
87. **Heidrich C, Templin MF, Ursinus A, Merdanovic M, Berger J, Schwarz H, de Pedro MA, Holtje JV.** 2001. Involvement of N-acetylmuramyl-L-alanine amidases in cell separation and antibiotic-induced autolysis of *Escherichia coli*. Molecular Microbiology **41:**167-178.
88. **Pennartz A, Genereux C, Parquet C, Mengin-Lecreulx D, Joris B.** 2009. Substrate-induced inactivation of the *Escherichia coli* AmiD N-acetylmuramoyl-L-alanine amidase highlights a new strategy to inhibit this class of enzyme. Antimicrob Agents Chemother **53:**2991-2997.
89. **Bernhardt TG, de Boer PA.** 2003. The *Escherichia coli* amidase AmiC is a periplasmic septal ring component exported via the twin-arginine transport pathway. Mol Microbiol **48:**1171-1182.
90. **Uehara T, Park JT.** 2007. An anhydro-N-acetylmuramyl-L-alanine amidase with broad specificity tethered to the outer membrane of *Escherichia coli*. J Bacteriol **189:**5634-5641.
91. **Jacobs C, Joris B, Jamin M, Klarsov K, Van Beeumen J, Mengin-Lecreulx D, van Heijenoort J, Park JT, Normark S, Frere JM.** 1995. AmpD, essential for both beta-lactamase regulation and cell wall recycling, is a novel cytosolic N-acetylmuramyl-L-alanine amidase. Mol Microbiol **15:**553-559.
92. **Uehara T, Parzych KR, Dinh T, Bernhardt TG.** 2010. Daughter cell separation is controlled by cytokinetic ring-activated cell wall hydrolysis. EMBO J **29:**1412-1422.
93. **Heidrich C, Ursinus A, Berger J, Schwarz H, Holtje JV.** 2002. Effects of multiple deletions of murein hydrolases on viability, septum cleavage, and sensitivity to large toxic molecules in *Escherichia coli*. J Bacteriol **184:**6093-6099.
94. **Höltje JV, Kopp U, Ursinus A, Wiedemann B.** 1994. The negative regulator of beta-lactamase induction AmpD is a N-acetyl-anhydromuramyl-L-alanine amidase. FEMS Microbiol Lett **122:**159-164.
95. **Park JT, Uehara T.** 2008. How bacteria consume their own exoskeletons (turnover and recycling of cell wall peptidoglycan). Microbiol Mol Biol Rev **72:**211-227.

96. **Liepinsh E, Genereux C, Dehareng D, Joris B, Otting G.** 2003. NMR structure of *Citrobacter freundii* AmpD, comparison with bacteriophage T7 lysozyme and homology with PGRP domains. J Mol Biol **327:**833-842.
97. **Kerff F, Petrella S, Mercier F, Sauvage E, Herman R, Pennartz A, Zervosen A, Luxen A, Frere JM, Joris B, Charlier P.** 2010. Specific structural features of the N-acetylmuramoyl-L-alanine amidase AmiD from *Escherichia coli* and mechanistic implications for enzymes of this family. J Mol Biol **397:**249-259.
98. **Sham LT, Barendt SM, Kopecky KE, Winkler ME.** 2011. Essential PcsB putative peptidoglycan hydrolase interacts with the essential FtsXSpn cell division protein in *Streptococcus pneumoniae* D39. Proc Natl Acad Sci U S A **108:**E1061-1069.
99. **Kajimura J, Fujiwara T, Yamada S, Suzawa Y, Nishida T, Oyamada Y, Hayashi I, Yamagishi J, Komatsuzawa H, Sugai M.** 2005. Identification and molecular characterization of an N-acetylmuramyl-L-alanine amidase Sle1 involved in cell separation of *Staphylococcus aureus*. Mol Microbiol **58:**1087-1101.
100. **Yamamoto H, Kurosawa S, Sekiguchi J.** 2003. Localization of the vegetative cell wall hydrolases LytC, LytE, and LytF on the *Bacillus subtilis* cell surface and stability of these enzymes to cell wall-bound or extracellular proteases. J Bacteriol **185:**6666-6677.
101. **Möll A, Dorr T, Alvarez L, Chao MC, Davis BM, Cava F, Waldor MK.** 2014. Cell separation in *Vibrio cholerae* is mediated by a single amidase whose action is modulated by two nonredundant activators. J Bacteriol **196:**3937-3948.
102. **Yakhnina AA, McManus HR, Bernhardt TG.** 2015. The cell wall amidase AmiB is essential for *Pseudomonas aeruginosa* cell division, drug resistance and viability. Mol Microbiol **97:**957-973.
103. **Frirdich E, Biboy J, Adams C, Lee J, Ellermeier J, Gielda LD, Dirita VJ, Girardin SE, Vollmer W, Gaynor EC.** 2012. Peptidoglycan-modifying enzyme Pgp1 is required for helical cell shape and pathogenicity traits in *Campylobacter jejuni*. PLoS Pathog **8:**e1002602.
104. **Nelson DE, Young KD.** 2000. Penicillin binding protein 5 affects cell diameter, contour, and morphology of *Escherichia coli*. J Bacteriol **182:**1714-1721.
105. **Sycuro LK, Wyckoff TJ, Biboy J, Born P, Pincus Z, Vollmer W, Salama NR.** 2012. Multiple peptidoglycan modification networks modulate *Helicobacter pylori*'s cell shape, motility, and colonization potential. PLoS Pathog **8:**e1002603.
106. **Tipper DJ, Strominger JL.** 1965. Mechanism of action of penicillins: a proposal based on their structural similarity to acyl-D-alanyl-D-alanine. Proc Natl Acad Sci U S A **54:**1133-1141.
107. **Potluri LP, de Pedro MA, Young KD.** 2012. *Escherichia coli* low-molecular-weight penicillin-binding proteins help orient septal FtsZ, and their absence leads to asymmetric cell division and branching. Mol Microbiol **84:**203-224.
108. **Ghosh AS, Chowdhury C, Nelson DE.** 2008. Physiological functions of D-alanine carboxypeptidases in *Escherichia coli*. Trends Microbiol **16:**309-317.
109. **Templin MF, Ursinus A, Holtje JV.** 1999. A defect in cell wall recycling triggers autolysis during the stationary growth phase of *Escherichia coli*. EMBO J **18:**4108-4117.
110. **Priyadarshini R, Popham DL, Young KD.** 2006. Daughter cell separation by penicillin-binding proteins and peptidoglycan amidases in *Escherichia coli*. J Bacteriol **188:**5345-5355.
111. **Romeis T, Holtje JV.** 1994. Specific interaction of penicillin-binding proteins 3 and 7/8 with soluble lytic transglycosylase in *Escherichia coli*. J Biol Chem **269:**21603-21607.
112. **Hartmann R, Holtje JV, Schwarz U.** 1972. Targets of penicillin action in *Escherichia coli*. Nature **235:**426-429.
113. **Tamura T, Imae Y, Strominger JL.** 1976. Purification to homogeneity and properties of two D-alanine carboxypeptidases I From *Escherichia coli*. J Biol Chem **251:**414-423.

114. **Cohen DN, Sham YY, Haugstad GD, Xiang Y, Rossmann MG, Anderson DL, Popham DL.** 2009. Shared catalysis in virus entry and bacterial cell wall depolymerization. J Mol Biol **387:**607-618.
115. **Ramadurai L, Jayaswal RK.** 1997. Molecular cloning, sequencing, and expression of *lytM*, a unique autolytic gene of *Staphylococcus aureus*. J Bacteriol **179:**3625-3631.
116. **Firczuk M, Mucha A, Bochtler M.** 2005. Crystal structures of active LytM. J Mol Biol **354:**578-590.
117. **Bochtler M, Odintsov SG, Marcyjaniak M, Sabala I.** 2004. Similar active sites in lysostaphins and D-Ala-D-Ala metallopeptidases. Protein Sci **13:**854-861.
118. **de Roca FR, Duche C, Dong S, Rince A, Dubost L, Pritchard DG, Baker JR, Arthur M, Mesnage S.** 2010. Cleavage specificity of *Enterococcus faecalis* EnpA (EF1473), a peptidoglycan endopeptidase related to the LytM/lysostaphin family of metallopeptidases. J Mol Biol **398:**507-517.
119. **Hale CA, de Boer PA.** 1999. Recruitment of ZipA to the septal ring of *Escherichia coli* is dependent on FtsZ and independent of FtsA. J Bacteriol **181:**167-176.
120. **Smith TJ, Blackman SA, Foster SJ.** 2000. Autolysins of *Bacillus subtilis*: multiple enzymes with multiple functions. Microbiology **146 (Pt 2):**249-262.
121. **Rawlings ND, Morton FR, Barrett AJ.** 2006. MEROPS: the peptidase database. Nucleic Acids Res **34:**D270-272.
122. **Kessler E, Safrin M, Olson JC, Ohman DE.** 1993. Secreted LasA of *Pseudomonas aeruginosa* is a staphylolytic protease. J Biol Chem **268:**7503-7508.
123. **Uehara T, Dinh T, Bernhardt TG.** 2009. LytM-domain factors are required for daughter cell separation and rapid ampicillin-induced lysis in *Escherichia coli*. J Bacteriol **191:**5094-5107.
124. **Ercoli G, Tani C, Pezzicoli A, Vacca I, Martinelli M, Pecetta S, Petracca R, Rappuoli R, Pizza M, Norais N, Soriani M, Arico B.** 2015. LytM proteins play a crucial role in cell separation, outer membrane composition, and pathogenesis in nontypeable Haemophilus influenzae. MBio **6:**e02575.
125. **Buist G, Steen A, Kok J, Kuipers OP.** 2008. LysM, a widely distributed protein motif for binding to (peptido)glycans. Mol Microbiol **68:**838-847.
126. **Goley ED, Comolli LR, Fero KE, Downing KH, Shapiro L.** 2010. DipM links peptidoglycan remodelling to outer membrane organization in *Caulobacter*. Mol Microbiol **77:**56-73.
127. **Poggio S, Takacs CN, Vollmer W, Jacobs-Wagner C.** 2010. A protein critical for cell constriction in the Gram-negative bacterium *Caulobacter crescentus* localizes at the division site through its peptidoglycan-binding LysM domains. Mol Microbiol **77:**74-89.
128. **Möll A, Schlimpert S, Briegel A, Jensen GJ, Thanbichler M.** 2010. DipM, a new factor required for peptidoglycan remodelling during cell division in *Caulobacter crescentus*. Mol Microbiol **77:**90-107.
129. **Bonis M, Ecobichon C, Guadagnini S, Prevost MC, Boneca IG.** 2010. A M23B family metallopeptidase of *Helicobacter pylori* required for cell shape, pole formation and virulence. Mol Microbiol **78:**809-819.
130. **Stohl EA, Chan YA, Hackett KT, Kohler PL, Dillard JP, Seifert HS.** 2012. *Neisseria gonorrhoeae* virulence factor NG1686 is a bifunctional M23B family metallopeptidase that influences resistance to hydrogen peroxide and colony morphology. J Biol Chem **287:**11222-11233.
131. **Anantharaman V, Aravind L.** 2003. Evolutionary history, structural features and biochemical diversity of the NlpC/P60 superfamily of enzymes. Genome Biol **4:**R11.
132. **Aramini JM, Rossi P, Huang YJ, Zhao L, Jiang M, Maglaqui M, Xiao R, Locke J, Nair R, Rost B, Acton TB, Inouye M, Montelione GT.** 2008. Solution NMR structure of the NlpC/P60 domain of lipoprotein Spr from *Escherichia coli*: structural evidence for a novel cysteine peptidase catalytic triad. Biochemistry **47:**9715-9717.

133. **Xu Q, Sudek S, McMullan D, Miller MD, Geierstanger B, Jones DH, Krishna SS, Spraggon G, Bursalay B, Abdubek P, Acosta C, Ambing E, Astakhova T, Axelrod HL, Carlton D, Caruthers J, Chiu HJ, Clayton T, Deller MC, Duan L, Elias Y, Elsliger MA, Feuerhelm J, Grzechnik SK, Hale J, Han GW, Haugen J, Jaroszewski L, Jin KK, Klock HE, Knuth MW, Kozbial P, Kumar A, Marciano D, Morse AT, Nigoghossian E, Okach L, Oommachen S, Paulsen J, Reyes R, Rife CL, Trout CV, van den Bedem H, Weekes D, White A, Wolf G, Zubieta C, Hodgson KO, Wooley J, Deacon AM, et al.** 2009. Structural basis of murein peptide specificity of a gamma-D-glutamyl-l-diamino acid endopeptidase. Structure **17:**303-313.
134. **Singh SK, Parveen S, SaiSree L, Reddy M.** 2015. Regulated proteolysis of a cross-link-specific peptidoglycan hydrolase contributes to bacterial morphogenesis. Proc Natl Acad Sci U S A **112:**10956-10961.
135. **Singh SK, SaiSree L, Amrutha RN, Reddy M.** 2012. Three redundant murein endopeptidases catalyse an essential cleavage step in peptidoglycan synthesis of *Escherichia coli* K12. Mol Microbiol **86:**1036-1051.
136. **Bisicchia P, Noone D, Lioliou E, Howell A, Quigley S, Jensen T, Jarmer H, Devine KM.** 2007. The essential YycFG two-component system controls cell wall metabolism in *Bacillus subtilis*. Mol Microbiol **65:**180-200.
137. **Cheng Q, Li H, Merdek K, Park JT.** 2000. Molecular characterization of the beta-N-acetylglucosaminidase of *Escherichia coli* and its role in cell wall recycling. J Bacteriol **182:**4836-4840.
138. **Yem DW, Wu HC.** 1976. Isolation of *Escherichia coli* K-12 mutants with altered level of beta-N-acetylglucosaminidase. J Bacteriol **125:**372-373.
139. **Romeis T, Vollmer W, Holtje JV.** 1993. Characterization of three different lytic transglycosylases in *Escherichia coli*. FEMS Microbiol Lett **111:**141-146.
140. **Uehara T, Park JT.** 2008. Growth of *Escherichia coli*: significance of peptidoglycan degradation during elongation and septation. J Bacteriol **190:**3914-3922.
141. **Burman LG, Park JT.** 1984. Molecular model for elongation of the murein sacculus of *Escherichia coli*. Proc Natl Acad Sci U S A **81:**1844-1848.
142. **de Jonge BL, Wientjes FB, Jurida I, Driehuis F, Wouters JT, Nanninga N.** 1989. Peptidoglycan synthesis during the cell cycle of *Escherichia coli*: composition and mode of insertion. J Bacteriol **171:**5783-5794.
143. **Cabeen MT, Jacobs-Wagner C.** 2010. The bacterial cytoskeleton. Annu Rev Genet **44:**365-392.
144. **Bi EF, Lutkenhaus J.** 1991. FtsZ ring structure associated with division in *Escherichia coli*. Nature **354:**161-164.
145. **Sontag CA, Staley JT, Erickson HP.** 2005. In vitro assembly and GTP hydrolysis by bacterial tubulins BtubA and BtubB. J Cell Biol **169:**233-238.
146. **Pilhofer M, Ladinsky MS, McDowall AW, Petroni G, Jensen GJ.** 2011. Microtubules in bacteria: Ancient tubulins build a five-protofilament homolog of the eukaryotic cytoskeleton. PLoS Biol **9:**e1001213.
147. **Larsen RA, Cusumano C, Fujioka A, Lim-Fong G, Patterson P, Pogliano J.** 2007. Treadmilling of a prokaryotic tubulin-like protein, TubZ, required for plasmid stability in *Bacillus thuringiensis*. Genes Dev **21:**1340-1352.
148. **Errington J.** 2015. Bacterial morphogenesis and the enigmatic MreB helix. Nat Rev Microbiol **13:**241-248.
149. **Dai K, Lutkenhaus J.** 1992. The proper ratio of FtsZ to FtsA is required for cell division to occur in *Escherichia coli*. J Bacteriol **174:**6145-6151.
150. **Moller-Jensen J, Jensen RB, Lowe J, Gerdes K.** 2002. Prokaryotic DNA segregation by an actin-like filament. EMBO J **21:**3119-3127.

151. **Ausmees N, Kuhn JR, Jacobs-Wagner C.** 2003. The bacterial cytoskeleton: an intermediate filament-like function in cell shape. Cell **115:**705-713.
152. **Fuchino K, Bagchi S, Cantlay S, Sandblad L, Wu D, Bergman J, Kamali-Moghaddam M, Flardh K, Ausmees N.** 2013. Dynamic gradients of an intermediate filament-like cytoskeleton are recruited by a polarity landmark during apical growth. Proc Natl Acad Sci U S A **110:**E1889-1897.
153. **Waidner B, Specht M, Dempwolff F, Haeberer K, Schaetzle S, Speth V, Kist M, Graumann PL.** 2009. A novel system of cytoskeletal elements in the human pathogen *Helicobacter pylori*. PLoS Pathog **5:**e1000669.
154. **Bowman GR, Comolli LR, Zhu J, Eckart M, Koenig M, Downing KH, Moerner WE, Earnest T, Shapiro L.** 2008. A polymeric protein anchors the chromosomal origin/ParB complex at a bacterial cell pole. Cell **134:**945-955.
155. **Edwards DH, Thomaides HB, Errington J.** 2000. Promiscuous targeting of *Bacillus subtilis* cell division protein DivIVA to division sites in *Escherichia coli* and fission yeast. EMBO J **19:**2719-2727.
156. **Lenarcic R, Halbedel S, Visser L, Shaw M, Wu LJ, Errington J, Marenduzzo D, Hamoen LW.** 2009. Localisation of DivIVA by targeting to negatively curved membranes. EMBO J **28:**2272-2282.
157. **Kühn J, Briegel A, Mörschel E, Kahnt J, Leser K, Wick S, Jensen GJ, Thanbichler M.** 2010. Bactofilins, a ubiquitous class of cytoskeletal proteins mediating polar localization of a cell wall synthase in *Caulobacter crescentus*. EMBO J **29:**327-339.
158. **Lutkenhaus JF, Wolf-Watz H, Donachie WD.** 1980. Organization of genes in the ftsA-envA region of the *Escherichia coli genetic* map and identification of a new fts locus (*ftsZ*). J Bacteriol **142:**615-620.
159. **Vaughan S, Wickstead B, Gull K, Addinall SG.** 2004. Molecular evolution of FtsZ protein sequences encoded within the genomes of archaea, bacteria, and eukaryota. J Mol Evol **58:**19-29.
160. **Nogales E, Downing KH, Amos LA, Lowe J.** 1998. Tubulin and FtsZ form a distinct family of GTPases. Nat Struct Biol **5:**451-458.
161. **Mukherjee A, Lutkenhaus J.** 1994. Guanine nucleotide-dependent assembly of FtsZ into filaments. J Bacteriol **176:**2754-2758.
162. **Mukherjee A, Lutkenhaus J.** 1998. Dynamic assembly of FtsZ regulated by GTP hydrolysis. EMBO J **17:**462-469.
163. **Lu C, Reedy M, Erickson HP.** 2000. Straight and curved conformations of FtsZ are regulated by GTP hydrolysis. J Bacteriol **182:**164-170.
164. **Lowe J, Amos LA.** 2000. Helical tubes of FtsZ from *Methanococcus jannaschii*. Biol Chem **381:**993-999.
165. **Bramhill D, Thompson CM.** 1994. GTP-dependent polymerization of *Escherichia coli* FtsZ protein to form tubules. Proc Natl Acad Sci U S A **91:**5813-5817.
166. **Erickson HP, Taylor DW, Taylor KA, Bramhill D.** 1996. Bacterial cell division protein FtsZ assembles into protofilament sheets and minirings, structural homologs of tubulin polymers. Proc Natl Acad Sci U S A **93:**519-523.
167. **Gonzalez JM, Jimenez M, Velez M, Mingorance J, Andreu JM, Vicente M, Rivas G.** 2003. Essential cell division protein FtsZ assembles into one monomer-thick ribbons under conditions resembling the crowded intracellular environment. J Biol Chem **278:**37664-37671.
168. **Lowe J, Amos LA.** 1999. Tubulin-like protofilaments in Ca^{2+}-induced FtsZ sheets. EMBO J **18:**2364-2371.
169. **Yu XC, Margolin W.** 1997. Ca2+-mediated GTP-dependent dynamic assembly of bacterial cell division protein FtsZ into asters and polymer networks *in vitro*. EMBO J **16:**5455-5463.

170. **Oliva MA, Cordell SC, Lowe J.** 2004. Structural insights into FtsZ protofilament formation. Nat Struct Mol Biol **11:**1243-1250.
171. **Goehring NW, Beckwith J.** 2005. Diverse paths to midcell: assembly of the bacterial cell division machinery. Curr Biol **15:**R514-526.
172. **Lutkenhaus J, Pichoff S, Du S.** 2012. Bacterial cytokinesis: From Z ring to divisome. Cytoskeleton (Hoboken) **69:**778-790.
173. **Natale P, Pazos M, Vicente M.** 2013. The *Escherichia coli* divisome: born to divide. Environ Microbiol **15:**3169-3182.
174. **Li Z, Trimble MJ, Brun YV, Jensen GJ.** 2007. The structure of FtsZ filaments in vivo suggests a force-generating role in cell division. EMBO J **26:**4694-4708.
175. **Meier EL, Goley ED.** 2014. Form and function of the bacterial cytokinetic ring. Curr Opin Cell Biol **26:**19-27.
176. **Monahan LG, Liew AT, Bottomley AL, Harry EJ.** 2014. Division site positioning in bacteria: one size does not fit all. Front Microbiol **5:**19.
177. **Jenkins C, Samudrala R, Anderson I, Hedlund BP, Petroni G, Michailova N, Pinel N, Overbeek R, Rosati G, Staley JT.** 2002. Genes for the cytoskeletal protein tubulin in the bacterial genus *Prosthecobacter*. Proc Natl Acad Sci U S A **99:**17049-17054.
178. **Schlieper D, Oliva MA, Andreu JM, Lowe J.** 2005. Structure of bacterial tubulin BtubA/B: evidence for horizontal gene transfer. Proc Natl Acad Sci U S A **102:**9170-9175.
179. **Sontag CA, Sage H, Erickson HP.** 2009. BtubA-BtubB heterodimer is an essential intermediate in protofilament assembly. PLoS One **4:**e7253.
180. **Andreu JM, Oliva MA.** 2013. Purification and assembly of bacterial tubulin BtubA/B and constructs bearing eukaryotic tubulin sequences. Methods Cell Biol **115:**269-281.
181. **Hoshino S, Maki T, Hayashi I.** 2012. Crystallization and preliminary X-ray data analysis of the pXO1 plasmid-partitioning factor TubZ from *Bacillus cereus*. Acta Crystallogr Sect F Struct Biol Cryst Commun **68:**1550-1553.
182. **Oliva MA, Martin-Galiano AJ, Sakaguchi Y, Andreu JM.** 2012. Tubulin homolog TubZ in a phage-encoded partition system. Proc Natl Acad Sci U S A **109:**7711-7716.
183. **Aylett CH, Izore T, Amos LA, Lowe J.** 2013. Structure of the tubulin/FtsZ-like protein TubZ from *Pseudomonas* bacteriophage PhiKZ. J Mol Biol **425:**2164-2173.
184. **Hoshino S, Hayashi I.** 2012. Filament formation of the FtsZ/tubulin-like protein TubZ from the *Bacillus cereus* pXO1 plasmid. J Biol Chem **287:**32103-32112.
185. **Erb ML, Kraemer JA, Coker JK, Chaikeeratisak V, Nonejuie P, Agard DA, Pogliano J.** 2014. A bacteriophage tubulin harnesses dynamic instability to center DNA in infected cells. Elife **3**.
186. **Kraemer JA, Erb ML, Waddling CA, Montabana EA, Zehr EA, Wang H, Nguyen K, Pham DS, Agard DA, Pogliano J.** 2012. A phage tubulin assembles dynamic filaments by an atypical mechanism to center viral DNA within the host cell. Cell **149:**1488-1499.
187. **Bork P, Sander C, Valencia A.** 1992. An ATPase domain common to prokaryotic cell cycle proteins, sugar kinases, actin, and hsp70 heat shock proteins. Proc Natl Acad Sci U S A **89:**7290-7294.
188. **Jones LJ, Carballido-Lopez R, Errington J.** 2001. Control of cell shape in bacteria: helical, actin-like filaments in *Bacillus subtilis*. Cell **104:**913-922.
189. **van den Ent F, Amos LA, Lowe J.** 2001. Prokaryotic origin of the actin cytoskeleton. Nature **413:**39-44.
190. **Holmes KC, Popp D, Gebhard W, Kabsch W.** 1990. Atomic model of the actin filament. Nature **347:**44-49.
191. **Bean GJ, Amann KJ.** 2008. Polymerization properties of the *Thermotoga maritima* actin MreB: roles of temperature, nucleotides, and ions. Biochemistry **47:**826-835.

192. **Esue O, Cordero M, Wirtz D, Tseng Y.** 2005. The assembly of MreB, a prokaryotic homolog of actin. J Biol Chem **280:**2628-2635.
193. **Salje J, van den Ent F, de Boer P, Lowe J.** 2011. Direct membrane binding by bacterial actin MreB. Mol Cell **43:**478-487.
194. **van den Ent F, Izore T, Bharat TA, Johnson CM, Lowe J.** 2014. Bacterial actin MreB forms antiparallel double filaments. Elife **3:**e02634.
195. **Wachi M, Doi M, Tamaki S, Park W, Nakajima-Iijima S, Matsuhashi M.** 1987. Mutant isolation and molecular cloning of *mre* genes, which determine cell shape, sensitivity to mecillinam, and amount of penicillin-binding proteins in *Escherichia coli*. J Bacteriol **169:**4935-4940.
196. **Daniel RA, Errington J.** 2003. Control of cell morphogenesis in bacteria: two distinct ways to make a rod-shaped cell. Cell **113:**767-776.
197. **Abhayawardhane Y, Stewart GC.** 1995. *Bacillus subtilis* possesses a second determinant with extensive sequence similarity to the *Escherichia coli mreB* morphogene. J Bacteriol **177:**765-773.
198. **Levin PA, Margolis PS, Setlow P, Losick R, Sun D.** 1992. Identification of *Bacillus subtilis* genes for septum placement and shape determination. J Bacteriol **174:**6717-6728.
199. **Varley AW, Stewart GC.** 1992. The *divIVB* region of the *Bacillus subtilis* chromosome encodes homologs of *Escherichia coli* septum placement (*minCD*) and cell shape (*mreBCD*) determinants. J Bacteriol **174:**6729-6742.
200. **Lee S, Price CW.** 1993. The *minCD* locus of *Bacillus subtilis* lacks the minE determinant that provides topological specificity to cell division. Mol Microbiol **7:**601-610.
201. **Defeu Soufo HJ, Graumann PL.** 2004. Dynamic movement of actin-like proteins within bacterial cells. EMBO Rep **5:**789-794.
202. **Figge RM, Divakaruni AV, Gober JW.** 2004. MreB, the cell shape-determining bacterial actin homologue, co-ordinates cell wall morphogenesis in *Caulobacter crescentus*. Mol Microbiol **51:**1321-1332.
203. **Carballido-Lopez R, Formstone A, Li Y, Ehrlich SD, Noirot P, Errington J.** 2006. Actin homolog MreBH governs cell morphogenesis by localization of the cell wall hydrolase LytE. Dev Cell **11:**399-409.
204. **Chiu SW, Chen SY, Wong HC.** 2008. Dynamic localization of MreB in *Vibrio parahaemolyticus* and in the ectopic host bacterium *Escherichia coli*. Appl Environ Microbiol **74:**6739-6745.
205. **Shih YL, Le T, Rothfield L.** 2003. Division site selection in *Escherichia coli* involves dynamic redistribution of Min proteins within coiled structures that extend between the two cell poles. Proc Natl Acad Sci U S A **100:**7865-7870.
206. **Carballido-Lopez R, Errington J.** 2003. The bacterial cytoskeleton: in vivo dynamics of the actin-like protein Mbl of *Bacillus subtilis*. Dev Cell **4:**19-28.
207. **Kawai Y, Daniel RA, Errington J.** 2009. Regulation of cell wall morphogenesis in *Bacillus subtilis* by recruitment of PBP1 to the MreB helix. Mol Microbiol **71:**1131-1144.
208. **Swulius MT, Chen S, Jane Ding H, Li Z, Briegel A, Pilhofer M, Tocheva EI, Lybarger SR, Johnson TL, Sandkvist M, Jensen GJ.** 2011. Long helical filaments are not seen encircling cells in electron cryotomograms of rod-shaped bacteria. Biochem Biophys Res Commun **407:**650-655.
209. **Garner EC, Bernard R, Wang WQ, Zhuang XW, Rudner DZ, Mitchison T.** 2011. Coupled, circumferential motions of the cell Wall synthesis machinery and MreB filaments in *B. subtilis*. Science **333:**222-225.
210. **van Teeffelen S, Wang S, Furchtgott L, Huang KC, Wingreen NS, Shaevitz JW, Gitai Z.** 2011. The bacterial actin MreB rotates, and rotation depends on cell-wall assembly. Proc Natl Acad Sci U S A **108:**15822-15827.

211. **Dominguez-Escobar J, Chastanet A, Crevenna AH, Fromion V, Wedlich-Soldner R, Carballido-Lopez R.** 2011. Processive movement of MreB-associated cell wall biosynthetic complexes in bacteria. Science **333:**225-228.
212. **Reimold C, Defeu Soufo HJ, Dempwolff F, Graumann PL.** 2013. Motion of variable-length MreB filaments at the bacterial cell membrane influences cell morphology. Mol Biol Cell **24:**2340-2349.
213. **Olshausen PV, Defeu Soufo HJ, Wicker K, Heintzmann R, Graumann PL, Rohrbach A.** 2013. Superresolution imaging of dynamic MreB filaments in *B. subtilis*--a multiple-motor-driven transport? Biophys J **105:**1171-1181.
214. **Divakaruni AV, Baida C, White CL, Gober JW.** 2007. The cell shape proteins MreB and MreC control cell morphogenesis by positioning cell wall synthetic complexes. Mol Microbiol **66:**174-188.
215. **Wagner JK, Galvani CD, Brun YV.** 2005. *Caulobacter crescentus* requires RodA and MreB for stalk synthesis and prevention of ectopic pole formation. J Bacteriol **187:**544-553.
216. **Mauriello EM, Mouhamar F, Nan B, Ducret A, Dai D, Zusman DR, Mignot T.** 2010. Bacterial motility complexes require the actin-like protein, MreB and the Ras homologue, MglA. EMBO J **29:**315-326.
217. **Muller FD, Schink CW, Hoiczyk E, Cserti E, Higgs PI.** 2012. Spore formation in *Myxococcus xanthus* is tied to cytoskeleton functions and polysaccharide spore coat deposition. Mol Microbiol **83:**486-505.
218. **Cowles KN, Gitai Z.** 2010. Surface association and the MreB cytoskeleton regulate pilus production, localization and function in *Pseudomonas aeruginosa*. Mol Microbiol **76:**1411-1426.
219. **Mazza P, Noens EE, Schirner K, Grantcharova N, Mommaas AM, Koerten HK, Muth G, Flardh K, van Wezel GP, Wohlleben W.** 2006. MreB of *Streptomyces coelicolor* is not essential for vegetative growth but is required for the integrity of aerial hyphae and spores. Mol Microbiol **60:**838-852.
220. **Strahl H, Burmann F, Hamoen LW.** 2014. The actin homologue MreB organizes the bacterial cell membrane. Nat Commun **5:**3442.
221. **van den Ent F, Lowe J.** 2000. Crystal structure of the cell division protein FtsA from *Thermotoga maritima*. EMBO J **19:**5300-5307.
222. **Szwedziak P, Wang Q, Freund SM, Lowe J.** 2012. FtsA forms actin-like protofilaments. EMBO J **31:**2249-2260.
223. **Lowe J, van den Ent F.** 2001. Conserved sequence motif at the C-terminus of the bacterial cell-division protein FtsA. Biochimie **83:**117-120.
224. **Pichoff S, Lutkenhaus J.** 2005. Tethering the Z ring to the membrane through a conserved membrane targeting sequence in FtsA. Mol Microbiol **55:**1722-1734.
225. **Szwedziak P, Wang Q, Bharat TA, Tsim M, Lowe J.** 2014. Architecture of the ring formed by the tubulin homologue FtsZ in bacterial cell division. Elife **3:**e04601.
226. **Tormo A, Vicente M.** 1984. The *ftsA* gene product participates in formation of the *Escherichia coli* septum structure. J Bacteriol **157:**779-784.
227. **Grangeon R, Zupan JR, Anderson-Furgeson J, Zambryski PC.** 2015. PopZ identifies the new pole, and PodJ identifies the old pole during polar growth in *Agrobacterium tumefaciens*. Proc Natl Acad Sci U S A **112:**11666-11671.
228. **Pichoff S, Lutkenhaus J.** 2002. Unique and overlapping roles for ZipA and FtsA in septal ring assembly in *Escherichia coli*. EMBO J **21:**685-693.
229. **Komeili A, Li Z, Newman DK, Jensen GJ.** 2006. Magnetosomes are cell membrane invaginations organized by the actin-like protein MamK. Science **311:**242-245.

230. **Breuner A, Jensen RB, Dam M, Pedersen S, Gerdes K.** 1996. The centromere-like *parC* locus of plasmid R1. Mol Microbiol **20:**581-592.
231. **van den Ent F, Moller-Jensen J, Amos LA, Gerdes K, Lowe J.** 2002. F-actin-like filaments formed by plasmid segregation protein ParM. EMBO J **21:**6935-6943.
232. **Ebersbach G, Gerdes K.** 2005. Plasmid segregation mechanisms. Annu Rev Genet **39:**453-479.
233. **Garner EC, Campbell CS, Mullins RD.** 2004. Dynamic instability in a DNA-segregating prokaryotic actin homolog. Science **306:**1021-1025.
234. **Goode BL, Eck MJ.** 2007. Mechanism and function of formins in the control of actin assembly. Annu Rev Biochem **76:**593-627.
235. **Salje J, Lowe J.** 2008. Bacterial actin: architecture of the ParMRC plasmid DNA partitioning complex. EMBO J **27:**2230-2238.
236. **Becker E, Herrera NC, Gunderson FQ, Derman AI, Dance AL, Sims J, Larsen RA, Pogliano J.** 2006. DNA segregation by the bacterial actin AlfA during *Bacillus subtilis* growth and development. EMBO J **25:**5919-5931.
237. **Derman AI, Becker EC, Truong BD, Fujioka A, Tucey TM, Erb ML, Patterson PC, Pogliano J.** 2009. Phylogenetic analysis identifies many uncharacterized actin-like proteins (Alps) in bacteria: regulated polymerization, dynamic instability and treadmilling in Alp7A. Mol Microbiol **73:**534-552.
238. **Cabeen MT, Herrmann H, Jacobs-Wagner C.** 2011. The domain organization of the bacterial intermediate filament-like protein crescentin is important for assembly and function. Cytoskeleton (Hoboken) **68:**205-219.
239. **Esue O, Rupprecht L, Sun SX, Wirtz D.** 2010. Dynamics of the bacterial intermediate filament crescentin in vitro and in vivo. PLoS One **5:**e8855.
240. **Cabeen MT, Charbon G, Vollmer W, Born P, Ausmees N, Weibel DB, Jacobs-Wagner C.** 2009. Bacterial cell curvature through mechanical control of cell growth. EMBO J **28:**1208-1219.
241. **Charbon G, Cabeen MT, Jacobs-Wagner C.** 2009. Bacterial intermediate filaments: in vivo assembly, organization, and dynamics of crescentin. Genes Dev **23:**1131-1144.
242. **Yoon KH, Yoon M, Moir RD, Khuon S, Flitney FW, Goldman RD.** 2001. Insights into the dynamic properties of keratin intermediate filaments in living epithelial cells. J Cell Biol **153:**503-516.
243. **Ingerson-Mahar M, Briegel A, Werner JN, Jensen GJ, Gitai Z.** 2010. The metabolic enzyme CTP synthase forms cytoskeletal filaments. Nat Cell Biol **12:**739-746.
244. **Long CW, Levitzki A, Koshland DE, Jr.** 1970. The subunit structure and subunit interactions of cytidine triphosphate synthetase. J Biol Chem **245:**80-87.
245. **Walshaw J, Gillespie MD, Kelemen GH.** 2010. A novel coiled-coil repeat variant in a class of bacterial cytoskeletal proteins. J Struct Biol **170:**202-215.
246. **Fiuza M, Letek M, Leiba J, Villadangos AF, Vaquera J, Zanella-Cleon I, Mateos LM, Molle V, Gil JA.** 2010. Phosphorylation of a novel cytoskeletal protein (RsmP) regulates rod-shaped morphology in *Corynebacterium glutamicum*. J Biol Chem **285:**29387-29397.
247. **Bagchi S, Tomenius H, Belova LM, Ausmees N.** 2008. Intermediate filament-like proteins in bacteria and a cytoskeletal function in *Streptomyces*. Mol Microbiol **70:**1037-1050.
248. **Lin L, Thanbichler M.** 2013. Nucleotide-independent cytoskeletal scaffolds in bacteria. Cytoskeleton (Hoboken) **70:**409-423.
249. **Flardh K.** 2003. Essential role of DivIVA in polar growth and morphogenesis in *Streptomyces coelicolor* A3(2). Mol Microbiol **49:**1523-1536.
250. **Holmes NA, Walshaw J, Leggett RM, Thibessard A, Dalton KA, Gillespie MD, Hemmings AM, Gust B, Kelemen GH.** 2013. Coiled-coil protein Scy is a key component of a multiprotein assembly controlling polarized growth in *Streptomyces*. Proc Natl Acad Sci U S A **110:**E397-406.

251. **Ditkowski B, Holmes N, Rydzak J, Donczew M, Bezulska M, Ginda K, Kedzierski P, Zakrzewska-Czerwinska J, Kelemen GH, Jakimowicz D.** 2013. Dynamic interplay of ParA with the polarity protein, Scy, coordinates the growth with chromosome segregation in *Streptomyces coelicolor*. Open Biol **3:**130006.
252. **Ausmees N.** 2013. Coiled coil cytoskeletons collaborate in polar growth of *Streptomyces*. Bioarchitecture **3:**110-112.
253. **Letek M, Ordonez E, Vaquera J, Margolin W, Flardh K, Mateos LM, Gil JA.** 2008. DivIVA is required for polar growth in the MreB-lacking rod-shaped actinomycete *Corynebacterium glutamicum*. J Bacteriol **190:**3283-3292.
254. **Omary MB, Ku NO, Tao GZ, Toivola DM, Liao J.** 2006. "Heads and tails" of intermediate filament phosphorylation: multiple sites and functional insights. Trends Biochem Sci **31:**383-394.
255. **Specht M, Schatzle S, Graumann PL, Waidner B.** 2011. *Helicobacter pylori* possesses four coiled-coil-rich proteins that form extended filamentous structures and control cell shape and motility. J Bacteriol **193:**4523-4530.
256. **Pilhofer M, Jensen GJ.** 2013. The bacterial cytoskeleton: more than twisted filaments. Curr Opin Cell Biol **25:**125-133.
257. **Letek M, Fiuza M, Ordonez E, Villadangos AF, Flardh K, Mateos LM, Gil JA.** 2009. DivIVA uses an N-terminal conserved region and two coiled-coil domains to localize and sustain the polar growth in *Corynebacterium glutamicum*. FEMS Microbiol Lett **297:**110-116.
258. **Oliva MA, Halbedel S, Freund SM, Dutow P, Leonard TA, Veprintsev DB, Hamoen LW, Lowe J.** 2010. Features critical for membrane binding revealed by DivIVA crystal structure. EMBO J **29:**1988-2001.
259. **Stahlberg H, Kutejova E, Muchova K, Gregorini M, Lustig A, Muller SA, Olivieri V, Engel A, Wilkinson AJ, Barak I.** 2004. Oligomeric structure of the *Bacillus subtilis* cell division protein DivIVA determined by transmission electron microscopy. Mol Microbiol **52:**1281-1290.
260. **Bramkamp M, Emmins R, Weston L, Donovan C, Daniel RA, Errington J.** 2008. A novel component of the division-site selection system of *Bacillus subtilis* and a new mode of action for the division inhibitor MinCD. Mol Microbiol **70:**1556-1569.
261. **Patrick JE, Kearns DB.** 2008. MinJ (YvjD) is a topological determinant of cell division in *Bacillus subtilis*. Mol Microbiol **70:**1166-1179.
262. **Ben-Yehuda S, Rudner DZ, Losick R.** 2003. RacA, a bacterial protein that anchors chromosomes to the cell poles. Science **299:**532-536.
263. **Wu LJ, Errington J.** 2003. RacA and the Soj-Spo0J system combine to effect polar chromosome segregation in sporulating *Bacillus subtilis*. Mol Microbiol **49:**1463-1475.
264. **Hempel AM, Wang SB, Letek M, Gil JA, Flardh K.** 2008. Assemblies of DivIVA mark sites for hyphal branching and can establish new zones of cell wall growth in *Streptomyces coelicolor*. J Bacteriol **190:**7579-7583.
265. **Meniche X, Otten R, Siegrist MS, Baer CE, Murphy KC, Bertozzi CR, Sassetti CM.** 2014. Subpolar addition of new cell wall is directed by DivIVA in mycobacteria. Proc Natl Acad Sci U S A **111:**E3243-3251.
266. **Donovan C, Sieger B, Kramer R, Bramkamp M.** 2012. A synthetic *Escherichia coli* system identifies a conserved origin tethering factor in Actinobacteria. Mol Microbiol **84:**105-116.
267. **Babudieri B.** 1950. [Nature of the so-called S-formen of Leptospira; their identification with *Hyphomicrobium vulgare* Stutzer & Hartleb; study of the latter]. Rend Ist Sup Sanit **13:**580-591.
268. **Laloux G, Jacobs-Wagner C.** 2013. Spatiotemporal control of PopZ localization through cell cycle-coupled multimerization. J Cell Biol **201:**827-841.

269. **Ebersbach G, Briegel A, Jensen GJ, Jacobs-Wagner C.** 2008. A self-associating protein critical for chromosome attachment, division, and polar organization in *caulobacter*. Cell **134:**956-968.
270. **Bowman GR, Comolli LR, Gaietta GM, Fero M, Hong SH, Jones Y, Lee JH, Downing KH, Ellisman MH, McAdams HH, Shapiro L.** 2010. *Caulobacter* PopZ forms a polar subdomain dictating sequential changes in pole composition and function. Mol Microbiol **76:**173-189.
271. **Saberi S, Emberly E.** 2010. Chromosome driven spatial patterning of proteins in bacteria. PLoS Comput Biol **6:**e1000986.
272. **Hay NA, Tipper DJ, Gygi D, Hughes C.** 1999. A novel membrane protein influencing cell shape and multicellular swarming of *Proteus mirabilis*. J Bacteriol **181:**2008-2016.
273. **Vasa S, Lin L, Shi C, Habenstein B, Riedel D, Kuhn J, Thanbichler M, Lange A.** 2015. beta-Helical architecture of cytoskeletal bactofilin filaments revealed by solid-state NMR. Proc Natl Acad Sci U S A **112:**E127-136.
274. **Hughes HV, Huitema E, Pritchard S, Keiler KC, Brun YV, Viollier PH.** 2010. Protein localization and dynamics within a bacterial organelle. Proc Natl Acad Sci U S A **107:**5599-5604.
275. **Hughes HV, Lisher JP, Hardy GG, Kysela DT, Arnold RJ, Giedroc DP, Brun YV.** 2013. Co-ordinate synthesis and protein localization in a bacterial organelle by the action of a penicillin-binding-protein. Mol Microbiol **90:**1162-1177.
276. **Randich AM, Brun YV.** 2015. Molecular mechanisms for the evolution of bacterial morphologies and growth modes. Front Microbiol **6:**580.
277. **Lin L.** 2013. Cytoskeletons as Polar Landmarks: Characterization of bactofilin homologs in *Myxococcus xanthus*. PhD. Philipps-Universität Marburg, Marburg an der Lahn.
278. **Shi C, Fricke P, Lin L, Chevelkov V, Wegstroth M, Giller K, Becker S, Thanbichler M, Lange A.** 2015. Atomic-resolution structure of cytoskeletal bactofilin by solid-state NMR. Sci Adv **1:**e1501087.
279. **Koch MK, McHugh CA, Hoiczyk E.** 2011. BacM, an N-terminally processed bactofilin of *Myxococcus xanthus*, is crucial for proper cell shape. Mol Microbiol **80:**1031-1051.
280. **Bulyha I, Lindow S, Lin L, Bolte K, Wuichet K, Kahnt J, van der Does C, Thanbichler M, Sogaard-Andersen L.** 2013. Two small GTPases act in concert with the bactofilin cytoskeleton to regulate dynamic bacterial cell polarity. Dev Cell **25:**119-131.
281. **Bulyha I, Schmidt C, Lenz P, Jakovljevic V, Hone A, Maier B, Hoppert M, Sogaard-Andersen L.** 2009. Regulation of the type IV pili molecular machine by dynamic localization of two motor proteins. Mol Microbiol **74:**691-706.
282. **Han S, Caspers N, Zaniewski RP, Lacey BM, Tomaras AP, Feng X, Geoghegan KF, Shanmugasundaram V.** 2011. Distinctive attributes of beta-lactam target proteins in *Acinetobacter baumannii* relevant to development of new antibiotics. J Am Chem Soc **133:**20536-20545.
283. **El Andari J, Altegoer F, Bange G, Graumann PL.** 2015. *Bacillus subtilis* bactofilins are essential for flagellar hook- and filament assembly and dynamically localize into structures of less than 100 nm diameter underneath the cell membrane. PLoS One **10:**e0141546.
284. **Sycuro LK, Pincus Z, Gutierrez KD, Biboy J, Stern CA, Vollmer W, Salama NR.** 2010. Peptidoglycan crosslinking relaxation promotes *Helicobacter pylori's* helical shape and stomach colonization. Cell **141:**822-833.
285. **Takacs CN, Poggio S, Charbon G, Pucheault M, Vollmer W, Jacobs-Wagner C.** 2010. MreB drives de novo rod morphogenesis in *Caulobacter crescentus* via remodeling of the cell wall. J Bacteriol **192:**1671-1684.
286. **Gitai Z, Dye NA, Reisenauer A, Wachi M, Shapiro L.** 2005. MreB actin-mediated segregation of a specific region of a bacterial chromosome. Cell **120:**329-341.

287. **Karczmarek A, Martinez-Arteaga R, Alexeeva S, Hansen FG, Vicente M, Nanninga N, den Blaauwen T.** 2007. DNA and origin region segregation are not affected by the transition from rod to sphere after inhibition of *Escherichia coli* MreB by A22. Mol Microbiol **65:**51-63.
288. **Bendezu FO, Hale CA, Bernhardt TG, de Boer PA.** 2009. RodZ (YfgA) is required for proper assembly of the MreB actin cytoskeleton and cell shape in *E. coli*. EMBO J **28:**193-204.
289. **Shiomi D, Sakai M, Niki H.** 2008. Determination of bacterial rod shape by a novel cytoskeletal membrane protein. Embo Journal **27:**3081-3091.
290. **Alyahya SA, Alexander R, Costa T, Henriques AO, Emonet T, Jacobs-Wagner C.** 2009. RodZ, a component of the bacterial core morphogenic apparatus. Proc Natl Acad Sci U S A **106:**1239-1244.
291. **Henriques AO, Glaser P, Piggot PJ, Moran CP, Jr.** 1998. Control of cell shape and elongation by the *rodA* gene in *Bacillus subtilis*. Mol Microbiol **28:**235-247.
292. **Kruse T, Bork-Jensen J, Gerdes K.** 2005. The morphogenetic MreBCD proteins of *Escherichia coli* form an essential membrane-bound complex. Mol Microbiol **55:**78-89.
293. **den Blaauwen T, de Pedro MA, Nguyen-Disteche M, Ayala JA.** 2008. Morphogenesis of rod-shaped sacculi. FEMS Microbiol Rev **32:**321-344.
294. **Ishino F, Park W, Tomioka S, Tamaki S, Takase I, Kunugita K, Matsuzawa H, Asoh S, Ohta T, Spratt BG, et al.** 1986. Peptidoglycan synthetic activities in membranes of *Escherichia coli* caused by overproduction of penicillin-binding protein 2 and RodA protein. J Biol Chem **261:**7024-7031.
295. **de Pedro MA, Donachie WD, Holtje JV, Schwarz H.** 2001. Constitutive septal murein synthesis in *Escherichia coli* with impaired activity of the morphogenetic proteins RodA and penicillin-binding protein 2. J Bacteriol **183:**4115-4126.
296. **Morgenstein RM, Bratton BP, Nguyen JP, Ouzounov N, Shaevitz JW, Gitai Z.** 2015. RodZ links MreB to cell wall synthesis to mediate MreB rotation and robust morphogenesis. Proc Natl Acad Sci U S A doi:10.1073/pnas.1509610112.
297. **van den Ent F, Leaver M, Bendezu F, Errington J, de Boer P, Lowe J.** 2006. Dimeric structure of the cell shape protein MreC and its functional implications. Mol Microbiol **62:**1631-1642.
298. **Vats P, Shih YL, Rothfield L.** 2009. Assembly of the MreB-associated cytoskeletal ring of *Escherichia coli*. Mol Microbiol **72:**170-182.
299. **White CL, Kitich A, Gober JW.** 2010. Positioning cell wall synthetic complexes by the bacterial morphogenetic proteins MreB and MreD. Mol Microbiol **76:**616-633.
300. **Mohammadi T, Karczmarek A, Crouvoisier M, Bouhss A, Mengin-Lecreulx D, den Blaauwen T.** 2007. The essential peptidoglycan glycosyltransferase MurG forms a complex with proteins involved in lateral envelope growth as well as with proteins involved in cell division in *Escherichia coli*. Mol Microbiol **65:**1106-1121.
301. **Banzhaf M, van den Berg van Saparoea B, Terrak M, Fraipont C, Egan A, Philippe J, Zapun A, Breukink E, Nguyen-Disteche M, den Blaauwen T, Vollmer W.** 2012. Cooperativity of peptidoglycan synthases active in bacterial cell elongation. Mol Microbiol **85:**179-194.
302. **Popp D, Narita A, Maeda K, Fujisawa T, Ghoshdastider U, Iwasa M, Maeda Y, Robinson RC.** 2010. Filament structure, organization, and dynamics in MreB sheets. J Biol Chem **285:**15858-15865.
303. **Biteen JS, Moerner WE.** 2010. Single-molecule and superresolution imaging in live bacteria cells. Cold Spring Harb Perspect Biol **2:**a000448.
304. **Kim SY, Gitai Z, Kinkhabwala A, Shapiro L, Moerner WE.** 2006. Single molecules of the bacterial actin MreB undergo directed treadmilling motion in *Caulobacter crescentus*. Proc Natl Acad Sci U S A **103:**10929-10934.
305. **Egan AJ, Vollmer W.** 2013. The physiology of bacterial cell division. Ann N Y Acad Sci **1277:**8-28.

306. **Aarsman ME, Piette A, Fraipont C, Vinkenvleugel TM, Nguyen-Disteche M, den Blaauwen T.** 2005. Maturation of the *Escherichia coli* divisome occurs in two steps. Mol Microbiol **55:**1631-1645.
307. **Haney SA, Glasfeld E, Hale C, Keeney D, He Z, de Boer P.** 2001. Genetic analysis of the *Escherichia coli* FtsZ.ZipA interaction in the yeast two-hybrid system. Characterization of FtsZ residues essential for the interactions with ZipA and with FtsA. J Biol Chem **276:**11980-11987.
308. **Durand-Heredia J, Rivkin E, Fan G, Morales J, Janakiraman A.** 2012. Identification of ZapD as a cell division factor that promotes the assembly of FtsZ in *Escherichia coli*. J Bacteriol **194:**3189-3198.
309. **Gueiros-Filho FJ, Losick R.** 2002. A widely conserved bacterial cell division protein that promotes assembly of the tubulin-like protein FtsZ. Genes Dev **16:**2544-2556.
310. **Low HH, Moncrieffe MC, Lowe J.** 2004. The crystal structure of ZapA and its modulation of FtsZ polymerisation. J Mol Biol **341:**839-852.
311. **Galli E, Gerdes K.** 2010. Spatial resolution of two bacterial cell division proteins: ZapA recruits ZapB to the inner face of the Z-ring. Mol Microbiol **76:**1514-1526.
312. **Arends SJ, Kustusch RJ, Weiss DS.** 2009. ATP-binding site lesions in FtsE impair cell division. J Bacteriol **191:**3772-3784.
313. **Corbin BD, Wang Y, Beuria TK, Margolin W.** 2007. Interaction between cell division proteins FtsE and FtsZ. J Bacteriol **189:**3026-3035.
314. **Corbin BD, Geissler B, Sadasivam M, Margolin W.** 2004. Z-ring-independent interaction between a subdomain of FtsA and late septation proteins as revealed by a polar recruitment assay. J Bacteriol **186:**7736-7744.
315. **Aaron M, Charbon G, Lam H, Schwarz H, Vollmer W, Jacobs-Wagner C.** 2007. The tubulin homologue FtsZ contributes to cell elongation by guiding cell wall precursor synthesis in *Caulobacter crescentus*. Mol Microbiol **64:**938-952.
316. **de Pedro MA, Quintela JC, Holtje JV, Schwarz H.** 1997. Murein segregation in *Escherichia coli*. J Bacteriol **179:**2823-2834.
317. **Fenton AK, Gerdes K.** 2013. Direct interaction of FtsZ and MreB is required for septum synthesis and cell division in *Escherichia coli*. EMBO J **32:**1953-1965.
318. **Chen JC, Beckwith J.** 2001. FtsQ, FtsL and FtsI require FtsK, but not FtsN, for co-localization with FtsZ during *Escherichia coli* cell division. Mol Microbiol **42:**395-413.
319. **Mercer KL, Weiss DS.** 2002. The *Escherichia coli* cell division protein FtsW is required to recruit its cognate transpeptidase, FtsI (PBP3), to the division site. J Bacteriol **184:**904-912.
320. **Fraipont C, Alexeeva S, Wolf B, van der Ploeg R, Schloesser M, den Blaauwen T, Nguyen-Disteche M.** 2011. The integral membrane FtsW protein and peptidoglycan synthase PBP3 form a subcomplex in *Escherichia coli*. Microbiology **157:**251-259.
321. **Di Lallo G, Fagioli M, Barionovi D, Ghelardini P, Paolozzi L.** 2003. Use of a two-hybrid assay to study the assembly of a complex multicomponent protein machinery: bacterial septosome differentiation. Microbiology **149:**3353-3359.
322. **Karimova G, Dautin N, Ladant D.** 2005. Interaction network among *Escherichia coli* membrane proteins involved in cell division as revealed by bacterial two-hybrid analysis. J Bacteriol **187:**2233-2243.
323. **Alexeeva S, Gadella TW, Jr., Verheul J, Verhoeven GS, den Blaauwen T.** 2010. Direct interactions of early and late assembling division proteins in *Escherichia coli* cells resolved by FRET. Mol Microbiol **77:**384-398.
324. **Müller P, Ewers C, Bertsche U, Anstett M, Kallis T, Breukink E, Fraipont C, Terrak M, Nguyen-Disteche M, Vollmer W.** 2007. The essential cell division protein FtsN interacts with the murein (peptidoglycan) synthase PBP1B in *Escherichia coli*. J Biol Chem **282:**36394-36402.

325. **Vollmer W, von Rechenberg M, Holtje JV.** 1999. Demonstration of molecular interactions between the murein polymerase PBP1B, the lytic transglycosylase MltA, and the scaffolding protein MipA of *Escherichia coli*. J Biol Chem **274:**6726-6734.
326. **Gerding MA, Ogata Y, Pecora ND, Niki H, de Boer PA.** 2007. The trans-envelope Tol-Pal complex is part of the cell division machinery and required for proper outer-membrane invagination during cell constriction in *E. coli*. Mol Microbiol **63:**1008-1025.
327. **Yeh YC, Comolli LR, Downing KH, Shapiro L, McAdams HH.** 2010. The caulobacter Tol-Pal complex is essential for outer membrane integrity and the positioning of a polar localization factor. J Bacteriol **192:**4847-4858.
328. **Stewart EJ, Madden R, Paul G, Taddei F.** 2005. Aging and death in an organism that reproduces by morphologically symmetric division. PLoS Biol **3:**e45.
329. **Burman LG, Raichler J, Park JT.** 1983. Evidence for diffuse growth of the cylindrical portion of the *Escherichia coli* murein sacculus. J Bacteriol **155:**983-988.
330. **Clarke-Sturman AJ, Archibald AR, Hancock IC, Harwood CR, Merad T, Hobot JA.** 1989. Cell wall assembly in *Bacillus subtilis*: partial conservation of polar wall material and the effect of growth conditions on the pattern of incorporation of new material at the polar caps. J Gen Microbiol **135:**657-665.
331. **Merad T, Archibald AR, Hancock IC, Harwood CR, Hobot JA.** 1989. Cell wall assembly in *Bacillus subtilis*: visualization of old and new wall material by electron microscopic examination of samples stained selectively for teichoic acid and teichuronic acid. J Gen Microbiol **135:**645-655.
332. **Mobley HL, Koch AL, Doyle RJ, Streips UN.** 1984. Insertion and fate of the cell wall in *Bacillus subtilis*. J Bacteriol **158:**169-179.
333. **Wientjes FB, Nanninga N.** 1989. Rate and topography of peptidoglycan synthesis during cell division in *Escherichia coli*: concept of a leading edge. J Bacteriol **171:**3412-3419.
334. **Joyce G, Williams KJ, Robb M, Noens E, Tizzano B, Shahrezaei V, Robertson BD.** 2012. Cell division site placement and asymmetric growth in *mycobacteria*. PLoS One **7:**e44582.
335. **Chauhan A, Lofton H, Maloney E, Moore J, Fol M, Madiraju MV, Rajagopalan M.** 2006. Interference of *Mycobacterium tuberculosis* cell division by Rv2719c, a cell wall hydrolase. Mol Microbiol **62:**132-147.
336. **Brown PJ, Kysela DT, Brun YV.** 2011. Polarity and the diversity of growth mechanisms in bacteria. Semin Cell Dev Biol **22:**790-798.
337. **Hirsch P.** 1974. Budding bacteria. Annu Rev Microbiol **28:**391-444.
338. **Margolin W.** 2009. Sculpting the bacterial cell. Curr Biol **19:**R812-822.
339. **Wagner JK, Brun YV.** 2007. Out on a limb: how the *Caulobacte*r stalk can boost the study of bacterial cell shape. Mol Microbiol **64:**28-33.
340. **Ong CJ, Wong ML, Smit J.** 1990. Attachment of the adhesive holdfast organelle to the cellular stalk of *Caulobacter crescentus*. J Bacteriol **172:**1448-1456.
341. **Ireland MM, Karty JA, Quardokus EM, Reilly JP, Brun YV.** 2002. Proteomic analysis of the *Caulobacter crescentus* stalk indicates competence for nutrient uptake. Mol Microbiol **45:**1029-1041.
342. **Pate JL, Ordal EJ.** 1965. The fine structure of two unusual stalked bacteria. J Cell Biol **27:**133-150.
343. **Gonin M, Quardokus EM, O'Donnol D, Maddock J, Brun YV.** 2000. Regulation of stalk elongation by phosphate in *Caulobacter crescentus*. J Bacteriol **182:**337-347.
344. **Wagner JK, Setayeshgar S, Sharon LA, Reilly JP, Brun YV.** 2006. A nutrient uptake role for bacterial cell envelope extensions. Proc Natl Acad Sci U S A **103:**11772-11777.

345. **Schlimpert S, Klein EA, Briegel A, Hughes V, Kahnt J, Bolte K, Maier UG, Brun YV, Jensen GJ, Gitai Z, Thanbichler M.** 2012. General protein diffusion barriers create compartments within bacterial cells. Cell **151:**1270-1282.
346. **Moore RL.** 1981. The biology of *Hyphomicrobium* and other prosthecate, budding bacteria. Annu Rev Microbiol **35:**567-594.
347. **Whittenbury R, Dow CS.** 1977. Morphogenesis and differentiation in *Rhodomicrobium vannielii* and other budding and prosthecate bacteria. Bacteriol Rev **41:**754-808.
348. **Badger JH, Eisen JA, Ward NL.** 2005. Genomic analysis of *Hyphomonas neptunium* contradicts 16S rRNA gene-based phylogenetic analysis: implications for the taxonomy of the orders 'Rhodobacterales' and Caulobacterales. Int J Syst Evol Microbiol **55:**1021-1026.
349. **Badger JH, Hoover TR, Brun YV, Weiner RM, Laub MT, Alexandre G, Mrazek J, Ren Q, Paulsen IT, Nelson KE, Khouri HM, Radune D, Sosa J, Dodson RJ, Sullivan SA, Rosovitz MJ, Madupu R, Brinkac LM, Durkin AS, Daugherty SC, Kothari SP, Giglio MG, Zhou L, Haft DH, Selengut JD, Davidsen TM, Yang Q, Zafar N, Ward NL.** 2006. Comparative genomic evidence for a close relationship between the dimorphic prosthecate bacteria *Hyphomonas neptunium* and *Caulobacter crescentus*. J Bacteriol **188:**6841-6850.
350. **Leifson E.** 1964. *Hyphomicrobium neptunium* sp. n. Antonie Van Leeuwenhoek **30:**249-256.
351. **Havenner JA, McCardell BA, Weiner RM.** 1979. Development of defined, minimal, and complete media for the growth of *Hyphomicrobium neptunium*. Appl Environ Microbiol **38:**18-23.
352. **Devine RA, Weiner RM.** 1990. *Hyphomonas* species metabolize amino-acids using Krebs cycle enzymes. Microbios **62:**137-153.
353. **Wali TM, Hudson GR, Danald DA, Weiner RM.** 1980. Timing of swarmer cell cycle morphogenesis and macromolecular synthesis by *Hyphomicrobium neptunium* in synchronous culture. J Bacteriol **144:**406-412.
354. **Shapiro L, Agabian-Keshishian N, Bendis I.** 1971. Bacterial differentiation. Science **173:**884-892.
355. **Weiner RM, Blackman MA.** 1973. Inhibition of deoxyribonucleic acid synthesis and bud formation by nalidixic acid in *Hyphomicrobium neptunium*. J Bacteriol **116:**1398-1404.
356. **Zerfas PM, Kessel M, Quintero EJ, Weiner RM.** 1997. Fine-structure evidence for cell membrane partitioning of the nucleoid and cytoplasm during bud formation in *Hyphomonas* species. J Bacteriol **179:**148-156.
357. **Poindexter J.** 1992. Dimorphic prosthecate bacteria: the genera *Caulobacter*, *Asticcacaulis*, *Hyphomicrobium*, *Pedomicrobium*, *Hyphomonas* and *Thiodendron*, vol 5, p 72–90. Springer New York, Life Sciences.
358. **Duchow E, Douglas HC.** 1949. *Rhodomicrobium vannielii*, a new photoheterotrophic bacterium. J Bacteriol **58:**409-416.
359. **Altschul SF, Gish W, Miller W, Myers EW, Lipman DJ.** 1990. Basic local alignment search tool. J Mol Biol **215:**403-410.
360. **Finn RD, Bateman A, Clements J, Coggill P, Eberhardt RY, Eddy SR, Heger A, Hetherington K, Holm L, Mistry J, Sonnhammer EL, Tate J, Punta M.** 2014. Pfam: the protein families database. Nucleic Acids Res **42:**D222-230.
361. **Ayache J, Beaunier L, Boumendil J, Ehret G, Laub D.** 2010. Artifacts in Transmission Electron Microscopy, p 125-170, Sample Preparation Handbook for Transmission Electron Microscopy: Methodology doi:10.1007/978-0-387-98182-6_6. Springer New York, New York, NY.
362. **Kuhlbrandt W.** 2014. Cryo-EM enters a new era. Elife **3:**e03678.
363. **Poindexter JS, Staley JT.** 1996. *Caulobacter* and *Asticcacaulis* stalk bands as indicators of stalk age. J Bacteriol **178:**3939-3948.

364. **Jiang C, Brown PJ, Ducret A, Brun YV.** 2014. Sequential evolution of bacterial morphology by co-option of a developmental regulator. Nature **506:**489-493.
365. **Kuru E, Hughes HV, Brown PJ, Hall E, Tekkam S, Cava F, de Pedro MA, Brun YV, VanNieuwenhze MS.** 2012. *In Situ* probing of newly synthesized peptidoglycan in live bacteria with fluorescent D-amino acids. Angew Chem Int Ed Engl **51:**12519-12523.
366. **Jones HE, Hirsch P.** 1968. Cell wall composition of *Hypomicrobium* species. J Bacteriol **96:**1037-1041.
367. **Schultz J, Milpetz F, Bork P, Ponting CP.** 1998. SMART, a simple modular architecture research tool: identification of signaling domains. Proc Natl Acad Sci U S A **95:**5857-5864.
368. **Letunic I, Doerks T, Bork P.** 2015. SMART: recent updates, new developments and status in 2015. Nucleic Acids Res **43:**D257-260.
369. **Lupas A.** 1996. Coiled coils: new structures and new functions. Trends Biochem Sci **21:**375-382.
370. **Odintsov SG, Sabala I, Marcyjaniak M, Bochtler M.** 2004. Latent LytM at 1.3A resolution. J Mol Biol **335:**775-785.
371. **Agrawal V, Kishan KV.** 2003. OB-fold: growing bigger with functional consistency. Curr Protein Pept Sci **4:**195-206.
372. **Goldman RC, Gange D.** 2000. Inhibition of transglycosylation involved in bacterial peptidoglycan synthesis. Curr Med Chem **7:**801-820.
373. **Zhang Y.** 2008. I-TASSER server for protein 3D structure prediction. BMC Bioinformatics **9:**40.
374. **Roy A, Kucukural A, Zhang Y.** 2010. I-TASSER: a unified platform for automated protein structure and function prediction. Nat Protoc **5:**725-738.
375. **Yang J, Yan R, Roy A, Xu D, Poisson J, Zhang Y.** 2015. The I-TASSER Suite: protein structure and function prediction. Nat Methods **12:**7-8.
376. **LLC S.** 2015. The PyMOL Molecular Graphics System, v1.8.
377. **Bupp K, van Heijenoort J.** 1993. The final step of peptidoglycan subunit assembly in *Escherichia coli* occurs in the cytoplasm. J Bacteriol **175:**1841-1843.
378. **Mengin-Lecreulx D, Texier L, Rousseau M, van Heijenoort J.** 1991. The murG gene of *Escherichia coli* codes for the UDP-N-acetylglucosamine: N-acetylmuramyl-(pentapeptide) pyrophosphoryl-undecaprenol N-acetylglucosamine transferase involved in the membrane steps of peptidoglycan synthesis. J Bacteriol **173:**4625-4636.
379. **Favini-Stabile S, Contreras-Martel C, Thielens N, Dessen A.** 2013. MreB and MurG as scaffolds for the cytoplasmic steps of peptidoglycan biosynthesis. Environ Microbiol **15:**3218-3228.
380. **Bean GJ, Flickinger ST, Westler WM, McCully ME, Sept D, Weibel DB, Amann KJ.** 2009. A22 disrupts the bacterial actin cytoskeleton by directly binding and inducing a low-affinity state in MreB. Biochemistry **48:**4852-4857.
381. **Iwai N, Nagai K, Wachi M.** 2002. Novel S-benzylisothiourea compound that induces spherical cells in *Escherichia coli* probably by acting on a rod-shape-determining protein(s) other than penicillin-binding protein 2. Biosci Biotechnol Biochem **66:**2658-2662.
382. **Lee TK, Tropini C, Hsin J, Desmarais SM, Ursell TS, Gong E, Gitai Z, Monds RD, Huang KC.** 2014. A dynamically assembled cell wall synthesis machinery buffers cell growth. Proc Natl Acad Sci U S A **111:**4554-4559.
383. **Herrmann H, Aebi U.** 2004. Intermediate filaments: molecular structure, assembly mechanism, and integration into functionally distinct intracellular Scaffolds. Annu Rev Biochem **73:**749-789.
384. **Rosskopf S.** 2014. Analyse der Peptidoglycan-Biosynthese in *Hyphomonas neptunium*. Master of Science. Philipps Universität Marburg, Marburg an der Lahn.

385. **Wheeler RT, Shapiro L.** 1999. Differential localization of two histidine kinases controlling bacterial cell differentiation. Mol Cell **4:**683-694.
386. **Biondi EG, Reisinger SJ, Skerker JM, Arif M, Perchuk BS, Ryan KR, Laub MT.** 2006. Regulation of the bacterial cell cycle by an integrated genetic circuit. Nature **444:**899-904.
387. **Leicht O.** 2010. Etablierung eines genetischen Systems zur Analyse der Zellpolarität in *Hyphomonas neptunium*Philipps-Universität Marburg, Marburg an der Lahn.
388. **van den Ent F, Johnson CM, Persons L, de Boer P, Lowe J.** 2010. Bacterial actin MreB assembles in complex with cell shape protein RodZ. EMBO J **29:**1081-1090.
389. **Kysela DT, Brown PJ, Huang KC, Brun YV.** 2013. Biological consequences and advantages of asymmetric bacterial growth. Annu Rev Microbiol **67:**417-435.
390. **Kawai Y, Mercier R, Errington J.** 2014. Bacterial cell morphogenesis does not require a preexisting template structure. Curr Biol **24:**863-867.
391. **Takacs CN, Hocking J, Cabeen MT, Bui NK, Poggio S, Vollmer W, Jacobs-Wagner C.** 2013. Growth medium-dependent glycine incorporation into the peptidoglycan of *Caulobacter crescentus*. PLoS One **8:**e57579.
392. **Sauvage E, Kerff F, Terrak M, Ayala JA, Charlier P.** 2008. The penicillin-binding proteins: structure and role in peptidoglycan biosynthesis. FEMS Microbiol Rev **32:**234-258.
393. **Dougherty TJ, Kennedy K, Kessler RE, Pucci MJ.** 1996. Direct quantitation of the number of individual penicillin-binding proteins per cell in *Escherichia coli*. J Bacteriol **178:**6110-6115.
394. **Jung A.** 2016. Chromosome arrangement and dynamics in the budding bacterium *Hyphomonas neptunium*. PhD. Philipps-Universität Marburg, Marburg an der Lahn.
395. **Ramamurthi KS, Losick R.** 2009. Negative membrane curvature as a cue for subcellular localization of a bacterial protein. Proc Natl Acad Sci U S A **106:**13541-13545.
396. **van Ooij C, Losick R.** 2003. Subcellular localization of a small sporulation protein in *Bacillus subtilis*. J Bacteriol **185:**1391-1398.
397. **Yamada S, Sugai M, Komatsuzawa H, Nakashima S, Oshida T, Matsumoto A, Suginaka H.** 1996. An autolysin ring associated with cell separation of *Staphylococcus aureus*. J Bacteriol **178:**1565-1571.
398. **Ausubel F, Brent, R., Kingston, R., Moore, D., Seidman, J., Smith, J., and Struhl, K.** 2002. Short protocols in molecular biology: A Compendium of methods from current protocols in molecular biology. John Wiley & Sons Inc.
399. **Sambrook J, Fritsch, E., and Maniatis, T.** 1989. Molecular Cloning. A Laboratory Manual. Cold Spring Harbor Laboratory Press, Cold Spring Harbor, NY.
400. **Stepanovic S, Vukovic D, Dakic I, Savic B, Svabic-Vlahovic M.** 2000. A modified microtiter-plate test for quantification of staphylococcal biofilm formation. J Microbiol Methods **40:**175-179.
401. **Moore RL, Hirsch P.** 1973. First generation synchrony of isolated *Hyphomicrobium* swarmer populations. J Bacteriol **116:**418-423.
402. **Strobel W.** 2010. Etablierung von genetischen Methoden zur Analyse der Zellteilung in *Hyphomonas neptunium*University of Marburg, Marburg an der Lahn.
403. **Karimova G, Pidoux J, Ullmann A, Ladant D.** 1998. A bacterial two-hybrid system based on a reconstituted signal transduction pathway. Proc Natl Acad Sci U S A **95:**5752-5756.
404. **Laemmli UK.** 1970. Cleavage of structural proteins during the assembly of the head of bacteriophage T4. Nature **227:**680-685.
405. **Chen JC, Viollier PH, Shapiro L.** 2005. A membrane metalloprotease participates in the sequential degradation of a *Caulobacter* polarity determinant. Mol Microbiol **55:**1085-1103.
406. **Zor T, Selinger Z.** 1996. Linearization of the Bradford protein assay increases its sensitivity: theoretical and experimental studies. Anal Biochem **236:**302-308.

407. **Bradford MM.** 1976. A rapid and sensitive method for the quantitation of microgram quantities of protein utilizing the principle of protein-dye binding. Anal Biochem **72:**248-254.
408. **Geer LY, Marchler-Bauer A, Geer RC, Han L, He J, He S, Liu C, Shi W, Bryant SH.** 2010. The NCBI BioSystems database. Nucleic Acids Res **38:**D492-496.
409. **Finn RD, Mistry J, Tate J, Coggill P, Heger A, Pollington JE, Gavin OL, Gunasekaran P, Ceric G, Forslund K, Holm L, Sonnhammer EL, Eddy SR, Bateman A.** 2010. The Pfam protein families database. Nucleic Acids Res **38:**D211-222.
410. **Bateman A, Coin L, Durbin R, Finn RD, Hollich V, Griffiths-Jones S, Khanna A, Marshall M, Moxon S, Sonnhammer EL, Studholme DJ, Yeats C, Eddy SR.** 2004. The Pfam protein families database. Nucleic Acids Res **32:**D138-141.
411. **Jones DT.** 1999. Protein secondary structure prediction based on position-specific scoring matrices. J Mol Biol **292:**195-202.
412. **Bryson K, McGuffin LJ, Marsden RL, Ward JJ, Sodhi JS, Jones DT.** 2005. Protein structure prediction servers at University College London. Nucleic Acids Res **33:**W36-38.
413. **Letunic I, Doerks T, Bork P.** 2009. SMART 6: recent updates and new developments. Nucleic Acids Res **37:**D229-232.
414. **Tsirigos KD, Peters C, Shu N, Kall L, Elofsson A.** 2015. The TOPCONS web server for consensus prediction of membrane protein topology and signal peptides. Nucleic Acids Res **43:**W401-407.
415. **Regh C.** 2015. Analyse der Transpeptidasen HNE_0929 und HNE_3551 in *Hyphomonas neptunium*. Bachelor of Science. Philipps-Universität Marburg, Marburg an de rLahn.
416. **Evinger M, Agabian N.** 1977. Envelope-associated nucleoid from Caulobacter crescentus stalked and swarmer cells. J Bacteriol **132:**294-301.
417. **Cserti E.** 2011. The analysis of budding in *Hyphomonas neptunium*. M.Sc of Science. Philipps-Universität Marburg, Marburg an der Lahn.
418. **Eisheuer S.** 2016. Characterization of the division apparatus in the budding bacterium *Hyphomonas neptunium*. PhD. Philipps-Universität Marburg, Marburg an der Lahn.
419. **Thanbichler M, Iniesta AA, Shapiro L.** 2007. A comprehensive set of plasmids for vanillate- and xylose-inducible gene expression in *Caulobacter crescentus*. Nucleic Acids Res **35:**e137.

Einverständniserklärung

Ich versichere, dass ich meine Dissertation:

„Control of morphogenesis in the budding Alphaproteobacterium *Hyphomonas neptunium* “

selbstständig, ohne unerlaubte Hilfe angefertigt und mich dabei keiner anderen als der von mir ausdrücklich bezeichneten Quellen und Hilfen bedient habe.

Die Dissertation wurde in der jetzigen oder einer ähnlichen Form noch bei keiner anderen Hochschule eingereicht und hat noch keinen sonstigen Prüfungszwecken gedient.

Marburg, den 06.07.2016 _____

Emőke Cserti